A contribution to photonic MEMS : study of optical resonators and interferometers based on all-silicon Bragg reflectors

Maurine Malak Karam

UNIVERSITÉ PARIS-EST

Ecole Doctorale

Mathématiques et Sciences et Technologies de l'Information et de la Communication (MSTIC)

THÈSE

Pour obtenir le grade de

Docteur de l'Université Paris-Est

Spécialité : Electronique, Optronique et Systèmes

Présentée et soutenue publiquement par

Maurine MALAK KARAM

Le 17 Novembre 2011

Contribution aux MEMS Photoniques :
Etude de Résonateurs et Interféromètres Optiques Basés sur des Réflecteurs de Bragg Tout Silicium

A Contribution to Photonic MEMS:
Study of Optical Resonators and Interferometers Based on All-Silicon Bragg Reflectors

Directeur de thèse

Professeur Tarik BOUROUINA

Jury

Lionel BUCHAILLOT, Directeur de recherche CNRS, IEMN	Rapporteur
Henri CAMON, Directeur de recherche CNRS, LAAS	Rapporteur
Ai-Qun LIU, Professeur, Nanyang Technological University NTU, Singapour	Examinateur
Wilfried NOELL, Directeur de recherche, EPFL, Suisse	Examinateur
Alain BOSSEBOEUF, Directeur de recherche CNRS, IEF, Université d'Orsay	Examinateur
Elodie RICHALOT, Professeur, Université Paris-Est, UPEMLV	Examinateur
Tarik BOUROUINA, Professeur, Université Paris-Est, ESIEE Paris	Examinateur

Invités

Dr. Olivier LE TRAON, Office National d'Etudes et de Recherches Aérospatiales, ONERA-Châtillon.

Dr. Hichem NOUIRA, Laboratoire National de Métrologie et d'Essais, LNE-Paris

Remerciements

L'achèvement de cette thèse ne pourrait pas être possible sans l'union de plusieurs acteurs en possession de bonté, de talents, d'outils et parfois de pouvoir. Il faut donc les reconnaître et leur rendre hommage.

Tout d'abord, je remercie les membres du jury, rapporteurs, examinateurs et invités pour avoir accepté le review de ma thèse, pour avoir pris le temps de lire mon manuscrit ainsi que pour l'effort qu'ils ont accordé pour comprendre le sujet qui est peut-être loin de leurs activités de recherches. Votre présence était remarquable et a rendu la soutenance un événement spécial. Merci à tous !

En premier lieu, je reconnais les différentes organisations qui ont financé mon projet de thèse. Je remercie l'ambassade de France en Egypte representée par le service Campus France du CFCC pour le premier financement que j'ai reçue pour commencer ma thèse. Ceci constituait un financement partiel de 11 mois sous forme d'une bourse du gouvernement francais. Dans ce conteste, je reconnais Mr. Fabien Flori de l'université Francaise d'Egypte pour le support de mon dossier de candidature. Je reconnais également nos collaborateurs du LNE-Paris et de l'ONERA, fondation EADS pour les financements ultérieurs que j'ai reçus pour continuer ma thèse et le post-doc qui suit.

En deuxième lieu vient le remerciement pour mes collègues du département et notamment, Dr. Philippe Basset pour le support financier qu'il a présenté de très bonne humeur et à plusieurs reprises durant toutes les années écoulées de la thèse. Je commémore également Prof Dan Angelescu qui nous a aidés à travers nos discussions constructives. Je voudrais remercier aussi Dr. Lionel Rousseau pour m'avoir appris l'outil le plus important pour l'ingénieur de MEMS : le dessin des masques. Je n'oublierai pas ton support et tes conseils très constructifs.

Je tiens à remercier l'administration de l'ED MSTIC de l'université Paris-Est représentée par Mme Sylvie Cach, ainsi que l'administration de l'ESIEE représentée par Mme Martine Elichabe et Prof Geneviève Baudoin de la direction de la recherche pour toute aide qu'elles m'ont présentée durant les années écoulées de la thèse. Je remercie également Mme Marie-Laure Lequeux, l'assistante de notre département pour son aide sur toutes les démarches adiministratives.

Mes sincères remerciements vont pour mes copains et mes copines du labo. Je remercie du fond du cœur mes amies de bureau Kim Ngoc Nguyen et Jayalakshmi Parasuraman. Je remercie aussi mes copains du département Systèmes Electroniques. En particulier, je remercie William César et Sébastian Wahl pour avoir pris le temps de corriger la version française mon manuscrit. Je remerice aussi Julien Pagazani et Alexandre Bongrain. Il ne faut pas oublier aussi Mr. Laurent Bues pour sa patience envers l'énorme nombre de commande que je lui ai demandé de faire passer durant ma thèse. Merci Laurent !

J'apprécie beaucoup l'aide qui m'a été présenté par les collègues du département Télécom, spécialement Dr. Jean-Luc Polleux avec qui on a réussi à fonder une plateforme de caractérisation pour les MEMS optiques. Je remercie aussi mes copains du département Télécom : Julien Schiellein et Carlos Viana.

Je remercie aussi Prof. Yves-Alain Peter de l'Ecole Polytechnique de Montréal, Canada pour m'avoir accueilli dans son labo durant le stage doctoral que j'ai effectué à Montréal pour 4 mois en 2010. Je remercie

aussi Hubert Camirand pour la bonne volonté présentée pour le travail au MEB. A ce propos, je remercie l'Université Paris-Est pour m'avoir accordé le financement nécessaire pour effectuer ce séjour à Montréal.

Il ne faut pas oublier l'équipe du SMM – Service de la salle blanche de l'ESIEE. En particulier, Mr. Frédéric Marty qui s'est occupé de presque toutes les réalisations technologiques des structures présentés dans ma thèse. Franchement, j'admire les photos MEB présentées dans ma thèse qui sont très impressionnantes. Tu as présenté ton aide toujours avec un très agréable sourire. Merci Fréd ! Je ne peux pas non plus oublier l'aide que m'a présenté Nicolas Pavy, Pascal Jouannard, Serge Didelon et Bruno Capellazzi. Je commémore aussi Mr. Bruno Mercier, le directeur de l'équipe SMM, pour avoir investi en moi en acceptant la réalisation des mes structures en salle blanche à temps pour sécuriser l'avancement de ma thèse.

Je voudrais remercier chaleuresement Dr. Anne-Françoise Obaton du LNE-Trappes pour le temps et l'effort qu'elle a consacré en vue d'explorer une nouvelle direction relative aux cavités incurvées. Le travail avec toi était une expérience intéressante et conviviale qui m'a permis de voir et de comprendre des choses au-delà de la thèse. Merci Anne-Françoise !

En avant dernier vient le remerciement à mes bons et généreux parents qui m'ont supporté et soutenu tout le long du trajet de mes études supérieures. Merci papa pour tout ce que tu as fait pour moi, merci maman pour ta patience, ton soutien spirituel et ta compréhension pour les moments difficiles.

Contre l'habitude, j'ai préféré mettre le dernier et plus grand remerciement à mon prof. Tarik Bourouina. Avant tout, je vous remercie d'avoir accepté la prise en charge de cette thèse seul, sans co-directeur contrairement à ce qui a été promis au début. Je tiens à vous remercier pour votre soutien depuis que je suis arrivée en France. Sans votre implication, vos profondes réflexions et votre ardeur le début et l'aboutissement de cette thèse ne pourrait jamais être garanti.

En effet, vous avez joué plusieurs rôles dans ma thèse. Vous n'étiez pas seulement un directeur de thèse. Vous étiez le metteur en scène si ça se dit, l'actionneur et le coordinateur sur tous les aspects, vraiment, un grand frère qui est très difficile à trouver. Sans votre courage, vos bons sens et vos bravos pour moi, ce travail n'aurait pas vu la lumière. Et comme vous me le disiez toujours, je vous le répète : « C'est difficile de trouver quelqu'un de bon ! ». Vous m'avez appris beaucoup de principes, je suis fière d'être votre étudiante. J'espère avoir assumé honnêtement mes charges envers vous.

Je m'excuse à toute personne qui lira cette page et qui ne trouvera pas son nom. C'est malgré moi que je t'ai oublié cher ami. Je te prie d'accepter mes excuses !

Finalement, j'espère avoir réalisé quelque chose de beau, marquant et noble pour l'ESIEE, l'établissement que j'ai tant désiré, tant aimé et tant apprécié. Merci ESIEE !

Maurine Malak
ESIEE Paris, France
2 Décembre 2011

Résumé court en Français

Ce travail de recherche a été mené afin d'introduire une nouvelle classe de résonateurs Fabry-Pérot (FP): Les cavités FP incurvées basées sur des miroirs de Bragg sans revêtement, de forme cylindrique et obtenues par micro-usinage du silicium. Une autre spécificité est la longueur de la cavité assez grande (L> 200 μm) combinée à un haut facteur de qualité Q (jusqu'à 10^4), pour répondre aux applications de type spectroscopique d'absorption améliorée par résonance optique, dans laquelle le produit est Q.L une figure de mérite. Dans ce contexte, l'architecture de base a été modélisée analytiquement pour déterminer les modes transverses d'ordre élevé soutenus par de telles cavités. Par conséquent, les conditions expérimentales qui conduisent à une excitation préférentielle (ou rejet) de ces modes ont été testées expérimentalement menant à la validation de notre modèle théorique et à une meilleure compréhension du comportement de la cavité. Une seconde architecture, basée sur la cavité FP incurvée avec une lentille cylindrique a été développée dans le but de fournir une architecture plus stable. Cette dernière a été également modélisée, fabriquée et caractérisée menant à l'amélioration attendue en termes de performances.

Enfin, comme complément à notre étude sur les résonateurs, nous avons commencé à explorer les applications des interféromètres optiques à base de miroirs de Bragg en silicium. À cette fin, un microsystème de mesure optique a été conçu, fabriqué et caractérisé, il consiste en une sonde optique pour la profilométrie de surface dans des milieux confinés, basé sur un interféromètre de Michelson monolithique en silicium.

Short Summary in English

This research work has been conducted to introduce a novel class of Fabry-Perot (FP) resonators: Curved FP cavity based on *coating-free Bragg mirrors of cylindrical shape*, obtained by silicon micromachining. Another specificity is the rather large cavity lengths (L>200 μm) combined with high quality factor Q (up to 10^4), for the purpose of applications requiring cavity enhanced absorption spectroscopy, in which the product Q.L is a figure of merit. In this contest, the basic architecture has been modeled analytically to know the high order transverse modes supported by such cavities. Hence, the experimental conditions which lead to preferential excitation (or rejection) of these modes have been tested experimentally leading to the validation of our theoretical model and to a better understanding of the cavity behaviour. A second architecture, based on the curved FP together with a fiber rod lens has been developed for the purpose of providing stable designs. It was also modeled, fabricated and characterized leading to the expected performance improvements.

Finally, as a complement to our study on resonators, we started exploring applications of optical interferometers based on similar micromachined silicon Bragg mirrors. For this purpose, an optical measurement microsystem was designed, fabricated and characterized; it consists of an optical probe for surface profilometry in confined environments, based on an all-silicon Michelson interferometer.

TABLE OF CONTENTS

PART III Sensing Applications of Optical Interferometers: Optical Profilometry

PART IV Concluding Remarks

LIST OF FIGURES

LIST OF TALBES

Première Partie

RÉSUMÉ LONG EN FRANÇAIS

LONG SUMMARY IN FRENCH

Résumé en Français de la thèse

I.1 Introduction et contributions originales

La communication par fibres optiques est le domaine d'applications qui a poussé les chercheurs à développer et à étudier les microsystèmes opto-électro-mécaniques (MEMS), notamment la recherche sur les microrésonateurs optiques. Parmi ces derniers, figurent les cavités destinées au multiplexage par répartition en longueur d'onde - « Wavelength Division Multiplexing (WDM) ». A l'origine, des microrésonateurs Fabry-Pérot (FP) à base de silicium, ont été développés comme filtres accordables et comme lasers à cavité externe. Ces cavités FP ont également trouvé un intérêt dans les applications métrologiques, dont la réfractométrie, les senseurs inertiels, la détection de gaz, ainsi que l'analyse chimique et biologique. Dans la plupart de ces applications, la largeur spectrale de la raie de résonance est d'un intérêt crucial lorsque l'on considère les performances du système, ce qui est également lié au facteur de qualité et à la finesse de la cavité. Des facteurs de qualité élevés sont souhaitables pour fournir une distinction entre des longueurs d'ondes spécifiques. La réflectance du miroir est donc d'importance majeure et c'est pour cela que les réflecteurs de Bragg sont préférés. Ces derniers peuvent-être obtenus, soit à partir de revêtements en couches minces de matériaux diélectriques, soit par le biais d'un micro-usinage du silicium, ce qui mène à des miroirs de Bragg verticaux de type Silicium-Air. Les miroirs de Bragg sont ainsi au cœur de nombreux composants optiques intégrés basés sur la propagation de la lumière en espace libre comme c'est le cas pour les résonateurs et les interféromètres. Ce travail de recherche met l'accent sur le développement de nouvelles architectures pour le résonateur de Fabry-Pérot et l'interféromètre de Michelson.

Cette thèse a pour contributions majeures d'avoir porté sur la la conception, la réalisation et la caractérisation de trois démonstrateurs, tous à base de miroirs de Bragg Silicium-air micro-usinés. Par ailleurs, chacun de ces démonstrateurs, ayant fait l'objet d'études comportementales tant au niveau de la modélisation que de l'expérimentation, a également révélé différentes perspectives d'applications. Ces dernières, étant très diverses, témoignent de l'impact potentiel de ces recherches.

Le premier démonstrateur concerne de nouvelles architectures proposées pour les cavités Fabry-Pérot à base de miroirs de surfaces incurvées et de forme cylindrique. Les structures réalisées montrent des performances supérieures en termes de facteur de qualité par rapport aux cavités conventionnelles à miroirs plans. Ainsi, ils présentent un fort potentiel pour les applications opto-fluidique et pourraient être utilisés dans les microsystèmes d'analyse de type *Lab-on-Chip*.

Le deuxième démonstrateur consiste en l'intégration d'un interféromètre de Michelson sous forme de sonde optique, destinée à la mesure dimensionnelle et à la profilométrie des surfaces cylindriques

dans des tubes creux de diamètre sub-millimétrique. Le prototype développé est étudié dans la gamme infrarouge.

I.2 Objectifs et Motivation

I.2.1 Objectifs

Cette thèse a deux principaux objectifs. Le premier objectif est de concevoir des microsystèmes innovants de micro-optiques et micro-opto-mécaniques (MEMS optiques) et d'explorer les phénomènes physiques impliqués dans le fonctionnement de tels microsystèmes. Le deuxième objectif est d'intégrer ces MEMS optiques compacts sur silicium pour créer des démonstrateurs de composants destinés à certaines applications exigeantes. L'une d'elle concerne la mesure, par voie optique, du profil de la surface intérieure des parois latérales de trous de diamètre sub-millimétrique.

I.2.2 Motivation

Ce travail de recherche a été motivé par de nombreuses raisons et avant tout par l'intérêt personnel pour la micro-optique et les MEMS. Notre motivation était de réaliser une étude approfondie sur un interféromètre optique particulier –le résonateur de Fabry-Pérot-, dans le but de fournir de nouvelles connaissances à la communauté scientifique. De plus, ce travail trouve sa place dans la stratégie du laboratoire ; en effet, à côté de la place importante des études fondamentales, l'intention est de déployer des MEMS optiques pour des applications *non télécom*, (très largement étudiées par ailleurs), mais en les ancrant plutôt dans le domaine des capteurs. En effet, les techniques optiques sont sans contact et ce sont donc des méthodes qui aident à préserver l'intégrité des structures mécaniques (forme et matériau demeurant ainsi un bloc monolithique de silicium monocristallin). Ceci évite également le recours à des signaux électriques, qui ne sont pas adaptés à certains environnements sévères et qui sont sensibles aux interférences avec des signaux parasites. Deux aspects différents peuvent alors être explorés : une performance métrologique supérieure pourrait être offerte par la solution optique ; idéalement, la résolution est estimée à moins du picomètre. Il est à noter que les solutions optiques sont connues pour leur grande rapidité et leur immunité aux grandeurs d'influence.

Finalement, ce travail de recherche a pu être entrepris du fait de la possibilité de tirer profit de l'expertise de l'ESIEE en matière de gravure par procédé de *Deep Reactive Ion Etching* (DRIE) pour développer des résonateurs optiques plus performants basés sur cette même technique. Ainsi, les activités du groupe « Composants Multiphysiques et Nanotechnologies » de l'ESIEE étend les sujets abordés précédemment dans le domaine des microsystèmes photoniques, particulièrement ceux basés sur des structures micro-usinées à base de miroir de Bragg silicium-air.

Ce fut également une occasion de développer un nouveau volet expérimental, qui est celui de la caractérisation de composants MEMS photoniques. A cet effet, une plate-forme optique a été montée et enrichie avec de nouveaux équipements de mesure.

I.3 Organisation du manuscrit

La thèse est organisée comme suit. Elle est divisée en quatre parties avec un volume total de neuf chapitres. Après le chapitre 1 introductif, la Partie I se compose de deux chapitres. Elle est consacrée à donner une vue synthétique sur les notions de base concernant les résonateurs optiques et les interféromètres, nécessaires à une meilleure compréhension de la suite de la présentation. Le Chapitre 2 donne un aperçu sur les résonateurs optiques et les définitions des principales caractéristiques des résonateurs optiques. Cette partie est suivie par une discussion sur les différentes architectures du résonateur Fabry-Pérot et leurs applications. A la suite, les interféromètres optiques sont décrits avec quelques unes de leurs applications. Le Chapitre 2 se termine par un bref aperçu des théories de base et les modèles d'analyse utilisés dans les chapitres suivants de la thèse. Le chapitre 3 est consacré à l'étude approfondie des briques de base recourant à des interfaces multiples silicium-air. La théorie d'empilement (*Multilayer Stack*) est reprise et appliquée à la conception et à l'étude des structures élémentaires: miroir de Bragg, filtres Fabry-Pérot. Le chapitre se termine par une étude de cas: le sélecteur de modes.

La Partie II porte sur les résonateurs Fabry-Pérot à base de miroirs incurvés. Elle se compose de trois chapitres. Le Chapitre 4 donne une introduction brève aux chapitres suivants inclus dans cette même partie. Nous mentionnons le sujet des architectures Fabry-Pérot incurvées discutées plus tard et leurs avantages par rapport aux cavités planaires conventionnelles. Ensuite, le Chapitre 5 décrit la première architecture qui présente une performance améliorée en termes de facteur de qualité, par rapport aux cavités conventionnelles planaires. Nous la nommerons cavité incurvée simple. La structure, son modèle et les résultats de mesure sont décrits en détail. Les résultats de caractérisation sont interprétés et comparés aux résultats analytiques. Les écarts ont été élucidés et expliqués. Le Chapitre 6 est consacré à la deuxième architecture nommée cavité Fabry-Pérot incurvée avec lentille-fibre. Un nouveau modèle de stabilité a été développé afin de s'assurer de la conception de cavités stables optiquement. Les résultats de mesure sont présentés et décrits en détail. Des calculs analytiques ont été effectués pour extraire les paramètres optiques obtenus après le processus de fabrication. Les variations des paramètres géométriques induites par le procédé de fabrication ont également été étudiées.

La Partie III se compose d'un seul chapitre, dédié à présenter une application spécifique des cavités et des interféromètres optiques à base de miroirs de Bragg. Dans le Chapitre 7, on présente l'application de l'interféromètre de Michelson pour réaliser une sonde optique de profilométrie, étudiée

pour un fonctionnement dans l'infrarouge. À cette fin, une architecture dédiée a été conçue pour permettre à terme, d'effectuer des mesures de topographie dans de tubes de section circulaire de taille sub-millimétrique. Dans ce chapitre, une attention particulière est consacrée à la modélisation et la simulation de l'ensemble du dispositif, afin de prédire ses performances et de soutenir les résultats de mesure présentés plus tard dans ce même chapitre.

La Partie IV se compose d'un chapitre ; il conclut la thèse tout en soulignant les résultats de base, les réalisations et les contributions majeures. Il se concentre également sur les perspectives et les orientations possibles qui peuvent émaner de cette thèse pour continuer ce travail de recherche.

I.4 Nouveauté des architectures proposées: cavités incurvées simples

Dans ce travail, nous proposons deux architectures pour surmonter les limitations des cavités FP planaires. La première architecture est inspirée des résonateurs sphériques où nous développons un design similaire mais en utilisant des miroirs incurvés de forme cylindrique. Ainsi, nous dépassons d'un premier cran les résonateurs planaires en incurvant les miroirs le long d'un plan transversal, en vue d'assurer leur stabilité. Dans cette première conception, nous réduisons le problème des pertes le long d'une direction transversale, en introduisant des réflecteurs de Bragg silicium-air de forme cylindrique, comme représenté schématiquement dans la Fig. I.1c. Le miroir cylindrique résultant pourrait être considéré comme une lentille concave dont l'axe optique z est dans le plan de la surface du substrat de silicium, il a une capacité de concentrer la lumière dans la direction x parallèle au plan du substrat de silicium. Dans la direction hors-plan, la direction y, la cavité se comporte par contre comme un miroir ordinaire planaire et le faisceau diverge après quelques aller-retours. Cette première conception offre l'avantage d'avoir une présentation beaucoup plus simple d'un point de vue géométrique, ce qui la rend plus adaptée à une analyse théorique détaillée. La modélisation analytique que nous avons développée est ainsi accessible à des fins de comparaison entre les résultats expérimentaux et les simulations. En effet, une telle comparaison semble être très utile pour une meilleure compréhension du comportement d'excitation sélectif des modes comme décrit ci-dessous.

En outre, dans la seconde architecture, nous introduisons une solution alternative à la configuration sphérique des miroirs (difficile à obtenir par micro-usinage) où une lentille-fibre (FRL) est utilisée pour fournir le confinement de la lumière dans la direction hors-plan, comme le montre la figure I.1d. Cela complète le confinement dans le plan réalisé grâce aux miroirs cylindriques, en focalisant le faisceau dans les deux plans transversaux.

De cette façon, nous suivons les résonateurs sphériques en utilisant deux éléments distincts: d'une part, le même miroir incurvé cylindrique, comme dans la première architecture, et d'autre part, le FRL, incurvé dans l'autre plan transversal, qui contribue à réduire les pertes de la cavité et améliore le facteur de qualité Q comme détaillé plus tard dans ce résumé.

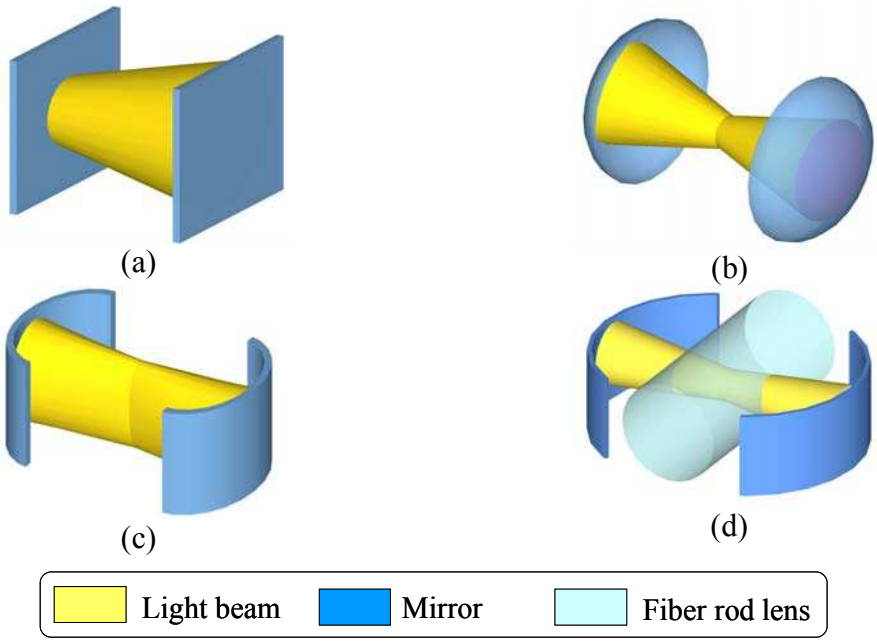

Fig. I.1 Représentation schématique des architectures Fabry-Pérot avec des formes de miroirs différentes: (a) des miroirs plans, (b) des miroirs sphériques donnant lieu à un confinement 2D de la lumière, (c) des miroirs cylindriques donnant lieu à un confinement 1D de la lumière et (d) des miroirs cylindriques combinés avec une lentille-fibre cylindrique, pour donner lieu à un confinement 2D de la lumière.

Dans ce qui suit, nous illustrons la modélisation et les mesures expérimentales effectuées pour les deux architectures basées sur les cavités incurvées. Nous commençons par la cavité incurvée simple.

De la Fig. I.2, nous pouvons décrire que le champ électromagnétique injecté par la fibre d'entrée subit trois transformations successives avec des pertes de puissance correspondantes, en passant par tout le système optique avant qu'il ne se propage dans la fibre de sortie. Les fonctions de transfert (de puissance) correspondantes sont utilisées pour construire un modèle complet afin d'étudier le comportement global du résonateur. Il apparaît évident que cela implique la multiplication de trois coefficients de transmission différents, qui dépendent chacun de la longueur d'onde $T = \Gamma \, . \, H_{cav} . \, O$:

(I) L'efficacité de couplage à l'entrée Γ: ce premier terme comprend le couplage de puissance du champ de lumière sortant de la fibre lentillée vers l'entrée de la cavité. Les pertes correspondant au couplage d'entrée sont décrites par le coefficient Γ, mentionnée comme étant l'efficacité du couplage d'entrée.

(II) La transmission de la cavité H_{cav}: ce terme décrit la réponse de la cavité à des modes de résonance différentes. Il implique une efficacité de couplage intra-cavité sur un trajet aller-retour de la lumière.

(III) L'efficacité de couplage en sortie O: Ce terme concerne le couplage de la cavité à la fibre de sortie. Mais puisque la fibre de sortie a été choisie peut accommoder des tailles dont le faisceau peut atteindre jusqu'à 56 µm, elle a une bonne efficacité de collection et son efficacité de couplage en sortie O peut être considéré comme très proche de l'unité: $O \sim 1$. Par conséquent, la

fonction de transfert globale de la transmittance de puissance T est obtenue par le produit $T = \Gamma \cdot H_{cav}$.

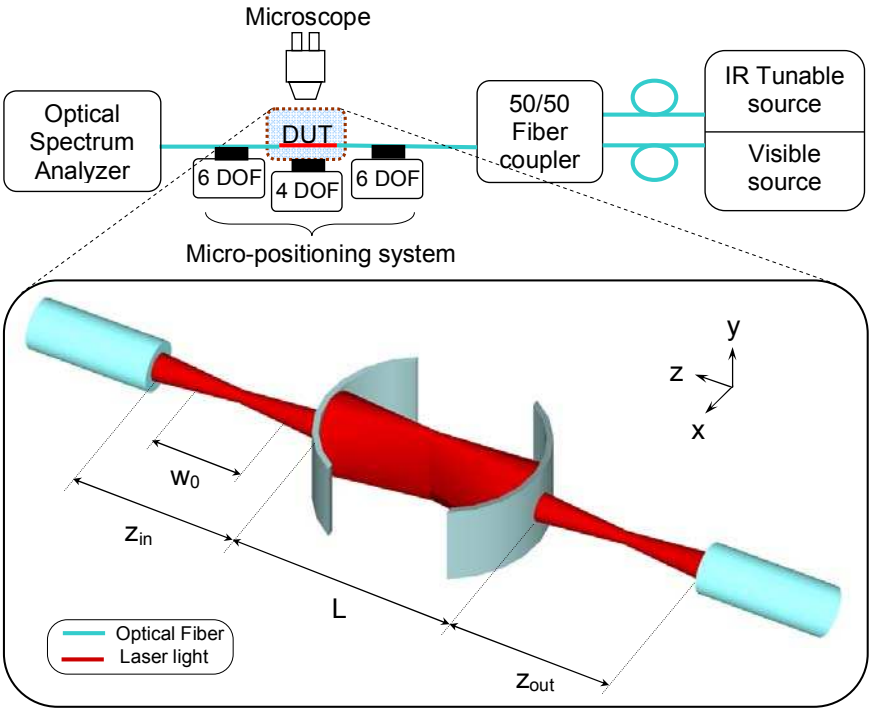

Fig. I.2 Représentation schématique du montage optique de mesure avec un encart intérieur relatif à l'arrangement de la cavité incurvée à l'égard des positions de la fibre d'entrée et de la fibre de sortie.

Les dispositifs présentés se composent principalement de deux miroirs de Bragg cylindriques, dont le rayon de courbure est R = 140 µm, espacés d'une distance L = 210 µm. Le miroir cylindrique est constitué d'une alternance de couches de silicium et d'air. Le silicium a une épaisseur de 3,67 µm, tandis que la couche d'air présente une épaisseur de 3,49 µm, les deux épaisseurs correspondent à un multiple impair du quart de la longueur d'onde de transmission (à λ = 1550 nm) dans le silicium et dans l'air, respectivement. Un autre design avec R = 200 µm et L ~ 300 µm a également été réalisé. Les dispositifs ont été fabriqués en utilisant le procédé DRIE de gravure profonde. Les photos MEB de quelques uns de ces dispositifs sont montrées dans la Fig. I.3.

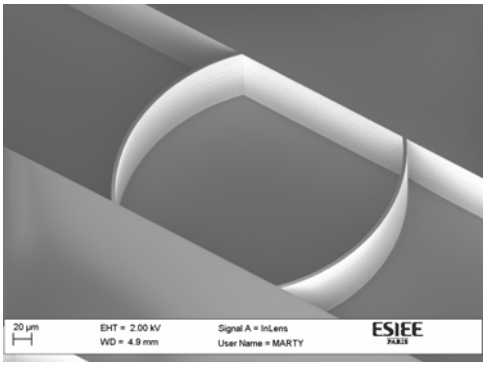

(a)

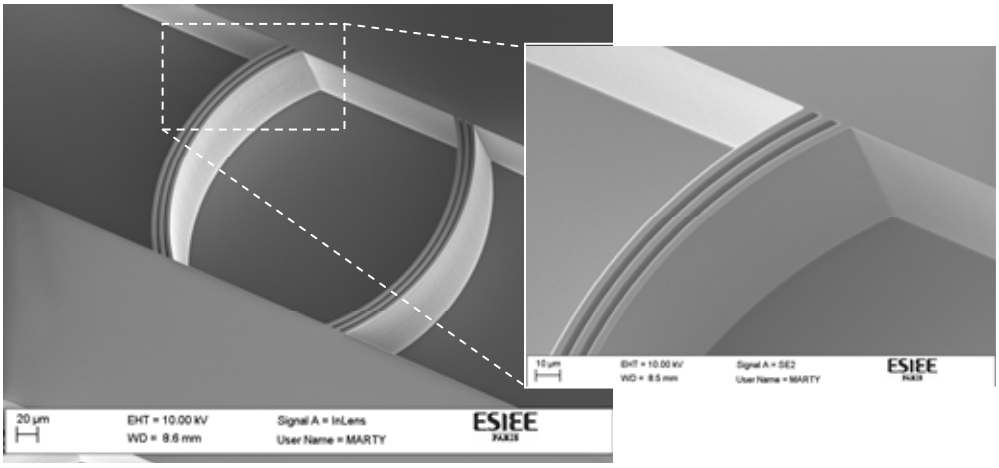

(b)

Fig. I.3 Photos MEB d'une cavité incurvée FP fabriquée (a) une couche de silicium unique, (b) des couches de silicium multiples (trois dans ce cas); l'encart montre une vue agrandie sur un réflecteur de Bragg en silicium-air.

Le montage optique, schématisé dans la Fig. I.2, se compose d'une source laser accordable Agilent (TLS) module 81949A, utilisé pour injecter de la lumière laser, et un analyseur MS9710B Anritsu spectre optique (OSA) utilisé comme un puissancemètre pour mesurer l'intensité de la lumière transmise. Une lumière laser visible à 635 nm a également été utilisée à des fins d'alignement. Les lumières visible et infrarouge sont couplées ensemble par un coupleur et injectées à travers la fibre lentillée vers le dispositif sous test (DUT). Une fibre lentillée similaire est utilisée pour recueillir la lumière transmise à travers le dispositif et de le coupler directement à l'analyseur de spectre optique (OSA). Les fibres lentillées de Corning ont une taille de spot de 18 µm et une distance de travail de 300 µm. Des positionneurs six axes ont été utilisés pour aligner chacune des fibres d'entrée et de sortie. Tous les éléments sont montés sur une table optique pour réduire les effets des vibrations.

Une autre expérience a été effectuée pour étudier l'efficacité du couplage de puissance entre la fibre et le mode couplé dans une cavité ayant une couche de silicium unique par miroir, cette expérience ciblant une excitation sélective des modes longitudinaux. À cette fin, la position de la fibre d'entrée par rapport au miroir d'entrée z_{in} était variable. Trois positions différentes ont été testées: z_{in} = 150 µm, z_{in} = 300 µm et z_{in} = 460 µm, la fibre de détection a été remplacée par une autre fibre lentillée caractérisée par son efficacité de collection. Le balayage en longueur d'onde a été réalisé aux trois positions de z_{in} : les réponses spectrales enregistrées sont superposées comme le montre Fig. I.4. L'observation des réponses spectrales révèle une sorte de périodicité: la forme obtenue se répète incluant non seulement les pics principaux des modes longitudinaux, notés dans la Fig. I.4 comme modes fondamentaux de type (0,0), mais aussi d'autres pics de résonance correspondant aux modes transverses de type (2,0). Ces modes ont été identifiés en calculant les longueurs d'onde de résonance de la cavité aux différents modes. De ces calculs, nous avons conclu que les pics supplémentaires se rapportent à l'excitation des

modes transverses (TEM_{20}), qui sont typiques des résonateurs fabriqués à partir de miroirs incurvés, aussi appelés modes Hermite-Gaussien.

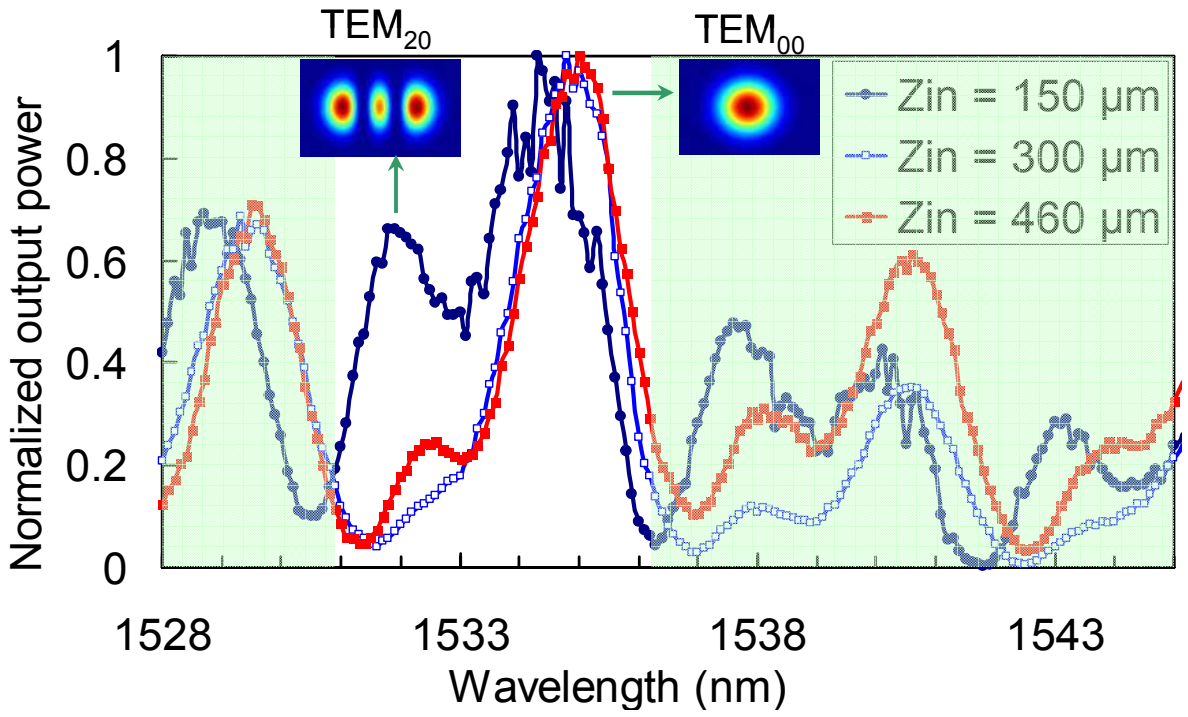

Fig. I.4 Réponses spectrales mesurées pour une cavité FP ayant une seule couche de silicium par miroir. La distance de couplage fibre-à-miroir était variée z_{in} = 150 µm, 300 µm et 460 µm. Le couplage le plus sélectif à des modes fondamentaux de type (0,0) est atteint lorsque z_{in} = 300 µm. Quant au mode transverse (2,0), nous obtenons soit un couplage efficace ou une extinction significative (d'un ratio de 7:1) est obtenue, quand z_{in} = 150 µm et z_{in} = 300 µm, respectivement. Les encarts illustrent les distributions de champ pour les modes (0,0) et (2,0), respectivement.

Une analyse comportementale a été effectuée pour étudier deux points :

(a) L'efficacité de couplage de puissance fibre-cavité Γ

Les calculs numériques ont été utilisés pour évaluer cette efficacité de couplage de puissance entre le champ E_{Fiber} injecté à partir d'une fibre optique monomode (mode fondamental gaussien) et le champ des différents modes transversaux $\Psi_{m,0}$ à l'entrée de la cavité. Le calcul s'effectue selon l'intégrale de projection donnée par :

$$\Gamma_{m,0} = \frac{\left| \iint_{(D)} E_{Fiber}(x,y,0) \cdot \Psi_{m,0}(x,y,0) dx\, dy \right|^2}{\iint_{(D)} \left| E_{Fiber}(x,y,0) \right|^2 dx\, dy \cdot \iint_{(D)} \left| \Psi_{m,0}(x,y,0) \right|^2 dx\, dy}. \qquad \text{(I.1)}$$

Tableau I.1 Efficacités de couplage en puissance $\Gamma_{m,0}$ entre le mode de la fibre (gaussien) et les modes (m, 0) du résonateur (Hermite-Gaussiens); valeurs calculées à λ = 1530 nm comparées aux valeurs obtenues par des résultats expérimentaux.

	z_{in} = 150 µm		z_{in} = 300 µm		z_{in} = 460 µm	
	Modèle	*Expérience*	Modèle	*Expérience*	Modèle	*Expérience*
$\Gamma_{0,0}$	96,7%	*63%*	99,93%	*99%*	89.14%	*89%*
$\Gamma_{1,0}$	0	--	0	--	0	--
$\Gamma_{2,0}$	3,14%	*37%*	0.07%	*1%*	9.15%	*11%*
$\Gamma_{3,0}$	0	--	0	--	0	--
$\Gamma_{4,0}$	0.15%	*0*	0.00%	*0*	1,41%	*0*
Total	100%	100%	100%	100%	99.7%	100%

Une analyse plus poussée des résultats expérimentaux a permis l'évaluation de Γ pour les différents modes à différentes positions z_{in}. A partir des résultats expérimentaux présentés ci-dessus, le couplage n'est observé que pour les modes de TEM_{00} et TEM_{20} de la cavité. Basé sur cette conclusion, nous avons simulé un processus de déconvolution où nous avons fait une combinaison linéaire de ces deux modes avec différents coefficients de couplage Γ_{00} et Γ_{20} puis, nous avons monté cette association avec les réponses expérimentales, comme indiqué dans les Fig. I.5 a, b et c.

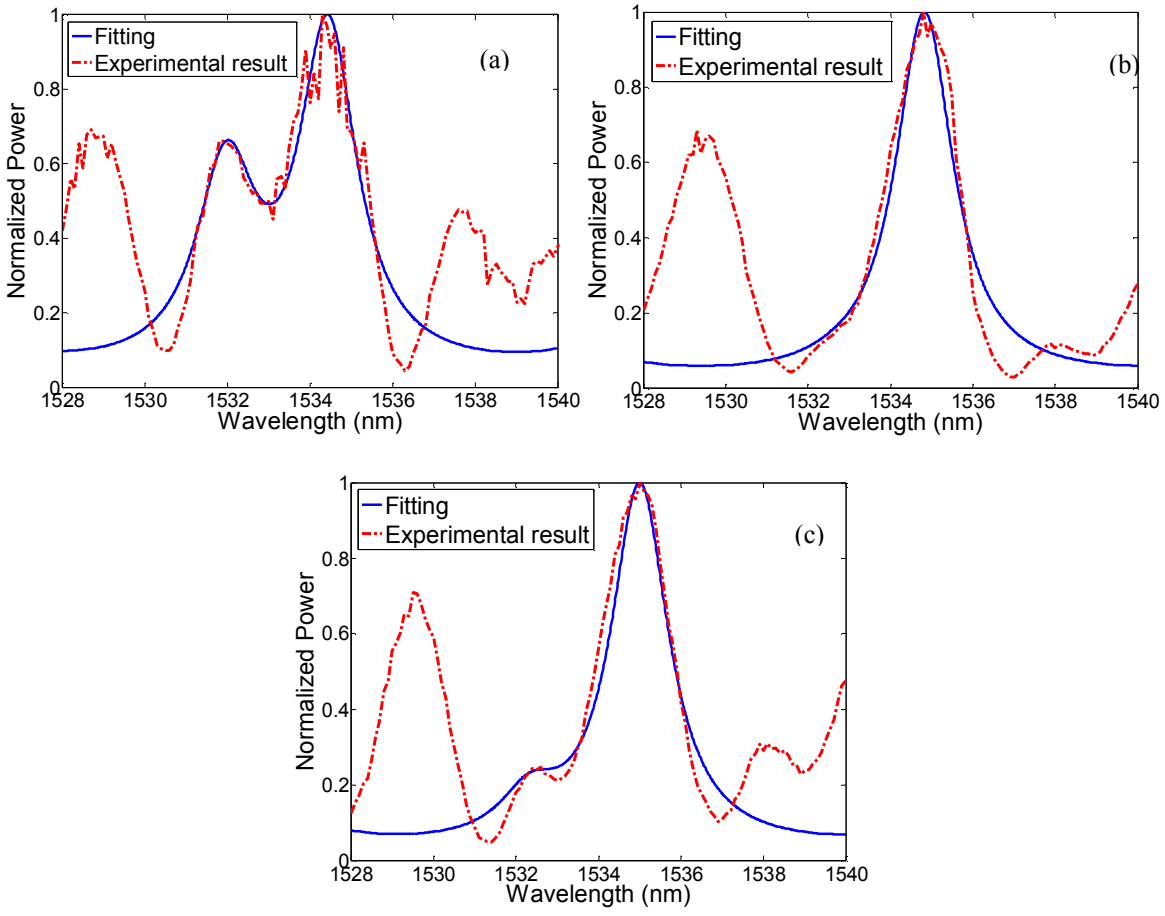

Fig. I.5 Fit des données mesurées à une combinaison de modes de TEM_{00} et TEM_{20}: (a) pour z_{in} = 150 µm, Γ_{00} = 63% et Γ_{20} = 37% (b) pour z_{in} = 300 µm, Γ_{00} = 99% et Γ_{20} = 1 % et (c) pour z_{in} = 460 µm, Γ_{00} = 89% et Γ_{20} =11%

(b) Pertes intra-cavité due à l'expansion du faisceau Gaussien

L'efficacité de couplage intra-cavité pour le trajet aller-retour des modes (m, 0) est estimée à des positions d'entrée différentes (z_{in}) de la fibre d'excitation, comme illustré dans la Fig. I.4. $\gamma_{m,0}$ est obtenu à partir de l'intégrale de projection suivant entre les champs d'un mode donné, avant et après l'aller-retour suivant la longueur de la cavité, respectivement:

$$\gamma_{m,0} = \frac{\left| \iint_{(D)} \Psi_{m,0}(x,y,0) \,.\, \Psi^{*}_{m,0}(x,y,2L)\, dx\, dy \right|^2}{\iint_{(D)} \left| \Psi_{m,0}(x,y,0) \right|^2 dx\, dy \,.\, \iint_{(D)} \left| \Psi_{m,0}(x,y,2L) \right|^2 dx\, dy} \qquad \text{(I.2)}$$

où (D) est le domaine du miroir. Les valeurs obtenues pour $\gamma_{0,0}$ et les facteurs de qualité Q correspondants issus de l'équation (I.1) sont présentés dans le tableau I.2, où nous avons considéré un miroir de réflexion = 72% correspondant à une seule couche de Bragg idéale.

Tableau I.2 Efficacité de couplage intra-cavité $\gamma_{0,0}$ et facteur Q pour une cavité avec une couche de silicium par miroir, calculée à λ = 1535 nm pour le mode (0,0) à trois distances de couplage différentes z_{in}

Position de la fibre d'entrée	**Efficacité de couplage calculée pour l'intra-cavité (aller-retour)** $\gamma_{0,0}$	***Q*-facteur théorique**	***Q*-facteur expérimental**
z_{in} **= 150 µm**	0.6196	1036.6	665.32
z_{in} **= 300 µm**	0.5795	952.77	792.77
z_{in} **= 460 µm**	0.4788	770.22	769.7

I.5 Aspects innovants des architectures proposées: cavités incurvées avec une lentille-fibre

Dans cette section, nous décrivons la deuxième architecture du résonateur dont l'objectif est de fournir une nouvelle amélioration complémentaire au facteur de qualité *Q* grâce au confinement de la lumière en 2D. La structure introduite émule les résonateurs sphériques dans le sens où l'effet de la sphéricité est toujours maintenu en utilisant une combinaison de deux éléments cylindriques: Les miroirs de Bragg cylindriques d'une part et la lentille-fibre d'autre part, comme illustré dans la Fig. I.6.

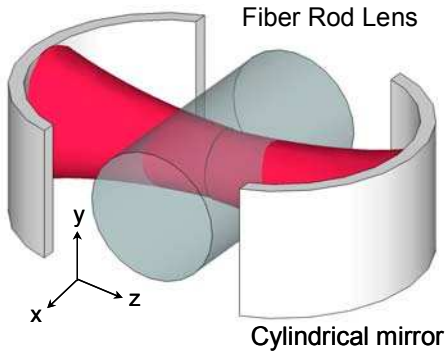

Fig. I.6 Résonateur avec lentille-fibre supplémentaire assurant le confinement hors plan, conduisant à une solution complète pour le confinement 2D et réduisant les pertes optiques dues à l'expansion du faisceau.

Compte tenu l'aspect innovant de l'architecture présentée, il n'existe pas de modèle analytique pour celle-ci dans la littérature. Ainsi, afin de concevoir un résonateur stable impliquant une lentille-fibre, nous cherchons à déduire des relations analytiques pour connaître les critères de sa stabilité. Notre analyse est basée sur l'approche matricielle des rayons pour laquelle le rayon est défini par une position «y» et un angle «Θ» par rapport à l'axe optique. L'objectif est de trouver une relation entre les différents paramètres géométriques de la cavité: le rayon de courbure R, la distance de propagation en espace libre d_{air} à et le diamètre de la fibre d_f.

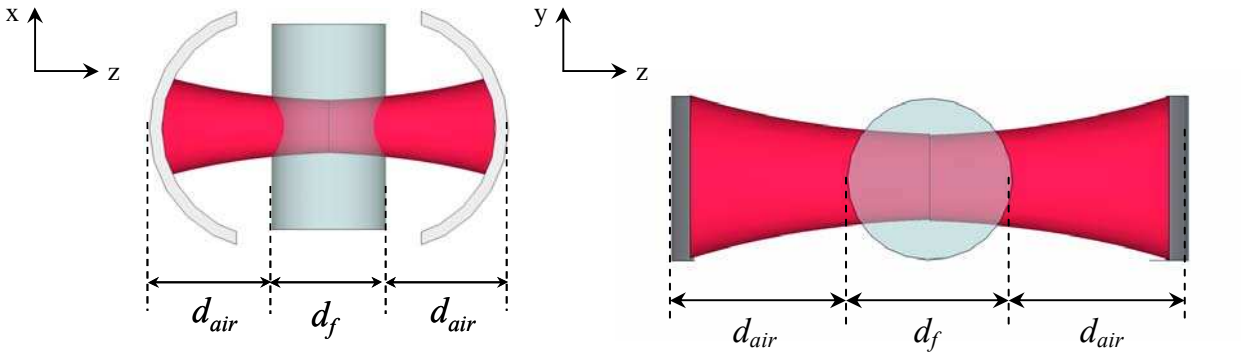

Fig. I.7 Vue de dessus et vue de face de l'architecture du résonateur dans les plans transversaux XZ et YZ respectivement, illustrant les distances de propagation à l'intérieur de la fibre d_f et dans l'air: 2 x d_{air}.

Après des manipulations mathématiques, nous obtenons dans le plan XZ :

$$0 \le \frac{d_{RT}}{|R|} \le 2 \qquad \text{(I.3)}$$

où d_{RT} est donnée par:

$$d_{RT} = 2d_{air} + \frac{d_f}{n_f} \qquad \text{(I.4)}$$

Tandis que dans le plan YZ, nous obtenons :

$$0 \le \left(1-2/n_f\right)+\left(4d_{air}/d_f\right)\left(1-1/n_f\right) \le 1 \qquad \text{(I.5)}$$

Combinant (I.4) et (I.5), nous obtenons enfin :

$$d_{air-\max} = \frac{d_f}{2\left(n_f-1\right)} \qquad \text{(I.6)}$$

$$R_{\max} = \frac{d_f}{2}\left\{\frac{2n_f-1}{n_f\left(n_f-1\right)}\right\} \qquad \text{(I.7)}$$

$$d_{air-\min} = \frac{d_f}{4}\left\{\frac{2-n_f}{n_f-1}\right\} \qquad \text{(I.8)}$$

$$R_{\min} = \frac{d_f}{4}\left\{\frac{2}{n_f}+\frac{2-n_f}{n_f-1}\right\} \qquad \text{(I.9)}$$

Comme mentionné ci-dessus, l'architecture schématisée dans la Fig. I.6 fournit une solution complète pour le confinement de la lumière en 2D, en raison de l'interface cylindrique supplémentaire de la lentille-fibre insérée dans la cavité cylindrique en silicium. Ces dispositifs ont été conçus, réalisés et mesurés. Tous les dispositifs fabriqués partagent des paramètres communs. Chaque couche de silicium a une épaisseur de 3,67 μm, tandis que la couche d'air a une largeur de 3,49 μm. Une ouverture sous forme de tranchée de longueur 1 cm environ et de largeur de 128 μm est partagée entre tous les dispositifs pour faciliter l'insertion de la lentille-fibre, dont le diamètre est de 125 μm. A contrariori, les cavités FP fabriquées diffèrent les unes des autres, soit dans la longueur physique de la cavité ou dans le nombre de couches de Bragg par miroir. A partir de ces paramètres, de nombreuses combinaisons ont été générées, mesurées et analysées. Une photo MEB d'un exemple de dispositif fabriqué est présentée dans la Fig. I.8.

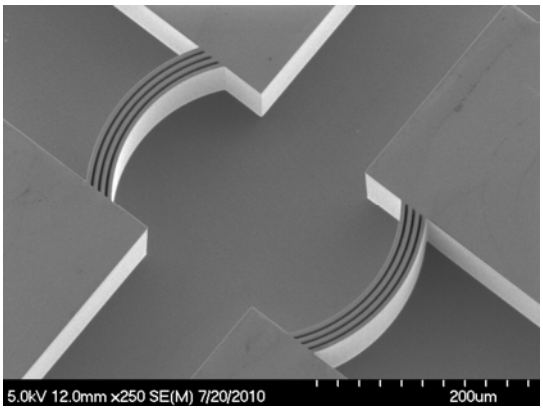

(a)

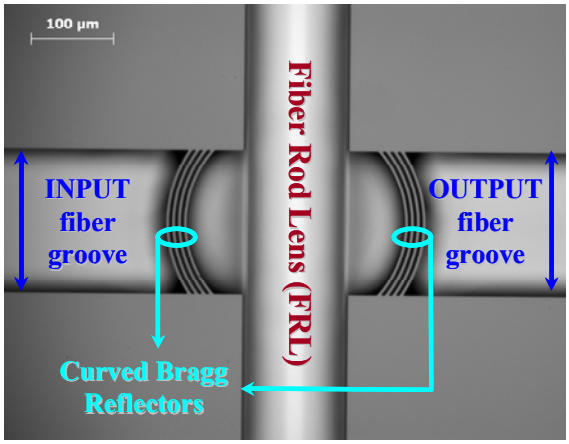

(b)

Fig. I.8 Résultat de fabrication d'un résonateur pour le confinement de la lumière en 2D (a) photo MEB de la cavité FP avec des miroirs de Bragg de forme cylindrique (ici 4 couches de silicium-air avec la tranchée DRIE de largeur adaptée à la lentille-fibre (b) Photo prise au microscope pour la structure de silicium avec la lentille-fibre placée à l'intérieur de la tranchée DRIE dans le but de collimater la lumière hors plan.

Les dispositifs fabriqués ont été mesurés à l'aide de fibres clivées dans le plan d'injection et de détection. Une source laser accordable est utilisée en conjonction avec un puissancemètre pour réaliser le balayage de longueur d'onde et l'enregistrement de la réponse spectrale. Deux micro-positionneurs, chacun 5 axes, ont été utilisés pour aligner les deux fibres d'injection et de détection. Une photo du montage optique est montrée dans la Fig. I.9. La valeur minimale enregistrée pour la largeur à mi-hauteur (FWHM) est de 0,1765 nm menant à un facteur de qualité Q de 8818. Ces valeurs sont obtenues pour la cavité A ayant quatre couches de silicium-air par miroir et une longueur physique L = 265,8 µm et un rayon de courbure R = 140 µm. La Fig. I.10 montre la réponse spectrale mesurée pour ce dispositif. Il est à noter, que dans notre cas, la longueur physique est très différente de la longueur optique due à la présence de la lentille-fibre, dont l'indice de réfraction n est de 1,47. Ainsi, la longueur optique est égale à 324,6 µm.

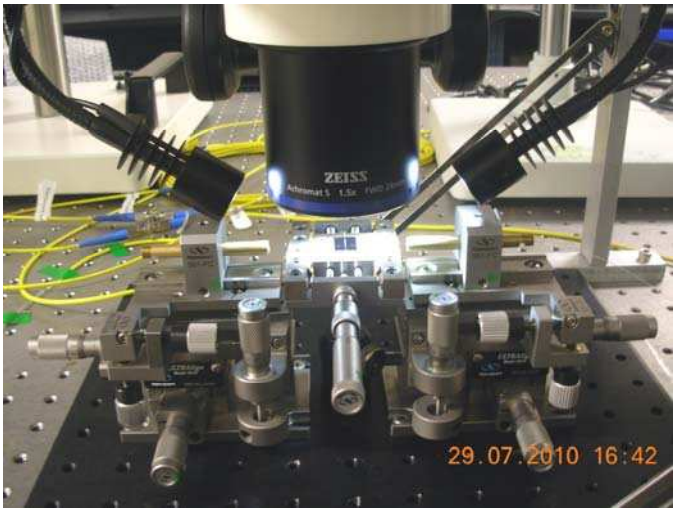

Fig. I.9 Photo du montage de caractérisation montrant le dispositif sous test (DUT), les micro-positionneurs et le microscope optique.

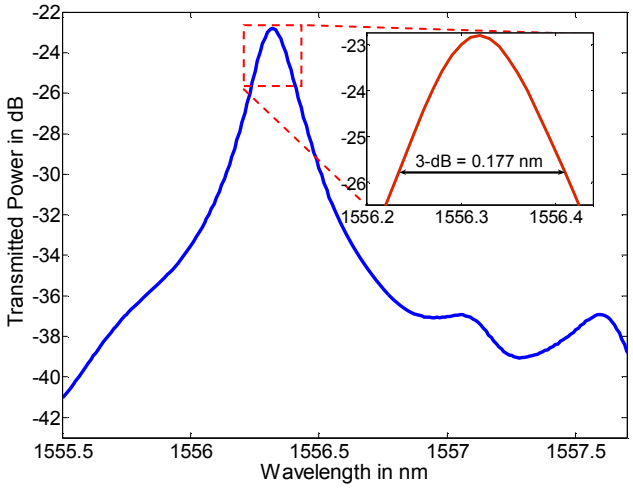

Fig. I.10 Réponse spectrale mesurée pour une cavité de longueur L = 265.8 µm, conçue avec des miroirs cylindriques de rayon de courbure R = 140 µm avec 4 couches de Bragg silicium-air. La largeur spectrale est 0.177 nm correspondent à un facteur Q de 8818.

D'autres dispositifs avec un nombre différent de couches de Bragg ont été testés pour étudier l'impact de la réflectance du miroir sur le facteur Q. Les résultats correspondants sont présentés dans Fig. I.11. Nous constatons que quand le nombre de couches N augmente, le facteur de qualité Q augmente en conséquence jusqu'à N = 4 où Q = 8818. Les résultats obtenus confirment la tendance des facteurs Q observée dans une cavité FP idéale avec miroirs plans et dont la relation est donnée par:

$$Q = \frac{2\pi nL}{\lambda_0}\left(\frac{\sqrt{\Re_{eff}}}{1-\Re_{eff}}\right) \qquad \text{(I.10)}$$

Où $\Re_{eff} = \gamma.\Re$, γ désigne l'efficacité de couplage identifiée comme l'élément principal des pertes dans ces cavités. La tendance de croissance de Q en fonction de N n'est plus applicable dès lors que N croît au delà de 4 ; en effet, pour N=5 le facteur Q diminue à 6068. Ceci pourrait être attribué à la perte de côtes (induites par la fabrication) qui devient plus prononcée lorsque N augmente. La perte de la dimension critique dégrade Q. Une tendance similaire a été observée pour la cavité B avec R = 200 µm. La Fig. I.11b montre une vue agrandie de la Fig. I.11a pour la cavité B ayant R = 200 µm, illustrant une dégradation similaire dans le facteur Q comme observé pour la première cavité avec R = 140 µm. Il est intéressant de mentionner que les cavités de type A sont plus performantes que les cavités ayant un R plus grand, qui ont tendance à se comporter comme des cavités à réflecteurs planaires.

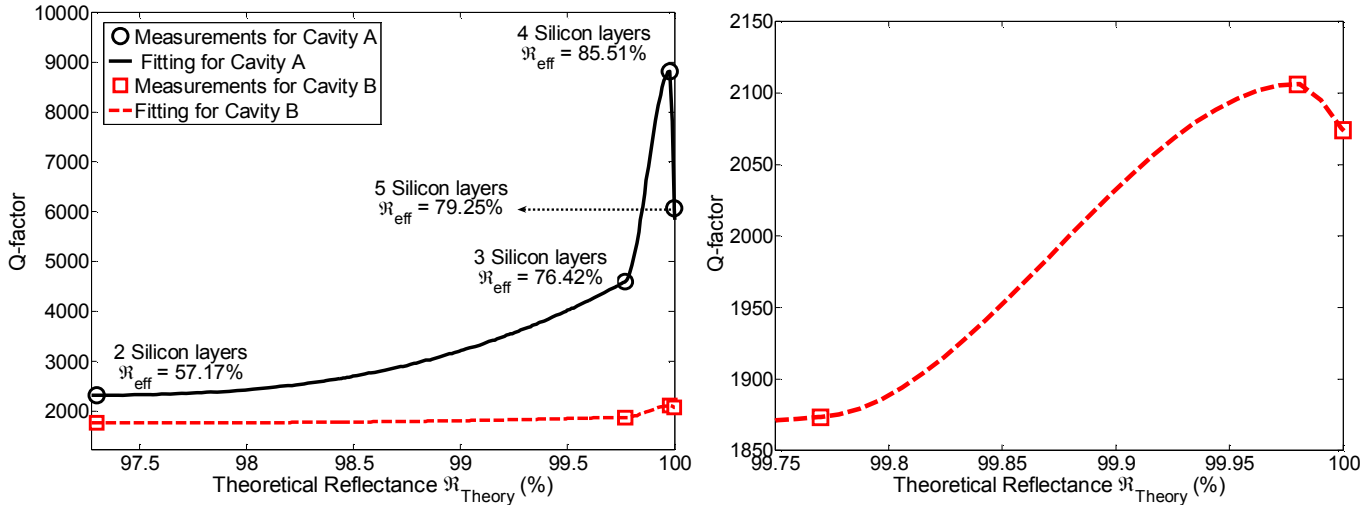

Fig. I.11 (a) Les valeurs expérimentales du facteur Q en fonction de la réflectance théorique des miroirs de Bragg incurvés pour les deux cavités A et B: La cavité A a une longueur L = 265,8 µm et un rayon de courbure R = 140 µm. Pour la cavité B, L = 385,6 µm et R = 200 µm. (b) Ce graphique donne une vue agrandie pour la cavité B illustrant une dégradation similaire du facteur Q comme observé pour la cavité A.

I.6 Sonde optique basée sur l'interféromètre Michelson

Cette section est consacrée à l'étude, la conception, la fabrication et la caractérisation préliminaire d'un microsystème optique de mesure dimensionnelle, basé sur l'interféromètre de Michelson. La largeur du système est dans la gamme sub-millimétrique et sa longueur est d'environ 1 cm. La configuration proposée ici représente le cœur d'un microprofilomètre optique. Le microsystème proposé est une sonde optique conçue pour effectuer des mesures sans contact, de diamètres et de défauts de circularité, dans des espaces confinés tels que les orifices d'injecteurs de carburant. Le premier prototype présenté dans le cadre de cette thèse est conçu pour fonctionner dans la gamme infrarouge autour de 1550 nm. Une vue schématique de la sonde optique proposée et un zoom sur l'architecture de l'interféromètre sont présentés dans les Fig. I.18a et Fig. I.18b.

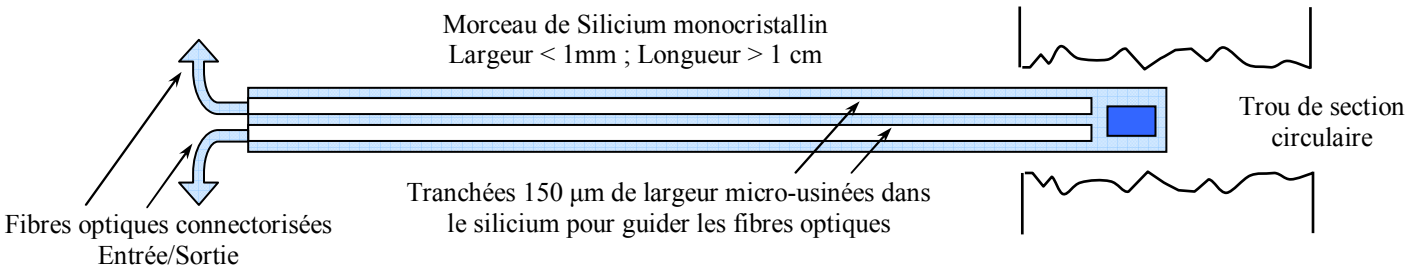

(a)

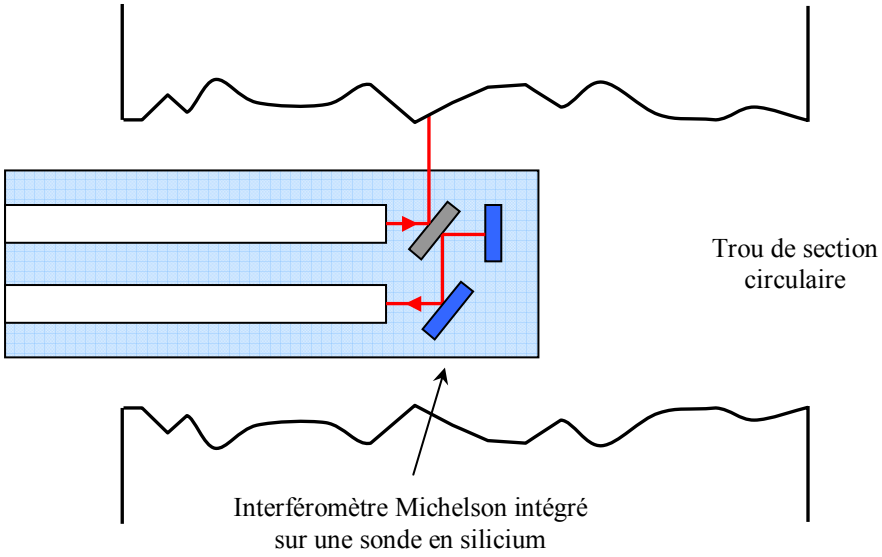

(b)

Fig. I.12 (a) Vue schématique de toute la sonde optique formée d'un bloc de silicium monocristallin et incorporant un interféromètre de Michelson (la tête de la sonde) et les tranchées formant des guides pour les entrées/sorties des fibres optiques. L'entrée est conçue pour injecter la lumière (monochromatique) et la sortie est conçue pour recueillir l'interférogramme lorsque la sonde est tournée autour de l'axe et translatée selon son axe. (b) Architecture adoptée pour l'interféromètre de Michelson.

La cellule unitaire est représentée de façon détaillée dans la Fig. I.19 avec les tranchées des fibres et les réservoirs utilisés pour recueillir l'excédent de colle utilisée pour le packaging. En outre, une vue agrandie de l'interféromètre de Michelson est montrée. Dans la Fig. I.19, nous retrouvons la lame séparatrice (*Beam splitter*-BS) et les deux miroirs agissant comme miroir de référence (placé à l'horizontale) et miroir de sortie (parallèle au BS) qui est utilisé pour transmettre l'interférogramme de transmission vers la fibre de sortie. Le second miroir du Michelson ne figure pas sur la puce ; il a été remplacé par la surface réfléchissante des éléments testés (DUT) comme illustré précédemment dans la Fig. I.18. La cellule unitaire de base est fixée au châssis du silicium rigide à l'aide de deux barres de silicium de petite taille. Ces barres sont brisées pour séparer les cellules unitaires de la plaquette de silicium après que la fabrication est complètement terminée. La largeur de sonde est de 550 µm et la longueur de sonde est de 4 mm. La largeur des tranchées de fibres est de 150 µm.

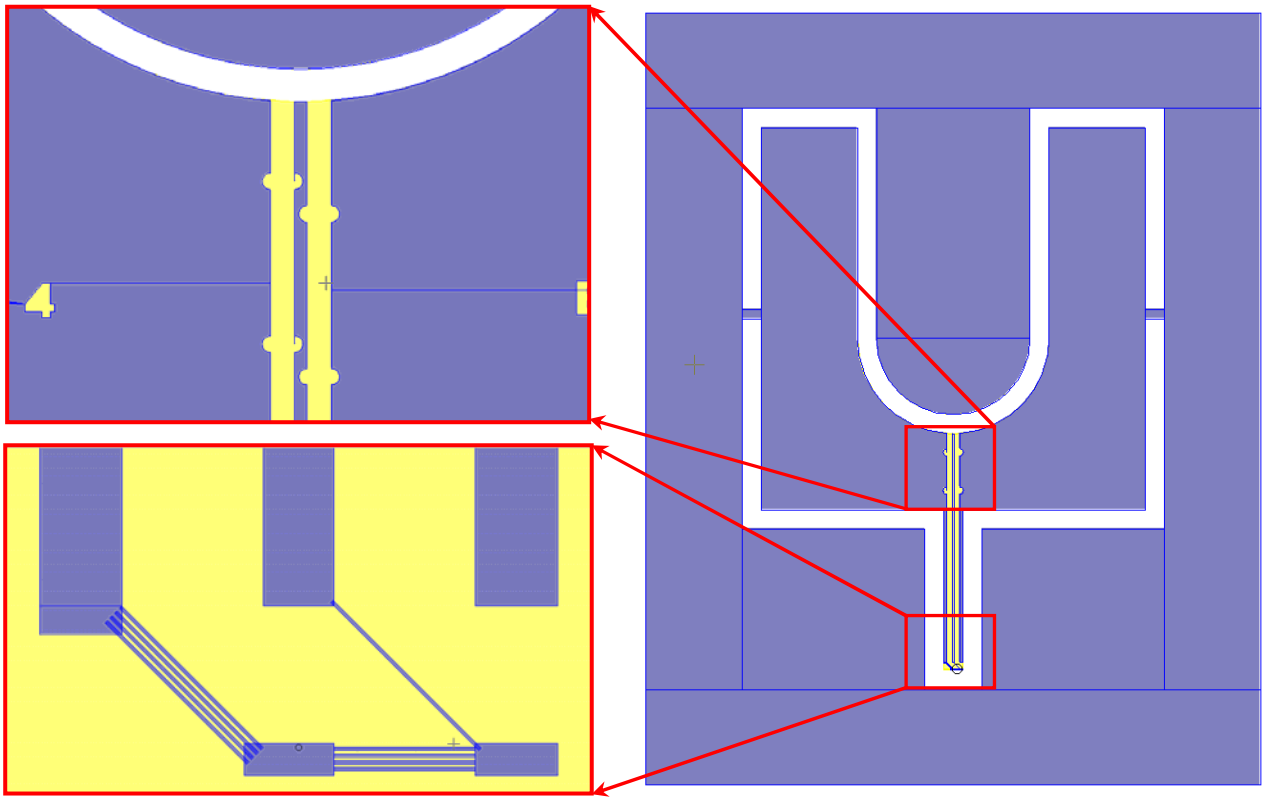

Fig. I.13 Masque du dispositif avec un zoom sur les tranchées des fibres, les réservoirs et l'interféromètre.

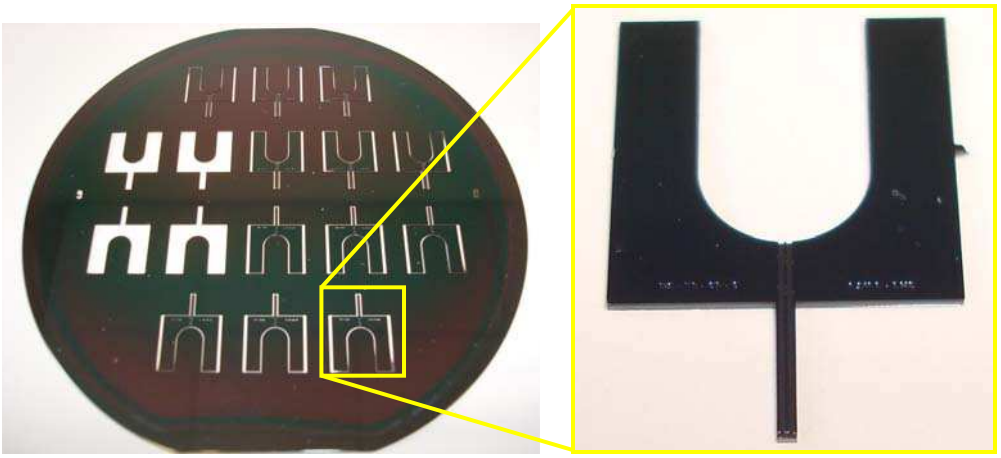

(a) (b)

Fig. I.14 (a) Photo de la plaquette réalisée comprenant 16 dispositifs (b) Photo d'un dispositif unitaire entier

Le banc de mesure se compose d'une source laser accordable dans les bandes C-L, reliée à une fibre lentillée à revêtement anti-reflet AR à travers un circulateur. La fibre repose dans une longue tranchée de 6 mm en forme de U, elle est utilisée simultanément pour l'injection et la détection de la lumière réfléchie couplée au retour du circulateur qui est relié à un puissancemètre optique. Le balayage de la longueur d'onde a été réalisé pour enregistrer l'interférogramme spectral de réflexion. Les spectres obtenus sont post-traités par FFT pour déterminer la différence de chemin optique $L_{opt} = 2nD$, où D est la distance et n l'indice de réfraction moyen.

Nous avons réalisé des mesures au moyen de deux sondes A et B ayant différents taux de séparation pour le BS (réflectance - Transmission = 75% -25% et 25% -75%, respectivement). Ces sondes ont été optimisées pour une utilisation avec des échantillons de réflectance basse et haute, respectivement. Les interférogrammes de réflexion pour la sonde A utilisée sur une plaquette de silicium sont présentés dans la Fig. I.21a pour différentes distances D. Malgré le déséquilibre important entre la réflectance du miroir de Bragg de référence (R_{Bragg} ~ 99,98%) et celle de la plaquette de silicium de test (R_{Si} ~ 30%), le dispositif présente un bon contraste (C ~ 50%). La Fig. I.21b présente des pics supplémentaires liés à l'épaisseur de la plaquette de silicium. Les FFTs superposées dans la Fig. I.22a se rapportent à la sonde B utilisée avec un miroir en aluminium, révélant des pics secondaires dont la localisation donne la différence de chemin optique et donc la distance D. La diminution observée dans l'amplitude des pics secondaires est due à la dégradation du contraste aux longues distances. Cette tendance, tracée dans la Fig. I.23, montre aussi que la sonde A utilisée avec un échantillon de silicium a une meilleure performance que la sonde B utilisée avec de l'aluminium. Cela confirme l'efficacité de l'optimisation des taux de séparation des BS de nos designs.

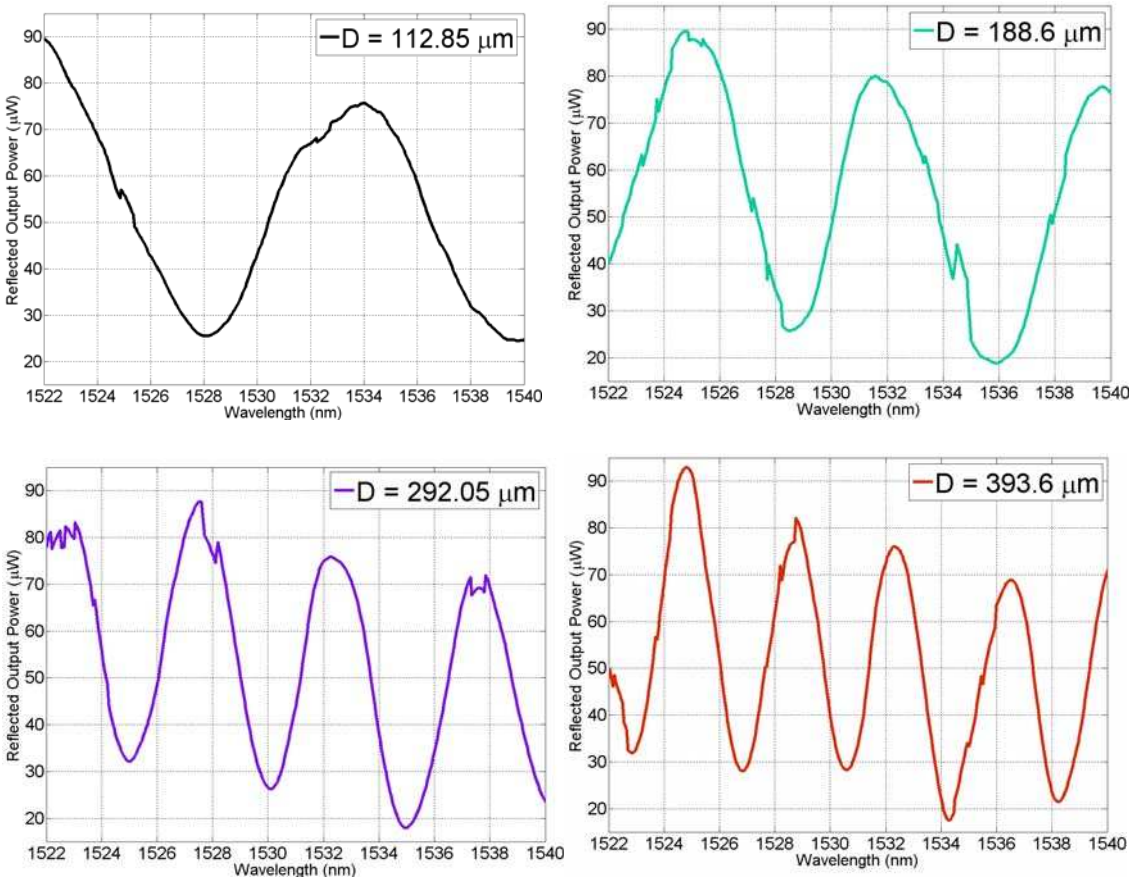

(a)

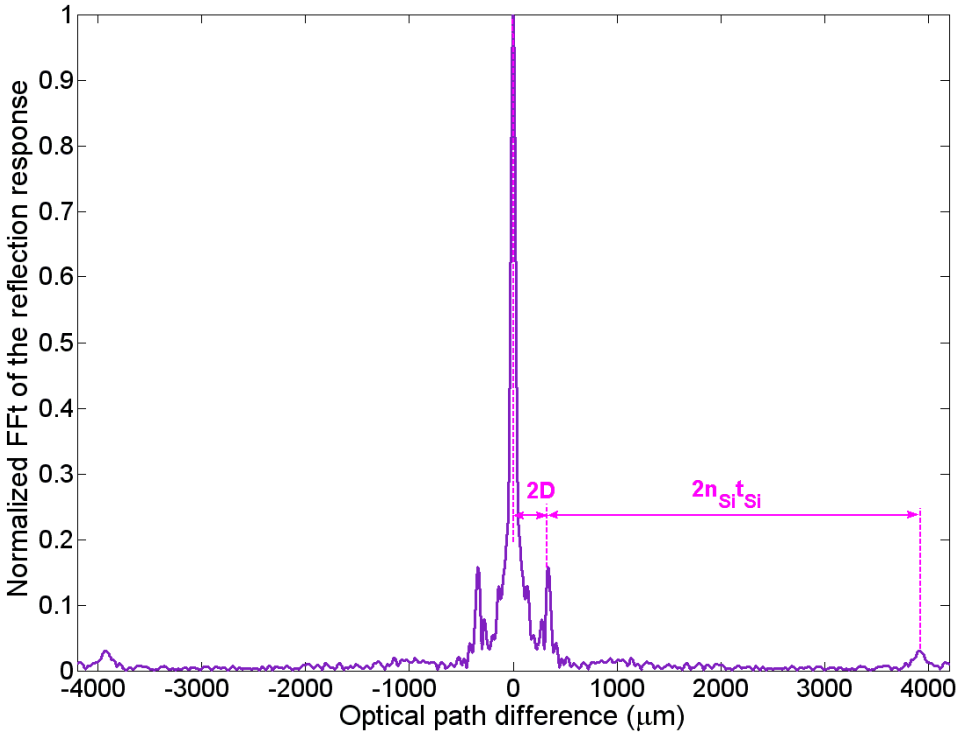

(b)

Fig. I.15 Réponse spectrales de l'interférogramme en réflexion (a) de la sonde optique A à différentes distances D d'un wafer de silicium utilisé comme surface réfléchissante. Taux de séparation du BS = 75% -25%. (b) Plaquette de silicium utilisée comme miroir de test en conjonction avec la sonde A. La distance échantillon-surface (1er pic) et l'épaisseur du wafer (2ème pic) sont obtenues toutes les deux à partir de cette dernière expérience.

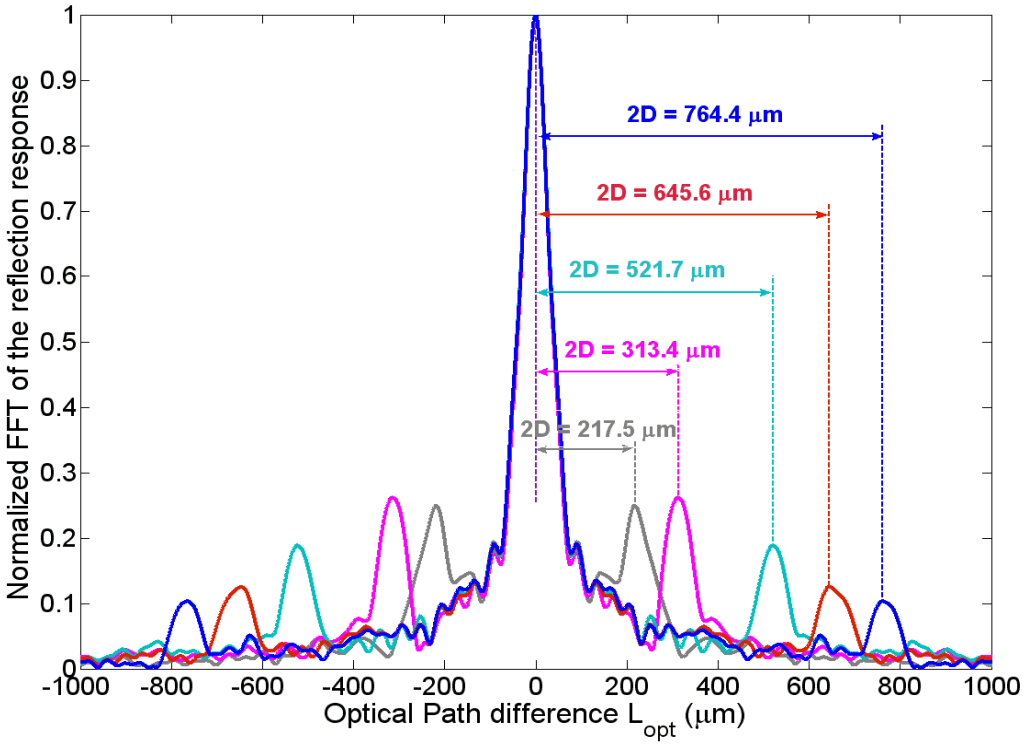

Fig. I.16 FFT des réponses de réflexion enregistrées à plusieurs distances. Une lame d'aluminium est utilisée comme un miroir de test en conjonction avec la sonde B.

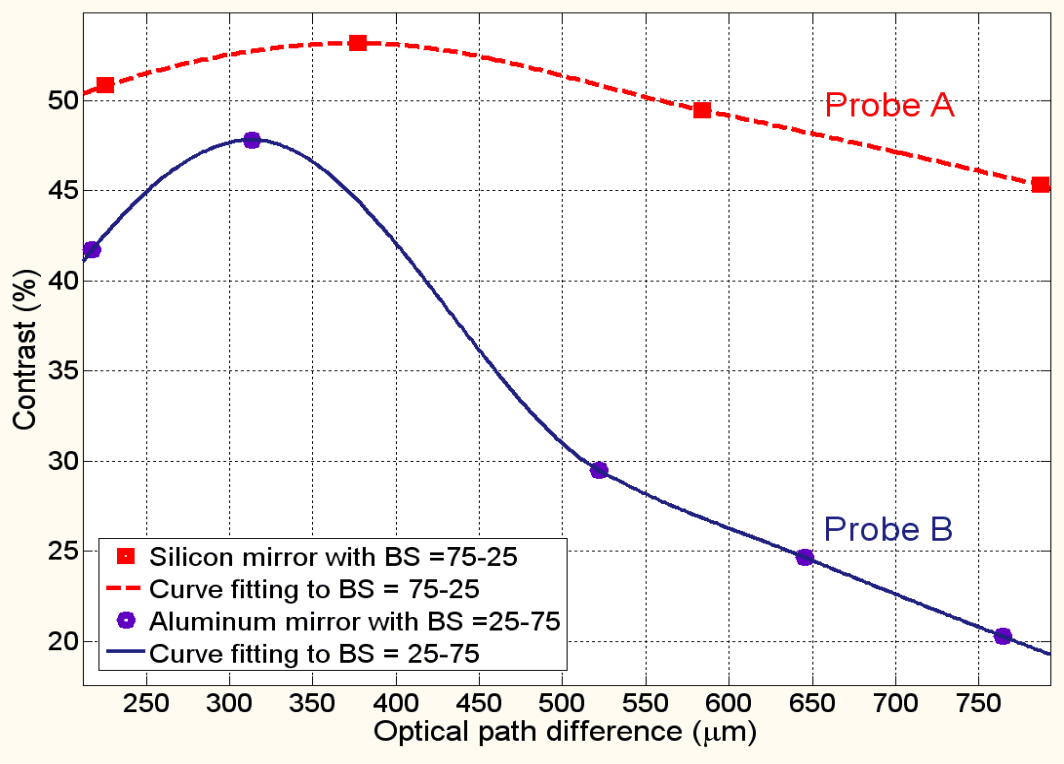

Fig. I.17 Contraste par rapport différence de chemin optique (2D) pour les deux sondes déployées dans nos expériences. La sonde A avec un taux de séparation 75% -25% présente une meilleure performance, conformément au modèle analytique développé.

I.7 Conclusion et Perspectives

Dans cette thèse, nous avons présenté la conception, la modélisation et les mesures pour différents designs de micro-cavités optiques et de micro-interféromètres optiques. Le travail de modélisation a été initié sur des briques de base puis sur une étude de cas (sélecteur de mode) dont les résultats sont présentés dans le chapitre 3 de la thèse.

Dans la deuxième partie, nous nous sommes concentrés sur l'étude d'une nouvelle classe de cavités FP basée principalement sur des miroirs de Bragg et sur des surfaces et des interfaces de forme cylindrique. La première conception repose sur des miroirs de Bragg cylindrique permettant de concentrer la lumière du faisceau dans un plan transversal, tout en bénéficiant d'une bonne réflectivité. Ils présentent un Q plus haut que celui des cavités à miroirs plans ; le Q maximum enregistré étant de 1999, correspondant à un FWHM minimum enregistré de 0,77 nm pour un dispositif basé sur 4 couches de silicium par miroir. Dans ce cas, la longueur de la cavité était de 210 μm. Outre l'amélioration de performances offerte par ce dispositif, il ouvre la voie à une exploration plus poussée pour des phénomènes physiques ; en particulier, l'excitation des modes transverses (ici TEM_{20}). Cette question a été vérifiée à la fois analytiquement et expérimentalement comme détaillé au chapitre 5. En outre, l'excitation sélective des modes transverses a été vérifiée expérimentalement et cela suggère des

applications potentielles pour le microdispositif comme un filtre sélecteur de mode, un commutateur sélectif en longueurs d'ondes, ou même comme multiplexeur d'ajout-rejet « Add-Drop ».

Le deuxième design également basé sur des miroirs de Bragg cylindriques; comprend en outre une lentille-fibre (FRL), ce qui permet la focalisation de la lumière dans les deux plans transversaux, apportant ainsi une solution complète de confinement de la lumière dans la cavité. Puisque l'architecture est nouvelle, un modèle simple a été développé pour en déduire les limites de stabilité et les rayons de courbure et longueurs de cavités correspondantes. Différentes variantes ont été fabriquées et testées expérimentalement pour étudier la tendance du facteur Q vis-à-vis de la réflectance du miroir. Le Q maximum enregistré est de 8818, correspondant au FWHM minimum enregistré de 0,177 nm pour un dispositif basé sur 4 couches de silicium par miroir pour une longueur de cavité physique de 265,8 μm. Certains calculs ont été effectués pour extraire la réflectance effective du miroir à partir des résultats expérimentaux.

Nous pouvons conclure que cette classe de cavités offre les avantages combinés de forts Q et de grandes longueurs de cavité, qui constituent un atout pour beaucoup d'applications, notamment celles basées sur la spectroscopie d'absorption améliorée par cavité (*Cavity Enhanced Absorption Spectroscopy* - CEAS), pour laquelle nous bénéficions d'une amplification du chemin optique effectif de la lumière, du fait des réflexions multiples à l'intérieur de la cavité.

Dans la troisième partie de la thèse, nous nous sommes concentrés sur l'application des interféromètres optiques dans le domaine des capteurs. L'application met en œuvre un micro-interféromètre de Michelson, dans le cadre d'une application pratique en l'utilisant comme une sonde pour la profilométrie optique, avec un fonctionnement dans la gamme infra-rouge. Dans ce domaine spectral, le micro-dispositif a été modélisé en détail et simulé pour prédire ses performances (contraste et puissance obtenus dans les interférogrammes de transmission et de réflexion) en prenant en compte l'effet de l'expansion du faisceau gaussien et pour des tailles de spot différentes.

Deuxième Partie

VERSION LONGUE RÉDIGÉE EN ANGLAIS

LONG VERSION REDACTED IN ENGLISH

Chapter 1
Introduction

1.1 Introduction and Novelty of the thesis

Optical fiber communication is certainly the application area which led to the most intensive research effort on optical microelectromechanical systems (Optical MEMS, also referred to as MOEMS [1-3]) which includes, among others, micro-optical resonators. Among these, silicon-based Fabry-Perot (FP) cavities, mainly intended to Wavelength Division Multiplexing, have been developed as tunable filters [4-9] and external cavity lasers [10-14]. More recently, such FP microcavities also found interest in sensing application, including refractometry [15-17] , inertial sensing [18], gas sensing [19-21] and chemical and biological analysis [17]. In most of these applications, the spectral line width is of special interest when considering the system performance, which is also related to the cavity finesse and quality factor [22]. High quality factors are desired to provide high distinction between specific wavelengths, as well as wavelength stability. Mirror reflectance is therefore of primary importance and Bragg reflectors are preferred due to their very high reflectance that can exceed 99.9 %. These Bragg mirrors can result either from thin-film coatings [23] or from silicon micromachining leading to silicon-air Bragg mirrors as in [6]. We can say that the Bragg mirrors lie at the core of most of high quality integrated optical components based on free space propagation of light, such as the resonators and the interferometers. In this research work, we focused on developing and studying novel architectures for the Fabry-Perot resonator and the Michelson interferometer based on micromachined Bragg mirrors.

Based on this technology, we worked in this thesis on the design, realization and study of three sets of microoptical interferometric devices intended to three different applications. The novelty of our contributions can be summarized in the following points.

The first set of devices concerns new architectures of Fabry-Perot microcavities based on curved surfaces. They show higher performance in terms of the quality factor compared to the conventional planar cavities due to improved light confinement. These devices also revealed the behaviour of selective excitation of higher order modes that are sustained in such cavities, suggesting application to Mode Selective and Wavelength Selective Switching. Furthermore, those cavities suggest numerous other applications in opto-fluidics.

The second prototype concerns the deployment of the Michelson interferometer as an optical probe for surface profilometry in tiny, sub-millimeter hollow tubes of circular cross section. In our case, the developed prototype is studied at the infrared wavelengths. Preliminary measurement results are presented for operation in that spectral range.

1.2 Objectives and Motivation

This thesis has two main objectives. Our first objective is to design innovative micro-optical and micro-opto-mechanical microsystems (optical MEMS) and explore the physical phenomena involved in the functioning of such microsystems. A second objective is to integrate such compact optical MEMS on silicon to create prototypes of devices for selected challenging applications. One application relates to optical measurement of surface profile inside the sidewalls of tiny holes, of sub-millimeter diameter.

We were motivated for conducting this research work for many reasons. The technical interest on micro-optics and MEMS comes in the first position. Then, our motivation was to achieve a thorough study on selected optical interferometers –Fabry-Perot resonators–, for the purpose of providing new knowledge to the scientific community. Then, comes the strategy of the laboratory; beside the important place of the fundamental studies, the intention is to deploy optical MEMS for non-telecom applications, by anchoring them to the field of sensors. Indeed, optical techniques are non-contact methods which help to preserve the integrity of the mechanical structures (shape and material, which remain a pure silicon monolithic block). This, in turn, avoids the employment of electrical signals which do not sustain harsh environments and parasitic interferences. Proceeding in this way, comes the exploration of two different aspects: superior metrological performance might be offered by the optical solution; ideally, resolution is estimated to the sub-pm. The excellent wavelength stability of laser sources can be taken as an advantage for achiving high quality dimensional meausrements. Optical solutions are known as well for their high speed and their immunity to influencing quantities.

One final motivation underlying the initiative for this research work is to gain profit from the expertise of ESIEE in the Deep Reactive Ion Etching process to develop more performant optical resonators based on this same technique. Thus, the activities of the Microsystems group of ESIEE enlarge the topics covered in the area of Photonic Microsystems, and specially those based on micromachined silicon-air Bragg structures.

This was also a good opportunity to tackle a new skill at ESIEE, which is the characterization of photonic MEMS components. In this contest, an optical platform has been established and enriched with equipments for optical measurement at ESIEE. It is being developed for the purpose of characterising of photonic MEMS components.

1.3 Impact on the scientific community

Coating-free silicon mirrors and corresponding optical cavities are of special interest, as they offer excellently combined optical and thermomechanical behaviors. First, single crystal silicon has low thermoelastic loss [24] leading to mechanical quality factors as high as 10^9 [25]. Secondly, silicon has

low absorption in the near infrared and, moreover, it offers the remarkable possibility of building monolithic, coating-free, high quality mirrors, as recently reported [26]. Primary needs for such high quality optical mirrors and cavities relate to fundamental research in several areas: gravitational wave detection [27], exploration of quantum limits through sub-Kelvin optical cooling [28, 29], lasers and cavity quantum electrodynamics experiments under high confinement [30]. In these areas, the concern is not only about achieving high optical quality factors (Q) but also small modal volumes (V), leading to a figure of merit of the form (Q/V) [31-33].

On the other hand, optical cavities with other specific properties are also required in biology and environmental science, namely in instruments dedicated either to single biological entities or microscopic particles for optical trapping [34], manipulation [35] and characterization [17], as well as fluid mixtures for analysis by optical spectroscopy techniques [36, 37]. When targeting such instruments in an ultra-compact lab-on-chip format, the main issue for optical cavities is to leave a distance (L) between the mirrors, that is long enough to allow both the introduction of a particle inside the cavity and a sufficiently long optical path for absorption spectroscopy. At the same time, light must remain confined inside the cavity despite the increased length of the latter for the purpose of achieving high finesse and quality factor. Most reports on high quality optical micro and nanoresonators relate to guided propagation of light inside rings, disks, or Fabry-Pérot (FP) cavities with access waveguides [38, 39] including solid or liquid media. They are also based on light confinement in a space in the order of 10 microns or less. Practically, the larger is the cavity; the lower will be the Q-factor of an optical resonator in the microscale. This trend relates to expansion of the Gaussian beam inside the cavity after several round trips; the beam eventually escapes from the cavity due to the short height of the reflectors. Therefore, the challenge of combining both high L and high Q can be evaluated by introducing $Q.L$ as a figure of merit. Earlier work on FP microcavities involving light propagation in air limited L to few 10's of microns [6, 16, 38-40]. The highest recorded $Q.L$ was around 10^6 μm for a silicon cavity of length 12 μm [39]. In this work, we achieved $Q.L = 4.2 \times 10^5$ μm over a length 210 μm in the simple curved cavity and 2.34×10^6 μm over a physical length of 265.8 μm in the cavity with Fiber Rod Lens.

Concerning the research carried on optical interferometers, we can say that high performance metrology requires highly stable references. When considering measurement of dimensions, the optical wavelength is among the most stable achievable dimension references to date. We can therefore take advantage of this wavelength stability for achieving metrological-grade dimensional measurements through implementing an interferometric method and this is our ultimate goal in that research. Interferometric methods are being already widely used in macroscopic instruments for the purpose of measuring film thickness, distance to obstacles as well as surface profiles. Herein, we introduce a miniaturized architecture that can achieve the same functions. For that purpose, we developed an

interferometric optical micro-probe, for non-contact measurement of distance-to-surface of samples in confined environments, such as holes and trenches whose lateral dimensions are in the order of hundreds of microns.

1.4 Organisation of the manuscript

This first chapter serves as an overall introduction to the thesis. Then, the thesis is divided into four parts leading to a total volume of nine chapters. Part I consists of two chapters and is devoted to give an introductory view about the optical resonators and interferometers. Chapter 2 gives an overview about the optical resonators and the definitions of the resonator optical characteristics. Then, follows the discussion about the various architectures of the Fabry-Perot resonator and their applications. After that, the optical interferometers are described along with their applications. Chapter 2 is ended with a brief outline to the basic theories or analytical models used in the following chapters of the thesis. Chapter 3 is dedicated to the comprehensive study of the building block based on Silicon-Air interfaces. The multilayer stack theory is resumed and applied to the design and study of common structures: Bragg mirror, Fabry-Perot filters. The chapter ends with simulations for a case of study: The mode selector.

Part II is dedicated to the use of curved optical surfaces and it consists of three chapters. Chapter 4 gives a brief introduction to later chapters included in this part. We just mention about the curved Fabry-Perot architectures discussed afterwards and their advantages with respect to conventional planar cavities. Then, chapter 5 describes the first architecture which exhibits an incremental higher performance in terms of the quality factor as compared to the conventional planar cavities. We name it the simple curved cavity. The structure, its related model and the measurement results are described in full details. Characterization results are interpreted and compared to the analytical results. Discrepancies have been elucidated and explained. Mode-selective filtering behaviour is observed and suggests application to a wavelength-selective filtering device. Chapter 6, however, is devoted to the second novel architecture using additional curved surfaces. It is named the curved Fabry-Perot cavity with Fiber Rod Lens. A new stability model has been derived to assure design of stable cavities. The measurement results are presented and described in full details. Analytical calculations have been made to extract the optical parameters obtained after the fabrication process. Tendencies of the device for variance of the geometrical parameter have also been studied.

Part III relates to applications of Bragg reflectors used either in resonators or in interferometers. This third part consists of one chapter, dedicated to present a specific application of the Michelson interferometer. In chapter 7, we present the application of the Michelson interferometer as a surface profiler working in the infrared range. For that purpose, an architecture is devised to allow surface profile measurements in tubes of circular cross section. In this chapter, special focus is attributed to the

modeling and simulations of the whole device to predict its performance and to support the measurement results presented later in this same chapter.

Part IV consists of one chapter and it concludes the thesis highlighting the basic results, the achievements, and the major contributions. It also focuses on the perspectives and the potential directions that may be followed to continue this research work.

PART I

Silicon-Based Optical Resonators and Interferometers: Background and Fundamentals

Chapter 2

Background and Fundamentals

The content of this chapter aims to introduce the optical background intended to facilitate understanding of the remaining parts of this thesis.

- First, we discuss about optical resonators, their main characteristics, their different architectures
- Secondly, we dicuss about optical interferometers, not limited to the Fabry-Perot and the Michelson interferometers, considered in our work, but also other interferometer architectures that might or have already been implemented in the form of photonic MEMS.
- Third, beam splitters and reflectors are discussed in detail as they are important building blocks of the studied optical Microsystems and their characteristics have a direct impact on system-level performance and behaviour.
- Fourth and last is the theoretical background related to Gaussian beam propagation and the closely related theoretical formalism of ABCD matrix formalism.

2.1 Optical resonators: Definition and fundamental properties

An optical resonator (or resonant optical cavity) is an arrangement of discrete or distributed optical components, which allows a beam of light to circulate in a closed path leading to constructive interference confined in limited space and related enhanced intensity profiles at certain wavelengths: these are the resonant modes and related resonant wavelengths, respectively. Besides these generic charcateristics, such resonators can be made in very different forms and different properties, presented in what follows.

2.1.1 Resonators with Discrete Components versus Waveguide Resonators

An optical resonator with discrete components can be made from discrete optical components (either bulky or miniaturized). On the other hand, in case of waveguide resonators the light is guided by the physical structure rather than travelling in free space.

Solid-state bulk lasers are using bulk-optical resonators. In this configuration the transverse mode properties depend on the arrangement and the size of the overall setup and the mode sizes can vary significantly along the path. In waveguide resonators the guiding structure can either be optical fibres, as in fibre lasers or integrated waveguides made of different materials built on substrates. In this type of resonators the transverse mode properties are determined by the local properties of the waveguide. There are also mixed types of resonators which combine discrete optical components as well as waveguide structures. Such resonators can be found in some fibre lasers.

2.1.2 Linear Resonators versus Ring Resonators

In linear (standing-wave) resonators the light bounces back and forth off two end mirrors. There are always counter propagating waves interfering with each other to form a standing-wave pattern due to the continuous circulation of light.

In ring resonators, light circulates in two different directions as shown in Fig. 2.1 and there is no end mirrors. However, in either type, a resonator may contain additional optical elements which are passed in each round trip. For example, a laser resonator contains a gain medium compensating for the losses in each round trip of the light. During those round trips, some effects such as diffraction, focussing defocusing and saturated absorption may occur.

(a) (b)

Fig. 2.1 A simple linear optical resonator with a curved folding mirror (a) and a four-mirror bow-tie ring resonator (b) [41].

2.1.3 Stable versus unstable bulk-optical resonators

With respect to bulk-optical resonators, stability means that rays injected into the system with some initial transverse offset position and angle will stay within the system during many round trips. For unstable resonators, some of these rays with unlimited increase in transverse offset will leave the optical system. The stability of a resonator depends on the properties and the arrangement of the optical components. Hence, things such as curvature of reflecting surfaces, other focusing effects, and distances between the components will affect the stability. Consequently changes in arm length or dioptric power of a focusing element would result in the resonator goes through one (for ring resonators) or two (for standing-wave resonators) stability zones. At the edges of such stability zones, the beam sizes at the resonator ends can either diverge or vanish.

2.1.4 Resonator Modes

Resonator modes are defined as being self-consistent field distributions of light – that is to say, they are electric field distribution which can be self-reproduced in each round trip inside the resonator (except that there are some associated power loss). Properties of resonator modes depend on several issues:

- For waveguide based resonators, the waveguide properties determine the transverse mode and it is unchanged all over the resonator as long as the waveguide properties are constant. A single transverse mode exists solely in case single-mode fibers are used.

- For discrete-optical resonators, the stability of the resonator is the issue determining the mode properties. For example, Hermite–Gaussian functions are the characteristic modes in stable resonators. In such resonators, the lowest-order mode (axial mode, fundamental mode) possesses a simple profile; higher-order modes, instead, have complex shapes. The ABCD matrix formalism is used to calculate modal properties. In the case of unstable resonators, the mode structures are much more complex and they are computed using numerical techniques. In general, the transverse mode size varies along the resonator axis for unstable resonators.

At each transverse mode pattern and for certain optical frequencies only, the optical phase is self reproduced after each round trip (wherein the round trip phase shift is an integer multiple of 2π). If these conditions are met, the mode frequencies also called resonance frequencies are obtained. They are nearly equidistant (not exactly equidistant due to chromatic dispersion). The frequency modes are spaced apart by a distance called the free spectral range (FSR) which is the inverse of the round trip group delay. We can conclude that the FSR decreases as the resonator length increases.

Another important definition, called Finesse relates to the ratio of the frequency spacing to the 3dB-width of the resonances. It is determined by the power losses per resonator round trip. A related measurement quantity is the Q factor, which is the ratio of resonance frequency to the bandwidth. Note that all these definitions are highlighted and quantified analytically in the next section of this chapter.

2.2 Basic notions: main characteristics of resonators and related performance

2.2.1 Resonant Wavelengths and resonant modes

Resonant wavelengths are the set of particular values of the wavelength, for which the cavity exhibits a resonance behaviour. These wavelengths correspond to maximum values (peaks) of the transmittance spectrum. For each resonant wavelength, there is a corresponding resonant mode and mode order. Fig. 2.2 gives the typical transmittance of a resonator (of Fabry-Perot type) illustrating the three first resonance peaks together with the corresponding modes and mode orders. For each mode there is a different distribution of the electromagnetic field confined inside the resonator.

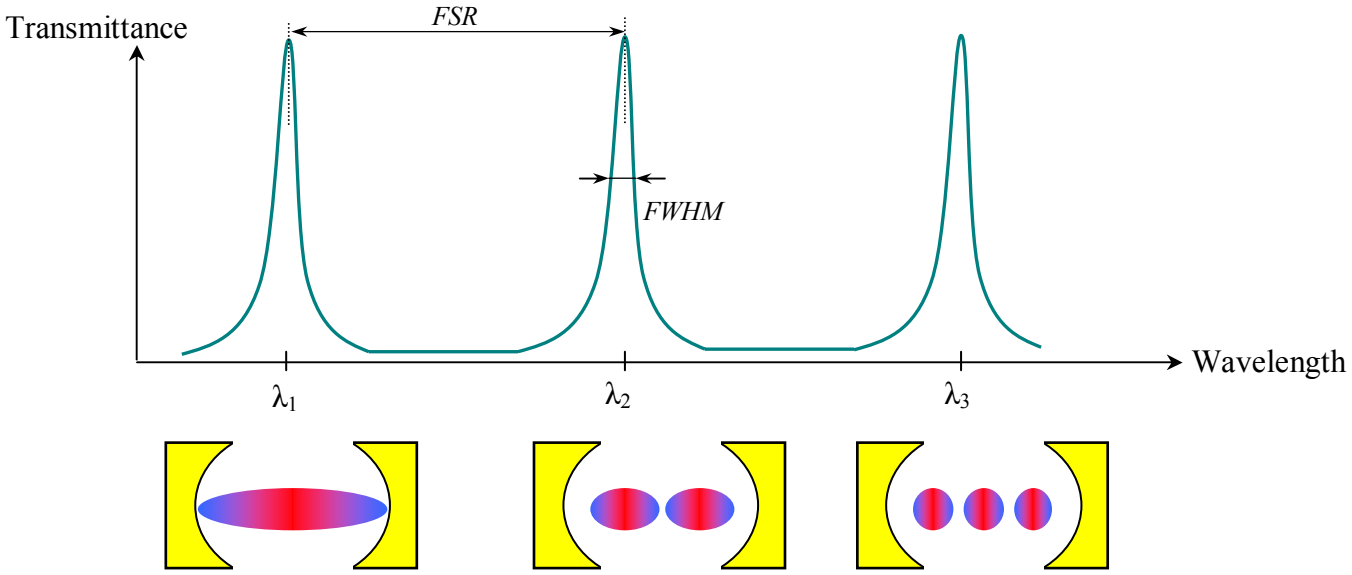

Fig. 2.2 Typical transmission response obtained by FP cavity and associated resonant modes

2.2.2 Linewidth or Full-Width at Half-Maximum (FWHM)

It is the 3-dB bandwidth of the resonator bandpass. It is mostly related to the reflectance of the mirrors in the FP cavity.

2.2.3 Free Spectral Range (FSR)

It is simply the period of the transmission or the reflection response of the optical resonator. It is the distance between successive peaks in the frequency response. It may be expressed in the frequency or in the wavelength domain.

2.2.4 Quality factor

The quality factor (Q) is the resonator ability to store energy. It is also defined as a measure of the sharpness or the selectivity of the resonance in the cavity. Theoretically, it is given by:

$$Q = \frac{2\pi\left(\text{energy stored in the system at resonance}\right)}{\left(\text{energy lost in a cycle of oscillation}\right)} \tag{2.1}$$

An equivalent definition used in experimental works is,

$$Q = \frac{\omega_0}{\Delta\omega_{1/2}} = \frac{f_0}{\text{FWHM}} = \frac{\lambda_0}{\Delta\lambda_{1/2}} \tag{2.2}$$

2.2.5 Finesse

At optical frequencies, the values of the Q-factor are astronomical because of the smallness of the optical wavelength. To avoid such large numbers and to provide a measure of the filtering properties, one uses another term: The Finesse. It is given by:

$$F = \frac{FSR}{FWHM} \tag{2.3}$$

2.2.6 Contrast (C)

It is defined as the ratio of the maximum and the minimum of the intensity transmission factor. This factor determines the crosstalk attenuation which is achievable when using the cavity for selecting a wavelength channel out of a set of channels. It is also known as the extinction ratio.

$$C = \frac{I_{\max}}{I_{\min}} \quad , \qquad \text{Extinction Ratio} = 10\log_{10}(C) \tag{2.4}$$

2.2.7 Fringe visibility (V)

It is defined as the ratio between the difference of the maximum and minimum intensities to the summation of the maximum and minimum intensities. It is a measure of the ability to distinguish between the transmitted or the reflected fringes. The value of V ranges between 0 and 1 and the higher it will be, the better will be the resonator response.

$$V = \frac{I_{\max} - I_{\min}}{I_{\max} + I_{\min}} \tag{2.5}$$

2.2.8 Tunability

Changing the cavity optical path length makes the cavity tunable. This is obtained mainly by varying the refractive index or even the physical length. In case slow tuning is afforded, the refractive index is changed by varying the gas pressure (typically air) inside the cavity.

Concerning the spacing between the reflecting plates, it can be changed either manually (using micrometer screws) or electromechanically. In case where fast tuning is requied, piezo-electric transducers are used. Then, the maximum transmission occurs when the optical path length equates to an integer multiple of half the light wavelength inside the cavity.

In the next section, we highlight the physical phenomena affecting the cavity finesse and quality factor.

2.3 Loss mechanisms

Optical loss in resonant structures leads to spectral broadening of resonant peak and reduction of resonant field enhancement. That is why the loss factor can not be neglected. The resonator action involves various loss mechanisms. Among them we can cite, absorption losses, scattering losses, reflection losses, insertion loss due to light coupling, polarization dependence loss, diffraction loss due to beam expansion outside the cavity domain and radiation (bending) losses. It is worth to mention that all these types cannot occur simultaneously in a certain resonator architecture. For example, reflection

losses cannot take place in microring resonator and radiation losses cannot take place in Fabry-Perot resonator. In the following section, we outline these different sources of losses to acquire a better understanding for the resonator functionality.

2.3.1 Scattering losses

For microresonators constructed using planar fabrication technology, the dominant loss mechanism is scattering due to edge roughness. The sidewall roughness of the guiding structure perturbs the propagating field and degrades the quality factor and the resonator finesse. It is worth to mention that scattering losses exist also in Fabry-Perot resonators due to sidewall roughness of the reflecting mirrors. This issue is illustrated in Fig. 2.3 for an optical waveguide and a microdisk resonator.

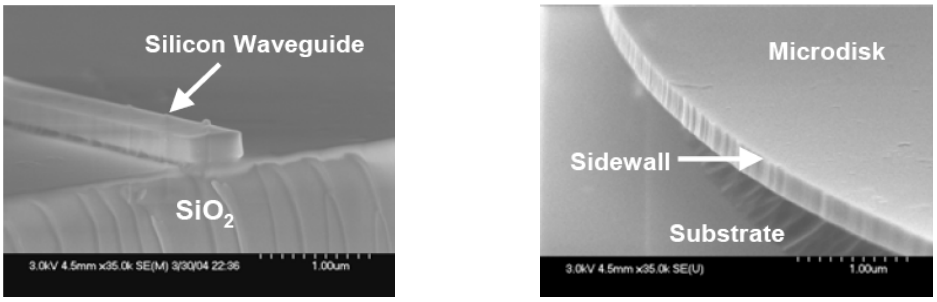

Fig. 2.3 SEM photos showing the edge roughness of a waveguide and microdisk resonator [42]

2.3.2 Bending losses – radiation losses

The fabrication of the ring resonator is of primary importance as it controls the loss. In microrings and pedestal waveguides devices, the loss is mainly dominated by various mechanisms namely, leakage to the substrate, scattering or contra-directional coupling due to edge roughness and bending.

Proper waveguide design helps reducing the substrate leakage loss. Process improvement translated into the application of high-resolution lithography, vertical photoresist sidewalls, and hard masks can help as well in reducing edge surface roughness. Bending losses are, however, governed by the refractive index contrast for the chosen materials. As known, for a given material, the index contrast puts a limit on the minimum ring resonator size as it determines the minimum bending radius over the in-plane direction. In most cases, the cladding material for the ring and for pedestal waveguide is air.

Bending losses is the mechanism wherein the light can not be maintained confined in the bended waveguide. This mechanism is associated with radiation taking place as a cylindrical components coming out of the structure. They are associated with azimuthal components resulting in spiral phase contours. Bending losses can be calculated precisely for cylindrical geometries in the low Q limit. Other techniques are used in the high Q limit. Out-of-plane radiation can not be ignored in finite 2D geometries.

2.3.3 Reflection losses

This kind of loss occurs mainly in Fabry-Perot resonators. It is due to the mirror reflectance which is different from unity. It is independent of the cavity length. It is to be noted that the reflection losses involve all the non-idealities of the mirror which involve in addition to the non-unity reflectance, the scattering at the mirror interfaces. This kind of loss does not exist in microring structures but it has an analog component called the coupling losses. It is related to the coupling coefficients in the directional couplers between the bus waveguide and the ring waveguide.

2.3.4 Absorption loss

The internal loss of the resonator is defined as the absorption loss. It originates from the absorption "scattering" of light by the cavity material. It is a kind of distributed loss directly proportional to the cavity length and hence, it increases as the interaction length increases. Chemical and biological applications involves the interaction of molecules and biological species with light propagating inside the cavity so that the different species could be recognized by spectral analysis. This, in addition, leads to absorption losses even if the cavity material is absorption free.

2.3.5 Insertion loss – Coupling losses

Insertion loss is the loss of signal power resulting from the insertion of a device in a transmission line or optical fiber and is usually expressed in decibels (dB). If the power transmitted to the device before insertion is P_T and the power received by the device after insertion is P_R, then the insertion loss in dB is given by:

$$IL = 10\log_{10}\left(\frac{P_R}{P_T}\right) \tag{2.6}$$

One of the sources for this loss is the mismatch between the field injected from the input fiber and the resonator modes. It is also named coupling losses

2.3.6 Diffraction loss

Gaussian beam propagating in unguided structures is subjected to beam diffraction which is the case in free space propagation resonators. After several round trips, the beam diffraction becomes more important and light escapes from the resonator boundaries leading to reduced transmitted power and degraded quality factor.

In fact, the Gaussian beam extends to a considerable distance from the axis and may not hit a reflecting surface. The fraction of the incident power that is not intercepted by the mirrors is called

diffraction losses. The diffraction loss is one of the reasons for the instability of Fabry-Perot resonator based on planar mirrors where no focusing takes place.

2.3.7 Polarization dependent loss (PDL)

In passive optical components, PDL is defined as the loss that varies as the polarization state of the propagating wave changes. It is expressed as the difference between the maximum and minimum loss in decibels as mentioned in (2.7). The Polarization dependent loss is a measure of the peak-to-peak difference in transmission of an optical component or system with respect to all possible states of polarization. It is the ratio of the maximum and the minimum transmission of an optical device with respect to all polarization states. The polarization dependence of the transmission properties of optical components has many sources. One of these sources is the material birefringence where the refractive index behaves differently for TE and TM polarizations. This loss is more pronounced in microring structures.

$$PDL = 10\log_{10}\left(\frac{P_{\max}}{P_{\min}}\right) \tag{2.7}$$

2.4 Architectures of optical resonators

We classify the optical resonators into two basic classes: (i) Standing wave resonators where the light forms a standing wave inside the cavity. Examples of such resonators are 1D-PC, 2D-PC and FP cavities) and (ii) travelling wave resonators where the light circulates inside the resonant cavity. Examples of such resonators are micro-ring resonators, disk resonators and microspheres. The different architectures are shown in Fig. 2.4.

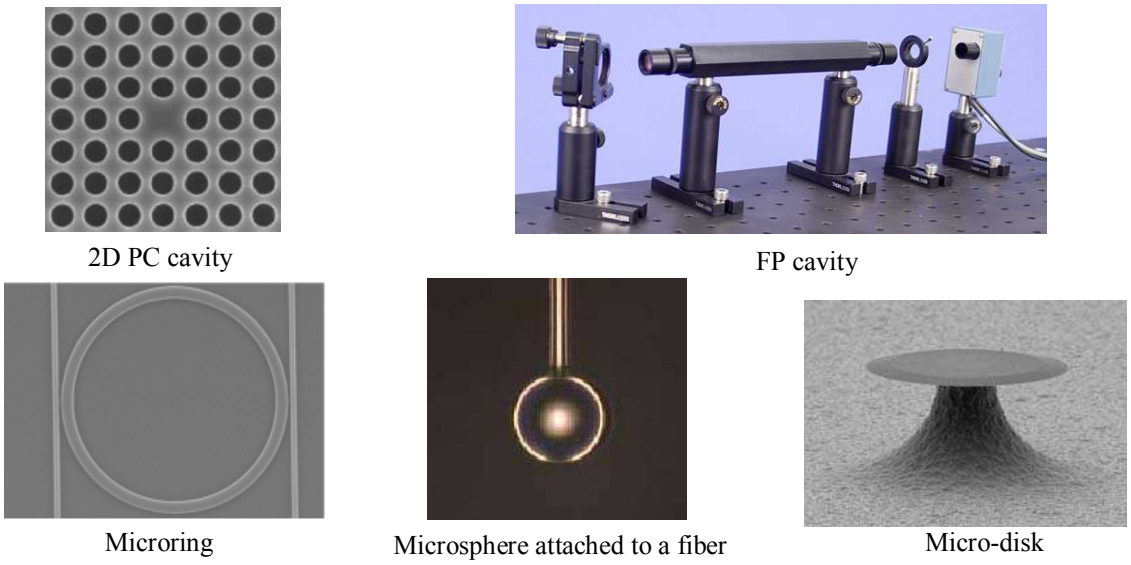

Fig. 2.4 Different architectures for the optical resonator classed into Standing waves and travelling waves resonators [43].

2.4.1 The Fabry-Perot resonator

2.4.1.1 Principle of operation

The principle of this filter was invented in 1899 by the French physicists Charles Fabry and Alfred Perot [44]. The operation principle is based on multiple reflections between reflecting interfaces. It consists of two highly reflective parallel mirrors are separated by a small distance referred to as Fabry-Perot (FP) etalon. Most of the light which encounters the first mirror is reflected, but some of it transmits, travels through the cavity (the space between the mirrors, often filled with some kind of dielectric e.g. liquid crystals), and strikes the second mirror. At the second mirror most of the light is reflected, while some transmits. The reflected light travels backwards, hitting the first mirror, where some of it again reflects and some transmits. The result is that depending on the spacing and index of refraction between the mirrors, at some wavelengths the multiple reflections interfere constructively. At these wavelengths the cavity resonates, so that the light passes through. For other wavelengths, the transmitted waves add out of phase and the reflected waves add in phase. At these wavelengths, the resonator overall transmission is low and the overall reflectivity is high.

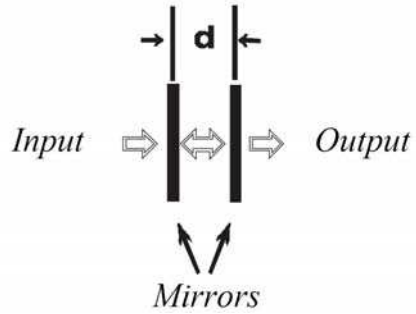

Fig. 2.5 The Fabry-Perot resonator [45]

2.4.1.2 Analytical model

To make the problem as familiar as possible, we consider the excitation of the cavity shown in Fig. 2.5 by an external source, such as a tunable laser or a variable-frequency oscillator. To keep the arithmetic to a minimum, we consider all waves, incident on the cavity from the left, inside the cavity, or transmitted through it to the right to be uniform plane waves of limited spatial extent transverse to the direction of propagation. Our task is to relate the fields, running wave intensities, and stored energy on the inside of the cavity to those quantities that we can measure on the outside.

Let us follow a wave as it bounces back and forth between the two mirrors. Consider the initial field at the plane just to the right of M_1, labeled by E_0. It propagates to M_2 and back to the starting plane and experiences an amplitude change of $\Gamma_1\Gamma_2$ and a phase factor $exp[—jk2d]$ as it travels that round trip and thus generates the field labeled E_1^+, which experiences the same trials and tribulations as E_0, and in turn generates E_2^+, and so on. At every point along the path from M_1 to M_2, the fields E_1^+, E_2^+, and so on are to be added to E_0 to which we assign the reference phase of 0°. There is an

assumed lagging phase angle φ, we have also assumed that the round trip phase shift (RTPS), $\theta = 2kd$, is almost but not quite an integral multiple of 2π rad. The deficiency labeled by φ, is related to kd by

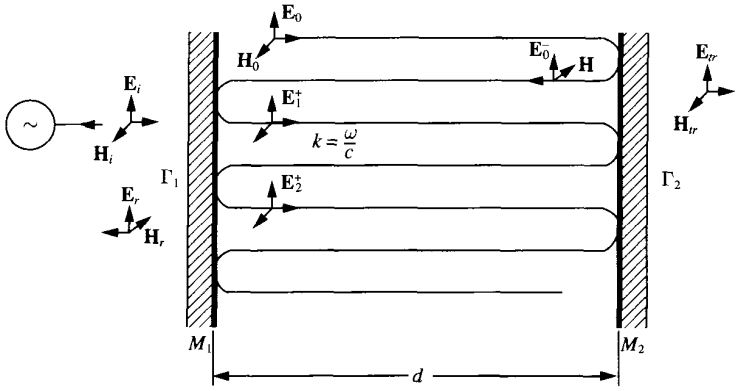

Fig. 2.6 Fabry-Perot optical cavity with ray tracing for deriving the transmission and reflection responses [22]

$$2\theta = 2kd = q2\pi - \varphi \tag{2.8}$$

where q is now an integer. Note that if the angle φ is significant, the total field propagating to the right inside the cavity is merely the difference between the origin and the spiral of phasors, quite similar to the straight-line distance between the beginning and end of a coiled rope.

The total electric field on the right side of M_1 and traveling to the right (indicated by the superscript "+") is given by the field E_0, which is that transmitted through the mirror from the source, plus the fields that have made 1 to N) round trips to M_2, back to M_1, and starting the (2 to N + 1) trip. The amplitudes of those fields are simply related to E_0 by the field reflection coefficient of each mirror. The phase of the N^{th} component, E_N, is delayed with respect to E_0 by N times the round trip phase shift of $2kd = 2\theta$ and N times the phase contributed by each mirror. While this last contribution can be important, let us ignore it for now in the interest of simplicity.

$$\begin{aligned} E_T^+ &= \sum E_N^+ = E_0 \left\{ 1 + \Gamma_1\Gamma_2 e^{-jk2d} + \left(\Gamma_1\Gamma_2 e^{-jk2d}\right)^2 + \ldots \right\} \qquad N \text{ trips} \\ &= E_0 \left[\frac{1}{1 - \Gamma_1\Gamma_2 e^{-j2\theta}} \right] \end{aligned} \tag{2.9}$$

where θ is the electrical (or optical) length of the cavity, and is equal to $\omega nd/c$. The total field returning from M_2, traveling to the left (indicated by the superscript "-") and incident on M_1 is just Γ_2 times E_T^+ times the round-trip phase factor.

$$E_T^- = \Gamma_2 e^{-j2\theta} E_T^+ = E_0 \left[\frac{\Gamma_2 e^{-j2\theta}}{1 - \Gamma_1\Gamma_2 e^{-j2\theta}} \right] \tag{2.10}$$

The running wave intensities I^+ and I^- are simply related to $E^{(+,-)}$ by $I = E.E^*/2\eta$ where the asterisk denotes complex conjugation. For the wave running to the right, we obtain,

$$I^+\left(z=0^+\right)=\frac{\left|E_0\right|^2}{2\eta}\left\{\frac{1}{1-\Gamma_1\Gamma_2 e^{-j2\theta}-\left(\Gamma_1\Gamma_2 e^{-j2\theta}\right)^*+\left|\Gamma_1\Gamma_2\right|^2}\right\}$$

$$=I_0\frac{1}{1-2\left|\Gamma_1\Gamma_2\right|\cos 2\theta+\left|\Gamma_1\Gamma_2\right|^2} \tag{2.11}$$

$$=I_0\frac{1}{1-2\left|\Gamma_1\Gamma_2\right|\left[1-2\sin^2\theta\right]+\left|\Gamma_1\Gamma_2\right|^2}$$

$$I^+\left(z=0^+\right)=\frac{\left|E_0\right|^2}{2\eta}\left\{\frac{1}{\left(1-\sqrt{R_1R_2}\right)^2+4\sqrt{R_1R_2}\sin^2\theta}\right\} \tag{2.12}$$

where we have assumed that the field reflection coefficients are real numbers and have substituted the power reflection coefficients $R_{1,2} = |\Gamma_{1,2}|^2$. The plane z = 0+ is just to the right of the surface of M_1.

The quantity $E_0^2/2\eta$ is an intensity and is simply the (power) transmission coefficient of M_1 times the incident intensity $T_1.[E_{inc}^2/2\eta]$, where $T_1 = 1 - R_1$ for lossless mirrors. In a similar fashion, the intensity transmitted through M_2 is the power transmission coefficient $T_2 = 1 - R_2$ times the intensity given by (2.12) since any thing that starts to the right from z = 0+ impinges on M_2 at z = d. After converting to reflectivities and incident intensity, we obtain an expression for the intensity or power transmission coefficient through the two mirrors.

$$I_t=\left\{\frac{\left|E_0\right|^2}{2\eta}=T_1I_{inc}=\left(1-R_1\right)I_{inc}\right\}\left\{\frac{T_2}{\left(1-\sqrt{R_1R_2}\right)^2+4\sqrt{R_1R_2}\sin^2\theta}\right\} \tag{2.13}$$

$$\text{Or}\quad T\left(\theta\right)=\frac{I_{trans}}{I_{inc}}=\left\{\frac{\left(1-R_1\right)\left(1-R_2\right)}{\left(1-\sqrt{R_1R_2}\right)^2+4\sqrt{R_1R_2}\sin^2\theta}\right\} \tag{2.14}$$

We conclude by deriving the cavity parameters, more details can be found in [22], [46]

$$f_0=\frac{qc}{2nd} \tag{2.15}$$

$$FSR_f=\frac{c}{2nd}\ ,\qquad FSR_\lambda=\frac{\lambda^2}{2nd} \tag{2.16}$$

$$FWHM_f=\frac{c}{2nd}\left\{\frac{1-\left(R_1R_2\right)^{1/2}}{\pi\left(R_1R_2\right)^{1/4}}\right\} \tag{2.17}$$

$$Q=\frac{f_0}{\Delta f_{1/2}}=\frac{2\pi nd}{\lambda_0}\left\{\frac{\left(R_1R_2\right)^{1/4}}{1-\left(R_1R_2\right)^{1/2}}\right\} \tag{2.18}$$

$$F=\frac{FSR}{FWHM}=\frac{\pi\left(R_1R_2\right)^{1/4}}{1-\left(R_1R_2\right)^{1/2}} \tag{2.19}$$

2.4.1.3 Applications of Fabry-Perot resonator

Applications of the FP resonator are diverse and can not be covered entirely in these few lines. Detailed review of applications of optical resonators can be found for instance in [47-50]. In fact, this thesis spotlights potential applications for a new class of the FP resonator in several domains of interest. So, we only highlight some of these applications for the matter of citation. FP resonator found interesting application in optical telecommunication, aeronautical applications and biosensing.

Due to the periodic nature of Fabry-Perot interferometry, Fabry-Perot etalon-based devices are ideally suited to wavelength locking for DWDM system lasers. Fabry-Perot etalon-based wavelength lockers have been used in long haul and metro applications to achieve more reliable results. In addition to wavelength lockers, optical filters and references using Fabry-Perot interferometry technology to provide periodic narrow passbands in both transmission and reflection modes serve as key components in calibration, control, and stabilization of tunable components and test instruments.

In all the Fabry-Perot interferometer applications, maintaining stability over environmental changes is the key behind its accuracy. Recent component and manufacturing process advancement has enabled these devices to be kept to within ±1.25 GHz accuracy in 0 to 70ºC operating and -40ºC to 85ºC in-storage environmental conditions throughout the devices' lifetime

Technological development enabled the realization of FP cavities with athermal properties. It offers the ability to precisely generate periodic spectrum, Fabry-Perot etalon-based wavelength filters can be designed to match any specified free spectral range with varying sharpness. The fringe patterns are aligned to the ITU grid, covering all available channels of the network. Because these filters are compact and do not need any active control, they offer many useful functions for wavelength calibration and stabilization.

FP cavities have also been employed for refractometry measurements as detailed in [15-17]. A final example for the use of FP in aeronautical applications, relates to displacement measurements as presented in [18].

2.4.2 Photonic crystal (PC) based resonators

The one-dimensional equivalent to photonic crystals are the dielectric Bragg mirrors [51], in which layers of different refractive indices, one quarter of the desired incident wavelength in thickness, are stacked to provide a maximum in reflectivity for light that is coherently back-reflected from all of the interfaces. In most cases the incident light is perpendicular to the mirror layers, and reflectivities over 99.9999% can be achieved in carefully prepared ion beam deposited Bragg reflectors. When a layer with a thickness different from a quarter of the wavelength (usually a half of a wavelength is chosen) is introduced between two Bragg mirrors, a Fabry-Perot cavity results, in which light is localized and concentrated within that layer.

The photonic crystal (PC) is one of the platforms that can enable the miniaturization of photonic devices and their large-scale integration. These microfabricated periodic nanostructures can be designed to form frequency bands (photonic bandgaps) within which the propagation of electromagnetic waves is forbidden irrespective of the propagation direction [52]. Depending on the dimensionality of spatial periodicity, we distinguish between several different classes of photonic crystals. One-dimensional photonic crystals are well-known dielectric stacks. If the periodicity is two dimensional (2D), we talk about 2D photonic crystals. Strictly speaking, these structures are assumed to be infinitely long in the direction perpendicular to the plane in which 2D periodicity exists. One of the most interesting applications of 2D PCs is photonic crystal fiber. In such a structure, light is confined to the core by the photonic band gap (PBG) and propagates down the fiber, along the PC holes. By introducing spatial periodicity in all three dimensions, real three-dimensional (3D) photonic crystals can be realized. 3D PCs can have complete bandgap, and therefore can control propagation of light in all directions. These structures can be realized using standard top-down etching techniques, multiple thin-film deposition techniques, self-assembly, micromanipulation.

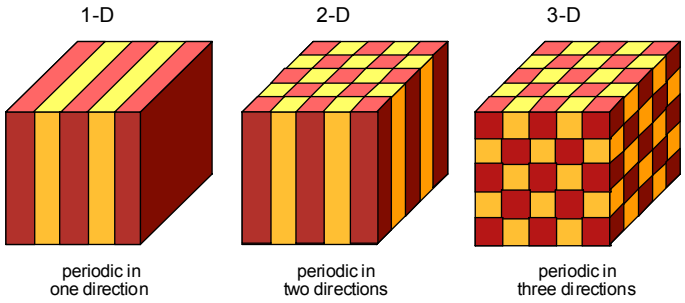

Fig. 2.7 Architectures of 1D, 2D and 3D photonic crystals [53]

In the next paragraph, we illustrate the operation of 1D and 2D PC using some simulation results. For 1D-PC, the periodic refractive index perturbation lifts frequency degeneracy: states concentrated in high index region have lower frequency as illustrated in Fig. 2.8. Inspection of the ω-k diagram shows a prohibited band where injected light with frequencies within the photonic band gap cannot propagate in the photonic crystal. It exhibits total reflection. Thus, 1D-PC's always have a band gap.

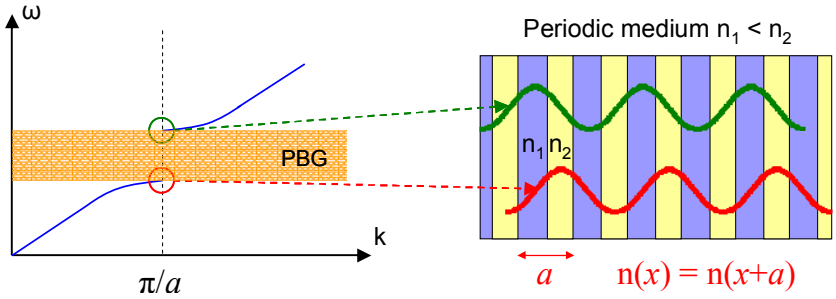

Fig. 2.8 1D-PC and their corresponding ω-k diagram [53]

Let's consider a distributed Bragg Reflector (1D-PC) consisting of alternating high n_2 and low index n_1 layers. Simulations for a structure of 20 periods of length a show that there is a forbidden

band. The reflection response of the 1D-PC, is like the multilayered mirror, steep and flat within a limited wavelength range.

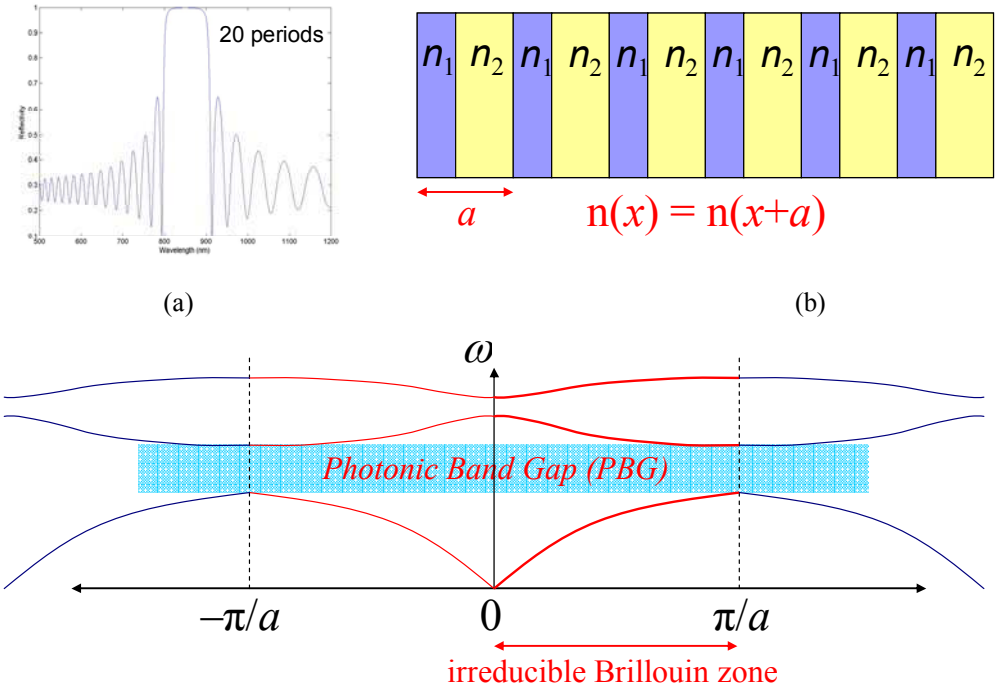

Fig. 2.9 1D-PC consisting of 20 periods of high and low layers (b). The reflection response (a) is plotted along with the ω-k diagram (c) [53]

Another point that we want to illustrate is the simulation for 2D-PC structure as shown in Fig. 2.10 and Fig. 2.11. Note that different k-directions correspond to different band gap frequencies.

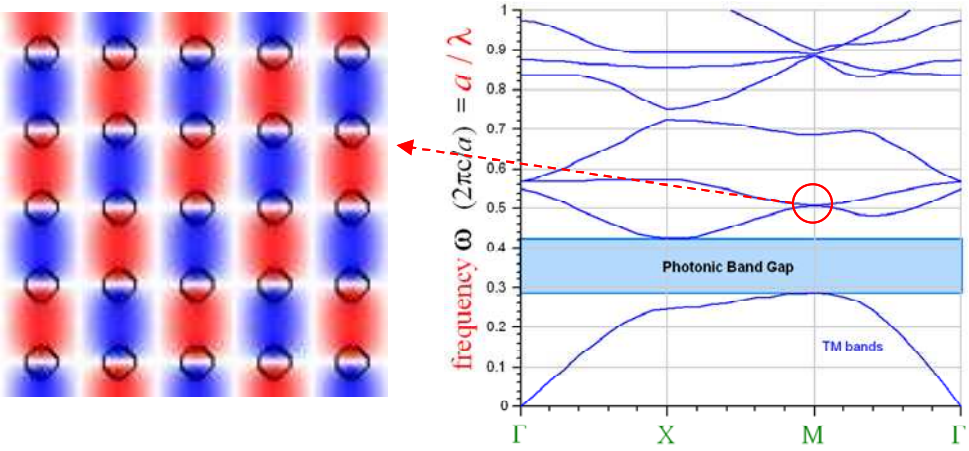

Fig. 2.10 Simulation for 2D-PC for a frequency in the upper band [53]

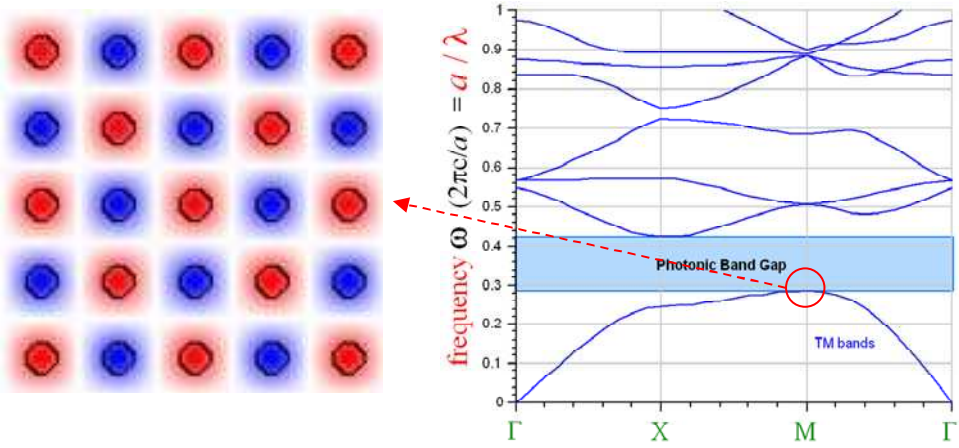

Fig. 2.11 Simulation for 2D-PC for a frequency in the lower band [53]

The photonic crystal resonator may take different geometries varying between 1D, 2D or 3D. Three different architectures are illustrated in Fig. 2.12. The first one is a 1D-PC based FP cavity. The second one is a 2D-PC in which a defect was introduced to perturb the periodicity of the 2D array and then, creates a cavity. The third architecture is 3D-PC with an introduced defect. It is to be noted that the PC cavity confines light in a small volume whose dimension is $\sim\lambda^3$.

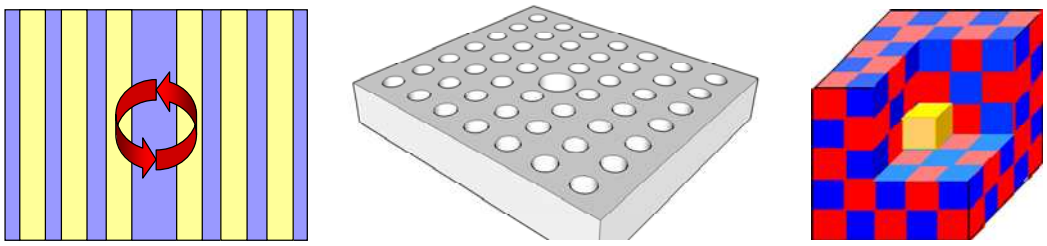

Fig. 2.12 Architectures of 1D, 2D and 3D PC resonators [53]

Simulations of the 1D structure show that there are forbidden frequencies as seen on the graph of the reflection response (Fig. 2.13a). Simulation for 2D structure exhibits a similar behaviour as graphed in Fig. 2.13b

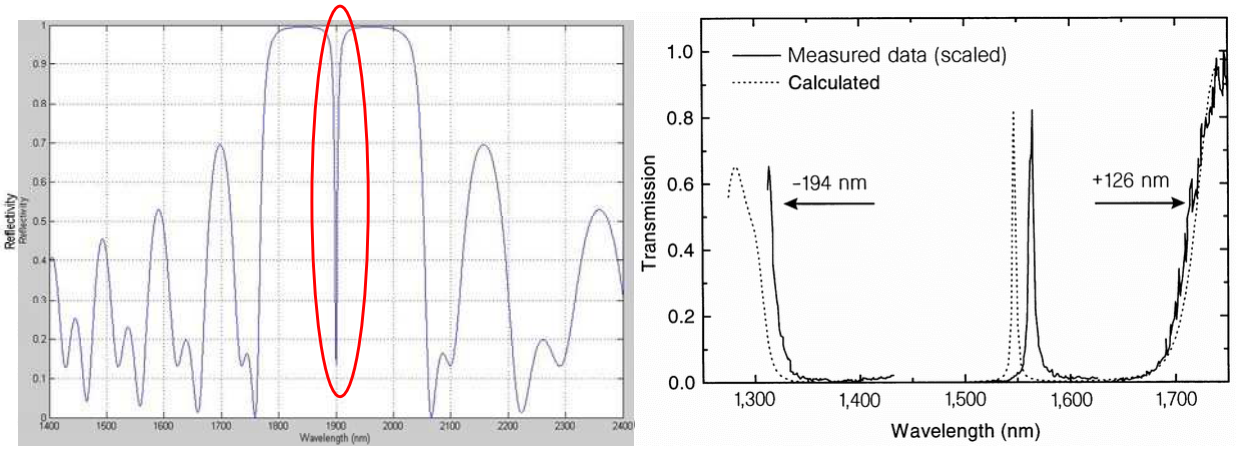

(a) (b)

Fig. 2.13 Reflection (a) and transmission (b) response for 1D and 2D PC structures [53]

2.4.3 Fiber Bragg grating (FBG) based resonators

2.4.3.1 Principle of operation

The periodic refractive index distributions in Fiber Bragg gratings make them typically like 1D photonic crystals structures. They are modeled by the coupled mode theory instead, but, in some sense, they exhibit similar characteristics. Though the different types of optical resonators and their highlighted applications, in this section, we focus on FBG because they are an interesting candidate as it finds other applications especially in the telecommunication area as discussed later in this section.

A fiber Bragg grating consists of a periodic modulation of the refractive index in the core of a single-mode optical fiber as shown in Fig. 2.14. These types of uniform fiber gratings, where the phase fronts are perpendicular to the fiber longitudinal axis with grating planes having constant period are considered the fundamental building blocks for most Bragg grating structures [46]. Light guided along the core of an optical fiber will be scattered by each grating plane. If the Bragg condition is not satisfied, the reflected light from each of the subsequent planes becomes progressively out of phase and will eventually cancel out. Additionally, light that is not coincident with the Bragg wavelength resonance will experience very weak reflection at each of the grating planes because of the index mismatch; this reflection accumulates over the length of the grating. When the Bragg condition is satisfied the contributions of reflected light from each grating plane add constructively in the backward direction to form a back-reflected peak with a center wavelength defined by the grating parameters. Oppositely to the Fabry-Perot interferometer, multiple reflected and transmitted waves result. For a specific wavelength the reflected waves all add in phase, and at this wavelength the grating appears to be highly reflective, while transmitting all the others.

The Bragg condition is when the grating period is half of the input light wavelength; this wavelength signal will be reflected coherently to make a large reflection. Expressed mathematically as:

$$\lambda = 2n_{eff}\Lambda \tag{2.20}$$

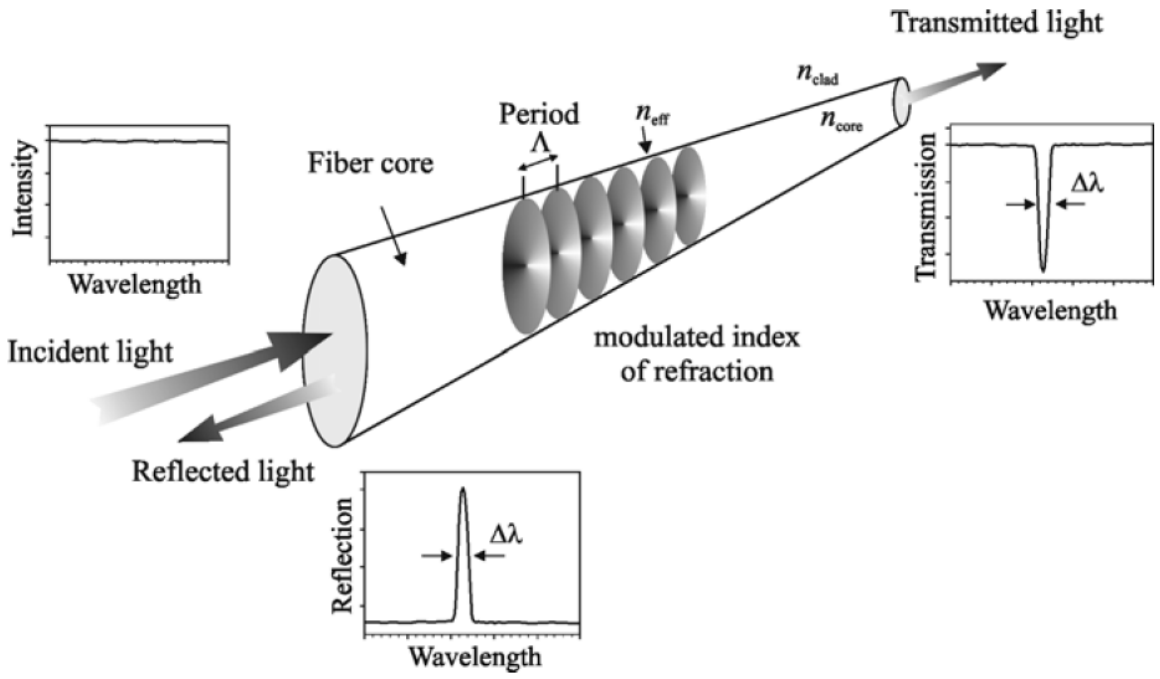

Fig. 2.14 Schematic representation of a Bragg grating inscribed into the core of an optical fiber. The period of the index of refraction variation is represented by Λ. A broadband light is coupled into the core of the fiber. Part of the input light is reflected (at the Bragg condition) and the rest is transmitted. The bandwidth of the reflected and transmitted light depends on the characteristics of the Bragg grating, its length and modulation depth [46]

These types of resonators consist of a region in which the index of the fiber varies periodically between high and low, and they are formed in optical finers by exposing the fiber to interferometric patterns from an ultraviolet (UV) laser as shown in Fig 2.15a or using a phase mask as shown in Fig. 2.15b.

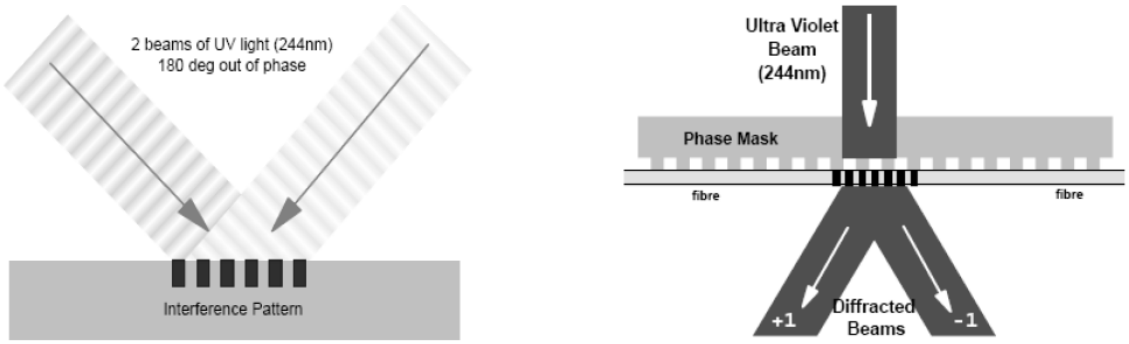

(a) (b)

Fig. 2.15 Setups used for fabricating fiber Bragg grating (a) using interference pattern and (b) using phase mask [54]

2.4.3.2 FBG types and applications

There exist many types of FBG. The following table summarizes the different types and the corresponding applications. Illustrations of optical setups involving FBG are shown in the Fig. 2.16.

Table 2.1 Different types of grating, their characteristics and their applications [55]

Types	Characters	Applications
Simple reflective gratings	Creates gratings on the fiber that meets the Bragg condition	Filter for DWDM, stabilizer, locker
Long period gratings	Significant wider grating periods that couples the light to cladding	Gain flattening filter, dispersion compensation
Chirped fiber Bragg gratings	A sequence of variant period gratings on the fiber that reflects multiple wavelengths	Gain flattening filter, dispersion compensation
Slanted fiber gratings	The gratings are created with an angle to the transmission axis	Gain flattening filter

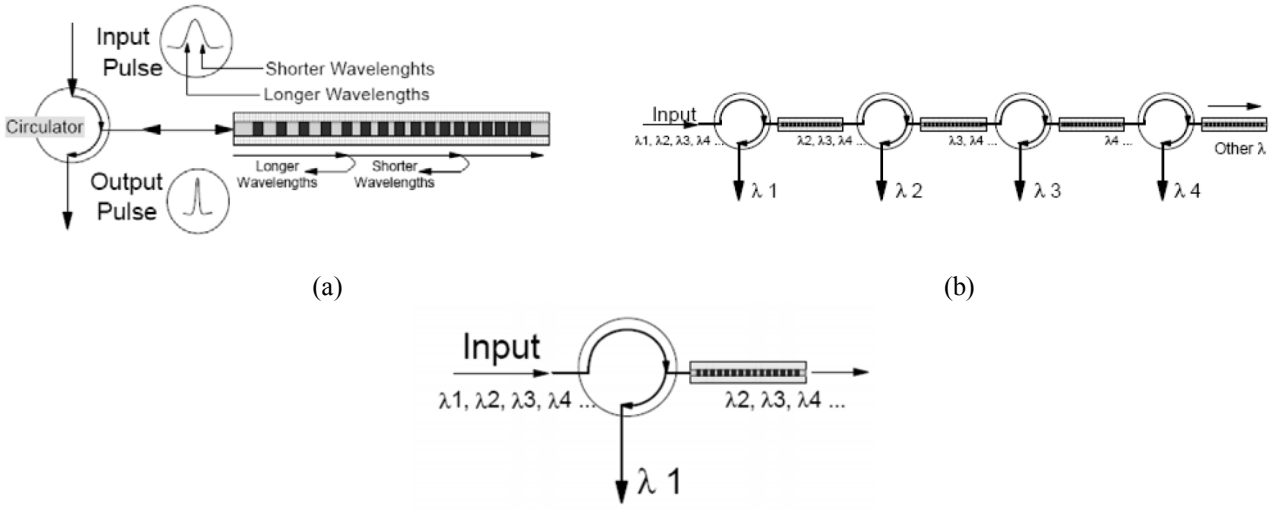

Fig. 2.16 Setups illustrating FBG used for dispersion compensation (a), demultiplexer in DWDM (b) and FBG filter (c) [54]

2.4.4 Microring resonator

2.4.4.1 Principle of operation

The proposal to use an integrated microring resonator for a bandpass filter has been made in 1969 by Marcatili [56]. The layout of the channel dropping filter is shown in Fig. 2.17

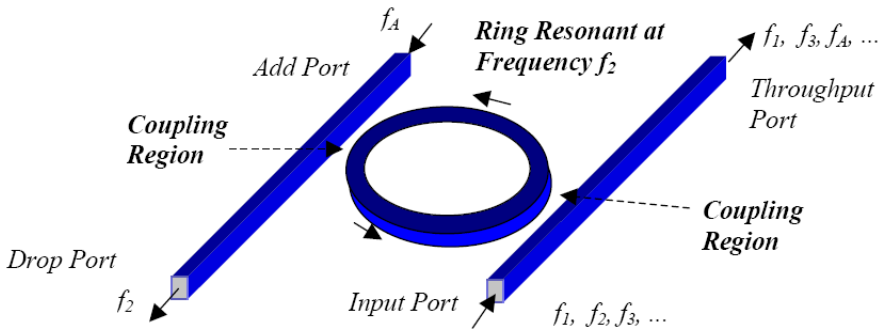

Fig. 2.17 Ring resonator channel dropping filter [45]

Microring resonators (MR) represent a class of filters with characteristics very similar to those of FP filters. However, they offer the advantage that the injected and reflected signals are separated in individual waveguides, and in addition, their design does not require any facets or gratings and is thus particularly simple. MRs evolved from the fields of fiber optic ring resonators and micron scale droplets. Their inherently small size (with typical diameters in the range between several to tens of micrometers), their filter characteristics, and their potential for being used in complex and flexible configurations make these devices particularly attractive or integrated optics or VLSI photonics applications.

The fundamental building blocks of microring-based devices are a microring plus one or two waveguides. In the former case this leads to two-port devices which act as all-pass filters and introduce a wavelength-dependent phase shift only (lossless case). This property is exploited for the realization of dispersion compensators. The ring (radius R) and the port waveguides are evanescently coupled and a fraction κ_1 of the incoming field is transferred to the ring. When the optical path-length of a roundtrip is a multiple of the effective wavelength λ constructive interference occurs and light is 'built up' inside the ring: the MR is ON resonance. As a consequence, periodic fringes appear in the wavelength response at the output ports as shown in Fig. 2.18. At resonance the drop port shows maximum transmission since a fraction κ_2 of the built-up field inside the ring is coupled to this port. In the through port the ring exhibits a minimum at resonance. In the ideal case with equal coupling constants at resonance all the power is directed to the drop port. Light coupled back to the through port after a roundtrip experiences an additional 180° phase shift with respect to the light coming directly from the in port, and as a consequence no light exits from the through port at resonance.

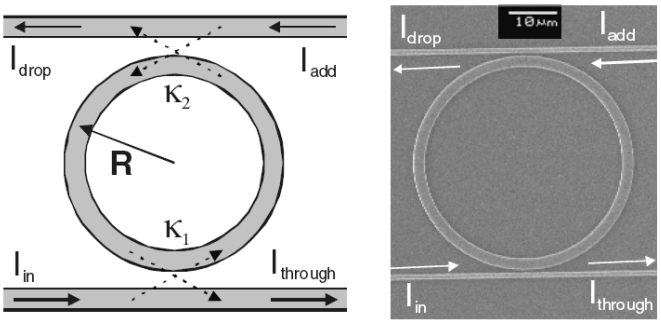

Fig. 2.18 Schematic drawing of a 4-port microring resonator (left) and SEM picture (right) with in- and output port waveguides [46]

2.4.4.2 Ring resonator parameters

By analogy to the FP resonator [44], the frequency parameters exhibit a strong analogy to the FP parameters. The FSR is given by:

$$FSR_\lambda \approx \frac{\lambda^2}{n2\pi R} \quad , \quad FSR_f = \frac{c}{n2\pi R} \tag{2.21}$$

The subscript λ or f denotes the wavelength or the frequency domain parameters. We notice that the round trip path length $2L$ has been replaced by the ring perimeter $2\pi R$.

The microring Finesse F which is the ratio between FSR and the 3-dB bandwidth is given by:

$$F = \frac{FSR}{FWHM} = \frac{\pi\left(X_1 X_2\right)^{1/4}}{1-\left(X_1 X_2\right)^{1/2}} \tag{2.22}$$

where X_i is the forward coupling coefficient given by:

$$X_i = \sqrt{\left(1-\kappa_i^2\right)} e^{L_r \alpha} \tag{2.23}$$

with α being the losses per length inside the ring and L_r the length of the optical path in the ring.

The FWHM is determined by the coupling constants and the loss inside the ring according to:

$$FWHM_f = \frac{c}{2\pi R n}\left(\frac{\sqrt{X_1 X_2}}{\pi \sqrt[4]{X_1 X_2}}\right) \tag{2.24}$$

One frequently chosen way of modeling the response of a single MR is the use of a scattering matrix model. This approach does not include polarization effects, but it is sufficient in many cases for the derivation of fundamental design parameters for different material systems.

In the scattering matrix model the MR is modeled as two couplers which couple a fraction κ_1 or κ_2 over to the cross port, and two delays φ_1 and φ_2 in-between as shown in Fig. 2.19. The optical fields in the inputs and outputs of the ring are related as follows:

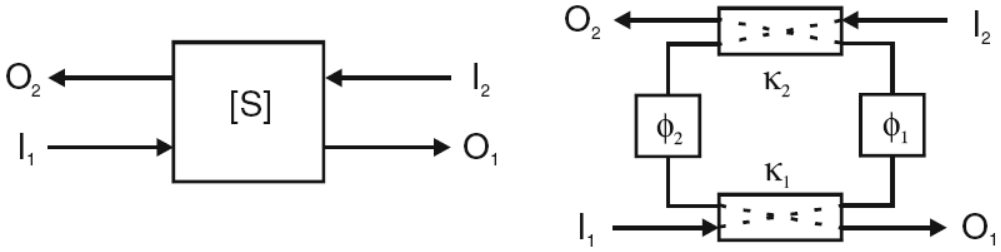

Fig. 2.19 Scattering matrix model of a microring resonator [46]

$$\begin{bmatrix} O_1 \\ O_2 \end{bmatrix} = \begin{bmatrix} S_{11} & S_{12} \\ S_{21} & S_{22} \end{bmatrix} \begin{bmatrix} I_1 \\ I_2 \end{bmatrix} \tag{2.25}$$

$$S_{11} = \frac{\mu_1 - \mu_2 \alpha_r^2 e^{-j\Delta\omega}}{1-\mu_1 \mu_2 \alpha_r^2 e^{-j\Delta\omega}} \tag{2.26}$$

$$S_{21} = -S_{12} = \frac{\kappa_1 \kappa_2 \alpha_r e^{-j\Delta\omega/2}}{1-\mu_1 \mu_2 \alpha_r^2 e^{-j\Delta\omega}} \tag{2.27}$$

$$S_{22} = \frac{\mu_2 - \mu_1 \alpha_r^2 e^{-j\Delta\omega}}{1-\mu_1 \mu_2 \alpha_r^2 e^{-j\Delta\omega}} \tag{2.28}$$

where $\mu_{1,2} = \sqrt{1-\kappa_{1,2}^2}$, α_r is the loss per roundtrip, $\Delta\omega = \omega_0 - \omega$, with $\omega_0 = mc/(n2\pi R)$ being the resonance frequency, while m is the resonance number. The delays φ_1 and φ_2 are related to the frequency and the optical path-lengths $L_{opt1,2}$ by $\varphi_{1,2} = \omega L_{opt1,2}/c$, and they are not necessarily identical to each other. The place of the couplers does not matter as long as the total roundtrip phase is the same. By use of this model, one can extract values for the coupling constants from the desired functional behavior and a given loss and radius.

With the scattering matrix model, the influence of the loss parameter on the MR response can be determined as well. Parameters such as filtering bandwidth, insertion loss, crosstalk, and channel separation can be determined in this way. These calculations will not detailed here, we just point out to the possibility of their derivation.

Another point addressed in this section, is the ring resonator geometry and fabrication issues. Microrings can be designed and fabricated in two generic coupling configurations as shown in Fig. 2.20. When the ring and waveguide are structured in the same waveguiding layer, the configuration is called ‘laterally coupled’. When the ring and the waveguides are in different layers, the configuration is called ‘vertically coupled’. The vertical coupling configuration has the advantage that the coupling depends mainly on the thickness of the layer in between which can be controlled very accurately during deposition, however, at the expense of an additional processing step for the ring layer. The lateral configuration uses a single layer only, but requires very accurate lithography and etching processes to open the gap between the straight waveguide parts and the ring with high precision. Another advantage of the vertical configuration is that the ring and waveguide layers do not have to be the same thickness which enhances the design freedom.

The fabrication of microring resonators is limited by the tolerances of the lithography and the etching processes. For the realization of the gap between the ring and the straight waveguide in a lateral configuration and using high index contrast, nanometer precision is required which can only be obtained by direct e-beam writing, focused ion beam milling, or high precision wafer steppers. In the vertical configuration this problem is circumvented as the coupling is now determined by the deposition process where nanometer precision can be obtained more easily. In this case, however, alignment is an issue as ring- and port waveguides are structured in two separate lithographic steps. This is especially important in the case of symmetrically coupled devices.

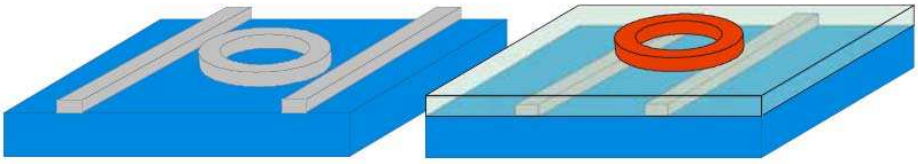

Fig. 2.20 3D drawing of ring laterally coupled (*left*) and vertically coupled (*right*) to the straight waveguides [46]

2.4.5 Disk resonator and Microspheres – WGM resonators

2.4.5.1 Principle of operation

Whispering gallery resonators are dielectric structures in which light waves are confined by continuous total internal reflection and focused by the surface [57]. WGMs can be observed in droplets and glass spheres for example. The light in WGM resonators is concentrated near the circumference of the device and is assigned a mode number and a mode order. The mode number, m_n, reveals the number of wavelengths around the circumference, and the mode order, m_o, reveals the number of maxima in the radial dependence of the electromagnetic field within the resonator. These modes can have very high Q factors if the losses due to reflection at the surface of the resonator are low. In addition to high Q-values, a high finesse is also obtained. The high Q-factor makes these resonators very attractive to be used in different domains such as: microlasers, narrow filters, optical switching, ultra-fine sensing, displacement measurements, high resolution spectroscopy, Raman sources and studies of nonlinear optical effects.

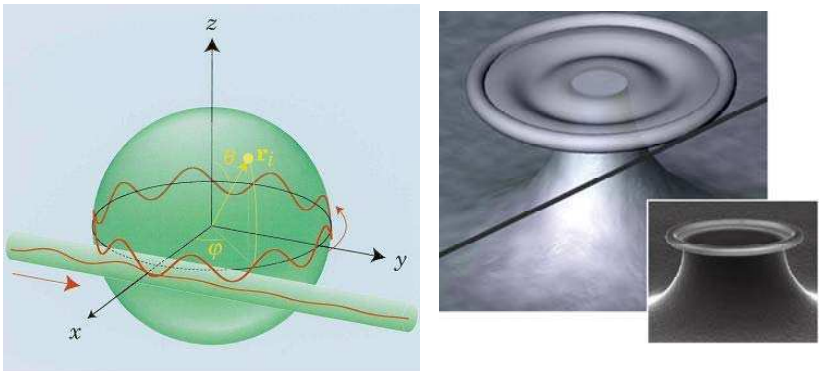

(a) (b)

Fig. 2.21 Schematic illustration of a microsphere (a) and disk resonator (b) coupled to optical fiber [43]

2.4.5.2 Comparison between losses in WGM resonators and microring resonators

In the past decade WGMs have attracted increasing attention for their ability to sustain very high Q-factors and low mode volumes. Microdisks and microrings constructed using the techniques of microfabrication and nanofabrication, however, can be readily constructed in a reproducible manner to designed dimensions down to dimensions less than 1 μm. The main drawback of planar fabricated microresonators is the surface roughness left on the edges due to etching processes that result in resonators of much lower quality factors. A ring has two bounding edges that can be used to properly design a single-moded guide. A disk only has one bounding edge; the other boundary is an effective one arising from an inner caustic. As a result, a disk can possess less scattering loss than that of corresponding ring geometry but is multi-moded. If the FSR is high, and/or the side coupling guides preferentially couple to one of the radial modes of the disk, then disks are preferable. If not, then ring geometry is better and the extra loss must be taken into account. A mode may be considered a

"whispering galley mode" if the confinement along some dimension is provided by only a single reflective interface. For a given core-to-cladding refractive-index difference, the loss at a given bend radius decreases with increasing waveguide width until a limit is reached where only the outer core interface is important for guiding. A mode of a curved waveguide (forming a ring) defined by two interfaces would be considered a whispering gallery mode if the inner caustic radius (defined by the azimuthal index m and the wavelength) lies between the inner and outer interfaces. In this regime, light cannot penetrate (towards the origin) beyond the inner caustic, and thus, the interior interface plays a negligible role in the guidance. Thus, a curved waveguide will have similar bending loss per unit radian as a disk with the same exterior radius. It is worthwhile pointing out the advantages and disadvantages of disks and rings. A microdisk may possess higher order radial modes primarily depending on the location of the inner caustic. These radial modes possess differing resonant wavelengths and thus might be discriminated against by properly choosing the excitation wavelength.

Depending on the quality factors associated with the modes, the resonant wavelength of a particular mode of a microdisk (defined by a radial and azimuthal number) might still overlap another. This may be a problem if only a single-mode is desired. A properly designed ring can be used instead to force single-radial-mode operation. However, the presence of an extra sidewall contributes to additional scattering losses.

2.4.5.3 Analytical model for WGM resonator

Whispering-gallery mode resonances correspond to light that is trapped in circular orbits just within the surface of the structure. The modes are most strongly coupled along the equatorial plane and they can be thought to propagate along zigzag paths around the sphere.

In the view of ray optics, the light is trapped inside the dielectric sphere by continuous total internal reflections at the curved boundary of surface. Whispering gallery modes occur at discrete frequencies that depend on index of refraction n_s and radius r_0 of the sphere. Each mode has a propagation constant β_l parallel to the surface and in the direction of the zigzag path. The propagation constant has a value:

$$\beta_l = \sqrt{\frac{l(l+1)}{R_0}} \tag{2.29}$$

The projection of the propagation constant is β_m and it has a value:

$$\beta_m = \frac{m}{R_0} \tag{2.30}$$

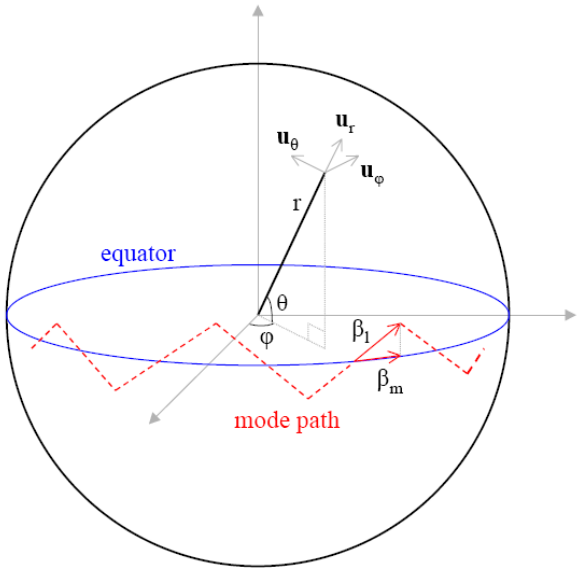

Fig. 2.22 Light propagation in microsphere [58]

Whispering gallery modes are characterized by two polarizations (transversal electric TE-modes and transversal magnetic TM-modes) and three mode numbers n, l and m which are the radial, angular and azimuthal mode numbers, respectively. The value of l is close to the number of wavelengths that fit into the optical length of the equator. The value $l - m + 1$ is equal to the number of field maxima in the polar direction, i.e. perpendicular to the equatorial plane. Mode number n is equal to the number of field maxima in the direction along the radius of the sphere and $2l$ is the number of maxima in the azimuthal variation of the resonant field around the equator. The resonant wavelength is determined by the values of n and l.

In this case, the electromagnetic field problems are solved in 3D spherical coordinates. When solving dynamic problems in spherical coordinates, spherical Bessel functions $j_n(x)$ and $n_n(x)$, corresponding spherical Hankel functions $h_n^{(1)}(x)$ and $h_n^{(2)}(x)$, associated Legendre functions $P_n^m(x)$ and $Q_n^m(x)$ and exponential functions $e^{\pm jm\varphi}$ are needed.

Spherical Bessel functions describe standing waves in the radial direction of spherical coordinates. Spherical Bessel functions are in close connection with ordinary Bessel functions of cylindrical coordinates. Spherical Bessel (and Hankel) functions $b_l(x) = j_l(x)$, $n_l(x)$, $h_l^{(1)}(x)$ and $h_l^{(2)}(x)$ can be calculated as:

$$b_l(kr) = \sqrt{\frac{\pi}{2kr}} B_{l+\frac{1}{2}}(kr) \tag{2.31}$$

where $B_{l+1/2}$ is the corresponding Bessel function in cylindrical coordinates. Spherical Hankel function $h_l^{(2)}(kr) = j_l(kr) - j_{nl}(kr)$ is essential because it describes spherical waves propagating outside the dielectric sphere and in the radial direction away from the center of the sphere.

2.4.5.4 Fabrication technique

The quality factors associated with silica microspheres have attracted much attention for their ultra-high Q factors which attain 10^{11}. Their traditional method of production relies on melting silica (usually a fiber tip) using a high power laser (CO_2 laser) or fusion splicer or an oxygen-hydrogen torch. Then, surface tension forces reshape the liquid glass into a sphere that is then allowed to cool. Unfortunately, this method does not allow for the fabrication of spheres of reproducible diameters, nor does it allow for spheres much smaller than 20 μm. Recent advances, however, have shown that selective reflow of patterned silica disk edges can result in resonators possessing ultra-high Q-factors typically found in microspheres. Propagating whispering gallery modes have been imaged by scanning a near-field probe across the surface of fused-silica microspheres, and silicon nitride cylindrical disks whereby light is collected (as it is injected) via frustrated total internal reflection.

2.4.5.5 Characterization techniques

In order to couple light in or out of the microsphere, it is necessary to utilize overlapping of the evanescent field of the whispering gallery modes with the evanescent field of a phase-matched optical waveguide. Such coupling has been implemented by use of tapered optical fibers, side-polished optical fibers and prisms. In most of the cases, microspheres are optically coupled by the use of tapered optical fiber with diameter of typically few micrometers. Tapered fibers are formed by heating and stretching a standard telecommunication single-mode fiber. The core vanishes and the situation is similar to the glass rod with an air cladding. The optical field from the fiber tunnels into the microsphere through evanescent coupling. The coupling strength and resulting Q-factor depends considerably on the refractive index of the microsphere, sphere dimensions, tapered fiber dimensions and relative positions of the components, the difference in propagation constants between fiber and sphere and on the spherical mode orders.

2.4.5.6 WGM applications

WGM's have attracted much attention due to potential applications in photonics, quantum electrodynamics (QED), atom optics and telecommunication. Such applications in technological and scientific fields are like: the realization of microlasers, narrow filters, optical switching, ultra fine sensing, displacement measurements, high resolution spectroscopy, Raman sources and studies of nonlinear optical effects. For example in the case of microlasers, microspheres offer large reduction in demanded pump power and fiber coupling provides a convenient method to transport optical power.

WGM resonators can be used in MOEMS for displacement measuring. At optical resonance, the power builds up in the cavity. This leads to an increase in the radiation pressure, which in turn generates a mechanical deformation for the cavity. The mechanical deformation changes the cavity geometry and consequently, the resonant wavelength changes and the cavity resonance wavelength becomes an out-of-resonance. At that time, the power decreases and the radiation pressure decreases as

well will leads to deformation removal. The cycle repeats again starting by optical resonance leading to power build up and so on. Then, we can say that we have mechanical oscillation.

Resonators can also be used for both refractometry and absorption spectroscopy. In refractometry, the refractive index change leads to the change of the optical path with in turn leads to the shift of the resonance wavelength. On the other hand, optical absorption of chemicals leads to the decrease of the extinction ratio due to light absorption by the analyzed species.

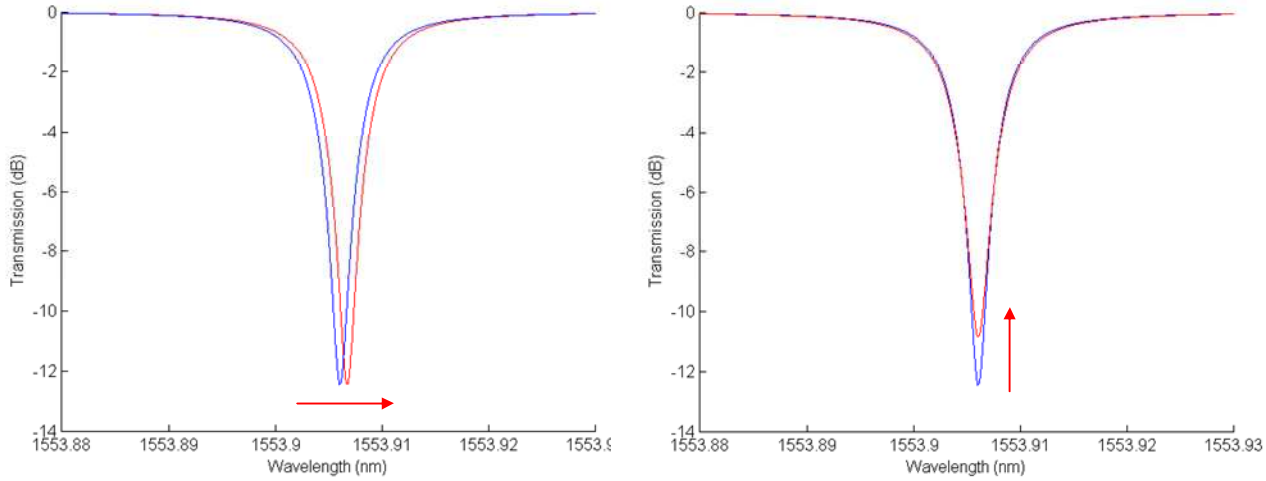

(a) (b)

Fig. 2.23 (a) Shift of the resonance wavelength in a refractometer. (b) Decrease of the extinction ratio in applications involving optical absorption [43]

2.4.6 General discussion about the applications of optical resonators

The applications of the different architectures have been detailed previously. In this section, we classify and summarize the application domains for the optical resonators following the advantages they can offer to the application in need. As mentioned earlier, applications of optical resonators are versatile. For example, some applications are based on the selective spectral transmission/reflection. Other applications are based on the increased optical path length. Others are based on the enhanced field amplitude. Accordingly, we can mention the follwing application classes with respect to the main advantages provided by optical resonators:

- Selective spectral transmission/reflection
  - Optical filters for WDM
- Increased optical path (interaction) length
  - Spectroscopy and sensing
  - Modulators and switches
  - Laser & cavity-enhanced LED
  - Slow light: coupled resonator optical waveguide (CROW)

- Cavity-enhanced photodetector
- Enhanced field amplitude
  - Non-linear optics
  - Cavity quantum-electrodynamics (QED)
  - Optical tweezers & MOEMS

2.5 Optical interferometers

Interferometric measurements require an optical arrangement in which two or more beams, derived from the same source but traveling along separate paths, are made to interfere. Interferometers can be classified as two - beam interferometers or multiple – beam interferometers according to the number of interfering beams; they can also be grouped according to the methods used to obtain these beams. The most commonly used form of beam splitter is a partially reflecting metal or dielectric film on a transparent substrate; other devices that can be used are polarizing prisms and dif fraction gratings. The best known types of two-beam interferometers are the Fizeau, the Michelson, the Mach-Zehnder, and the Sagnac interferometers; the best known multiple-beam interferometer is the Fabry-Perot interferometer. Hereafter, the basic types of interferometers are outlined without going into deep details. The interested reader is asked to refer to [59]

2.5.1 The Fabry-Perot interferometer

The Fabry-Perot device has been discussed as a resonator in an earlier section of this chapter. In this section, we look to it as an interferometer. In fact, an alternate arrangement where the Fabry-Perot etalon has anti-reflective coatings applied to the two surfaces of a single glass plate. The two lenses serve to collimate the light from a point on the extended source in the region of the cavity and to then image this point onto the screen. The screen is located in the focal plane of the lens so that fringes of equal inclination localized at infinity are viewed. Light of a fixed wavelength will traverse the etalon only at certain well-defined angles. Extremely sharp multiple-beam circular fringes in transmission are produced on the screen, and their profile is the same as that shown in Fig. 2.24. If the source is not monochromatic, a separate independent circular pattern is formed for each wavelength. The location or scale of the fringes is dependent on the wavelength. If the source is composed of two closely spaced wavelengths, the ring structure is doubled, and the separation of the two sets of rings allows the hyperfine structure of the spectral lines to be evaluated directly. More complicated spectra, usually composed of discrete spectral lines, can also be measured. Then, the Fabry-Perot interferometer is an important example of a system which makes use of multiple-beam interference and it serves as a high-resolution spectrometer and also as an optical resonator.

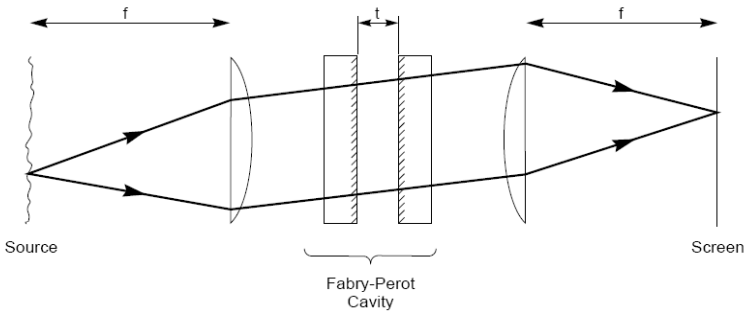

Fig. 2.24 The Fabry-Perot interferometer [60]

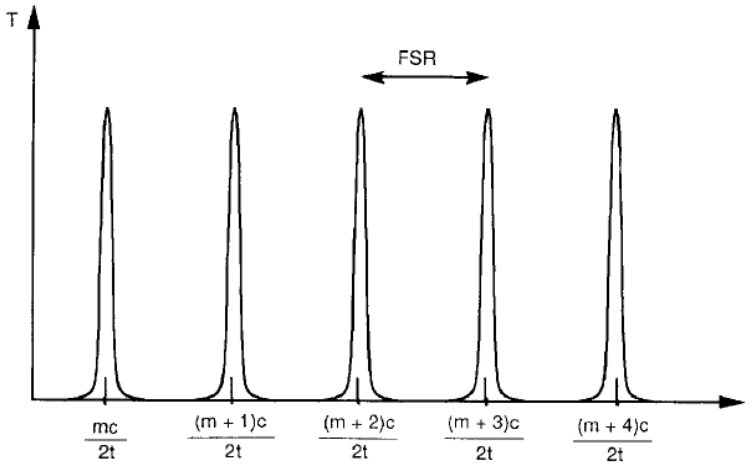

Fig. 2.25 The transmission of a Fabry-Perot cavity as a function of frequency [60]

2.5.2 The Michelson interferometer

The Michelson interferometer, shown schematically in Fig. 2.26, uses a plate beam splitter with one face partially silvered to divide and recombine the beams. The two interfering wavefronts are produced by the reflections from the two mirrors. As can be seen, one of the beams traverses the beam splitter three times, while the other traverses it only once. Accordingly, a compensating plate of the same thickness as the beam splitter is introduced in the second beam to equalize the optical paths in glass. This cancels the effects of the dispersion of the glass beam splitter and allows the system to be used with white light since the optical path difference is the same for all wavelengths.

If the extended source is polychromatic, colored fringes localized at the mirrors result. They are straight for tilted mirrors. The fringes will have high visibility only if the apparent mirror separation or OPD is smaller than the coherence length of the source. Another way of stating this is that the order of interference m must be small to view the colored fringes. As m increases, the fringes will wash out. The direct analogy here is a thin film. As the mirror separation is varied, the fringe visibility will vary. The fringe visibility as a function of mirror separation is related to the source frequency spectrum and this interferometer forms the basis of a number of spectrometers.

With an extended source, the interference pattern is similar to that produced in a layer of air bounded by the mirror M_1 and M_2', the image of the other mirror in the beam splitter. With collimated light, fringes of equal thickness are obtained. The Michelson interferometer modified to use collimated light is known as the Twyman-Green interferometer and is used extensively in optical testing. The Twyman - Green interferometer, and is a special case of point-source illumination with the source at infinity. Plane waves fall on both mirrors, and if the mirrors are flat, nonlocalized equispaced fringes are produced. Fringes of equal thickness can be viewed by imaging the mirrors onto the observation screen. If one of the mirrors is not flat, the fringes represent changes in the surface height. The two surfaces are compared as in the Fizeau interferometer. This interferometer is an invaluable tool for optical testing.

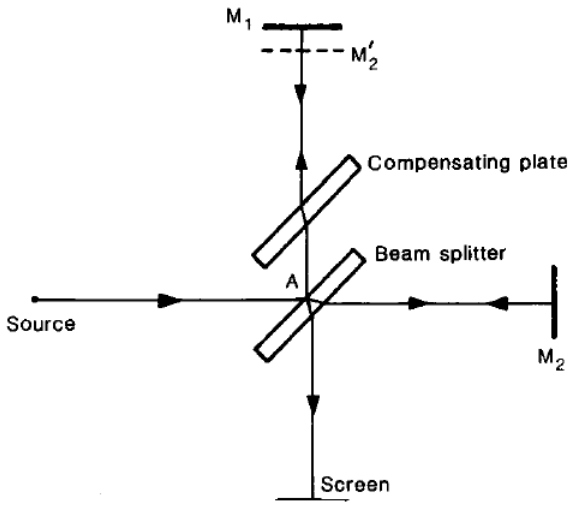

Fig. 2.26 The Michelson interferometer [59]

2.5.3 Other main architectures of optical interferometers

2.5.3.1 The Fizeau interferometer

The Fizeau interferometer compares one optical surface to another by placing them in close proximity. A typical arrangement is shown in Fig. 2.27a, where the extended source is filtered to be quasi-monochromatic or a monochromatic source is used directly. A small air gap is formed between the two optical surfaces, and fringes of equal thickness are observed between the two surfaces. Along a fringe, the gap is of constant thickness, and adjacent fringes correspond to a change of thickness of a half wavelength. This interferometer is sometimes referred to as a Newton interferometer.

2.5.3.2 The Mach-Zehnder interferometer (MZI)

The Mach-Zehnder interferometer uses two beam splitters and two mirrors to divide and recombine the beams. As shown in Fig. 2.27b, the fringe spacing and the plane of localization of the fringes obtained with an extended source can be controlled by varying the angle between the beams and their lateral separation when they emerge from the interferometer. This makes it possible to use a pulsed

ruby laser, which may be operating in more than one transverse mode, as the source. Because the measurement path is traversed only once, and the separation of the beams can be made as large as desired, this interferometer is well suited to studies of gas flows, heat transfer, and the temperature distribution in flames and plasmas.

2.5.3.3 The Sagnac interferometer

In the Sagnac interferometer, as shown in Fig. 2.27c, the two beams traverse the same closed path in opposite directions. Because of this, the interferometer is extremely stable and easy to align, even with an extended broadband light source. Modified versions of the Sagnac interferometer have been used for rotation sensing. When the interferometer is rotated with an angular velocity v about an axis making an angle θ with the normal to the plane of the interferometer, a phase shift φ is introduced between the beams given by the relation:

$$\varphi = \frac{8\pi\omega A\cos\theta}{\lambda c} \tag{2.32}$$

where A is the area enclosed by the light path, λ is the wavelength , and c is the speed of light .

2.5.3.4 Polarization interferometers

Polarization interferometers have found their most extensive application in interference microscopy. The Nomarski interferometer, shown schematically in Fig. 2.27d, uses two Wollaston (polarizing) prisms to split and recombine the beams. If the separation of the beams in the object plane (the lateral shear) is small compared to the dimensions of the object, the optical path difference corresponds to the phase gradients in the test object. A similar setup is also used in reflection to study the surface structure of opaque objects.

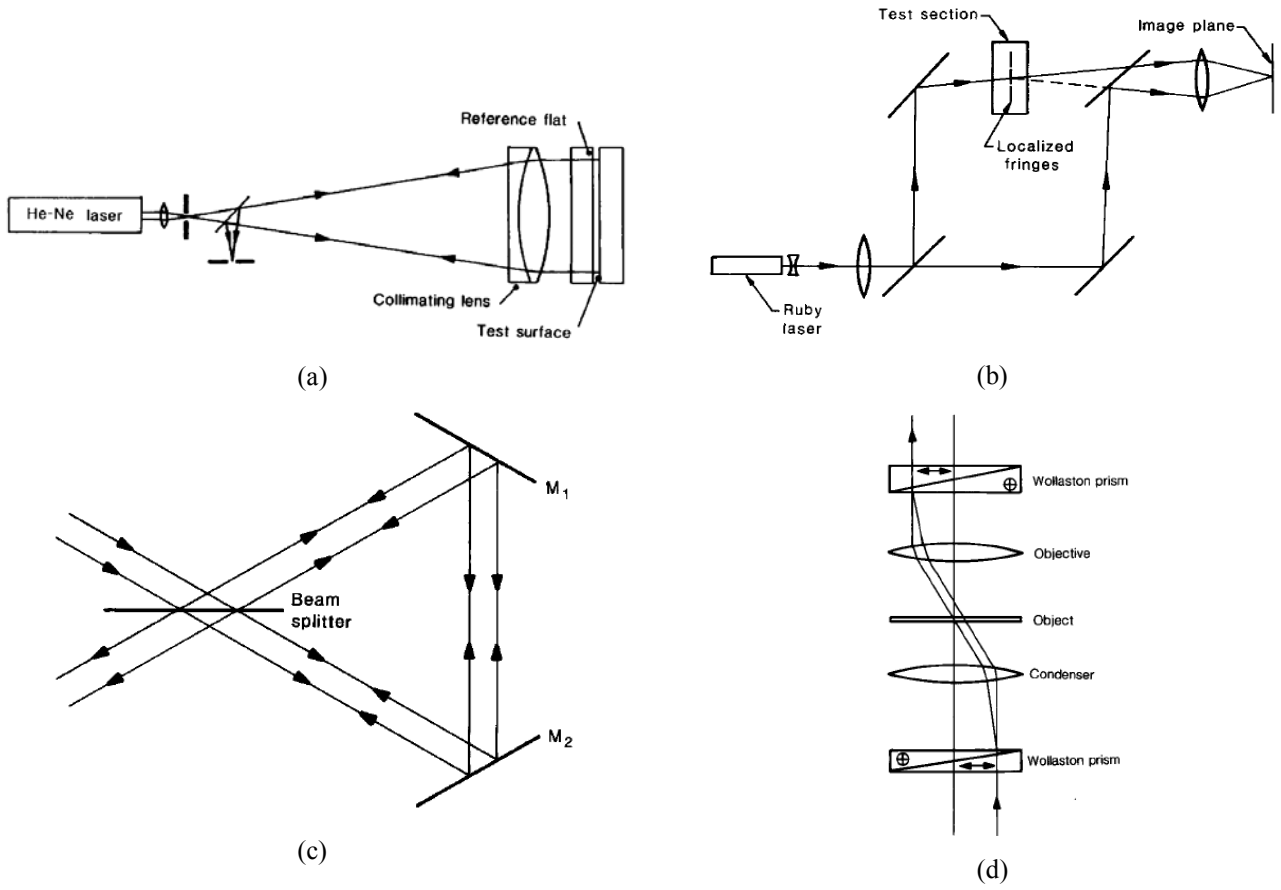

Fig. 2.27 Main architectures of other optical interferometers [59] : (a) The Fizeau interferometer (b) The Mach-Zehnder interferometer (c) The Sagnac interferometer (d) The Nomarski interferometer (type of polarization interferometers)

2.5.4 Application of interferometers

Optical interferometers have made feasible a variety of precision measurements using the interference phenomena produced by light waves. After a brief survey of the basic types of interferometers, we summarize some of the applications for these interferometers. They can be used for applications involving the measurements of lengths and small changes in length; optical testing; studies of surface structure; measurements of the pressure and temperature distribution in gas flows and plasmas; measurements of particle velocities and vibration amplitudes; rotating sensing; measurements of temperature, pressure, and electric and magnetic fields; wavelength measurements, and measurements of the angular diameter of stars, as well as, possibly, the detection of gravitational waves. A more comprehensive review of applications of optical interferometers may be found for instance in [61], [62].

2.6 Beam splitters and Reflectors

2.6.1 Basic architectures of Beam splitters

Several different physical forms of beam splitters are illustrated in Fig. 2.28 [60]. The simplest (Fig. 2.28b) consists of a coating on a transparent plane-parallel substrate. If the two derived beams are to traverse identical paths, a cemented beam splitter is used (Fig. 2.28c). The lateral displacement of the transmitted beam introduced by these forms can be avoided with a beam-splitting cube (Fig. 2.28f) . To reduce the stray reflected light in the system, the free surfaces of these beam splitters can be antireflection-coated. Alternatively, the coatings can be deposited onto an approximately 2 μm-thick nitrocellulose pellicle (Fig. 2.28a). The latter is an integral part of the multilayer and may introduce an interference pattern into the spectral reflectance and transmittance characteristics. Pellicle beam splitters are very light and yet quite sturdy. They are, however, subject to vibrations caused by air currents and acoustical waves. The mechanical design of rugged, environmentally stable mounts for these types of beam splitters have been discussed by Heinrich et al., Pellicles made of Mylar have been used at temperatures down to 4 K.

In general, the transmission and reflection coefficients T and R will depend on the polarization of the incident radiation. The polarization effect can be reduced through the use of more complicated thin-film designs, but usually at the expense of other performance aspects. Achromatic or color-selective beam-splitting arrangements have been described in which the two derived beams have intensities that are completely polarization-independent over a very wide spectral region. They consist of three identical beam splitters arranged in such a way that each beam undergoes identical reflections and transmissions on passing through the system (Fig. 2.28n).

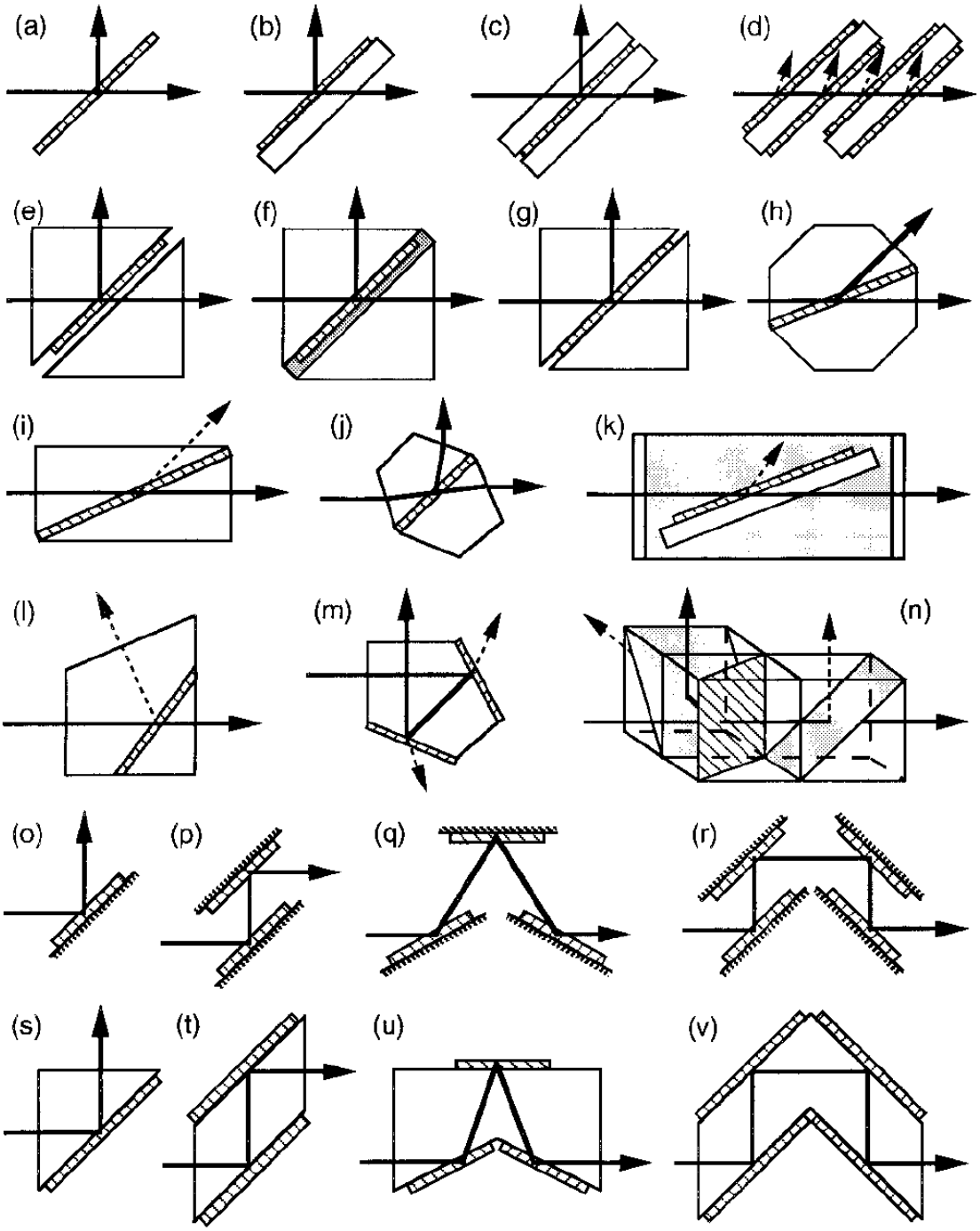

Fig. 2.28 Schematic representation of some arrangements for beam splitters, polarizers, phase retarders, and multiple reflection devices. Thin films are represented in the diagrams by narrow shaded rectangles. Heavy lines ending in an arrow represent the path of the utilized radiation. Broken lines correspond to beams that are not used. The angles of incidence depend on the application [60]

2.6.2 Other architectures of beam splitters

2.6.2.1 Achromatic Beam Splitters

These devices are introduced into an incident beam of radiation when it is desired to divide it into two beams of approximately equal relative spectral composition but propagating in two different directions. In neutral beam splitters, the quantity $0.5(R_p + R_s)_{\theta=45^\circ}$ is always close to the reflectance at

normal incidence, even though the individual R_p and R_s values may be quite different. The reflectance of absorbing, uncemented beam splitters depends also on the direction of incidence. The optimum values of T and R depend on the application. For example, for a binocular eyepiece on a non-polarizing microscope, the most important requirement is $T_s + T_p = R_p + R_s$ (Fig. 2.29a). For a vertical illuminator ($R_pT_p + R_sT_s$) should be a maximum (Fig. 2.29b). The condition for maximum fringe contrast in some interferometers requires that $R_{1,p}T_p = R_{2,p}T_p$ and $R_{1,s}T_s = R_{2,s}T_s$ (Fig. 2.29c). This is satisfied automatically by all non-absorbing and by absorbing cemented beam splitters. The occasional requirement that the phase change on reflection be the same for radiation incident onto the beam splitter from opposite sides is automatically satisfied at the design wavelength by all-dielectric coatings composed of λ/4 layers, but not by uncemented metal beam splitters.

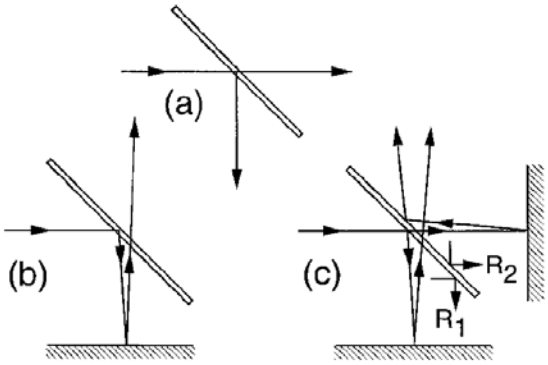

Fig. 2.29 Three different ways of using beam splitters [60]

2.6.2.2 Nonpolarizing Beam Splitters

For some applications it is important that the beam splitter introduce no polarization effects. It has shown that, with the appropriate single layer on the face of a suitable high-refractive index prism, it is possible to construct a polarization-independent beam splitter. This device is quite achromatic and, in addition, by changing the angle of incidence of the beam on the prism, the beam-splitting ratio can be tuned over a wide range of values. The principle of frustrated total internal reflection can also be used to design beam splitters that have a very good performance. In these devices, radiation is incident at a very oblique angle onto an air gap or low-refractive-index films at the interface between two prisms (Fig. 2.28 e,f) . Unfortunately, the performance of such systems is very sensitive to the angle of incidence. In many applications, it is important that the beam splitter be relatively insensitive to the angle of incidence. One way is to reduce the angle of incidence as much as possible (Fig. 2.28 h). However, in many cases a 45° angle of incidence is mandatory. Relatively polarization-insensitive beam splitters based on dielectric-metal-dielectric layer systems embedded between two prisms have been described. Much work has been done to find solutions based on dielectric layers only. However, the improvement is frequently at the expense of the width of the spectral region over which the beam splitter is effective.

2.6.2.3 Color-selective Beam Splitters

For various technological applications, a beam of light must be divided into several components of different color. All-dielectric color-selective beam splitters (*dichroics*) are used for this purpose because they are practically lossless and because their transition wavelengths can be selected at will. They are essentially cut-off filters usually designed for use at 45° incidence. Their spectral characteristics normally depend on the polarization of the incident radiation. The effect of this and of the variations in the angle of incidence and thickness of the coatings on the chromaticity coordinates of dichroic beam splitters for television cameras was investigated by Pohlack. If necessary, the polarization of the derived beams can be reduced through the use of auxiliary normal-incidence cut-off filters.

2.6.3 Reflectors

Mirror systems are increasingly being used, particularly in the X-ray, ultraviolet, and infrared regions of the spectrum [63]. Although it is relatively simple to construct a reflecting device that will perform satisfactorily across a broad-frequency band, the same cannot be said of refracting systems. For example, a silicon or germanium lens designed for the infrared will be completely opaque in the visible. Mirrors have other attributes that also contribute to their usefulness. A mirror might simply be a piece of black glass or a finely polished metal surface. In the past, mirrors were usually made by coating glass with silver, which was chosen because of its high efficiency in the UV and IR. Vacuum-evaporated coatings of aluminum on highly polished substrates have become the accepted standard for quality mirrors. Protective coatings of silicon monoxide or magnesium fluoride are often layered over the aluminum as well. In special applications (e.g., in lasers), where even the small losses due to metal surfaces cannot be tolerated, mirrors formed of multi-layered dielectric films are indispensable. A new generation of lightweight precision mirrors continues to be developed for use in large-scale orbiting telescopes; the technology is by no means static.

2.6.3.1 Planar mirrors

As with all mirror configurations, planar mirrors can be either front- or back-surfaced. The latter types are most commonly found in everyday use because it allows the metallic reflecting layer to be completely protected behind glass. In contrast, the majority of mirrors designed for more critical technical usage are front-surfaced.

A number of practical devices utilize rotating planar mirror systems—for example, choppers, beam deflectors, image rotators, and scanners. Mirrors are frequently used to amplify and measure the slight rotations of certain laboratory apparatus (galvanometers, torsion pendulums, current balances, etc.). The ability to rapidly redirect a beam of light is an inherent virtue of planar mirrors that has been utilized for centuries; the single-lens reflex camera is just one application that comes to mind. Today

micromirrors, small enough to pass through the eye of a needle, have become part of the flourishing MOEMS (Micro-OptoElectro-Mechanical Systems) technology. The telecommunications network that delivers worldwide telephone, fax, and Internet services is undergoing a quiet microphotonic revolution as it sheds its electronic elements and moves toward becoming entirely optical. Electronic switches are expensive, bulky, and, by optic standards, unacceptably slow. Accordingly, the crucial component needed for that transition is the optical switch. Micromirrors that can tilt side-to-side and top-to-bottom in a matter of milliseconds are presently one of the most promising approaches.

2.6.3.2 Aspherical mirrors

Curved mirrors that form images very much like those of lenses or curved refracting surfaces have been known since the time of the ancient Greeks. Euclid, who is presumed to have authored the book entitled Catoptrics, discusses in it both concave and convex mirrors. Nowadays, paraboloidals are used in a great variety of applications from flashlight and automobile headlight reflectors to giant radio-telescope antennas, from microwave horns and acoustical dishes to optical telescope mirrors and Moon-based communications antennas. The convex paraboloidal mirror is also possible but is far less widely in use.

2.6.3.3 Important properties in the mirror design

There are many factors that enter into the design of a mirror or mirror system, but the most important requirement is optical performance. Dimensional stability, weight, durability, and cost are some of the factors to be traded off before an effective design can be established. The loading conditions during fabrication, transportation, and use and the thermal environment play a substantial role in materials selection. To satisfy the end-use requirements, the optical, structural, and thermal performance must be predictable. Each of these factors has a set of parameters and associated material properties that can be used to design an optic to meet performance goals. For optical performance, the shape or optical figure is the key performance factor followed by the optical properties of reflectance, absorbance, and complex refractive index. The optical properties of a mirror substrate material are only important when the mirror is to be used bare (i. e., with no optical coating).

2.6.3.4 Applications of mirrors in optical communication systems

The power of integration combined with the MEMS enabled the realization of compact moving micromirrors (Fig. 2.30). Then, they found numerous applications in various devices. Among them, we cite interferometers, optical scanners, optical routers, video-projector, cross connect switch and grating light valve. For the shake of illustration, we mention about the Digital Micromirror Devices (DMD) developed by DLP for projection display in video projectors as shown in Fig. 2.31. Another interesting device used extensively in optical telecommunication is the cross connect switch. The basic idea relies on moving the micromirror for routing light between cross or bar states in the 2x2 switch schematized in Fig. 2.32a. Later, this idea was generalized to realize the 2D MEMS switch for routing

light on a larger scale in the NxN cross connect switch (16x16). Larger array sizes have a weak performance because of light diffraction. A 3D MEMS switch (Fig. 2.32c) was also realized using two separate arrays of 2D micromirrors (array of 100x100). Fibers with integrated collimators were used because long paths are run by the light. It is worth to mention the mirror arrays shown in Fig. 2.33 used for light modulation and wavelength division demultiplexing in grating light valves.

Most of the above-mentionned application areas of micro-mirrors relate to *Display* and to *Fiber Communications*. There are other more marginal applications (though rapidly emerging) related to optical scanners used for instance in barcode readers [64-68] and more recently for biomedical imaging applications [69-71], such as optical tomography [72-74].

As mentioned in the introduction of this thesis, we are focusing on the exploration of a new class of applications related to sensing and analysis Microsystems.

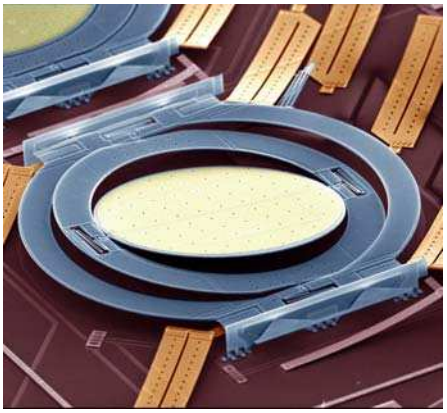

Fig. 2.30 Integrated MEMS mirror (Lambda router – Lucent technologies, Bell laboratories) [75]

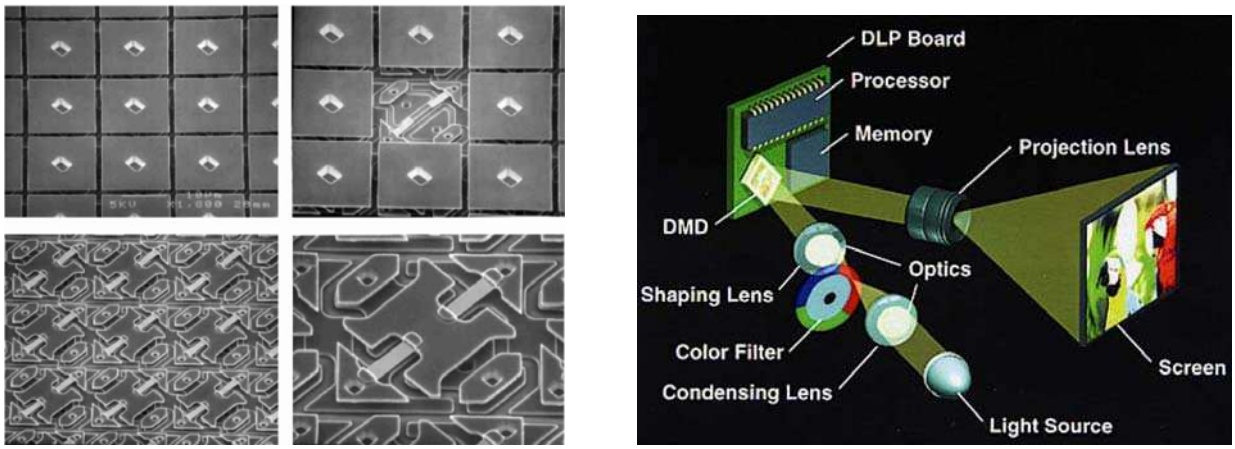

Fig. 2.31 Digital Micromirror Devices (Texas Instruments) and principle of projection display using DMD [75, 76]

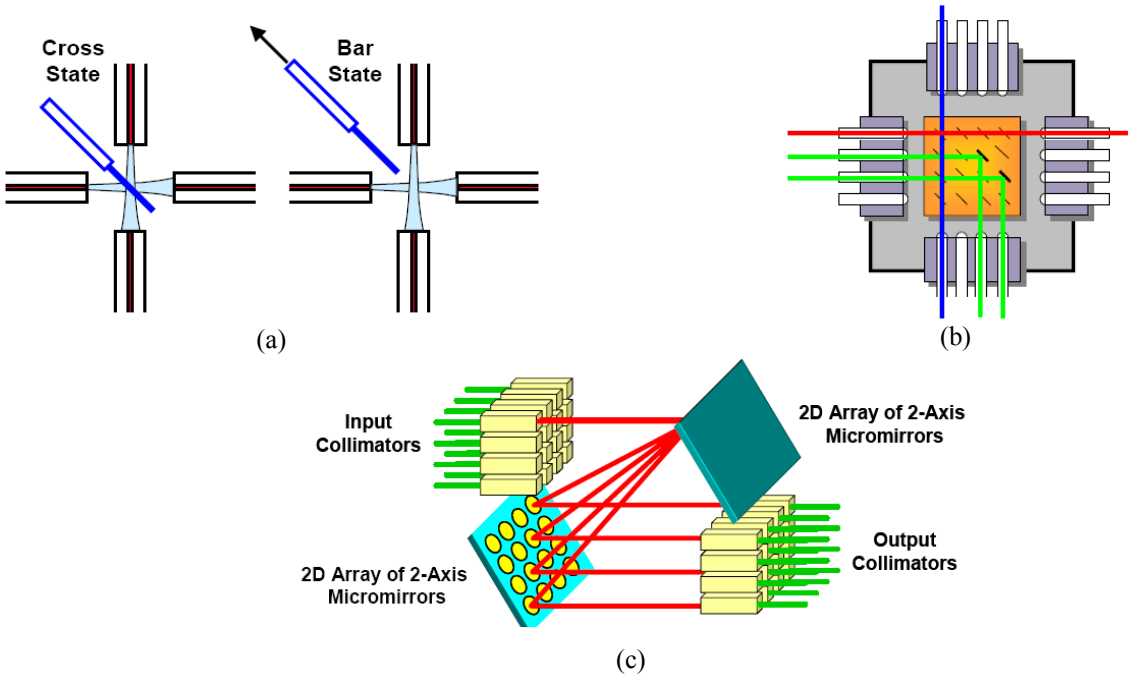

Fig. 2.32 Schematic illustrations for 2x2 optical switch (a), 2D optical switch (b) and 3D cross connect switch (c) [75]

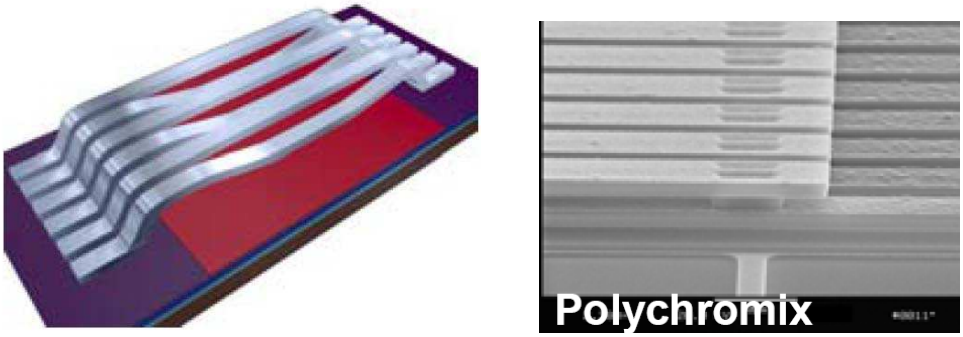

Fig. 2.33 Grating light valve and SEM photo of the device (polychromix) [75]

2.7 Basic theories of Gaussian beams and Matrix optics

2.7.1 Review on Gaussian beam

Waves with wavefront normals making small angles with the z axis are called paraxial waves. They must satisfy the paraxial Helmholtz equation given by [77], [78]:

$$\nabla_T^2 A - j2k\frac{\partial A}{\partial z} = 0 \qquad (2.33)$$

A is the complex envelope of the wave and k is the wavenumber. An important solution of this equation that exhibits the characteristics of an optical beam is a wave called the Gaussian beam. The beam power is principally concentrated within a small cylinder surrounding the beam axis. The intensity distribution in any transverse plane is a circularly symmetric Gaussian function centered about the beam axis. The width of this function is minimum at the beam waist and grows gradually in both directions.

A paraxial wave is a plane wave e^{-jkz} (with wavenumber $k = 2\pi/\lambda$ and wavelength λ) modulated by a complex envelope *A(r)* that is a slowly varying function of position. The complex amplitude is:

$$U(r) = A(r)\exp(-jkz) \tag{2.34}$$

The envelope is assumed to be approximately constant within a neighborhood of size λ, so that the wave is locally like a plane wave with wavefront normals that are paraxial rays.

For the complex amplitude *U(r)* to satisfy the Helmholtz equation, $\nabla^2 U + k^2 U = 0$, the complex envelope *A(r)* must satisfy the paraxial Helmholtz equation stated above. One solution of the paraxial Helmholtz equation provides the Gaussian beam. It is obtained from the paraboloidal wave by use of a simple transformation. We have then,

$$A(r) = \frac{A_1}{q(z)}\exp\left[-jk\frac{\rho^2}{2q(z)}\right],\ q(z) = z - \xi \tag{2.35}$$

When ξ is purely imaginary, say $\xi = -jz_0$ where z_0 is a real quantity known as the Rayleigh range, and $\rho = (x^2 + y^2)^{1/2}$, we have the complex envelope of the Gaussian beam

$$A(r) = \frac{A_1}{q(z)}\exp\left[-jk\frac{\rho^2}{2q(z)}\right],\ q(z) = z + jz_0 \tag{2.36}$$

To separate the amplitude and the phase of this complex envelope, we write the complex function *1/q(z)* in terms of its real and imaginary parts by defining two new real functions *R(z)* and *W(z)*, such that

$$\frac{1}{q(z)} = \frac{1}{R(z)} - j\frac{\lambda}{\pi W^2(z)} \tag{2.37}$$

W(z) and *R(z)* are measures of the beam width and wavefront radius of curvature, respectively. Substituting (2.5) into (2.4) and using (2.2), an expression for the complex amplitude U(r) of the Gaussian beam is obtained:

$$U(r) = A_0\frac{W_0}{W(z)}\exp\left[-\frac{\rho^2}{W^2(z)}\right]\exp\left[-jkz - jk\frac{\rho^2}{2R(z)} + j\xi(z)\right] \tag{2.38}$$

where:

$$W(z) = W_0\left[1 + \left(\frac{z}{z_0}\right)^2\right]^{1/2} \tag{2.39}$$

$$R(z) = z\left[1 + \left(\frac{z_0}{z}\right)^2\right] \tag{2.40}$$

$$\xi(z) = \tan^{-1}\frac{z}{z_0} \tag{2.41}$$

$$W_0 = \left(\frac{\lambda z_0}{\pi} \right)^{1/2} \tag{2.42}$$

A new constant $A_0 = A_1/jz_0$ has been defined for convenience.

The expression for the complex amplitude of the Gaussian beam is central to this part. It contains two parameters, A_0 and z_0, which are determined from the boundary conditions. All other parameters are related to the Rayleigh range z_0 and the wavelength λ.

2.7.1.1 Gaussian beam properties

(a) Intensity

The optical intensity $I(r) = |U(r)|^2$ is a function of the axial and the radial distances z and ρ

$$I(\rho, z) = I_0 \left[\frac{W_0}{W(z)} \right]^2 \exp\left[-\frac{2\rho^2}{W^2(z)} \right] \tag{2.43}$$

where $I_0 = |A_0|^2$. At each value of z the intensity is a Gaussian function of the radial distance ρ. This is why the wave is called a Gaussian beam. The Gaussian function has its peak at $\rho = 0$ (on axis) and drops monotonically with increasing ρ. The width $W(z)$ of the Gaussian distribution increases with the axial distance z as illustrated in Fig. 2.34.

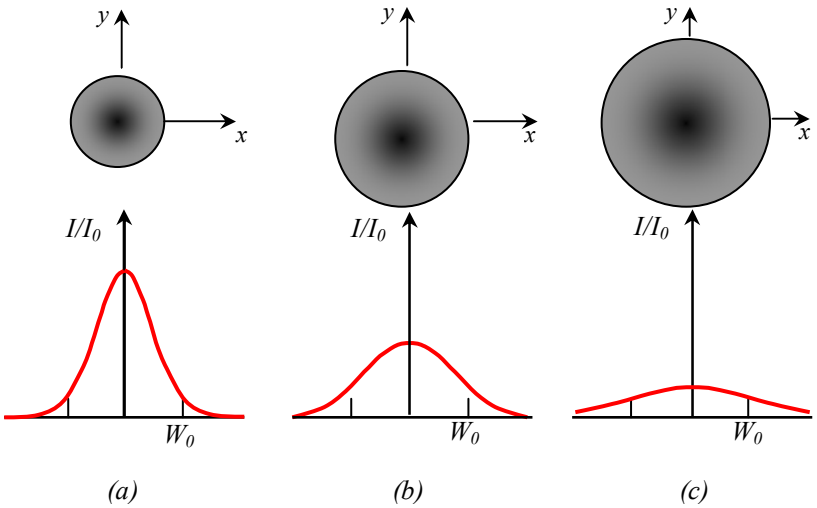

Fig. 2.34 The normalized beam intensity I/I_0 as a function of the radial distance ρ at different axial distances (a) $z = 0$; (b) $z = z_0$; (c) $z = 2z_0$

On the beam axis ($\rho = 0$) the intensity

$$I(0, z) = I_0 \left[\frac{W_0}{W(z)} \right]^2 = \frac{I_0}{1 + (z/z_0)^2} \tag{2.44}$$

has its maximum value I_0 at $z = 0$ and drops gradually with increasing z, reaching half its peak value at $z = \pm z_0$ (Fig. 2.35). When $|z| \gg z_0$, $I(0, z) \approx I_0 z_0^2/z^2$, so that the intensity decreases with the distance in

accordance with an inverse-square law. The overall peak intensity $I(0,0) = I_0$ occurs at the beam center ($z = 0, \rho = 0$).

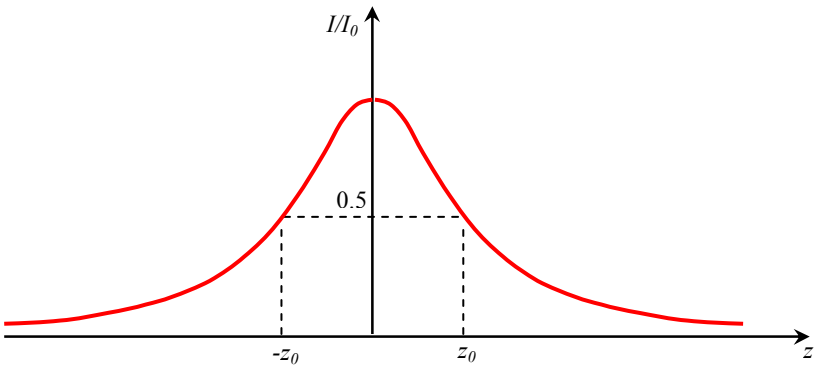

Fig. 2.35 The normalized beam intensity I/I_0 at points on the beam axis (ρ=0) as a function of z

(b) Power

The total optical power carried by the beam is the integral of the optical intensity over a transverse plane (say at a distance z),

$$P = \int_0^\infty I(\rho, z) 2\pi\rho d\rho \tag{2.45}$$

which gives:

$$P = \frac{1}{2} I_0 \left(\pi W_0^2\right) \tag{2.46}$$

The result is independent of z, as expected. Thus the beam power is one-half the peak intensity times the beam area. Since beams are often described by their power P, it is useful to express I, in terms of P using (2.46) and to rewrite (2.44) in the form

$$I(\rho, z) = \frac{2P}{\pi W^2(z)} \exp\left[-\frac{2\rho^2}{W^2(z)}\right] \tag{2.47}$$

The ratio of the power carried within a circle of radius ρ_0 in the transverse plane at position z to the total power is:

$$\frac{1}{P}\int_0^{\rho_0} I(\rho, z) 2\pi\rho d\rho = 1 - \exp\left[-\frac{2\rho_0^2}{W^2(z)}\right] \tag{2.48}$$

The power contained within a circle of radius $\rho_0 = W(z)$ is approximately 86% of the total power. About 99% of the power is contained within a circle of radius $1.5W(z)$.

(c) Beam Radius

Within any transverse plane, the beam intensity assumes its peak value on the beam axis, and drops by the factor $1/e^2 \approx 0.135$ at the radial distance $\rho = W(z)$. Since 86% of the power is carried within a circle of radius $W(z)$, we regard $W(z)$ as the beam radius (also called the beam width). The dependence of the beam radius on z is governed by:

$$W(z) = W_0\left[1+\left(\frac{z}{z_0}\right)^2\right]^{1/2} \tag{2.49}$$

It assumes its minimum value W_0 in the plane $z = 0$, called the beam waist. Thus W_0 is the waist radius. The waist diameter $2W_0$ is called the spot size. The beam radius increases gradually with z, reaching $\sqrt{2}W_0$ at $z = z_0$, and continues increasing monotonically with z as shown in Fig. 2.36. For $z \gg z_0$ the first term of (2.42) may be neglected, resulting in the linear relation:

$$W(z) \approx \frac{W_0}{z_0} z = \theta_0 z \tag{2.50}$$

where $\theta_0 = W_0/z_0$. Using (2.42), we can also write:

$$\theta_0 = \frac{\lambda}{\pi W_0} \tag{2.51}$$

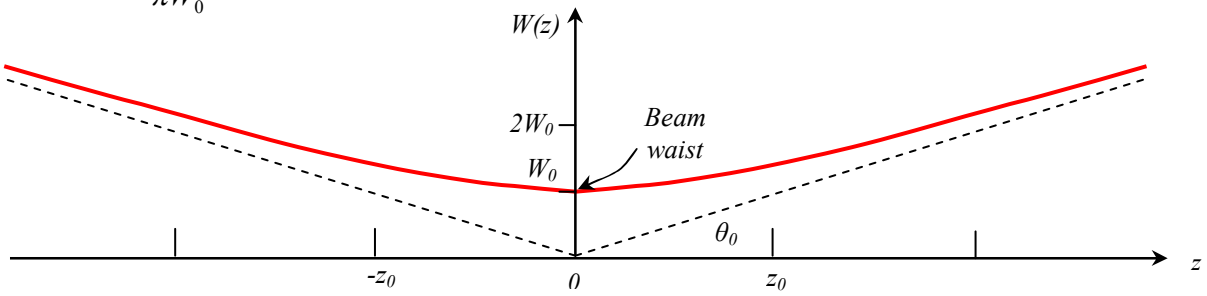

Fig. 2.36 The beam radius $W(z)$ has its minimum value W_0 at the waist ($z = 0$), reaches $\sqrt{2}W_0$ at $z = \pm z_0$, and increases linearly with z for large z.

(d) Beam divergence

Far from the beam center, when $z \gg z_0$, the beam radius increases approximately linearly with z, defining a cone with half-angle θ_0. About 86% of the beam power is confined within this cone. The angular divergence of the beam is therefore defined by the angle:

$$\theta_0 = \frac{2}{\pi}\frac{\lambda}{2W_0} \tag{2.52}$$

The beam divergence is directly proportional to the ratio between the wavelength λ and the beam-waist diameter $2W_0$. If the waist is squeezed, the beam diverges. To obtain a highly directional beam, therefore, a short wavelength and a fat beam waist should be used.

(e) Depth of Focus

Since the beam has its minimum width at $z = 0$, as shown in Fig. 2.36, it achieves its best focus at the plane $z = 0$. In either direction, the beam gradually grows "out of focus." The axial distance within which the beam radius lies within a factor $\sqrt{2}$ of its minimum value (i.e., its area lies within a factor of 2 of its minimum) is known as the depth of focus or confocal parameter (Fig. 2.37). It can be seen from (2.42) that the depth of focus is twice the Rayleigh range,

$$2z_0 = \frac{2\pi W_0^2}{\lambda} \tag{2.53}$$

The depth of focus is directly proportional to the area of the beam at its waist, and inversely proportional to the wavelength. Thus when a beam is focused to a small spot size, the depth of focus is short and the plane of focus must be located with greater accuracy. A small spot size and a long depth of focus cannot be obtained simultaneously unless the wavelength of the light is short. For $\lambda = 633$ nm (He-Ne laser line), for example, a spot size $2W_0 = 2$ cm corresponds to a depth of focus $2z_0 = 1$ km. A much smaller spot size of 20 μm corresponds to a much shorter depth of focus of 1 mm.

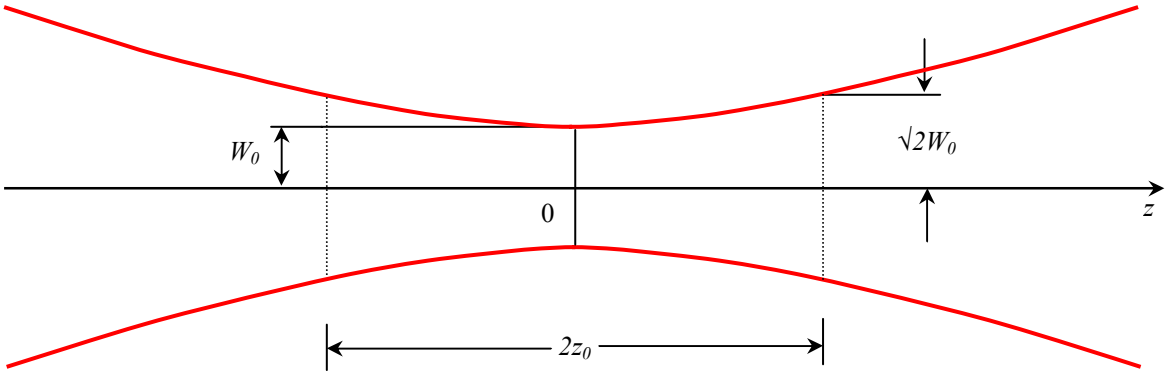

Fig. 2.37 The depth of focus of a Gaussian beam.

(f) Phase

The phase of the Gaussian beam is, from (2.38)

$$\varphi(\rho,z) = kz - \xi(z) + \frac{k\rho^2}{2R(z)} \tag{2.54}$$

On the beam axis ($\rho = 0$) the phase,

$$\varphi(0,z) = kz - \xi(z) \tag{2.55}$$

comprises two components. The first, kz, is the phase of a plane wave. The second represents a phase retardation $\zeta(z)$ given by (2.41) which ranges from $-\pi/2$ at $z = -\infty$ to $+\pi/2$ at $z = \infty$, as illustrated in Fig. 2.38. This phase retardation corresponds to an excess delay of the wavefront in comparison with a plane wave or a spherical wave. The total accumulated excess retardation as the wave travels from $z = -\infty$ to $z = \infty$ is π. This phenomenon is known as the Guoy effect.

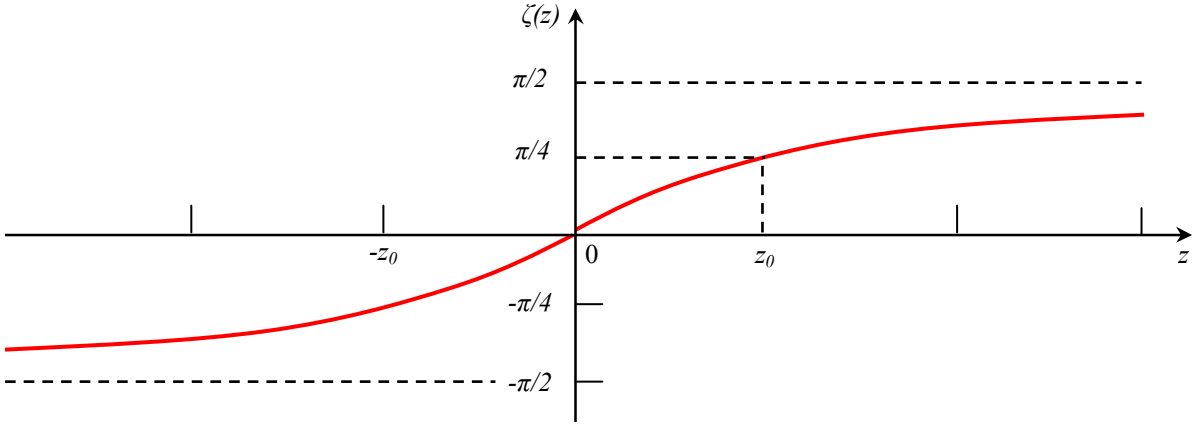

Fig. 2.38 $\zeta(z)$ is the phase retardation of the Gaussian beam relative to a uniform plane wave at points on the beam axis.

(g) Wavefronts

The third component in (2.54) is responsible for wavefront bending. It represents the deviation of the phase at off-axis points in a given transverse plane from that at the axial point. The surfaces of constant phase satisfy $k[z + \rho^2/2R(z)] - \zeta(z) = 2\pi q$. Since $\zeta(z)$ and $R(z)$ are relatively slowly varying, they are approximately constant at points within the beam radius on each wavefront. We may therefore write $z + \rho^2/2R = q\lambda + \zeta\lambda/2\pi$, where $R = R(z)$ and $\zeta = \zeta(z)$. This is precisely the equation of a paraboloidal surface of radius of curvature R. Thus $R(z)$, plotted in Fig. 2.39, is the radius of curvature of the wavefront at position z on the beam axis. As illustrated in Fig. 2.39, the radius of curvature $R(z)$ is infinite at $z = 0$, corresponding to planar wavefronts. It decreases to a minimum value of $2z_0$ at $z = z_0$. This is the point at which the wavefront has the greatest curvature (Fig. 2.40). The radius of curvature subsequently increases with further increase of z until $R(z) \approx z$ for $z \gg z_0$. The wavefront is then approximately the same as that of a spherical wave. For negative z, the wavefronts follow an identical pattern, except for a change in sign. We have adopted the convention that a diverging wavefront has a positive radius of curvature, whereas a converging wavefront has a negative radius of curvature.

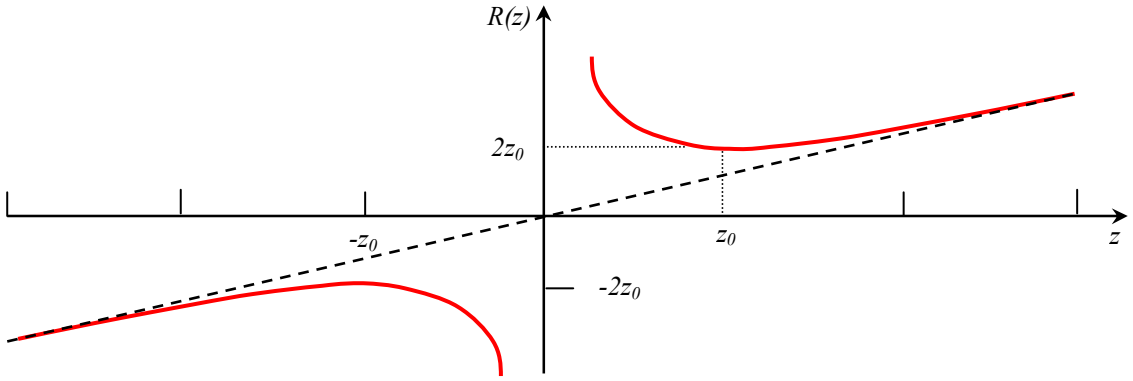

Fig. 2.39 The radius of curvature R(z) of the wavefronts of a Gaussian beam.
The dashed line is the radius of curvature of a spherical wave.

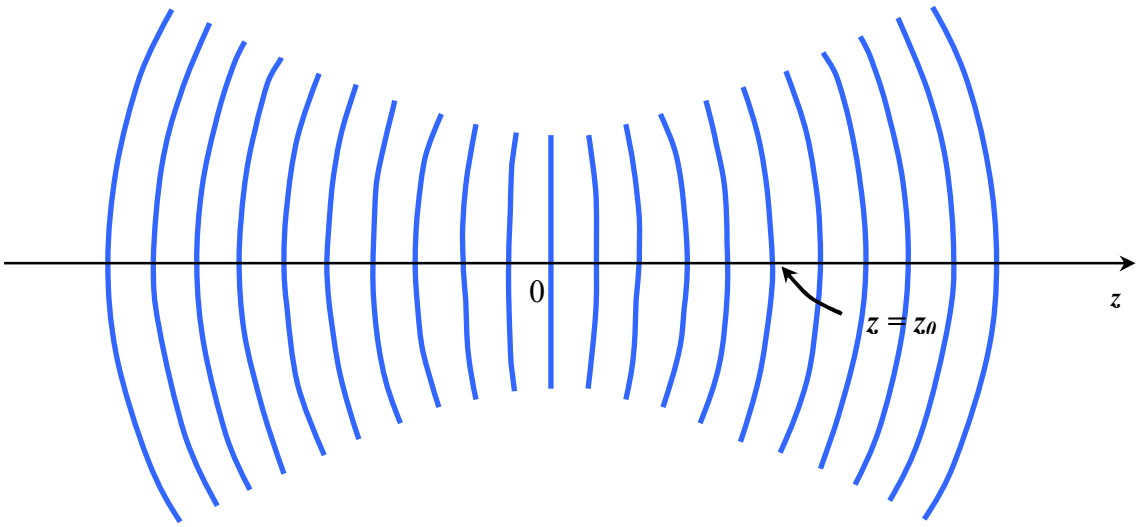

Fig. 2.40 Wavefronts of a Gaussian beam.

2.7.2 Matrix Optics

Matrix optics is a technique for tracing paraxial rays [78]. The rays are assumed to travel only within a single plane, so that the formalism is applicable to systems with planar geometry and to meridional rays in circularly symmetric systems.

A ray is described by its position y and angle θ with respect to the optical axis. These variables (y,θ) are altered as the ray travels through the optical system. In the paraxial approximation, the position and angle of the input and output planes of an optical system are related by two linear algebraic equations. As a result, the optical system is described by 2x2 ray-transfer matrix.

The convenience of using matrix methods lies in the fact that the ray-transfer matrix of a cascade of optical components is a product of the ray-transfer matrices of the individual components. Matrix optics therefore provides a formal mechanism for describing complex optical systems in the paraxial approximation.

2.7.2.1 Ray-transfer matrix: ABCD matrix

Consider a circularly symmetric optical system formed by a succession of refracting and reflecting surfaces all centered about the same optical axis. The z axis lies along the optical axis and points in the general direction in which the rays travel. Consider rays in a plane containing the optical axis, say the yz plane. We proceed to trace a ray as it travels through the system (as it crosses the transverse planes at different axial distances). A ray crossing the transverse plane at z is completely characterized by the coordinate y of its crossing point and the angle θ.

An optical system is a set of optical components placed between two transverse planes at z_1 and z_2 referred to as the input and output planes, respectively as schematized in Fig. 2.41. The system is characterized completely by its effect on an incoming ray of arbitrary position and direction (y_1, θ_1). It steers the ray so that it has new position and direction (y_2, θ_2) at the output plane.

In the paraxial approximation, when all angles are sufficiently small so that $\sin\theta \approx \theta$, the relation between (y_2, θ_2) and (y_1, θ_1) is linear and can generally be written in the form:

$$y_2 = Ay_1 + B\theta_1 \tag{2.56}$$

$$\theta_2 = Cy_1 + D\theta_1 \tag{2.57}$$

Where A, B, C and D are real numbers. Equations (2.56) and (2.57) may be written in the matrix form:

$$\begin{pmatrix} y_2 \\ \theta_2 \end{pmatrix} = \begin{pmatrix} A & B \\ C & D \end{pmatrix} \begin{pmatrix} y_1 \\ \theta_1 \end{pmatrix} \tag{2.58}$$

The matrix M whose elements are A, B, C, D characterizes the optical system completely since it permits (y_2,θ_2) to be determined for any (y_1,θ_1). It is known as the ray-transfer matrix.

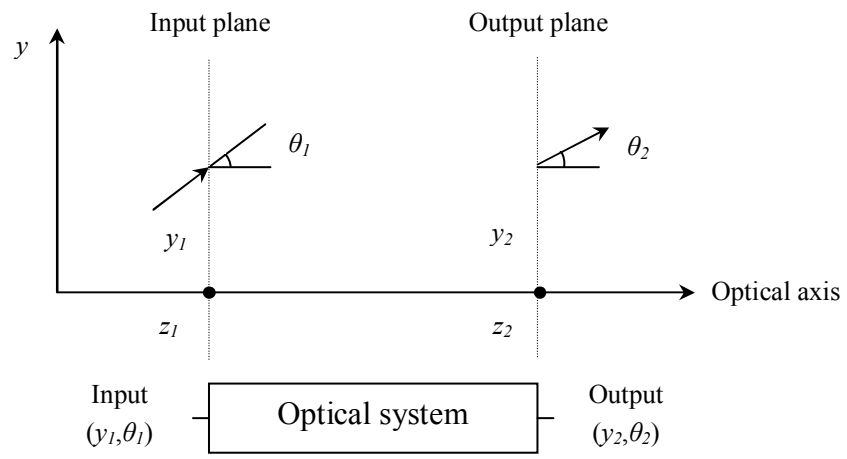

Fig. 2.41 Schematic illustration for ray traveling through an optical system

In a similar way for a cascade of optical components whose ray-transfer matrices are M_1, M_2, …., M_N , the system is equivalent to a single optical component of ray-transfer matrix M such that:

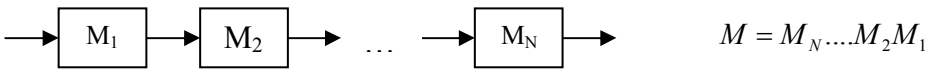

Fig. 2.42 Schematic illustration for a cascaded optical system

Notice the order of matrix multiplication where we start by the matrix of the last element M_N and we end with the matrix of the first crossed element M_1.

2.7.2.2 Periodical Optical System

A periodic optical system is a cascade of identical unit systems. An example is the reflection of light between two parallel mirrors forming an optical resonator; in this case, the ray traverses the same unit system repeatedly. Now, we present the general theory of ray propagation in periodic optical systems formulated using matrix methods.

Let's consider a periodic optical system composed of identical unit systems, each with a ray-transfer matrix (*A, B, C, D*). A ray enters the system with initial position y_0 and slope θ_0. To determine the position and slope (y_m , θ_m) of the ray at the exit of the m^{th} stage, we apply the *ABCD* matrix *m* times,

$$\begin{pmatrix} y_m \\ \theta_m \end{pmatrix} = \begin{pmatrix} A & B \\ C & D \end{pmatrix}^m \begin{pmatrix} y_0 \\ \theta_0 \end{pmatrix} \tag{2.59}$$

We can also apply the relations (2.60) and (2.61) iteratively to determine (y_1 , θ_1) and (y_0 , θ_0) and then (y_2 , θ_2) from (y_1 , θ_1) using a computer.

$$y_{m+1} = Ay_m + B\theta_m \tag{2.60}$$

$$\theta_{m+1} = Cy_m + D\theta_m \tag{2.61}$$

We now proceed by deriving equations that govern the dynamics of the position y_m , m = 0,1,… irrespective of the angle θ_m. This is achieved by eliminating θ_m from (2.5) and (2.6). We get then,

$$\theta_m = \frac{y_{m+1} - Ay_m}{B} \tag{2.62}$$

Replacing m with m+1 in (2.62) yields:

$$\theta_{m+1} = \frac{y_{m+2} - Ay_{m+1}}{B} \tag{2.63}$$

Substituting (2.63) and (2.62) into (2.60) gives:

$$y_{m+2} = 2by_{m+1} - F^2 y_m \tag{2.64}$$

where:

$$b = \frac{A+D}{2} \tag{2.65}$$

$$F^2 = AD - BC = \det[M] \tag{2.66}$$

Equation (2.64) is a linear difference equation governing the ray matrix position y_m. It can be solved iteratively using a computer. It is useful however to derive an explicit expression for y_m by solving equation (2.64). As in linear differential equations, a solution satisfying a linear difference equation and the initial conditions is a unique solution. It is therefore appropriate to make a judicious guess for the solution of (2.64). Therefore, we use a trial solution of the form:

$$y_m = y_0 h^m \tag{2.67}$$

where h is a constant. Substituting into (2.64) immediately shows that the trial solution is suitable provided that h satisfies the quadratic algebraic equation

$$h^2 - 2bh + F^2 = 0 \tag{2.68}$$

$$h = b \pm j\left(F^2 - b^2\right)^{1/2} \tag{2.69}$$

The results can be simplified by defining the variable:

$$\varphi = \cos^{-1}\frac{b}{F} \tag{2.70}$$

So that: $b = F\cos\varphi$ and $\left(F^2 - b^2\right)^{1/2} = F\sin\varphi$. Therefore, $h = F\left(\cos\varphi \pm j\sin\varphi\right) = F\exp\left(\pm j\varphi\right)$, whereupon (2.67) becomes: $y_m = y_0 F^m \exp\left(\pm jm\varphi\right)$.

A general solution may be constructed from the two solutions with positive and negative signs by forming their linear combination. The sum of the two exponential functions can always be written as a harmonic function so that:

$$y_m = y_{\max} F^m \sin\left(m\varphi + \varphi_0\right) \tag{2.71}$$

where y_{max} and φ_0 are constants to be determined from the initial conditions y_0 and y_1. In particular, $y_{max} = y_0 / \sin \varphi_0$.

In most of the applications, det[M] = 1 and $F = 1$, in which case the solution for the ray position is:

$$y_m = y_{\max} \sin\left(m\varphi + \varphi_0\right) \tag{2.72}$$

For y_m to be a harmonic function, $\varphi = \cos^{-1} b$ must be real. This requires that:

$$|b| \le 1 \qquad \text{or} \qquad \frac{|A+D|}{2} \le 1 \tag{2.73}$$

If, instead, $|b| > 1$, φ is then imaginary and the solution is a hyperbolic function (cosh or sinh) which increases without bound. A harmonic solution ensures that y_m is bounded for all m with a maximum value of y_{max}. The bound $|b| \le 1$ therefore provides a condition of stability of the ray trajectory.

Chapter 3

Basic Building Blocks Based on Silicon-Air Interfaces – Comprehensive Study

3.1 Introduction

Since the Bragg layers, also referred as to 1D photonic crystal, lies at the core of many optical devices, this chapter is devoted to the study of the theory underlying the design of multilayered structures [79]. The corresponding analytical model is explained in details in section 3.2 followed in the following sections, by various design examples for the shake of illustration.

Of special interest are the Silicon-Air Bragg mirrors obtained by DRIE micromachining. They are considered as an important building block leading to a wide variety of applications. First, we elaborate on the use of this building block in resonant cavities and in interferometers (section 3.3) and a literature survey is given on this topic. Finally, we conclude this work by a case of study for a special structure: The mode selector, covered in section 3.4).

3.2 Theory and Modeling of the Bragg reflectors

Under specific conditions, a stack of multilayered structure gives rise to nearly perfect optical reflectance, approaching 100 %, as compared to the reflectance from a single interface. This is the main characteristic that makes the interest in such structures, called Bragg reflectors or Bragg mirrors. This phenomenon of enhanced reflectivity might be explained by the fact that the presence of two (or more) interfaces means that a number of light beams will be produced by successive reflections, that may interfere constructively (or destructively, when considering anti-reflective surfaces), and the properties of the multilayered film will be determined by the summation of these beams. This might be the case in thin film assemblies. In thick assemblies however, the later phenomenon does not take place. Before going into the analytical details, we differentiate between thin and thick films. We say that the film is thin when interference effects can be detected in the reflected or transmitted light, that is, when the path difference between the beams is less than the coherence length of the light, and thick when the path difference is greater than the coherence length. Note that no interference can be observed when effects of light absorption dominate within the film, even in the case of thin films. The same film can appear thin or thick depending entirely on the illumination conditions. The thick case can be shown to be identical with the thin case integrated over a sufficiently wide wavelength range or a sufficiently large range of angles of incidence. Normally, we will find that the films on the substrates can be treated as thin while the substrates supporting the films can be considered thick.

In the upcoming treatment, we show analytically a generalized model applicable for an absorbing thin film assembly. The obtained result applies equally well for non-absorbing films.

Let's consider the arrangement shown in Fig. 3.1 where we denote positive-going waves by the symbol + and negative-going waves by the symbol -. Applying the boundary conditions on the electromagnetic field components at interface B (chosen as the origin of *z*-axis), we have:

Continuity of the tangential components of the electric filed gives (E_b being the tangential component of the resultant electric field):

$$E_b = E_{1b}^{+} + E_{1b}^{-} \tag{3.1}$$

Continuity of the tangential components of the magnetic filed gives (H_b being the tangential component of the resultant magnetic field):

$$H_b = H_{1b}^{+} - H_{1b}^{-} = \eta_1 E_{1b}^{+} - \eta_1 E_{1b}^{-} \tag{3.2}$$

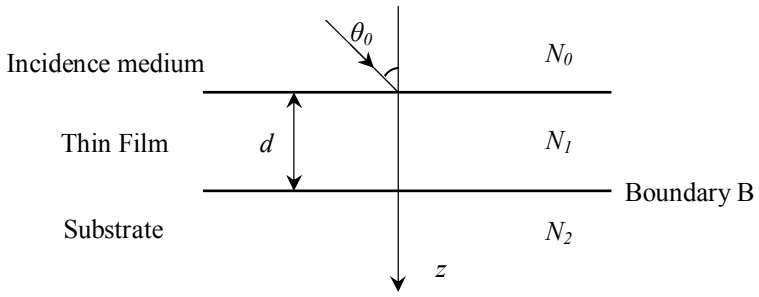

Fig. 3.1 Plane wave incidence on a thin film

where η represents the medium admittance such that: $\eta = H/E$.

The negative sign in (3.2) comes from the convention used for the field propagation direction such that the right hand rule relating *E, H* and *K* (wave vector, along the propagation direction) is always satisfied. In writing equations (3.1) and (3.2), we assume that: Common phase factors have been omitted, and the substrate is thick enough such that no field is reflected back from it.

$$E_{1b}^{+} = \frac{1}{2}\left(H_b / \eta_1 + E_b\right) \tag{3.3}$$

$$E_{1b}^{-} = \frac{1}{2}\left(-H_b / \eta_1 + E_b\right) \tag{3.4}$$

$$H_{1b}^{+} = \eta_1 E_{1b}^{+} = \frac{1}{2}\left(H_b + \eta_1 E_b\right) \tag{3.5}$$

$$H_{1b}^{-} = -\eta_1 E_{1b}^{-} = \frac{1}{2}\left(H_b - \eta_1 E_b\right) \tag{3.6}$$

The fields at the other interface A at the same instant and at a point with identical *x* and *y* coordinates can be determined by altering the phase factors of the waves to allow for a shift in the *z* coordinate from 0 to -*d*. The phase factor of the positive-going wave will be multiplied by $exp(i\delta)$ while the negative-going phase factor will be multiplied by $exp(-i\delta)$, where

$$\delta = \frac{2\pi N_1 d}{\lambda}\cos\theta_1 \tag{3.7}$$

N_1 is the refractive index in medium 1, θ_1 is the angle between the z-axis and the propagation direction in medium 1 and λ is the free space wavelength. The values of E and H at interface A become:

$$E_{1a}^{+} = E_{1b}^{+}e^{i\delta} = \frac{1}{2}\left(H_b/\eta_1 + E_b\right)e^{i\delta} \tag{3.8}$$

$$E_{1a}^{-} = E_{1b}^{-}e^{-i\delta} = \frac{1}{2}\left(-H_b/\eta_1 + E_b\right)e^{-i\delta} \tag{3.9}$$

$$H_{1a}^{+} = H_{1b}^{+}e^{i\delta} = \frac{1}{2}\left(H_b + \eta_1 E_b\right)e^{i\delta} \tag{3.10}$$

$$H_{1a}^{-} = H_{1b}^{-}e^{-i\delta} = \frac{1}{2}\left(H_b - \eta_1 E_b\right)e^{-i\delta} \tag{3.11}$$

So that:

$$\begin{aligned} E_a &= E_{1a}^{+} + E_{1a}^{-} = E_b\left(\frac{e^{i\delta}+e^{-i\delta}}{2}\right) + H_b\left(\frac{e^{i\delta}-e^{-i\delta}}{2\eta_1}\right) \\ &= E_b\cos\delta + H_b\frac{i\sin\delta}{\eta_1} \end{aligned} \tag{3.12}$$

$$\begin{aligned} H_a &= H_{1a}^{+} + H_{1a}^{-} = E_b\eta_1\left(\frac{e^{i\delta}-e^{-i\delta}}{2}\right) + H_b\left(\frac{e^{i\delta}+e^{-i\delta}}{2}\right) \\ &= E_b i\eta_1\sin\delta + H_b\cos\delta \end{aligned} \tag{3.13}$$

In the matrix notation, we finally obtain the following formulation:

$$\begin{bmatrix} E_a \\ H_a \end{bmatrix} = \begin{bmatrix} \cos\delta & \left(i\sin\delta\right)/\eta_1 \\ i\eta_1\sin\delta & \cos\delta \end{bmatrix}\begin{bmatrix} E_b \\ H_b \end{bmatrix} \tag{3.14}$$

This matrix relates the tangential components of E and H at the incident interface to tangential components of E and H transmitted through the final interface and it is known as the characteristic matrix of the thin film [M].

Now, let us consider an assembly of thin films as shown in Fig. 3.2

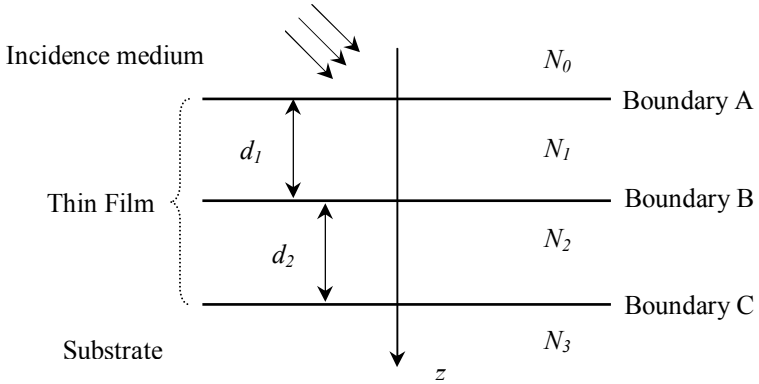

Fig. 3.2 Plane wave incidence on a thin film assembly

By adding another film to the single film shown in Fig. 3.1, then we can write:

$$\begin{bmatrix} E_b \\ H_b \end{bmatrix} = \begin{bmatrix} \cos\delta_2 & (i\sin\delta_2)/\eta_2 \\ i\eta_2 \sin\delta_2 & \cos\delta_2 \end{bmatrix} \begin{bmatrix} E_c \\ H_c \end{bmatrix} \tag{3.15}$$

Combining with equation (3.14) to get the field at interface A, then we can write:

$$\begin{bmatrix} E_a \\ H_a \end{bmatrix} = \begin{bmatrix} \cos\delta_1 & (i\sin\delta_1)/\eta_1 \\ i\eta_1 \sin\delta_1 & \cos\delta_1 \end{bmatrix} \begin{bmatrix} \cos\delta_2 & (i\sin\delta_2)/\eta_2 \\ i\eta_2 \sin\delta_2 & \cos\delta_2 \end{bmatrix} \begin{bmatrix} E_c \\ H_c \end{bmatrix} \tag{3.16}$$

This result can be immediately extended to the general case of an assembly of q layers, when the characteristic matrix is simply the product of the individual matrices taken in the correct order,

$$\begin{bmatrix} E_a \\ H_a \end{bmatrix} = \left\{ \prod_{r=1}^{q} \begin{bmatrix} \cos\delta_r & (i\sin\delta_r)/\eta_r \\ i\eta_r \sin\delta_r & \cos\delta_r \end{bmatrix} \right\} \begin{bmatrix} E_m \\ H_m \end{bmatrix} \tag{3.17}$$

where E_m and H_m are the electric and magnetic fields components in the substrate plane.

Dividing both sides of equation (3.17) by H_m, we get:

$$\begin{bmatrix} B \\ C \end{bmatrix} = \begin{bmatrix} E_a/E_m \\ H_a/E_m \end{bmatrix} = \left\{ \prod_{r=1}^{q} \begin{bmatrix} \cos\delta_r & (i\sin\delta_r)/\eta_r \\ i\eta_r \sin\delta_r & \cos\delta_r \end{bmatrix} \right\} \begin{bmatrix} 1 \\ \eta_m \end{bmatrix} \tag{3.18}$$

$$\text{where } \delta_r = \frac{2\pi N_r d_r}{\lambda} \cos\theta_r \tag{3.19}$$

$$\eta_r = \Upsilon N_r \cos\theta_r \text{ for s-polarisation (TE)} \tag{3.20}$$

$$\eta_r = \Upsilon N_r / \cos\theta_r \text{ for p-polarisation (TM)} \tag{3.21}$$

$$\Upsilon = (\varepsilon_0/\mu_0)^{1/2} = 2.6544\times10^{-3} S \text{ (Free space admittance)} \tag{3.22}$$

Then, the admittance of the thin film assembly is:

$$Y = \frac{H_a}{E_a} = \frac{H_a/E_m}{E_a/E_m} = \frac{C}{B} \tag{3.23}$$

The amplitude reflection coefficient and the reflectance are then given by:

$$\rho = \frac{\eta_0 - Y}{\eta_0 + Y} \tag{3.24}$$

$$R = \left(\frac{\eta_0 - Y}{\eta_0 + Y}\right)\left(\frac{\eta_0 - Y}{\eta_0 + Y}\right)^* = \left(\frac{\eta_0 B - C}{\eta_0 B + C}\right)\left(\frac{\eta_0 B - C}{\eta_0 B + C}\right)^* \tag{3.25}$$

In this part, we look over the case of absorbing layers. Knowing that K is propagation vector:

$$K^2 = K_x^2 + K_z^2 \tag{3.26}$$

From Snell's law, $K_{x0} = K_{xr} = K_{xm}$ this leads to:

$$N_0 \sin\theta_0 = N_r \sin\theta_r = N_m \sin\theta_m \tag{3.27}$$

In case of absorbing medium, N_r is complex and in general, it can be expressed as a complex number:

$$N_r = n - ik \tag{3.28}$$

Then, $K_{zr}^2 = K_r^2 - K_{xr}^2 = K_0^2\left(N_r^2 - N_0^2\sin^2\theta_0\right) = K_0^2\left(n^2 - k^2 - 2ink - N_0^2\sin^2\theta_0\right)$ (3.29)

$$\delta_r = K_{zr}d_r = K_0 d_r\left(n^2 - k^2 - 2ink - N_0^2\sin^2\theta_0\right)^{1/2}$$

Then,
$$= \frac{2\pi}{\lambda} d_r\left(n_r^2 - k_r^2 - 2in_r k_r - N_0^2\sin^2\theta_0\right)^{1/2} \tag{3.30}$$

Accordingly, we get:

The admittance of layer *r* in s-polarization:

$$\eta_{rs} = \Upsilon\left(n_r^2 - k_r^2 - 2in_r k_r - N_0^2\sin^2\theta_0\right)^{1/2} \tag{3.31}$$

The admittance of layer *r* in p-polarization:

$$\eta_{rp} = \frac{\Upsilon_r^2}{\eta_{rs}} = \frac{\Upsilon^2\left(n_r - ik_r\right)^2}{\eta_{rs}} \tag{3.32}$$

In this last part of the analytical model, we present closed form relations for the transmittance *T* and the absorbance *A* using the definition of irradiance.

If we consider the net irradiance at the exit of the assembly I_k:

$$I_k = \frac{1}{2}\mathrm{Re}\left(E_k H_k^*\right) = \frac{1}{2}\mathrm{Re}\left(\eta_m^*\right)E_k E_k^* \tag{3.33}$$

The net irradiance at the entrance of the assembly I_a:

$$I_a = \frac{1}{2}\mathrm{Re}\left(E_a H_a^*\right) = \frac{1}{2}\mathrm{Re}\left(\frac{E_a}{E_k}\cdot\frac{H_a^*}{E_k^*}\right)E_k E_k^* = \frac{1}{2}\mathrm{Re}\left(BC^*\right)E_k E_k^* \tag{3.34}$$

Let the incident irradiance be denoted by I_i, then the irradiance actually entering the assembly becomes:

$$I_a = \left(1-R\right)I_i = \frac{1}{2}\mathrm{Re}\left(BC^*\right)E_k E_k^* \tag{3.35}$$

$$\text{Then, } I_i = \frac{\mathrm{Re}\left(BC^*\right)E_k E_k^*}{2\left(1-R\right)} \tag{3.36}$$

The transmittance is then given by:

$$T = \frac{I_k}{I_i} = \frac{\mathrm{Re}\left(\eta_m\right)\left(1-R\right)}{\mathrm{Re}\left(BC^*\right)} \tag{3.37}$$

From equation (3.25), we get:

$$T = \frac{4\eta_0\,\mathrm{Re}\left(\eta_m\right)}{\left(\eta_0 B + C\right)\left(\eta_0 B + C\right)^*} \tag{3.38}$$

Knowing that $A + R + T = 1$ from the energy conservation rule, then A becomes:

$$A = 1 - R - T = (1 - R)\left(1 - \frac{\mathrm{Re}(\eta_m)}{\mathrm{Re}(BC^*)}\right) \tag{3.39}$$

From equation (3.25), we get:

$$A = \frac{4\eta_0 \,\mathrm{Re}(BC^* - \eta_m)}{(\eta_0 B + C)(\eta_0 B + C)^*} \tag{3.40}$$

3.3 Microfabricated Silicon-Air Bragg as basic building blocks in cavities and interferometers

3.3.1 Literature survey

Many groups worked on the realisation of silicon-Air Bragg reflectors as basic building blocks in Fabry-Perot (FP) cavities as well as in Michelson interferometers. When considering Fabry-Perot cavities, the use of high reflectance Bragg mirrors is intended to achieve high quality factor Q at the corresponding resonant wavelengths. The use of silicon restricts the wavelength range to the infra-red region. In the same time, light coupling using optical fibers is facilitated by the microfabrication of U-grooves for supporting the fibers with pre-alignment capability. Among the groups working on this topic, we can cite Lipson and Yeatman [40, 51] from the imperial college who realized FP cavities obtained by KOH etching on SOI substrate. The best reported value of Q was 2395 in static designs while it was limited to 515 in the MEMS designs due to the rotation associating the translation of the MEMS mirror. Thus, the mirrors became unparallel and the Q-factor degraded. Another group is the group of Ecole Polytechnique de Montreal who realized FP cavity for inertial sensing [80] on SOI. Their Q was limited to 662. A third group is that of Yun and Lee from Gwangju Institute of Science and Technology, Korea who realized thermally tuned FP cavities [81], they obtained a Q of 1373. A fourth group is that of Pruessner et al. [7, 8, 16, 82] from Naval Research Laboratory, Washington D.C. who realised FP cavities with integrated SOI rib waveguides by cryogenic etching. They recorded a Q factor of 27,000. Lastly, our group at ESIEE Paris was among the pioneers in this domain. In our first achievements, we realized FP cavities with different architectures [6]; the best recorded Q was 1291 for FP structure working as a notch filter. More recently, the performance was improved using cylindrical Bragg mirrors of cylindrical shapes combined with a fiber rod lens, leading to Q = 8818 on quite large cavities exceeding L = 250 µm [83], an unreached value for the figure of merit $Q.L$, which is of primary importance for cavity enhancement applications. Table 3.1 summarizes the specifications of the different designs discussed above.

Table 3.1 Summary of the specifications for state-of-the-art FP cavities

	Lispon et Yeatman Imperial college UK	**Zandi et al. EPM Canada**	**Yun and Lee GIST Korea**	**Pruessner et al. Washington D.C**	**Saadany et al. ESIEE France**	**Malak et al. ESIEE France**
Cavity length	3.3 µm	27.1 µm	----	12 µm	10 µm	250 µm
Tuning range	Static design : 70 nm MEMS design: 10 nm	30 nm	9 nm	6.7 nm	----	----
Number of silicon layers /mirror	3	3	2	2	3	4
***Q*-factor**	**Static design:** $Q = 2395$ **MEMS design:** $Q = 515$ $Q_{MEMS} < Q_{static}$ Because the displacement creates a rotation for the moving mirror.	$Q = 662$	$Q_{average} = 1373$ (estimated from the response of a rejection filter)	$Q = 27000$	$Q_{Trans} = 1291$	$Q = 8818$

3.3.2 Fabrication technology for Si-Air Bragg reflectors (for MEMS and for fixed structures)

In this section, the basic steps of the fabrication process for MEMS structures involving Bragg layers are highlighted. The process described here and shown in Fig. 3.3 pertains to the (optional) integration of MEMS structures together with the Bragg mirrors.

Starting from a raw SOI wafer, we proceed by making thermal oxidation for the whole wafer. In the next step, photoresist (PR) is used to cover the entire wafer where it acts as a mask for photolithography. The PR is then patterned using UV exposure over the DRIE layout mask. Since the PR is a positive type, the areas exposed to UV remain soft while the non-exposed areas become hard and they can not be removed in the development step. Now, the hardened PR acts as a protection mask for the originally oxidized silicon which is patterned using either Reactive Ion etching (RIE) or Buffer HydroFluoric acid (BHF). The role of PR ends here and it is completely removed from the wafer.

The fabrication process continues by the metal deposition over the whole wafer. The metal is patterned by photolithography using the frontside metal layout mask and then etched. In the next step, metal is deposited on the backside of the wafer where it is patterned by the backside layout mask and then etched. We turn again to the front side to make Deep Reactive Ion etching (DRIE) for the silicon structure layer. At that level, both the oxide and the aluminum serve as mask materials for silicon etching by DRIE. Processing the backside again, DRIE is done for the backside, in this case, only aluminum serve as mask material for silicon etching by DRIE. The process ends by releasing the MEMS structure in which the insulating oxide is removed by vapor HF.

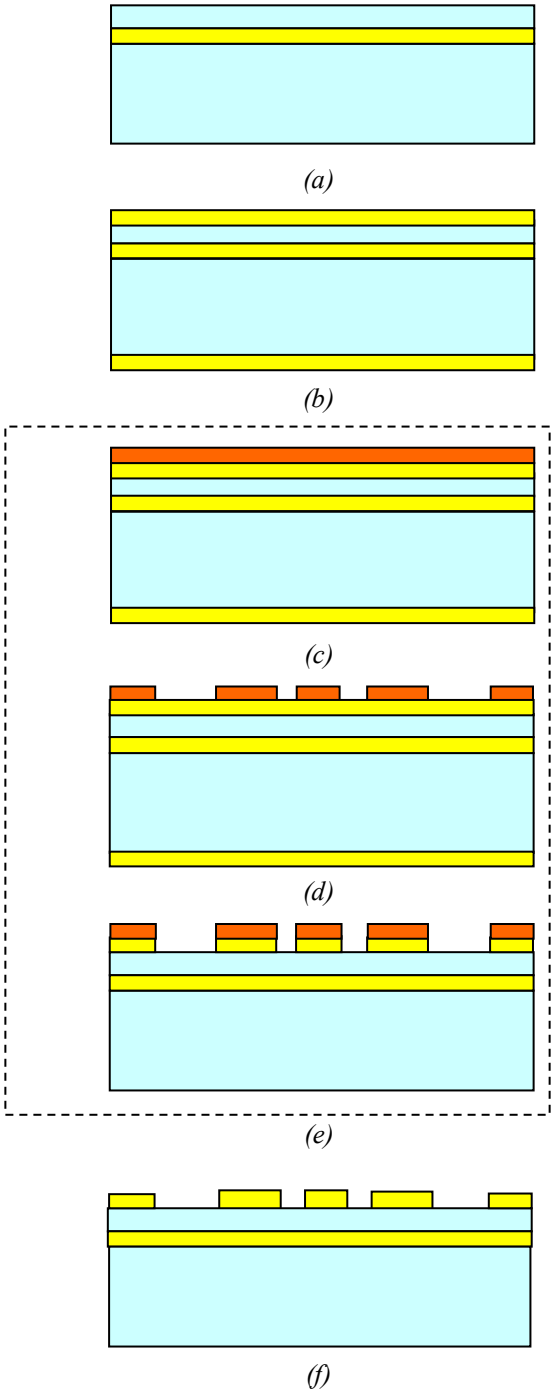

(a) Initial SOI Wafer

(b) Thermal Oxydation

(c) Photoresist spin-coating

(d) Patterning Photoresist by UV exposure and further development

(e) Oxide etching (using Photoresist patterns as a protection mask material) either by BHF or by RIE

(f) Photoresist removal

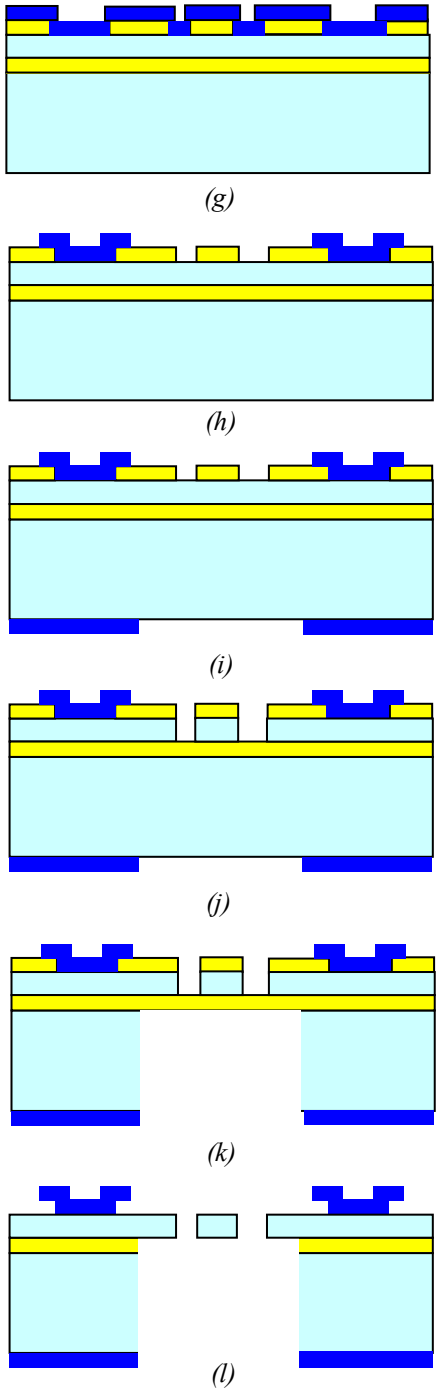

(g) Aluminum deposition (sputtering)

(h) Lithography patterning and aluminum etching

(i) Metal deposition on the backside, patterning using proper mask and then, etching.

(j) DRIE Etching for the frontside (Note that here, both oxide and aluminum serve as mask materials for silicon etching by DRIE

(k) DRIE Etching for the backside (Note that in this case, only aluminum serve as mask material for silicon etching by DRIE)

(l) Release (oxide removal by vapor HF)

Fig. 3.3 (a-l) Basic steps of the fabrication process for MEMS structures co-integrated with Si-Air Bragg mirrors.

For the fixed structures involving Bragg mirrors presented in this research work, the process differs from the one detailed above. So, in the next paragraph, we highlight the fabrication process as shown in Fig. 3.4, used for the realization of the fixed structures.

Starting with an ordinary silicon wafer, a thermal oxidation process is carried for both sides of the wafer to achieve an oxide thickness = 1.7 µm. Next, PR used as a mask for photolithography, is sputtered over the entire wafer. This step is followed by the photolithography for DRIE mask for the front side and the PR is patterned accordingly. The following step is the plasma etching for the oxide.

This photolithography ends by PR removal. Then, we start processing for the back side by depositing aluminium. Next, we pattern the aluminium mask by photolithography using the back side layout mask. Then, we proceed by DRIE etching over 300 µm for the back side and the process ends up with DRIE etching for the front side over 100 µm. Note that all steps performed on the backside are optional, depending on the nature of the target device.

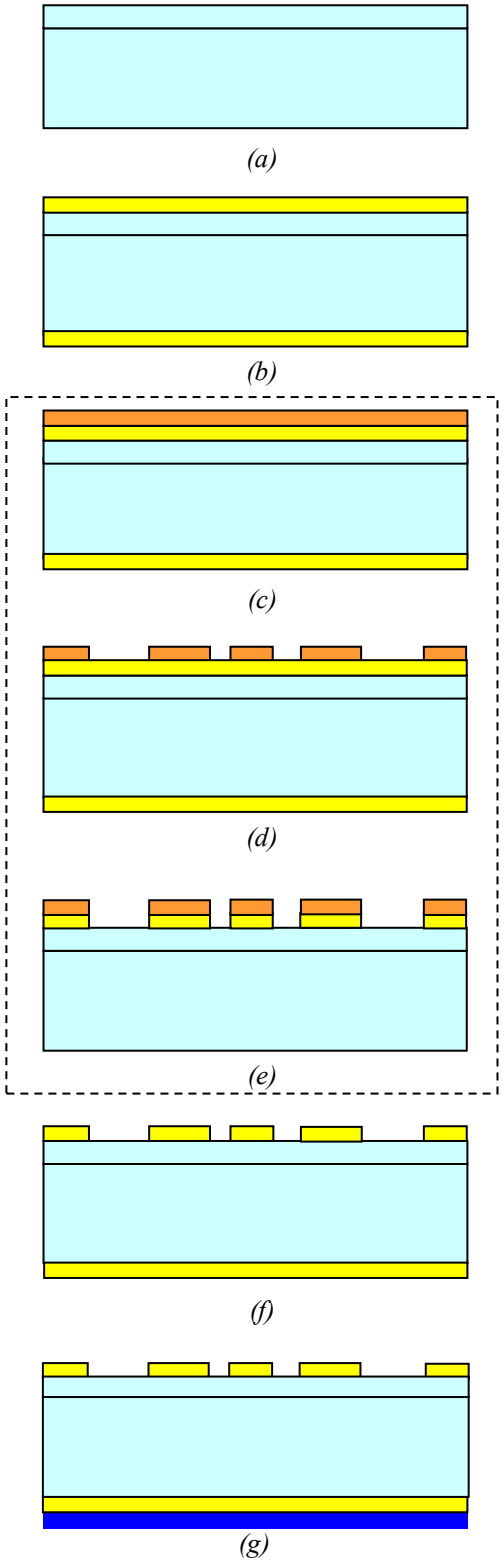

(a) Initial Silicon wafer = 400 µm

(b) Thermal Oxydation 1.7 µm

(c) Front side Photolithography for DRIE (PR sputtering)

(d, e) Plasma etching for the oxide

(f) PR removal

(g) Aluminium deposition – back side

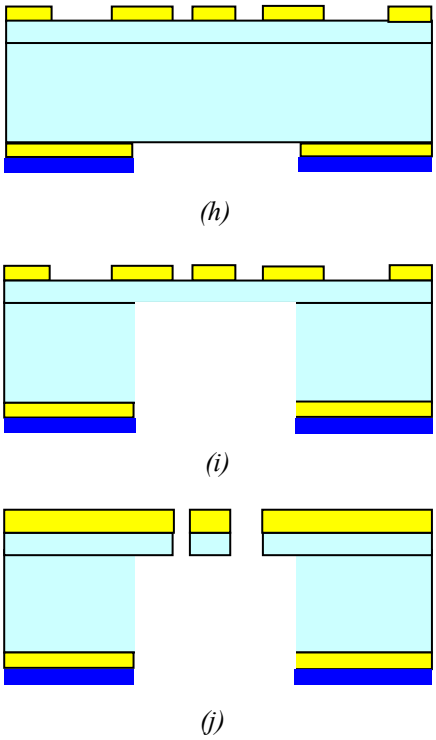

(h) DRIE Photolithography (Oxide + Aluminum)

(i) DRIE Etching – back side 300 um

(j) DRIE Etching – front side 100 um

Fig. 3.4 (a-j) Basic steps of the fabrication process for fixed structures involving Bragg mirrors.

3.3.3 Modeling and Simulation of Planar Bragg mirror reflectors

Based on the analytical model presented in section 3.2, if we have a single layer whose thickness is an odd number of quarter the wavelength, the characteristic matrix of the layer [M] becomes:

$$[M] = \pm \begin{bmatrix} 0 & i/\eta \\ i\eta & 0 \end{bmatrix} \tag{3.41}$$

So, if we stack a combination of several layers alternatively of High refractive index, denote *H*, and Low refractive index, denoted *L*, whose thickness is an odd number of λ/4 (where λ is the wavelength in the corresponding medium), we can construct a high reflectance mirror named Bragg mirror. In the particular case where we stack a combination of five quarter-wave layers which are different, mathematical manipulation of the equivalent characteristic matrix yields an equivalent admittance for the assembly:

$$Y = \frac{\eta_1^2 \eta_3^2 \eta_5^2}{\eta_2^2 \eta_4^2 \eta_m} \tag{3.42}$$

where the definitions presented previously are kept unchanged.

For $\eta_m = \eta_0$, and considering similar indices for the high and low layers as well so that, $\eta_1 = \eta_3 = \eta_5 = \eta_H$ and $\eta_2 = \eta_4 = \eta_L$, the reflectance of the assembly becomes:

$$R = \left(\frac{\eta_0 - Y}{\eta_0 + Y}\right)\left(\frac{\eta_0 - Y}{\eta_0 + Y}\right)^* = \left(\frac{1 - \left(\frac{\eta_H}{\eta_L}\right)^6}{1 + \left(\frac{\eta_H}{\eta_L}\right)^6}\right)^2 \tag{3.43}$$

In general, for a pair (p) of *HL* layers with similar η_m and η_0, we can write:

$$R = \left(\frac{1 - \left(\frac{\eta_H}{\eta_L}\right)^{2p}}{1 + \left(\frac{\eta_H}{\eta_L}\right)^{2p}}\right)^2 \tag{3.44}$$

Based on these derivations, we built a MATLAB code to design the Bragg mirrors. In this comprehensive study, we focus mainly on the impact of the number of Bragg layers, the layer thickness and the technological errors on the reflectance and the transmittance of the Bragg mirror. In all the upcoming results, we consider absorption free layers with a silicon refractive index n_{Si} = 3.478 and air refractive index n_{air} = 1.

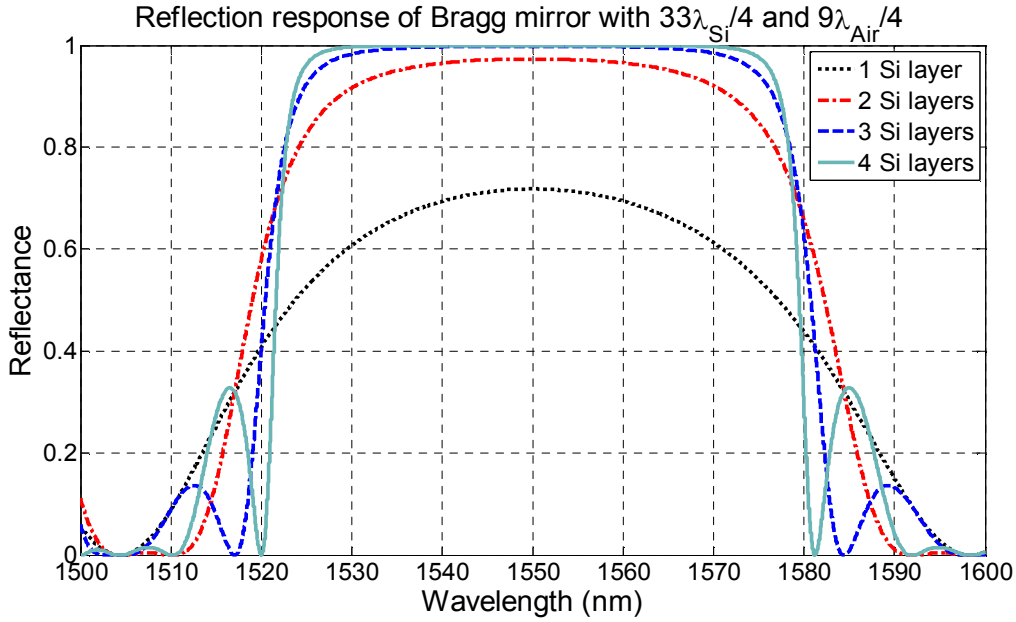

Fig. 3.5 Reflectance of Bragg mirrors for different numbers of HL pairs

For the simulation results shown in Fig. 3.5, we choose a silicon thickness = 3.67 µm ($33\lambda_{Si}/4$) and air thickness = 3.49 µm ($9\lambda_{air}/4$) because they are relatively easy values to obtain technologically (as compared to single quarter wavelength $\lambda_{Si}/4$ = 0,11 µm and $\lambda_{air}/4$ = 0,58 µm). We notice that the reflectance in the mid-band increases as the number of layers increases which goes in accordance with relation (3.44). In fact, the reflectance increases from 71.8 % (single Si layer) up to 99.98 % (4 Si layers) when the number of *HL* pairs increases from single to four. Also, the mirror response becomes

sharper and its bandwidth (BW) decreases as the number of layers increases. In the case of single layer, the BW is about 65 nm and it goes down to 58 nm as the *HL* pairs increases to 4.

In the next simulation, we study the impact of the silicon layers thickness on the mirror bandwidth. For this shake, we consider 4 *HL* pairs with fixed air layers thickness 3.49 µm ($9\lambda_{air}/4$), while the thickness of the silicon layers is increased from $\lambda_{Si}/4$ up to $25\lambda_{Si}/4$ in steps of $2\lambda_{Si}$. Simulation results, depicted in Fig 3.6, show that the mirror BW decreases as the thickness of the silicon layers increases. For silicon thickness $\lambda_{Si}/4$, the 3dB-BW = 238 nm and it decreases to 73 nm at a thickness of $25\lambda_{Si}/4$.

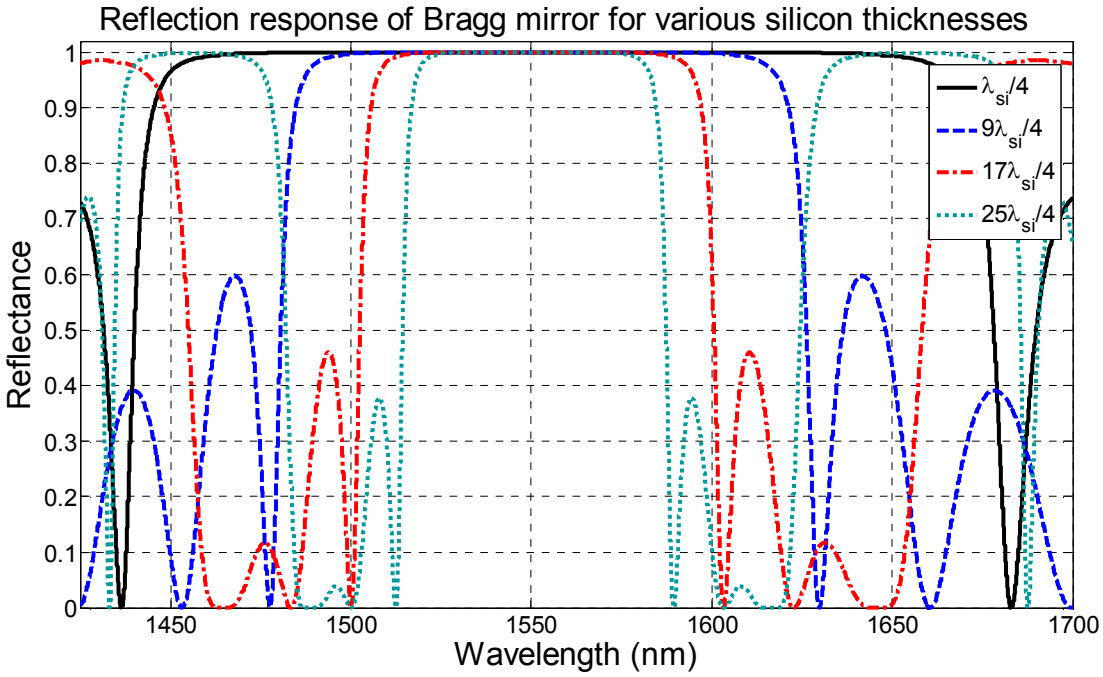

Fig. 3.6 Reflectance of 4 *HL* pairs for various *H* thicknesses, *L* thickness is fixed to $9\lambda_{air}/4$

If on the other hand, we fix the thickness of the silicon layers to $33\lambda_{Si}/4$, for the same 4 *HL* pairs, and increase the thickness of the air layers from $\lambda_{air}/4$ up to $13\lambda_{air}/4$ in steps of λ_{air}. A similar effect is noticed but on a smaller BW scale since the BW decreases from 65 nm at L thickness = $\lambda_{air}/4$, to 55 nm at L thickness = $13\lambda_{air}/4$. The corresponding results are shown in Fig. 3.7. Comparing between both results, we can say that the decrease in the H thickness is more pronounced than the decrease in the L thickness in terms of the bandwidth. Good control of the H thickness can give rise Bragg mirrors with large BW.

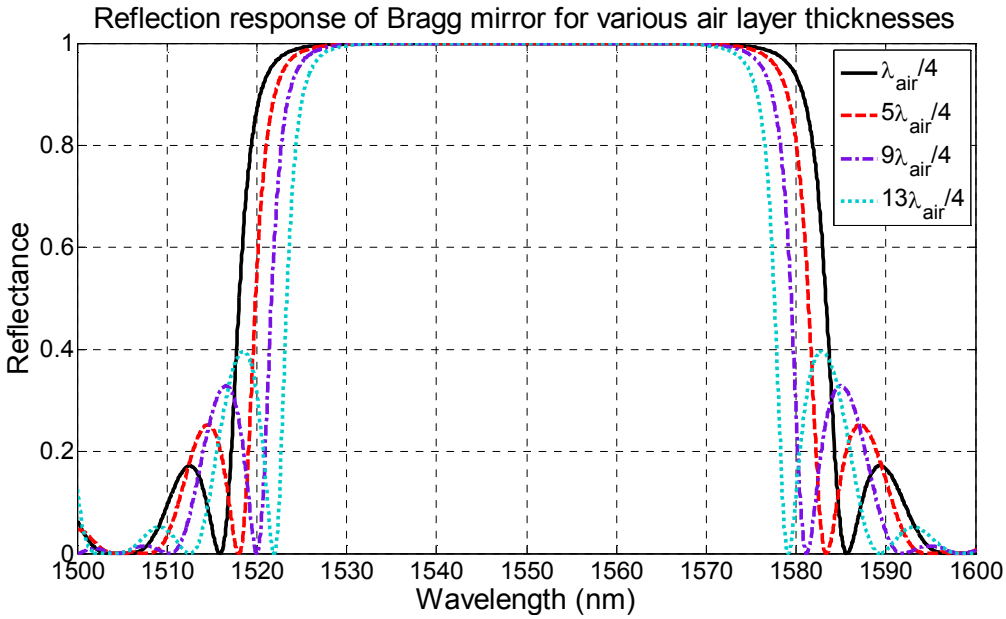

Fig. 3.7 Reflectance of 4 *HL* pairs for various *L* thicknesses, *H* thickness is fixed to $33\lambda_{Si}/4$

Another point of interest for the Bragg mirror is the technological error. The critical dimension, defined as the minimum feature size on the technology mask, can not be maintained as the original design and it translates into reduced layer thicknesses on the fabricated device. In fact, the thickness of the silicon layer may vary (increase or decrease) and the air layer follows the opposite trend (decreases or increases). Then, the device performance degrades. This issue is obvious in Fig. 3.8 where various error values are introduced into the mirror original design. We notice that the overall response shifts toward the left side as the error decreases from 100 nm to -100 nm in steps of 50 nm. Comparing the obtained responses to the error free design, we see that the mirror reflectance might turn from 99.98 % ideally to 0.6 % for an introduced error = ± 100 nm which means that the multilayered designs are not tolerant to fabrication errors in exceeding 50 nm.

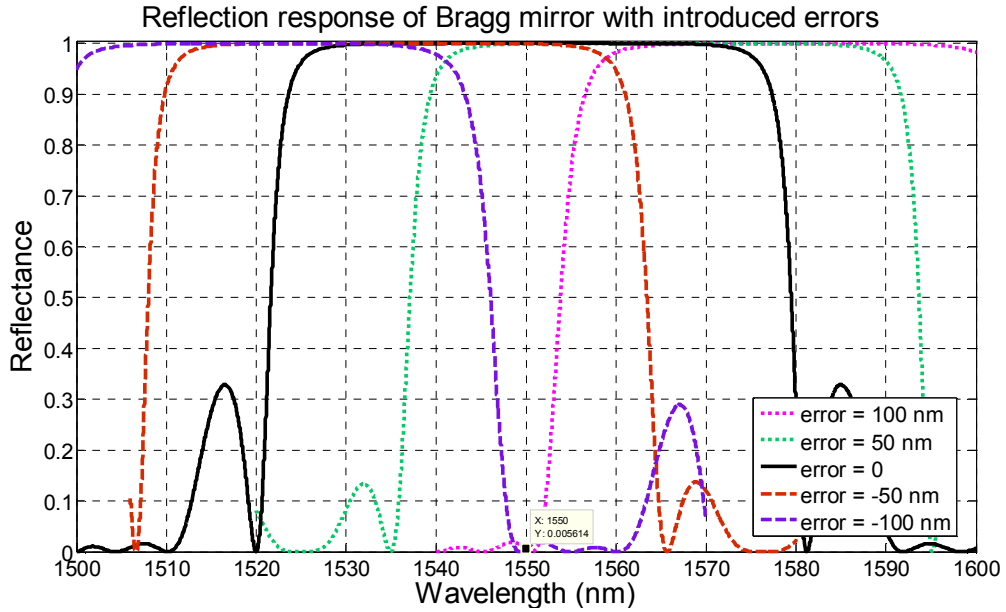

Fig. 3.8 Reflectance of 4 *HL* pairs for *L* thicknesses = $9\lambda_{air}/4$, *H* thickness = $33\lambda_{Si}/4$ and several introduced errors.

3.3.4 Modeling and Simulation FP cavity based on Bragg mirrors

If instead of the stack of high reflectance mirror, we introduce a gap layer whose thickness is an integer number of half the wavelength then the characteristic matrix [M] of this layer becomes:

$$[M] = \pm \begin{bmatrix} 1 & 0 \\ 0 & 1 \end{bmatrix} \tag{3.45}$$

Thus, we can easily get a Fabry-Perot (FP) resonator if we combine 2 stacks of quarter wavelengths thick acting as high reflectance mirrors separated by a gap layer of half wavelength thick.

In the next part, we illustrate, by the help of MATLAB simulations, the properties of such FP resonators where we study the impact of several parameters on the resonator spectral response. Parameters of particular interest for this comprehensive study: the mirror reflectance controlled by the number of Bragg layers per mirror, the impact of technological errors and the cavity gap length. In what follows, unless otherwise stated, we consider that the silicon Bragg layers of thickness = 3.67 µm ($33\lambda_{Si}/4$), the air Bragg layer has a thickness of 3.49 µm ($9\lambda_{air}/4$) and the gap layer has a width = 10.075 µm ($13\lambda_{Si}/2$). The silicon refractive index n_{Si} is taken = 3.478 and all the layers are considered absorption free.

We start our study by increasing gradually the number of Bragg layers. As shown in Fig. 3.9 , we found that the FWHM of the resonator decreases from 7.6 nm for single Si layer/mirror, to 0.56 nm for double Si layer/mirror, to 0.046 nm for 3 Si layers/mirror and finally the FWHM becomes 0.004 nm for 4 Si layers/mirror. This is due to the increase in the mirror reflectance which goes from 71.8 % for single layer to 99.98 % for 4 Si layers. Also, the contrast improves and the minimum level goes from -10 dB up to -70 dB and the resonator sharpness improves as well.

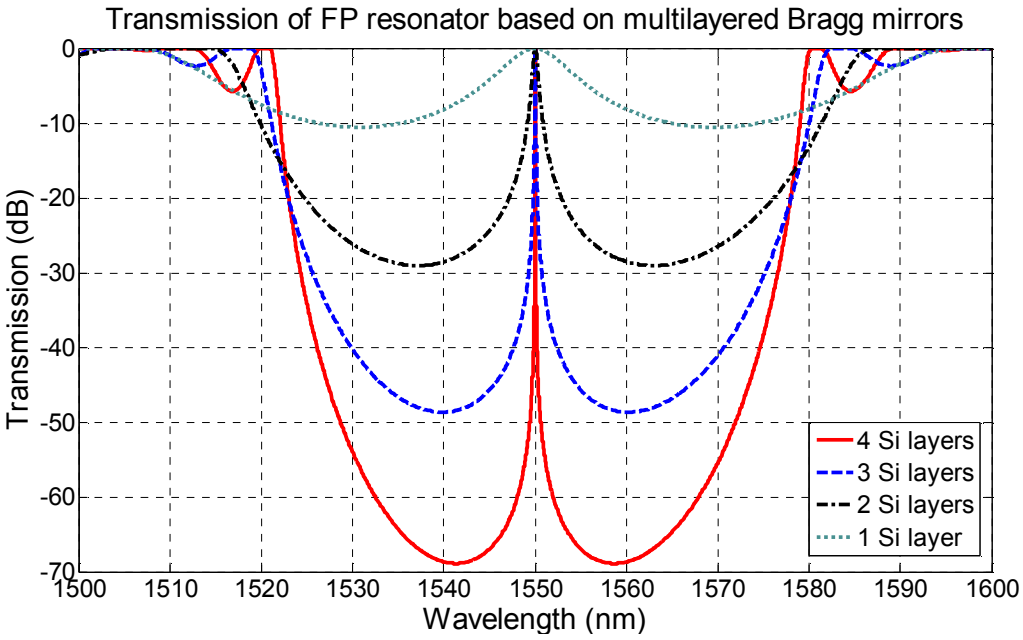

Fig. 3.9 Transmission of FP resonator for different number of silicon layers per mirror.

Now, if we consider the case of 4 Si layers/mirror with introduced errors (ε) therein, we obtain the curves shown in Fig. 3.10 .We notice that the central wavelength λ_0 shifts from 1550 nm by ±8.5 nm as ε = ± 50 nm. For ε = ± 100 nm, λ_0 shifts by 18.15 nm. In addition, the FWHM of the peak increases from 0.004 nm for the error free case to 0.007 nm for ε = ± 50 nm and it reaches 0.029 nm for ε = ±100 nm. This might be explained by reference to previous simulations carried on Bragg mirrors with introduced errors. As mentioned earlier, the overall response of the mirror shifts right (left) as error increases (decreases) and this is the reason underlying the shift in the resonance wavelength. In addition, the maximum reflectance of the mirror decreases from 99.98 % (in the error free case) to 99.97 % (for ±50 nm error) to 99.93 % (for ±100 nm), that's why the FWHM increases.

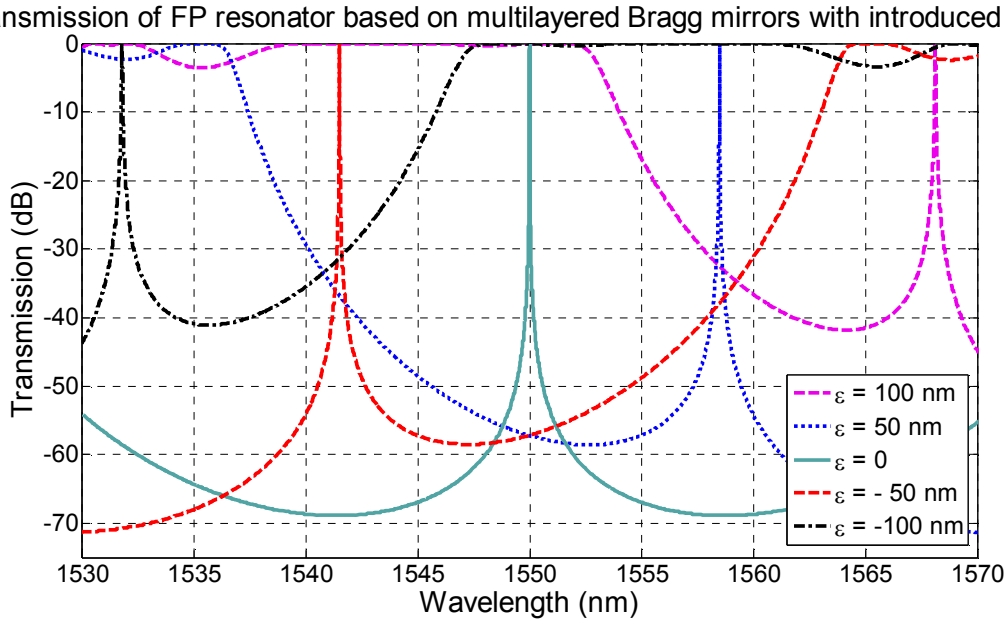

Fig. 3.10 Transmission of FP resonator for different errors.

By scanning over the wavelength for the cases of ε = -50 nm and ε = -100 nm, we notice that other resonance peaks, with larger FWHM and reduced contrast, appear in the spectral response of the cavity. This result seems strange and it does not go in accordance with the designed FSR for the error free cavity. In fact, the designed cavity gap length = 10.075 μm corresponding to a quasi FSR = 119.2 nm and a resonance wavelength = 1550 nm.

This issue might be explained by looking over the reflection response of the Bragg mirrors with introduced errors as shown in Fig. 3.11, we find that they are shifted as compared to the error free design. Moreover, they exhibit a non-negligible reflectance between 1575 nm and 1600 nm and so the design performs as a good resonator.

Analyzing the simulation results, we come out with a new definition for the cavity length named: The effective length L_{eff}. This new parameter suggests that the effective reflecting interfaces of the resonator lie inside the Bragg reflectors and not between the inner interfaces as conventionally thought and so it gives rise to unexpected resonances within the quasi FSR. Making inverse calculations for the

simulation results shown in Fig. 3.12, we find that for ε = -50 nm, the FSR = 52.15 nm corresponding to L_{eff} = 23 μm and for ε = -100 nm, the FSR = 47.7 nm corresponding to L_{eff} = 25.18 μm.

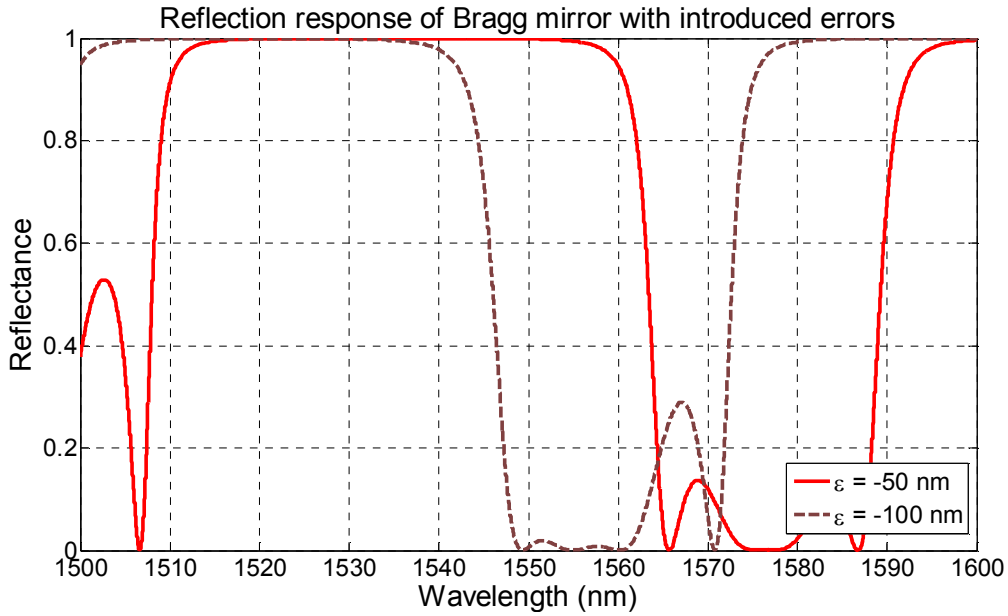

Fig. 3.11 Reflection response of Bragg mirrors for errors = -50 nm and -100 nm.

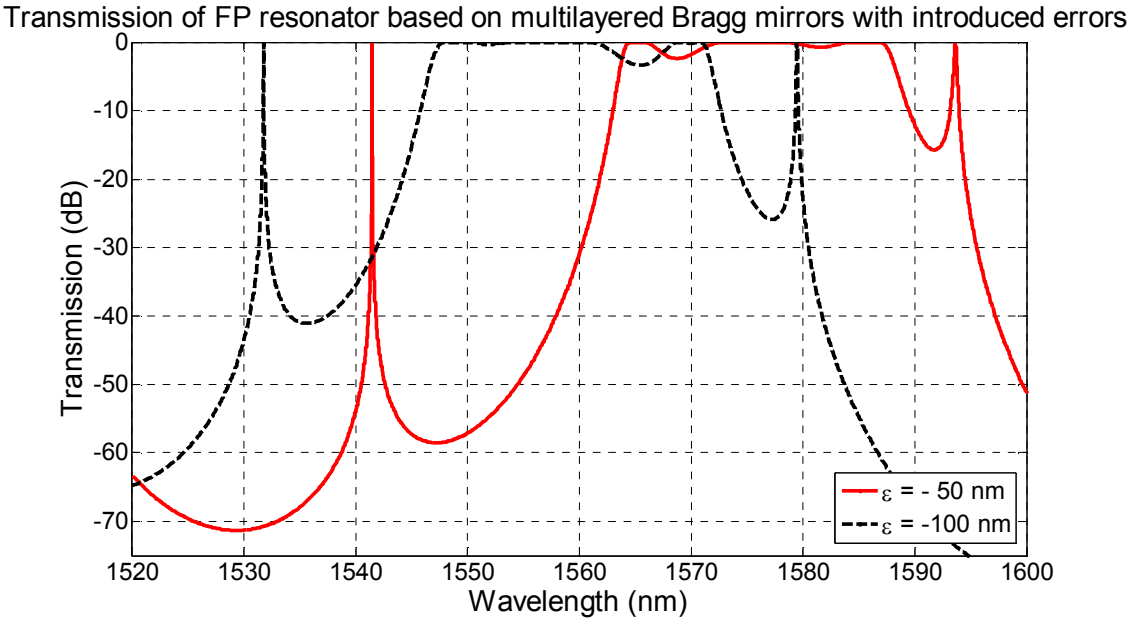

Fig. 3.12 Zoom out on the transmission response of FP resonator for errors = -50 nm and -100 nm.

3.3.5 Multilayered Si-Air structures for Anti-Reflection purposes

Antireflection surfaces (usually obtained through additional material coatings) can be obtained also from silicon micromachinned Bragg structures. They can range from a simple single layer having virtually zero reflectance at just one wavelength, to a multilayer system of more than a dozen layers, having virtually zero reflectance over a range of several octaves. The type used in any particular application will depend on a variety of factors, including the substrate material, the wavelength region,

the required performance and the cost. There is no systematic method for the design of antireflection coatings. Trial and error assisted by approximate techniques and by accurate computer calculation, is frequently employed. Very promising designs can be further improved by computer refinement. Several different approaches can be used in designing AR coating. In this section, we will limit our discussion to the single layer design only. Complicated analytical formulas can be derived for the case of multilayer coating and they lie outside the scope of this work so they will not be presented.

The vast majority of antireflection coatings are required for matching an optical element into air. The simplest form of antireflection coating is a single layer. Consider Fig. 3.13. Since two interfaces are involved, we have 2 reflected rays, each representing the amplitude reflection coefficient at an interface. If the incident medium is air, then, provided the index of the film is lower than the index of the substrate, the reflection coefficient at each interface will be negative, denoting a phase change of 180°. The resultant minimum is at the wavelength for which the phase thickness of the layer is 90°, that is, a quarter-wave optical thickness, when the two rays are completely opposed. Complete cancellation at this wavelength, that is, zero reflectance, will occur if the rays are of equal length. This condition, in the notation of Fig. 3.13, is

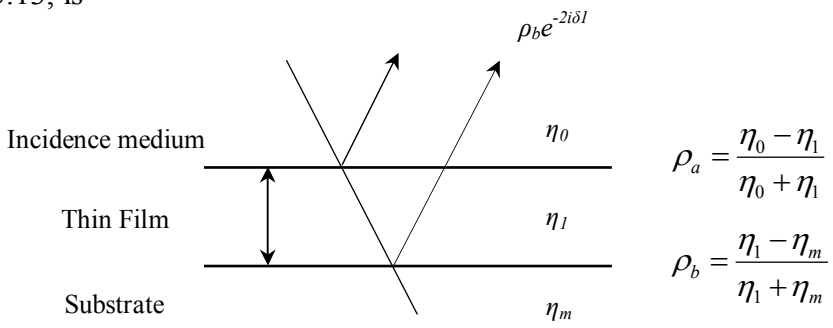

Fig. 3.13 Schematic illustration of substrate coated with a single film.

$$\frac{y_0 - y_1}{y_0 + y_1} = \frac{y_1 - y_m}{y_1 + y_m} \tag{3.46}$$

which requires:

$$\frac{y_1}{y_0} = \frac{y_m}{y_1} \tag{3.47}$$

$$\text{Or, } n_1 = \sqrt{n_0 n_m} \tag{3.48}$$

The condition for a perfect single-layer antireflection coating is, therefore, a quarter-wave optical thickness of material with optical admittance equal to the square root of the product of the admittances of substrate and medium. It is seldom possible to find a material of exactly the optical admittance which is required. If there is a small error, ε, in y_1 such that:

$$y_1 = (1+\varepsilon)\sqrt{y_0 y_m} \tag{3.49}$$

Then,

$$R = \left(\frac{-2\varepsilon - \varepsilon^2}{2 + 2\varepsilon + \varepsilon^2} \right)^2 \approx \varepsilon^2 \qquad (3.50)$$

provided that ε is small. A 10 % error in y_1, therefore, leads to a residual reflectance of 1 %.

Zinc sulphide has an index of around 2.2 at 2 μm. It has sufficient transparency for use as a quarter-wave antireflection coating over the range 0.4–25 μm. Germanium, silicon, gallium arsenide, indium arsenide and indium antimonide can all be treated satisfactorily by a single layer of zinc sulphide. There is thus no room for manoeuvre in the design of a single-layer coating.

In practice, the refractive index is not a parameter that can be varied at will. Materials suitable for use as thin films are limited in number and the designer has to use what is available. A more rewarding approach, therefore, is to use more layers, specifying obtainable refractive indices for all layers at the start, and to achieve zero reflectance by varying the thickness. Then, too, there is the limitation that the single-layer coating can give zero reflectance at one wavelength only and low reflectance over a narrow region. A wider region of high performance demands additional layers.

3.3.6 Tilted FP cavity as a Notch Filter

In this part, we focus on another interesting application for devices based on Bragg structures. In particular, we study FP cavity based on multilayered mirrors but under oblique incidence [6]. The device design differs from the case of normal incidence since the rays will propagate obliquely in the layers and the optical thicknesses for both the silicon and the air layers shall be calculated differently. In this case, we must ensure that $\delta = m\pi/2$ to obtain the same matrix as in equation (3.41), and then we will solve the problem inversely to get the corresponding thicknesses $H(L) = d_{Si(Air)}$ which yields:

$$\delta_{Si(air)} = \frac{2\pi n_{Si(air)} d_{Si(air)}}{\lambda_0} \cos\left(\theta_{Si(air)}\right) = \frac{m\pi}{2} \qquad (3.51)$$

$$d_{Si(air)} = \frac{m\lambda_0}{4 n_{Si(air)} \cos\left(\theta_{Si(air)}\right)} \qquad (3.52)$$

Using equation (3.52), we will consider $H=d_{Si}$= 3.76 μm using odd multiple m = 33 and $L=d_{Air}$ = 3.84 μm using the odd multiple m = 7. In the upcoming simulations, we will take the thickness of the HL layers as mentioned previously. For the gap thickness G under oblique incidence, we have to satisfy the condition $\delta = m\pi$. By following the same analytical treatment as before, we will get:

$$G = \frac{m\lambda_0}{2 n_{air} \cos\left(\theta_{air}\right)} \qquad (3.53)$$

So, we will consider G = 14.25 μm using odd multiple m = 13.

The studied architecture consists of two stacks of tilted Bragg mirrors separated by an air gap layer. While the FP configuration with normal incidence works only in transmission, the tilted architecture, shown in Fig. 3.14, allows working either in transmission or in reflection. In the case of tilted FP, it behaves as a notch filter, suitable for dropping a particular wavelength. This is due to the 45° tilt angle of the cavity with respect to incident light.

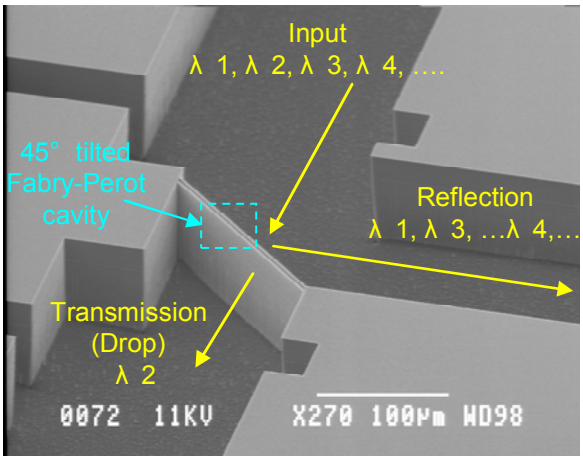

Fig. 3.14 45° tilted FP filter made of two Si layers separated by an air gap [6]

Simulating a structure based on the parameters stated above, we obtain the results shown in Fig. 3.15 and Fig. 3.16. As obvious, the FWHM of the filter reduces as the number of Silicon layers/mirror increases as it translates into higher reflectance. This device might have good potential in WDM systems where it can be used as an Add-Drop multiplexer. Also, it might be of interest for application involving tunable lasers as will be detailed in the next section of this chapter.

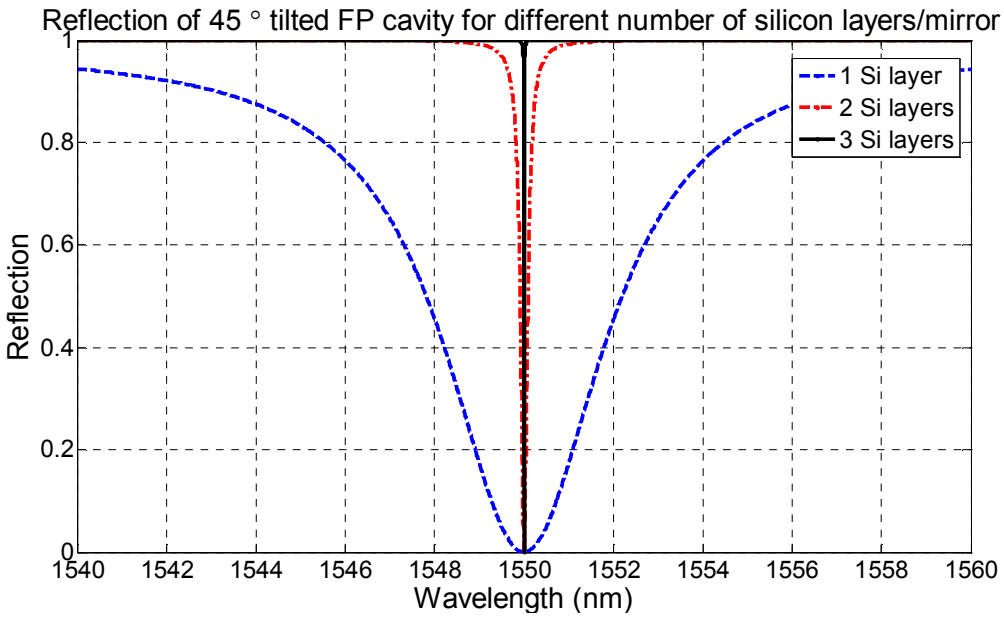

Fig. 3.15 Reflection response of tilted FP cavity for different number of silicon layers/mirror

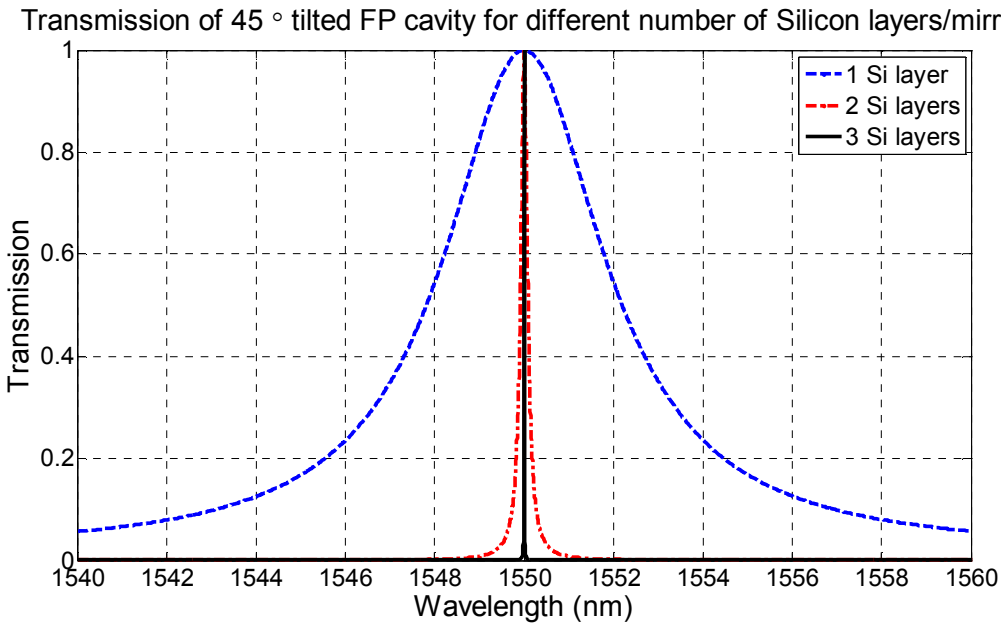

Fig. 3.16 Transmission response of tilted FP cavity for different number of silicon layers/mirror

Simulation results show that the FWHM decreases from 4.5 nm for the single silicon layer to 0.18 nm for the double layer design and it exhibits further decreases to 0.008 nm for the triple layer design.

Now, if we consider a tilted FP cavity with mirrors of HLH configuration but with different angles of incidence, we obtain a spectral response with a shift in the resonance wavelength as illustrated in Fig. 3.17. Varying the angle of incidence by 0.5° around 45° results in 9 nm shift of the resonance wavelength. Then, proper design for rotational actuator to integrate with the tilted cavity, suggests the use of the whole package as a MEMS tunable filter. The next section highlights the potential of the tilted FP cavity in tunable laser source module.

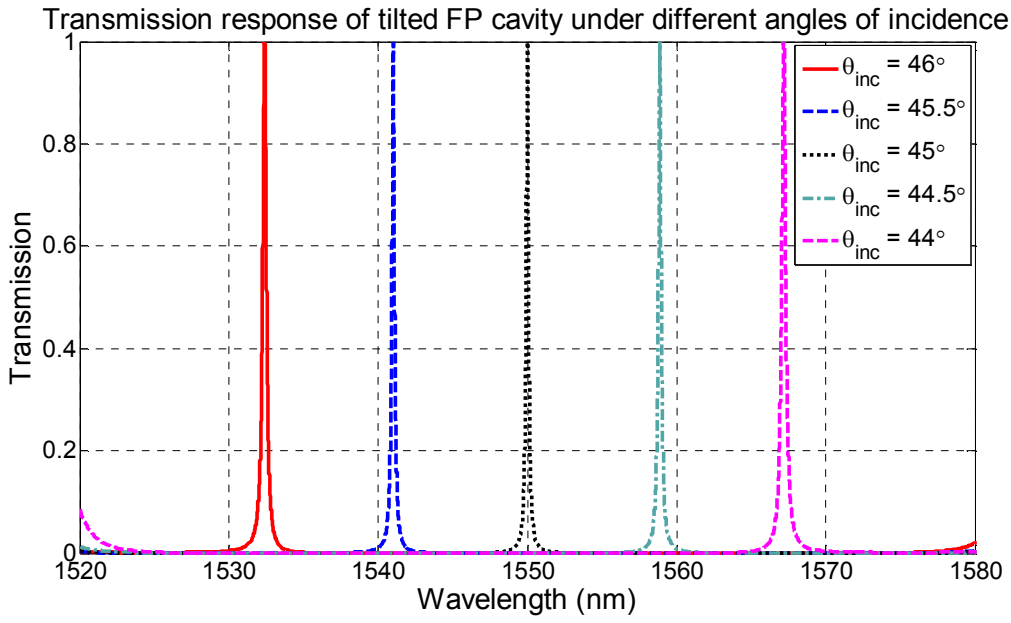

Fig. 3.17 Transmission response of tilted FP cavity in HLH configuration under different angles of incidence

A last point to mention about the tilted FP cavity is the sensitivity of the design to fabrication errors. Considering a HLH combination for both mirrors, and introducing errors from 100 nm down to -100 nm in steps of 50 nm, we notice from Fig. 3.18 that the resonance wavelength shifts by about ±7 nm for an increase of ±50 nm. Also, the FWHM increases from 0.18 nm for the error free design to 0.25 nm for an introduced error of 50 nm. It reaches 0.55 nm for an introduced error of 100 nm. Thus, the structure is not tolerant very to fabrication errors and the filter shall be designed, fabricated and tested carefully before integration into optical systems.

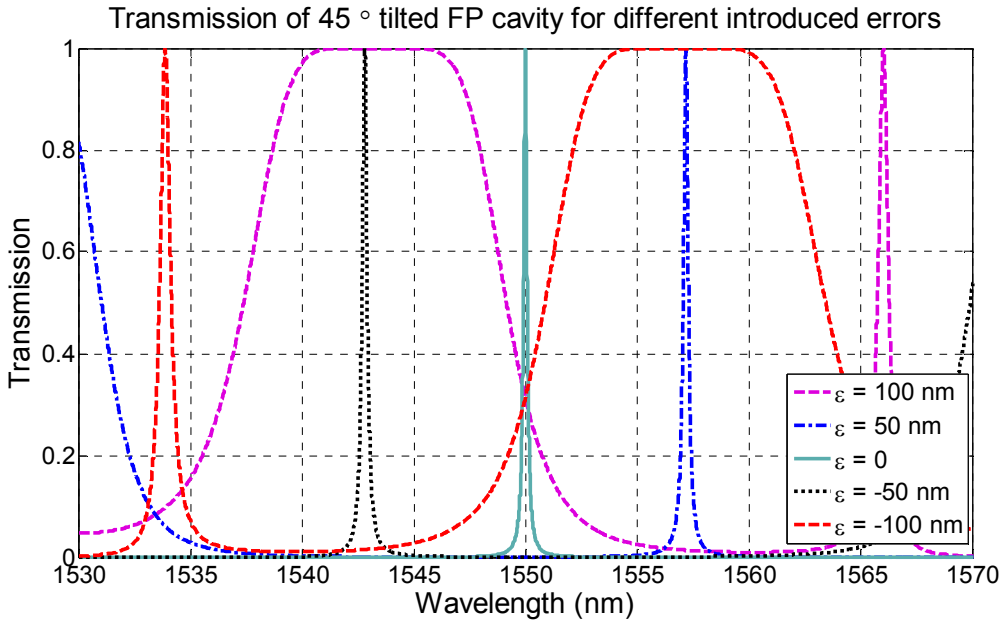

Fig. 3.18 Transmission response of tilted FP cavity for FP cavity with HLH mirror for different errors.

3.3.7 Tilted FP cavity as a Mode Selector

By completing the architecture surrounding the tunable tilted FP cavity with an active laser cavity and an external mirror, then we obtain a compact tunable laser by tuning the angle incident upon the tilted FP cavity. As mentioned above, the tuning might be achieved by rotating the tilted FP. Tilted FP cavities are of special interest, since they reject undesirable wavelengths off the optical axis. Therefore, they appear as interesting candidates for mode selection in external cavity tunable lasers. Indeed, as these types of lasers exhibit a competition between several longitudinal modes, there is a need for a mode selection mechanism in order to obtain single mode operation and avoid mode hopping during tuning. The main interest in using tilted FP etalon rather than a FP cavity with normal incidence is to avoid parasitic reflections due to additional FP cavities that appear when adding the mode selector. Fig. 3.19a illustrates the principle of the mode selector based on a 45° tilted FP cavity. The corresponding simulated transmission is shown as well, which confirms the operation principle. It is worth mentioning that the performed simulation is very basic, since it does not take into account losses. In particular,

plane waves are considered here rather than Gaussian beams. Figs. 3.19b and Fig. 3.19c illustrate simulations of parts of the architecture.

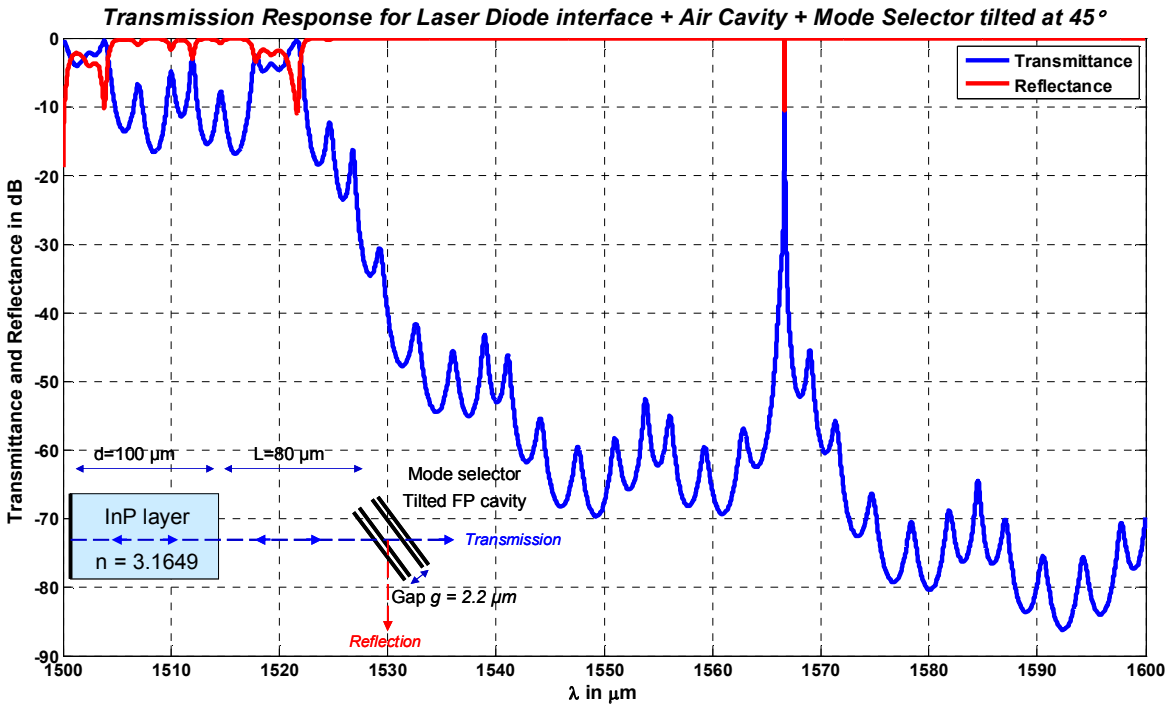

(a)

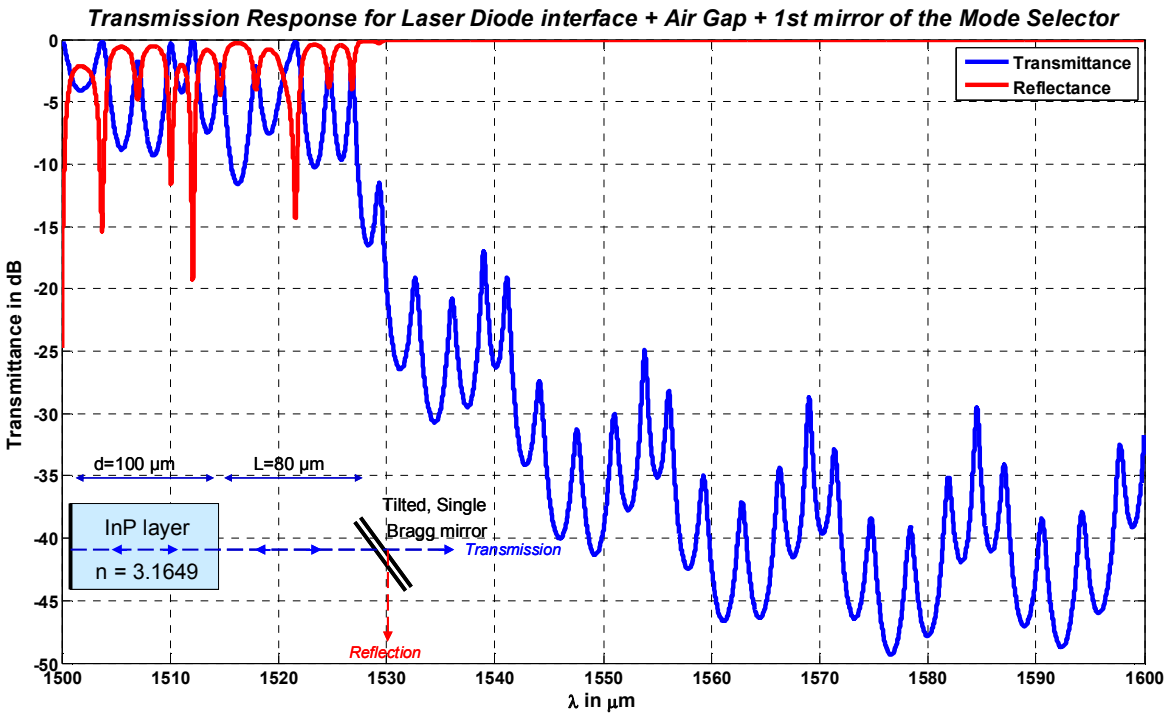

(b)

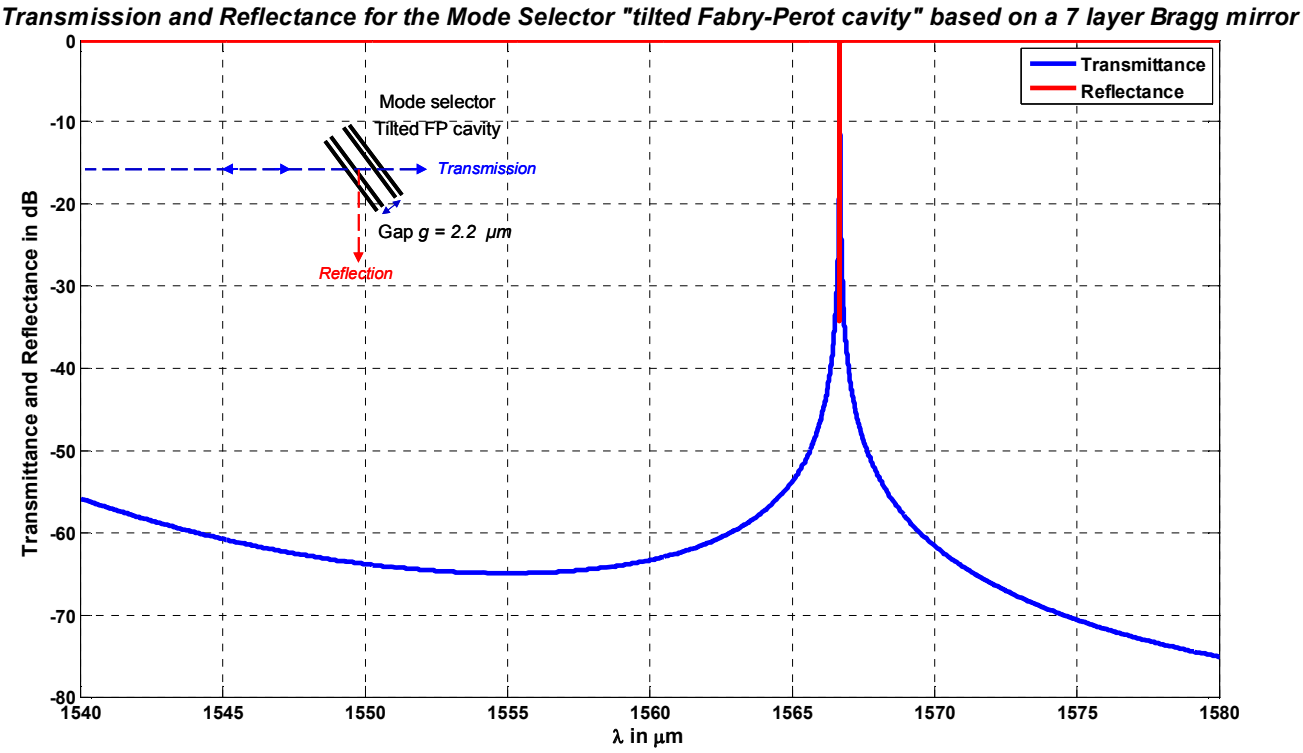

(c)

Fig. 3.19 Tilted FP etalon as a laser mode selector. Whole systems (a) and parts of the system (b) and (c)

Tuning is achieved either by rotating the cavity further or by controlling its gap g, as shown in Figs. 3.20a and 3.20b. Tuning range of 30 nm is shown as the result of gap tuning of 150 nm. The increase in the separation distance L doesn't affect the peak position as shown in Fig. 3.20c.

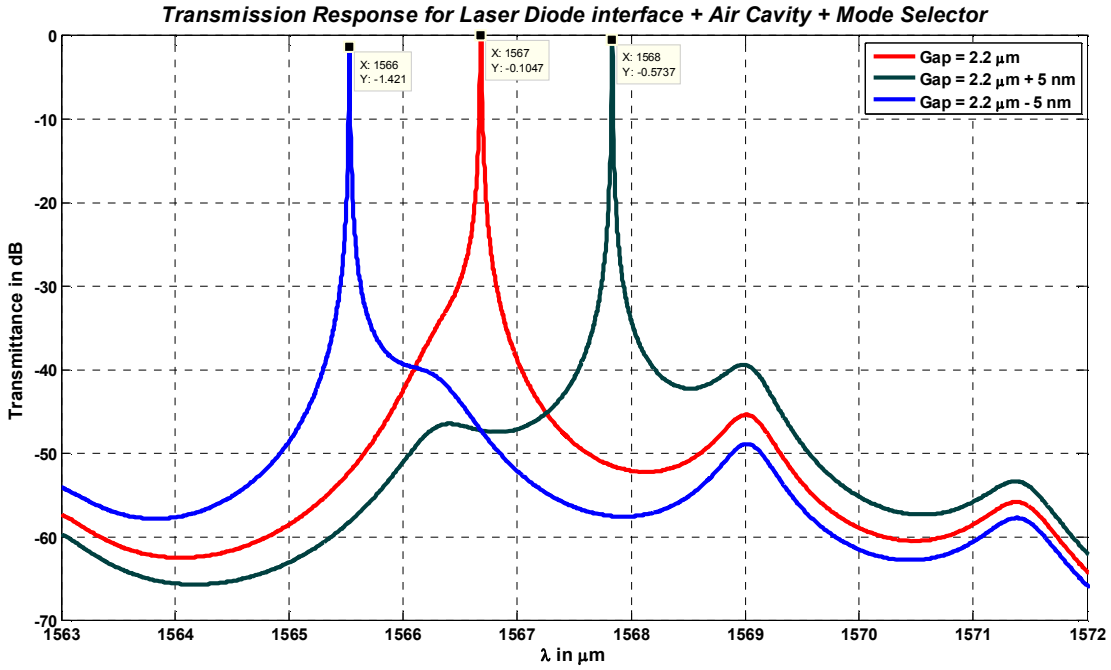

(a)

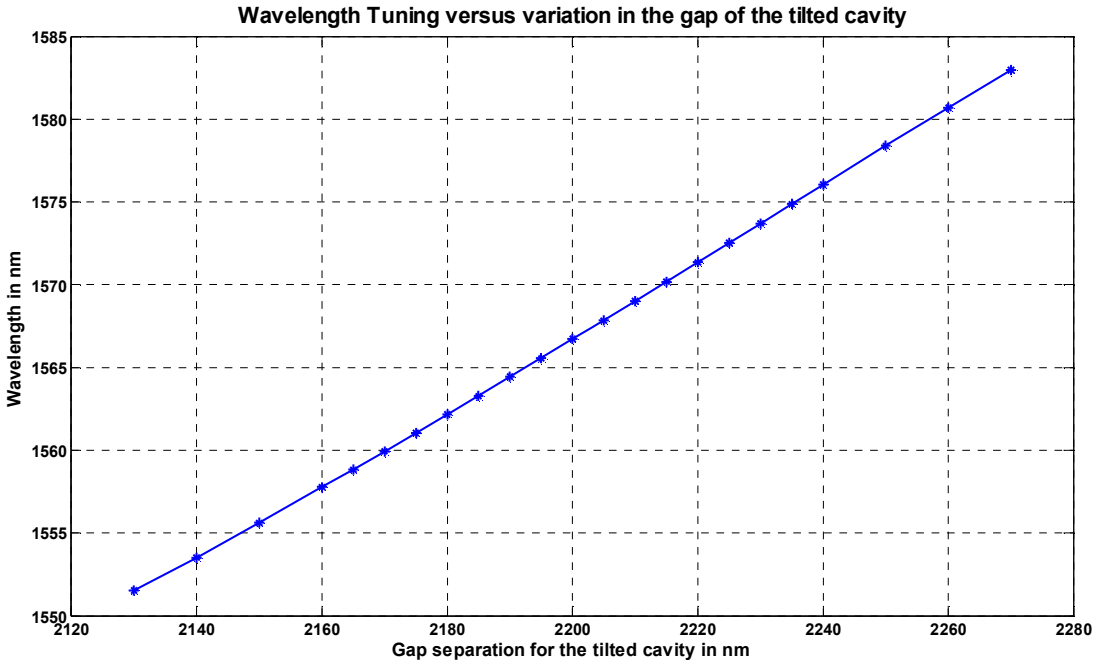

(b)

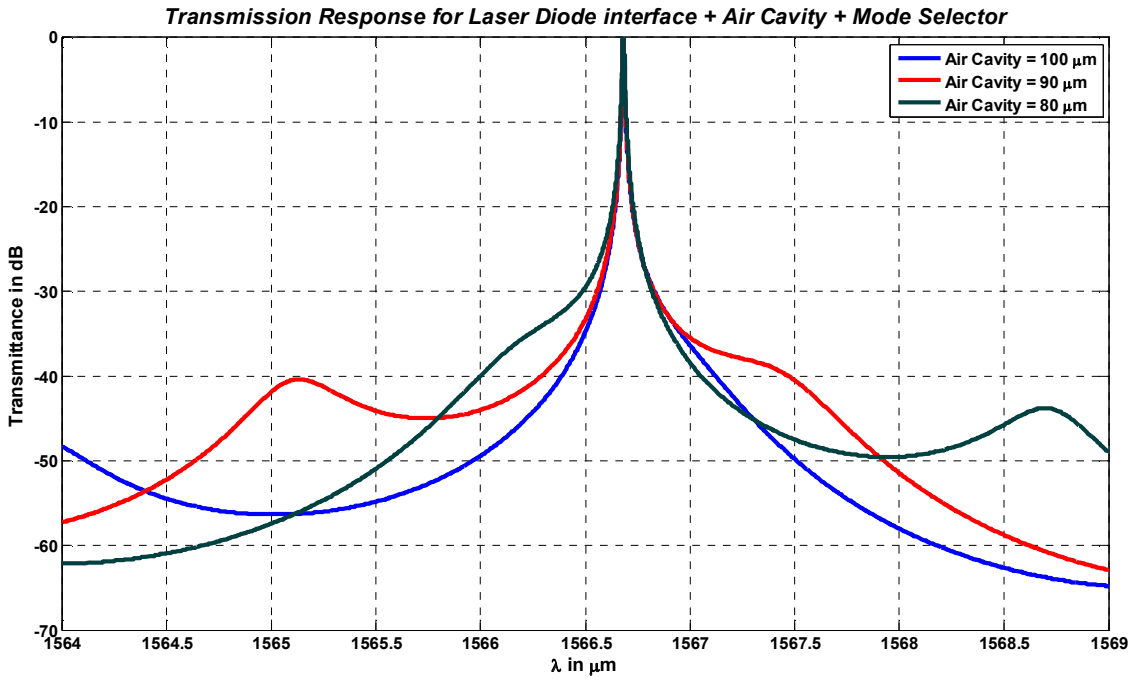

(c)

Fig. 3.20 (a) and (b) Simulated wavelength tuning by control of the gap g of the tilted FP cavity (c) no wavelength shift is noticed when varying the distance L between the mode selector and the InP layer.

3.3.8 Other applications

Other applications involving multilayered structures are non-numerous; among these we can cite the beam splitter of controlled characteristics. This discussion is left for chapter 8 of this thesis where it will be described in details.

3.4 Conclusion and Perspectives

In this chapter, a rigorous model for the multilayer stack theory has been presented. It constitutes the tool used for the design and the modeling of the structures introduced in the next chapters of this thesis. Various simulations have been carried to study the impact of the geometrical parameters (thickness, number of Bragg layers and tilt angle) and the technological errors on the device performance. The chapter is concluded with a case of study: The mode selector which is the tilted FP cavity based on vertical Bragg mirror. The device is simulated together with a laser source using the theory presented earlier in order to evaluate the performance aspects of the device.

PART II

Optical Microresonators with Curved Surfaces

Chapter 4

Novelty of Our Approach

4.1 Introduction to curved resonators

The early versions of FP microcavities, including those with silicon-air Bragg mirrors (cf. 3.3.1), comprised two *planar* mirrors separated by the cavity gap length L. Due to its Gaussian nature, light undergoes many round trips between the mirrors while expanding before eventually getting out of the micromirrors boundaries due to their short heights, limited to a few tens of micrometers. In the same time, light also encounters diffraction effects at the mirrors boundaries.

Planar resonators are therefore referred to as *unstable resonators*. Hence, FP cavities with planar mirrors, as shown in Fig. 4.1a, are not optimal regarding loss since the diverging light rapidly escapes the cavity after some round-trips. This effect is responsible of the reduced quality factor observed in planar micromirrors and it forces the designer to reduce the cavity length to few tens of microns to avoid excessive losses. Earliest reports about FP cavities based on spherical mirrors, shown in Fig 4.1b, demonstrate their excellent focusing capability. The curvature of the mirror focuses the beam in both transverse directions. Unlike FP cavities with planar mirrors, such resonators are considered as *stable resonators* because they prevent the light escape from the cavity boundaries. They were generally implemented from metallic gold plated spherical mirrors to maintain a high reflectance and hence, a spectral response with high finesse. Albeit their high performance, the spherical resonators are difficult to realize practically since current microfabrication technologies set limitations on the realization of in-plane spherical surfaces only.

4.2 Novelty of the proposed architectures: Simple curved cavities, FRL cavities

In this work, we propose two architectures to overcome the limitations of planar FP cavities. The first architecture is inspired from the spherical resonators where we develop a similar design but using curved mirrors of cylindrical shape, which can be obtained on silicon by DRIE. Thus, we go one step forward over the planar resonators by curving the mirrors along one transverse plane to provide stability. Furthermore, we introduce silicon-Air Bragg reflectors of cylindrical shape to provide high reflectance as well. Hence, by introducing silicon-air Bragg reflectors of cylindrical shape in this first design, we reduce the issue of loss along one transverse direction only, while maintaing highly reflective mirrors, as schematically depicted in the inset of Fig. 4.1c. The resulting cylindrical mirror might be considered as a concave lens whose optical axis, z, is in the plane of the silicon surface; it has a focusing capability in the x direction parallel to the plane of the silicon wafer. In the out-of-plane, y

direction, the cavity behaves like an ordinary planar mirror and the beam therefore diverges along this y direction. This first design offers the advantage of having a much simpler geometrical layout, which makes it suitable for a detailed analysis with appropriate theoretical modeling. Analytical modeling is accessible for the purpose of comparing between experimental results and simulations. Indeed, such comparison appeared to be very useful for a better understanding of the depicted behavior of selective mode excitation as described in chapter 5.

Furthermore, in the second architecture, we introduce an alternative solution to the spherical mirrors configuration where a Fiber Rod Lens (FRL) is used to provide light confinement in the out-of-plane direction, as shown in Fig 4.1d leading to a complete solution for light confinement. This complements the in-plane confinement achieved thanks to the cylindrical mirrors, to focus the beam in both transverse planes. This way, we emulate the spherical resonators using two discrete elements: The same curved cylindrical mirror, as in the first architecture, and the FRL, curved in the other transverse plane, which helps reducing the cavity losses and improves the *Q*-factor as detailed later in chapter 6.

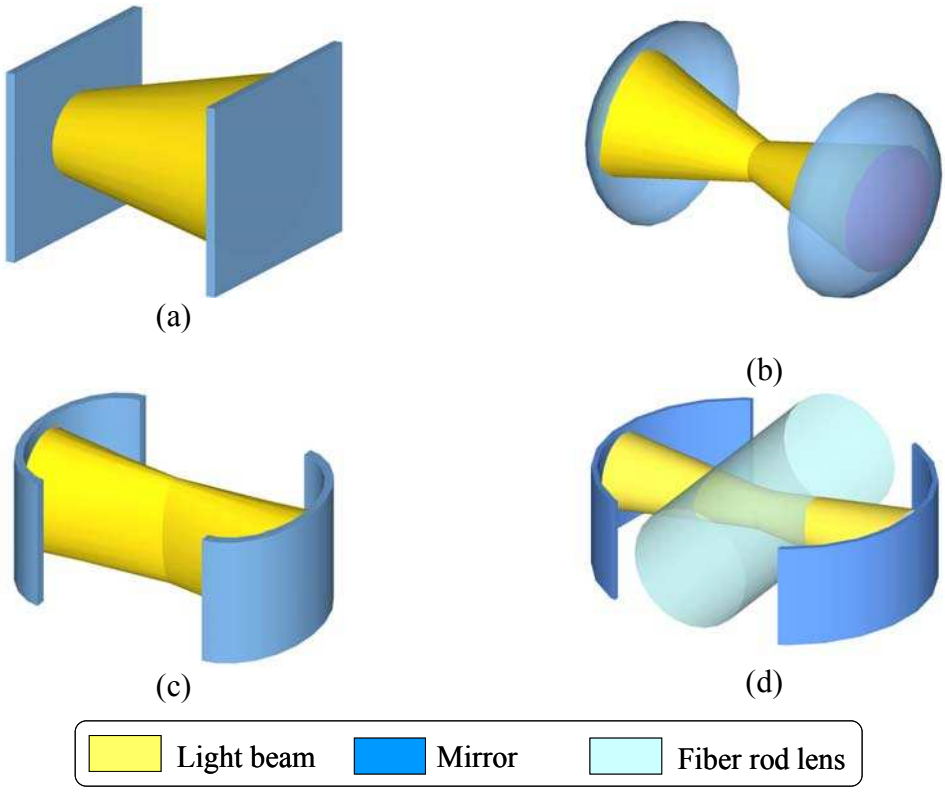

Fig. 4.1 Schematic representation of Fabry-Perot architectures with different mirror shapes: (a) Planar mirrors, (b) Spherical mirror providing 2D-confinment of light, (c) Cylindrical mirrors providing 1D-confinment of light and (d) Cylindrical mirrors combined with a fiber-rod-lens, also providing 2D-confinment of light as in case (b).

Chapter 5

Optical Resonator Architecture Based on Cylindrical Bragg Mirrors

5.1 Introduction

As discussed earlier, conventional *in-plane* FP silicon microcavities, based on planar mirrors, were extensively studied [6-9, 16, 20, 80-82] but such cavities are known to be unstable due to unavoidable losses. In fact, when considering a Gaussian beam, launched from a (lensed) optical fiber into the cavity, the beam spot size continuously expands after each round trip and eventually escapes the resonator boundaries (Fig. 5.1a). This issue forces the designers to limit the cavity length to only a few tens of microns, as larger length implies higher losses, leading to rather poor performance. However, when considering curved mirrors whose radii of curvature fits the wavefront radius of curvature of the beam at specific locations, then light bounces back and forth without divergence (Fig. 5.1b), leading to the desired confinement.

(a) (b)

Fig. 5.1 Illustration of Gaussian beams properties in FP cavity (a) expansion of the spot size after single reflection by planar mirror (b) confinement of the beam after multiple reflections by curved mirrors, whose radii of curvature fits with the beam radius of curvature at the specific mirror locations.

Therefore the concept idea consists first of replacing the planar mirrors by cylindrical Bragg mirrors that act like focusing lenses in the in-plane direction (Fig. 5.2). In the out-of-plane direction, the cavity behaves as an ordinary FP cavity with planar mirrors. In theory, an FP cavity with spherical mirrors (Curved in both in-plane and out-of-plane directions) would be the best choice for its focusing capability in both directions. In principle, such 3D surfaces can be obtained by silicon micromachining [84]. However, when considering in-plane propagation of light, the technological challenge becomes much higher.

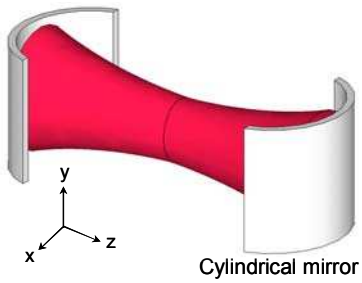

Fig. 5.2 Proposed architectures of Fabry-Pérot micro-resonators with free-space propagation of light and confinement by cylindrical mirrors to insure in-plane 1D confinement.

5.2 Theory and modeling of the curved cavities

5.2.1 Theoretical Background on spherical resonators: Applicability to cylindrical resonators

The Gaussian beam is not the only solution to the paraxial Helmholtz equation(5.1) [78] (refer to ch2 for a detailed discussion about Gaussian beams). There are may other solutions including beams with non-Gaussian intensity distributions. Of particular interest are the beams that have a paraboloidal wavefronts like the Gaussian beams. Beams of paraboloidal wavefronts are important since they match the curvature of spherical mirrors of large radius. They can therefore reflect between two spherical mirrors that form a resonator without being altered. Thus, they form the modes of the resonator, whose complex envelope A obeys the following relation (cf. eq. 2.33 in chapter 2).

$$\left(\frac{\partial^2}{\partial x^2}+\frac{\partial^2}{\partial y^2}\right)A-i2k\frac{\partial A}{\partial z}=0 \tag{5.1}$$

Consider a wave whose complex envelope is modulated version of the Gaussian beam A_G such that:

$$A(x,y,z)=X\left[\sqrt{2}\frac{x}{W(z)}\right]Y\left[\sqrt{2}\frac{y}{W(z)}\right]\exp\left[jZ(z)\right]A_G(x,y,z) \tag{5.2}$$

where *X(-), Y(-)* and *Z(-)* are real functions. The wave, if it exists, has the following 2 properties:

- The phase is the same as that of the underlying Gaussian wave, except for an excess phase *Z(z)* that is independent of x and y. If *Z(z)* is a slowly varying function of z, the two waves have paraboloidal wavefronts with the same radius of curvature *R(z)*. These two waves are therefore focused by thin lenses and mirrors in precisely the same manner.
- The magnitude given by:

$$A_o X\left[\sqrt{2}\frac{x}{W(z)}\right]Y\left[\sqrt{2}\frac{y}{W(z)}\right]\left[\frac{W_o}{W(z)}\right]\exp\left[-\frac{x^2+y^2}{W^2(z)}\right] \tag{5.3}$$

  where $A_o = A_l/jz_o$, is a function of *x/W(z)* and *y/W(z)* whose widths in the x and y directions vary with z in accordance with the same scaling factor *W(z)*. As z increases, the intensity distribution in the transverse plane remains fixed, except for a magnification factor *W(z)*. This distribution is a Gaussian function modulated in the x and y directions by the functions $X^2(-)$and $Y^2(-)$.

Now, substituting into (5.1) and using the fact that A_G satisfies (5.1), we get:

$$\frac{1}{X}\left(\frac{\partial^2 X}{\partial u^2}-2u\frac{\partial X}{\partial u}\right)+\frac{1}{Y}\left(\frac{\partial^2 Y}{\partial \upsilon^2}-2u\frac{\partial Y}{\partial \upsilon}\right)+kW^2(z)\frac{\partial Z}{\partial z}=0 \tag{5.4}$$

where $u=\sqrt{2}x/W(z)$ and $\upsilon=\sqrt{2}y/W(z)$

Taking into account the conditions stated earlier, solution yields the Hermite polynomials:

$$X(u)=H_l(u) \text{ where } l=0,\ 1,\ 2,\ldots \tag{5.5}$$

$$Y(\upsilon) = H_m(\upsilon) \text{ where } m = 0, 1, 2,\ldots \tag{5.6}$$

$$\text{and } Z(z) = (l+m)\zeta(z) \text{ where } \zeta(z) = \tan^{-1}(z/z_0) \tag{5.7}$$

Note that: $H_0(u) = 1$, $H_1(u) = 2u$ and the recurrence relation is given by:

$$H_{l+1}(u) = 2uH_l(u) - 2lH_{l-1}(u) \tag{5.8}$$

Then, the complex amplitude turns to be:

$$A_{m,n}(x,y,z) = A_{m,n}\left[\frac{W_0}{W(z)}\right]H_m\left[\sqrt{2}\frac{x}{W(z)}\right]H_n\left[\sqrt{2}\frac{y}{W(z)}\right]\exp\left[-jkz - jk\frac{x^2+y^2}{2R(z)} + j(m+n+1)\zeta(z)\right] \tag{5.9}$$

Returning back to the problem of the cylindrical resonators and establishing an analogy between spherical and cylindrical resonators, we can say that the solution obtained here above can still be applied for our case. Actually, the cylindrical mirror is a spherical mirror with a single transverse dependence, let's say *x*, then the Hermite solution *X(u)* can be maintained. However, for the other transverse direction *y*, the mirror surface is planar and the solution is simply, a Gaussian beam (that is $m = 0$ corresponding to $H_m = H_0 = 1$).Accordingly, we can write:

$$\begin{aligned} A_{l,0}(x,y,z) = A_{l,0}&\left[\frac{W_0}{W(z)}\right]H_l\left[\sqrt{2}\frac{x}{W(z)}\right]\exp\left[-\frac{x^2}{W_x^2(z)} - \frac{y^2}{W_y^2(z)}\right] \\ &\times\exp\left[-jkz - jk\left(\frac{x^2}{R_x(z)} + \frac{y^2}{R_y(z)}\right) + j(l+1)\zeta(z)\right] \end{aligned} \tag{5.10}$$

Note than even the radius of curvature ρ_y for the cylindrical mirror along *y* direction tends to infinity, the corresponding radius R_y of the wavefront do not. It actually increases gradually as the number of reflections increases according to the expansion of the light beam.

5.2.2 Stability study

The stability of the device described in this chapter has been studied using the ray matrix formalism [78], so we will only outline the procedure followed and the results obtained. After inspection of the design, we find that the discrete elements that the ray encounters are basically:

1. Reflection from a concave mirror given by:

$$K_1 = \begin{pmatrix} 1 & 0 \\ -2/R & 1 \end{pmatrix} \tag{5.11}$$

R being the radius of curvature of the cylindrical mirror

2. Free space propagation region inside the cavity of length *L*, given by:

$$K_2 = \begin{pmatrix} 1 & L \\ 0 & 1 \end{pmatrix} \tag{5.12}$$

The equivalent matrix K_{eq} after a full round trip in the cavity is then given by:

$$K_{eq} = K_1 K_2 K_1 K_2 \tag{5.13}$$

Referring to chapter 2, we get the stability condition from the K_{eq} matrix:

$$0 \le \frac{L}{|R|} \le 2 \tag{5.14}$$

Thus the length "*L*" of a stable cavity should be limited to *2R*, which is actually the same limit as for spherical mirrors.

5.2.3 Resonator model

One can see from Fig. 5.3 that the light field injected by the input fiber undergoes three successive transformations with the corresponding power losses, when passing through the whole optical system before it propagates into the output fiber. The corresponding (power) transfer functions are used to build a complete model for studying the resonator behaviour. Obviously, it involves the multiplication of three different wavelength-dependent transmission coefficients, $T = \Gamma \,.\, H_{cav} .\, O$:

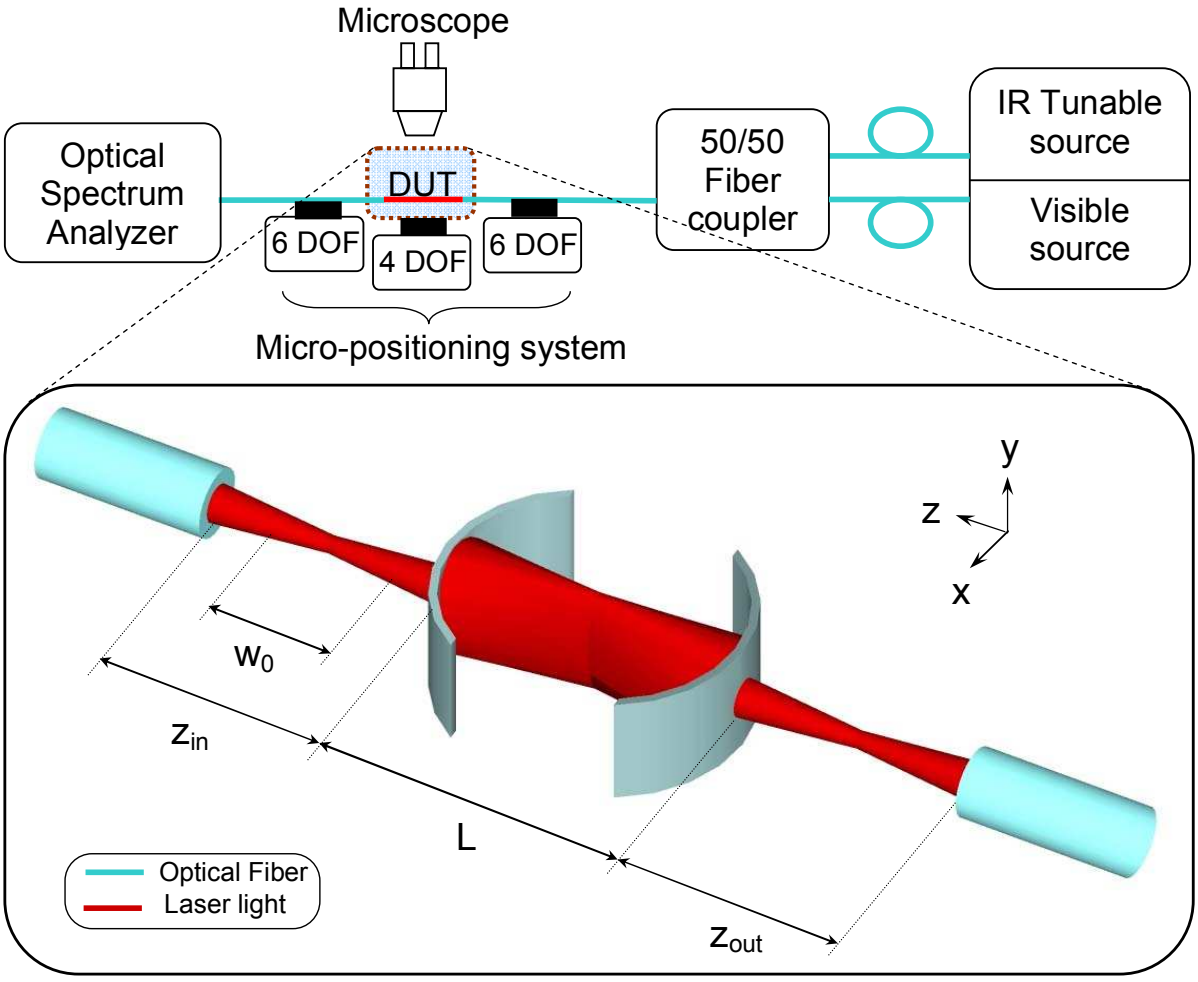

Fig. 5.3 Schematic representation of the measurement setup with an inset related to the arrangement of the curved cavity with respect to positions of the fiber input and fiber output.

(I) *Input coupling efficiency Γ:* this first term involves power coupling of the light field coming out from the input lensed fiber to the cavity entrance. The corresponding input coupling losses are described by the coefficient Γ, referred as the (input) coupling efficiency.

(II) *Cavity transmittance H_{cav}*: this second term describes the cavity response at the different resonance modes. It involves an intra-cavity round-trip coupling efficiency γ, as detailed below.

(III) *Output coupling efficiency O:* This third term concerns the coupling from the cavity to the output fiber.

Since the chosen output fiber can accommodate spot sizes up to 56 µm, it has good collection efficiency and its output coupling efficiency O can be considered very close to unity: $O \sim 1$. Therefore the overall transfer function of the power transmittance T is obtained by the product $T = \Gamma \, . \, H_{cav}$.

Before presenting the experimental results and details about theoretical analysis, we highlight the basic assumptions:

(a) E_{Fiber} is the transverse component of the electromagnetic field injected from the lensed fiber and is considered as a pure Gaussian beam that is given by:

$$E_{Fiber}(x,y,z=0) = \sqrt{\frac{\sqrt{2}}{w_x w_y}} \, e^{-\left(\frac{x^2}{w_x^2}+\frac{y^2}{w_y^2}\right)} \, e^{-jk\left(\frac{x^2}{2R_x}+\frac{y^2}{2R_y}\right)} \tag{5.15}$$

(b) $\Psi_{m,n}$ denotes the electric field transverse components representing the cavity electromagnetic resonant modes. The cavity, case of study, is supposed to support Hermite-Gaussian transverse modes $\Psi_{m,n}$ [85], which are the typical modes of resonators made from spherical mirrors and whose analytical expression was adapted here to the cylindrical shape of the mirrors. The degeneracy applies for order m only, along the x direction, while the fundamental (order $n=0$) Gaussian mode profile is kept along the y direction. Hereafter, we therefore consider only the transverse part of the modes supported by the cylindrical cavity:

$$\Psi_{m,0}(x,y) = \sqrt{\frac{\sqrt{2}}{w_x w_y}} \, H_m\left(\frac{\sqrt{2}\,x}{w_x}\right) \, e^{-\left(\frac{x^2}{w_x^2}+\frac{y^2}{w_y^2}\right)} \, e^{-jk\left(\frac{x^2}{2R_x}+\frac{y^2}{2R_y}\right)} \tag{5.16}$$

where w_x and w_y denote the beam size in the x and the y directions; R_x and R_y are the beam radii of curvature in the x and y directions; H_m is the Hermite polynomial function of order m.

(c) As we are working in the limits of the paraxial approximation, we adopted the scalar notation for $\Psi_{m,0}$ as no longitudinal component is observed. Indeed, this is an acceptable approximation as the divergence angle of the studied Gaussian beam is less than 3,5° in our case and thus, longitudinal components of the electric field could be neglected [85].

(d) In addition, as we consider only the modes at the cavity entrance $z = 0$, then, the longitudinal (z) dependence of the cavity modes and the corresponding third mode order q do not appear in

equation (5.16). Actually, there is a different set of transverse modes $\Psi_{m,0}$ for each longitudinal mode of order q. All these modes have their own resonance frequencies, written as follows:

$$\nu_{m,n,q} = \frac{c}{2n_{air}L}\left[q + (1+m+n)\frac{arc\cos(1-L/R)}{\pi}\right] \tag{5.17}$$

where the mode order n was taken equal to *0; c* is the speed of light in free space and n_{air} is the refraction index of air. The corresponding resonance wavelengths are: $\lambda_{m,n,q} = c/\nu_{m,n,q}$.

(e) All calculations that will follow, concerning the fiber-to-cavity coupling efficiency Γ and the intra-cavity round-trip coupling efficiency γ are done numerically based on the corresponding equations presented hereafter. The basic assumptions are the following: (i) the calculation domain extends from [-100 µm, 100 µm] in both x and y directions; (ii) the Bragg mirror is assumed to be thin and transparent in the infra-red range. Thus, the injected field crosses the cavity, keeping the initial values of the beam size and radii of curvature; (iii) the beam size differs in the x and y directions as the curved mirror focuses the beam in x while it has no effect on it in the y direction.

5.3 Design description

The presented devices mainly consists of two cylindrical Bragg mirrors, whose radius of curvature are R = 140 µm, spaced apart by a distance L = 210 µm. The cylindrical mirror is made of an alternation of silicon and air layers. The silicon has a thickness of 3.67 µm, while the air layer has a thickness of 3.49 µm, both thicknesses correspond to an odd multiple of quarter the transmission wavelength (at λ = 1550 nm) in silicon and in air, respectively. Another design with R = 200 µm and $L \sim 300$ µm has also been realized. The device has been fabricated using the improved Deep Reactive Ion Etching (DRIE) process presented in [86]. SEM photo of the device is shown in Fig. 5.4.

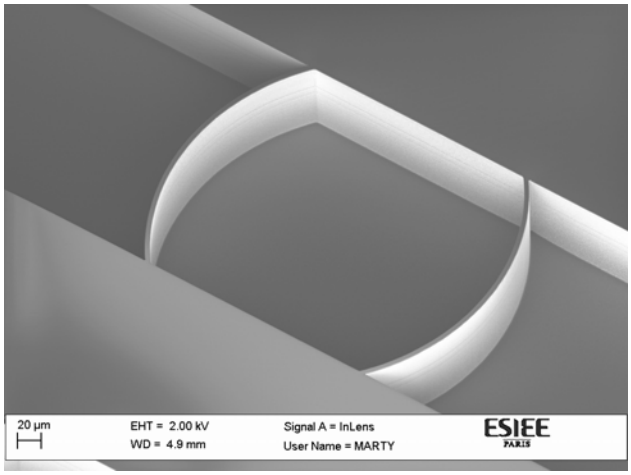

(a)

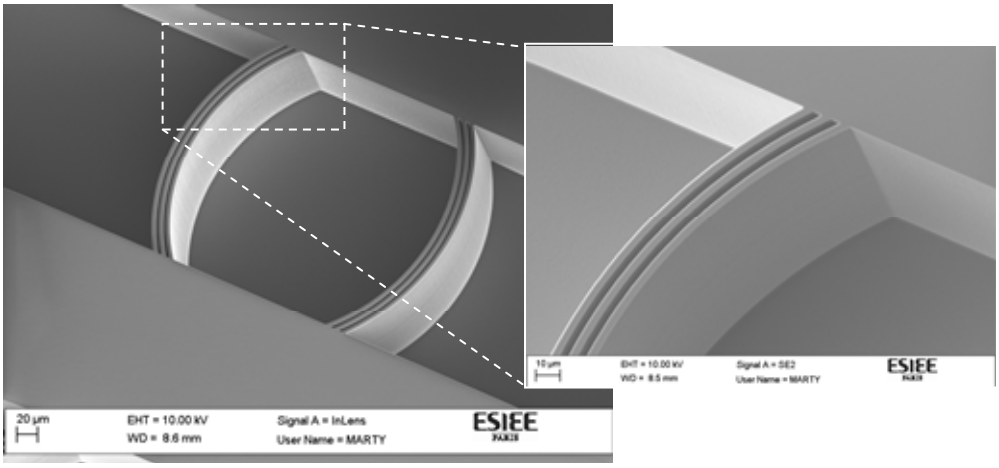

(b)

Fig. 5.4 SEM photos of a fabricated curved FP cavity with (a) single silicon layer, (b) multiple silicon layers (three in this case); the inset shows a magnified view on a silicon-air Bragg reflector.

5.4 Experimental evidence of wavelength selective filters

5.4.1 Experimental work

The optical setup, schematized in Fig. 5.3, consists of an Agilent tunable laser source (TLS) module 81949A used to inject the laser light, and an Anritsu MS9710B optical spectrum analyzer (OSA) used as a powermeter to measure the transmitted light. A visible laser light at 635 nm was also used for alignment purposes. The visible light and the infrared light are coupled through a directional coupler and injected into the lensed fiber to the device under test (DUT). A similar lensed fiber is used to collect the light transmitted through the device and to couple it directly to the OSA. The lensed fibers from Corning have a spot size of 18 µm and a working distance of 300 µm. Six axis positioners were used to align each fiber in the input and output grooves. All elements are mounted on an optical table to reduce vibration effects.

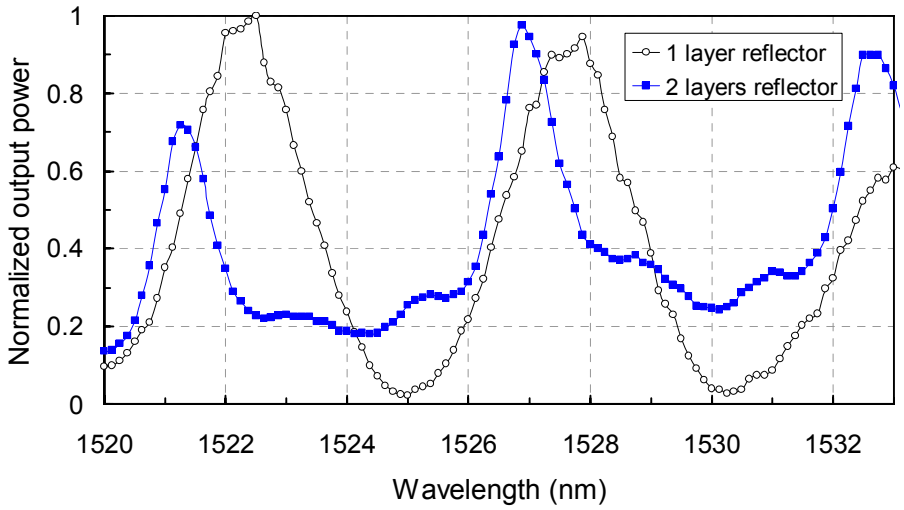

Fig. 5.5 Measured spectral responses for a FP cavity with cylindrical silicon-air Bragg reflectors having one and two silicon layers per mirror, respectively, illustrating the improvement of resonator finesse with the number of layers.

The spectral responses shown in Fig. 5.5 relate to cavities having one and two silicon layers per mirror and separations of 210 µm and 195.6 µm, respectively. The wavelength spacing between two consecutive longitudinal resonant modes, referred as free spectral range (FSR), was found to be 5.375 nm for the single-silicon layer mirror cavity and 5.625 nm for the two-silicon layer mirror cavity. These values are somewhat close to the theoretical FSRs estimated to be 5.537 nm and 5.953 nm, respectively. We ascribed the observed mismatch to the concept of the cavity effective length L_{eff}. Indeed, in our case, the cavity mirrors consist of concave Distributed Bragg Reflectors (DBR) that can be reduced to two single reflecting walls located *inside* their corresponding DBRs. Thus, the *effective length* of the cavity becomes larger than the *physical distance* measured between the inner shells of the DBRs. In addition, one can notice from Fig. 5.5 that the cavity becomes eventually more selective as the number of silicon layers increases. For the two layers design, the mirror reflectivity is expected theoretically to be 97.3%, compared to 72% for the single layer design. A comparison between the results is shown in table 5.1.

Table 5.1 Summary of experimental results comparing single and double layers cavities.

	1 silicon layer	**2 silicon layers**
Central wavelength	1527.9 nm	1526.9 nm
Q-factor	652	1059
Line width (FWHM)	2.34 nm	1.44 nm

Another experiment was done to study the power coupling efficiency and related mode matching between the fiber and the cavity with a single silicon layer, targeting a selective excitation of the longitudinal modes. For this purpose, the position z_{in} of the input fiber with respect to the entrance mirror was varied as shown in Fig. 5.6. Three different positions were tested: z_{in}=150 µm, z_{in}=300 µm and z_{in} = 460 µm, the detection fiber was replaced by another lensed fiber characterized by its better collection efficiency. Wavelength sweep was carried out at three different z_{in} positions and the corresponding recorded spectral responses are superimposed as shown in Fig. 5.7. Observing the cavity spectral responses, we notice a kind of periodicity: the pattern being repeated includes not only the main peaks of the longitudinal modes, denoted in Fig. 5.7 as modes of type (0,0), but also some other resonance peaks corresponding to transverse modes of type (2,0). These modes were identified by calculating the resonance wavelengths of the different cavity modes as listed in table 5.2. From the calculations, we concluded that the additional peaks pertain to the excitation of the transverse modes (TEM_{20}), which are typical in resonators made from curved mirrors, also referred to as Hermite-Gaussain modes [85].

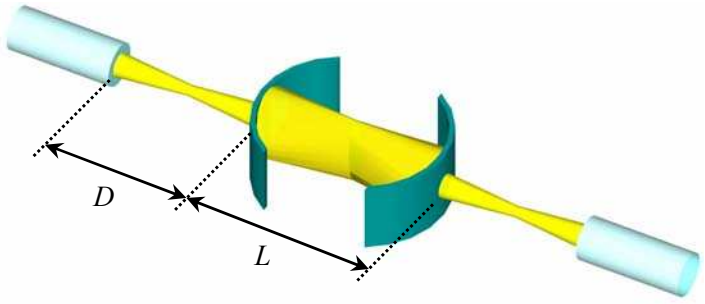

Fig. 5.6 Schematic illustration of the lensed fiber positioning with respect to the cavity. The cavity length L governs wavelength tuning. The fiber-to-cavity distance D ($=z_{in}$) controls the selective excitation of transverse modes.

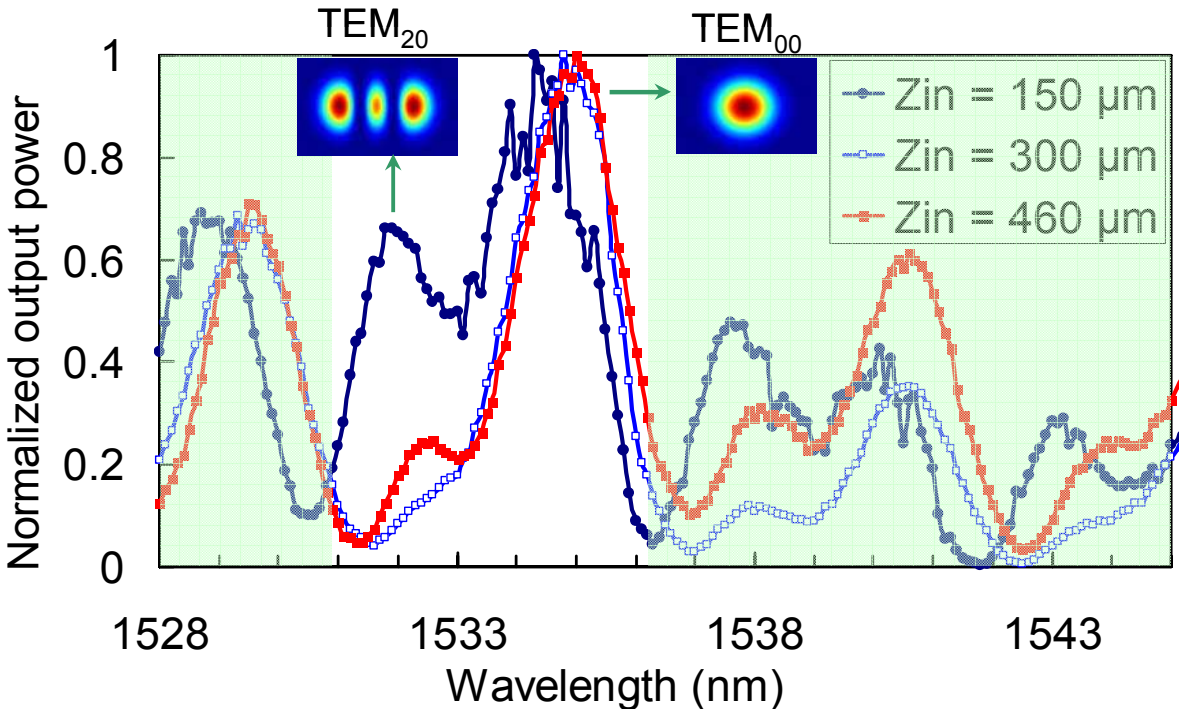

Fig. 5.7 Measured spectral responses of a FP cavity having a single silicon layer per mirror. The fiber-to-mirror coupling distance was varied z_{in} = 150 µm, 300 µm and 460 µm. The most selective coupling to fundamental modes of type (0,0) is achieved when z_{in} = 300 µm, also corresponding to twice the position of the fiber beam waist. As for the transverse mode (2,0), either effective coupling or noticeable extinction (of ratio of 7:1) is obtained, when z_{in} = 150 µm and z_{in} = 300 µm, respectively. Insets illustrate the field distributions for modes (0,0) and (2,0), respectively.

Table 5.2 shows the experimentally observed resonance wavelengths in the explored range, together with the calculated values obtained from equation (5.17). Among these theoretical possible resonance modes, some have been found experimentally and indicated in table 5.2 in italic characters. For each resonance, the mode orders are also indicated.

Table 5.2 Theoretical and experimental resonance wavelengths for the different *(m,n,q)* cavity modes in the wavelength range between 1528-1545 nm. The wavelength values observed experimentally are given in italic characters

Transverse mode order *(m,n)*	**Longitudinal mode order *q***	**q=270**	**q=271**	**q=272**	**q=273**	**q=274**
(0,0)	Theory			1540.5	1534.9	1529.3
	Experiment			*1540,6*	*1535*	*1529,5*
(2,0)	Theory	1544.7	1539.0	1533.4		
	Experiment	*1543,9*	*1538,0*	*1532,4*		

5.4.2 Behavioral analysis

(a) Fiber-to-cavity power coupling efficiency Γ

As the field injected from the lensed fiber (Gaussian beam) is not perfectly matched to the cavity modes (Hermite Gaussian modes), there is a need for estimating this mismatch, as it represents also a source of losses. There is also an interest of controlling this mismatch for the purpose of selective mode excitation. This source of loss was taken into account in our resonator model by the power coupling efficiency term Γ, which is also part of the resonator transfer function. It is obvious that Γ depends on the field distribution and therefore on the cavity mode order *(m,n)*.

Numerical calculations were used to evaluate this power coupling efficiency between the field E_{Fiber} injected from a single mode optical fiber (fundamental Gaussian mode) and the field of the different transverse cavity modes $\Psi_{m,0}$ at the cavity entrance. The calculation is done according to a normalized overlap integral:

$$\Gamma_{m,0} = \frac{\left| \iint_{(D)} E_{Fiber}(x,y,0) \cdot \Psi_{m,0}(x,y,0) dx\, dy \right|^2}{\iint_{(D)} \left| E_{Fiber}(x,y,0) \right|^2 dx\, dy \cdot \iint_{(D)} \left| \Psi_{m,0}(x,y,0) \right|^2 dx\, dy}. \qquad (5.18)$$

The injected fundamental mode (E_{Fiber}) is purely Gaussian; it has a beam waist of w_0=18 µm and waist position at 150 µm from the fiber output. The transverse cavity modes ($\Psi_{m,0}$) from *m=0* to *m=4* were examined. The calculated coupling efficiencies $\Gamma_{m,0}$ are shown in table 5.3 below for a wavelength of 1530 nm and coupling distances z_{in} of 150 µm, 300 µm and 460 µm (same values were chosen for the measurements). Since the integral calculation is done numerically, the mentioned numbers involve a very small numerical error which makes the sum of the coupling efficiencies slightly less than 100%. Neglecting this numerical error, we can consider that there is almost no coupling to modes higher than order (4,0) except in the case where z_{in} = 460 µm, where only 99,7% of the available power is coupled to the modes up to (4,0), leaving the remaining 0,3% of the injected power to higher order modes. The limits of integration were taken between [-100 µm, 100 µm] in both *x* axis and *y* axis, these limits being large enough for the considered beam size, whose waist is 18 µm. The simulation results show that only the modes with odd peaks can be excited since the coupling with modes of even peaks is null due to symmetry reasons. In addition, the coupling efficiency decreases significantly as the mode order *m* increases and, moreover, it varies as a function of the fiber input position (z_{in}). A case of particular interest is when the coupling distance z_{in} is equal to 300 µm, leading to very selective excitation of the longitudinal modes, that is, the fundamental modes (0,0), with a drastic extinction of all other transverse modes.

Table 5.3 Power coupling efficiencies $\Gamma_{m,0}$ between the fiber mode (Gaussian) and the *(m,0)* resonator modes (Hermite-Gaussian); calculated values at λ=1530 nm and values obtained by fitting to experimental results.

	z_{in} = 150 um		**z_{in} = 300 um**		**z_{in} = 460 um**	
	Model	*Fit to experiment*	Model	*Fit to experiment*	Model	*Fit to experiment*
$\Gamma_{0,0}$	96,7%	*63%*	99,93%	*99%*	89.14%	*89%*
$\Gamma_{1,0}$	0	--	0	--	0	--
$\Gamma_{2,0}$	3,14%	*37%*	0.07%	*1%*	9.15%	*11%*
$\Gamma_{3,0}$	0	--	0	--	0	--
$\Gamma_{4,0}$	0.15%	*0*	0.00%	*0*	1,41%	*0*
Total	100%	100%	100%	100%	99.7%	100%

Next is the comparison between our theoretical and experimental results. The analysis is done by comparing the calculated coupling efficiencies shown in table 5.3 and the experimental spectral responses shown in Fig. 5.7, where modes are identified through their resonance wavelengths. First, it appears from peak wavelengths in the measured spectra shown in Fig. 5.7 that the odd resonant modes (1,0) and (3,0) are not excited, as expected from our calculations of the corresponding coupling efficiencies shown in table 5.3. Comparing the calculations presented in table 5.3 and the experimental results, we can infer that the mode of type (2,0) becomes noticeable at z_{in} = 150 μm and 460 μm, as its coupling efficiency is non-negligible at these positions. The mode (2,0) has the highest coupling efficiency at z_{in} = 150 μm. Mode (4,0) has much reduced coupling efficiency and, as expected, it is not easily observable in the experiments.

On the other hand, it is worth mentioning that the fundamental resonant mode (0,0) is best coupled at z_{in} = 300 μm (99.93%) while the modes (2,0) and (4,0) are weakly coupled as their resonance peaks are not very high. This can be explained by the fact that the beam size at the boundaries of the cavity (mirror locations) is similar to the fiber mode at z_{in} = 300 μm, which leads to optimal conditions for selective mode coupling with the cavity fundamental (longitudinal) modes together with noticeable extinction of the transverse modes.

Further analysis of the experimental results enabled the evaluation of Γ for the different modes at different positions z_{in}. From the experimental results presented above, noticeable coupling is observed only on the modes TEM_{00} and TEM_{20} of the cavity. Based on this conclusion, we simulated a deconvolution process where we made a linear combination of these two modes with different coupling coefficients Γ_{00} and Γ_{20} and then, we fitted this combination to the experimental responses as shown in Fig. 5.8 a, b and c.

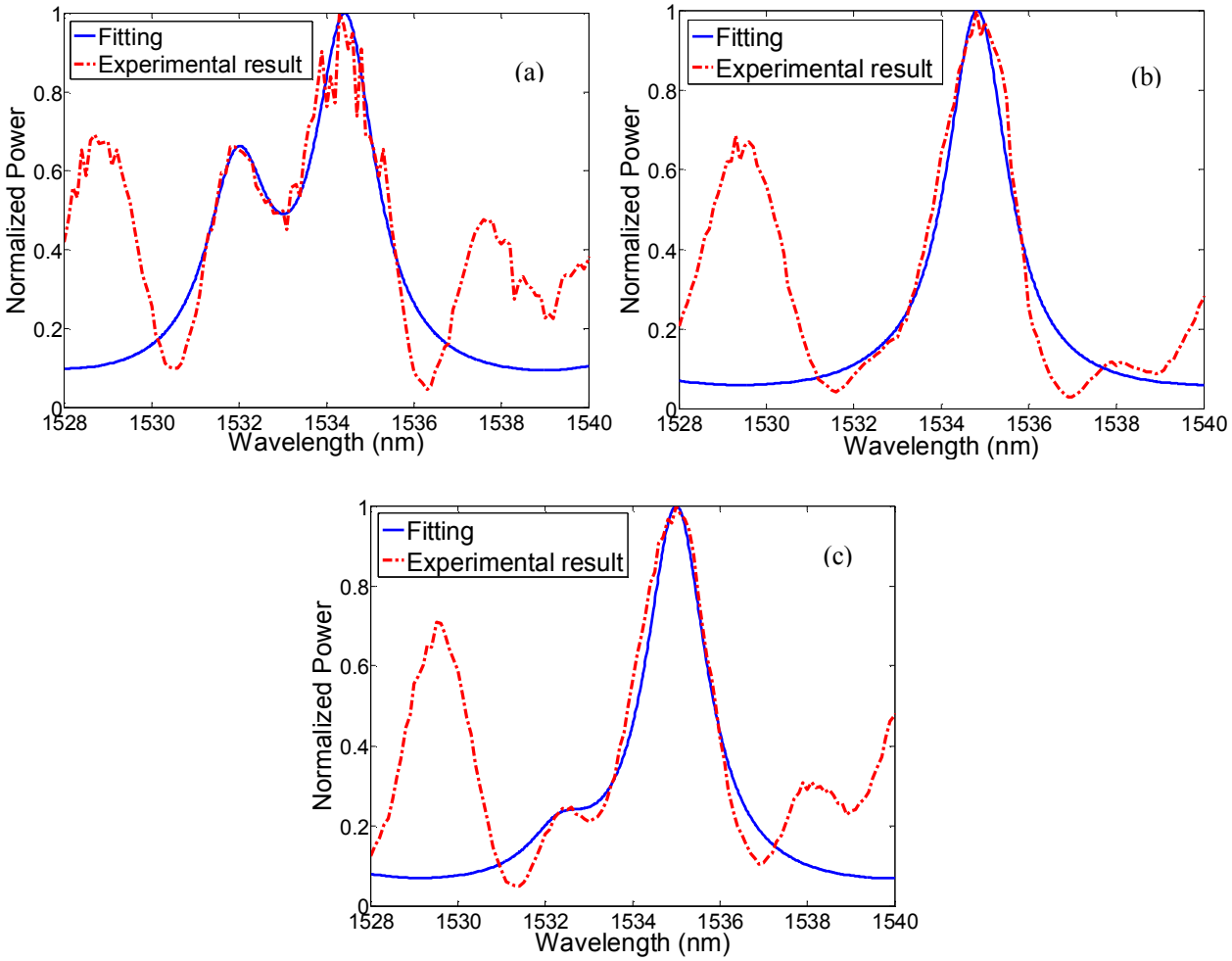

Fig. 5.8 Fitting of measured data to a combination of modes TEM_{00} and TEM_{20}: (a) for z_{in} = 150 µm, Γ_{00} = 63% and Γ_{20} = 37% , (b) for z_{in} = 300 µm, Γ_{00} = 99% and Γ_{20} = 1% and (c) for z_{in} = 460 µm, Γ_{00} = 89% and Γ_{20} = 11%

In this process, the resonance peaks were described by Airy functions given by equation (5.19) below, with effective mirror reflectance $\Re_{eff} = \sqrt{\gamma} \cdot \Re$ = 61% and cavity length L around 214 µm. Matching is achieved between the trial values of Γ_{00} and Γ_{20} corresponding to the best fit with experiments, and those obtained by numerical calculations using equation (5.18). While this matching is very good in the case of z_{in} = 300 µm and z_{in} = 460 µm, a quite large discrepancy is observed in the case of z_{in} = 150 µm. This deficiency is not fully understood and might be attributed to angular misalignment of the input fiber that leaded to a strong coupling to mode (2,0) (37% instead of 3.14%). Another possible explanation might be related to the fact that the excitation spot size is smaller than the mode size, which happens when z_{in} = 150 µm, also corresponding to the position of the optical fiber beam waist.

(b) Intra-cavity loss due to beam expansion

The cavity (power) transmittance at the vicinity of a given resonant mode can be expressed by a proper Airy function:

$$H_{cav} = \frac{1}{1 + \frac{4\sqrt{\gamma}\,\Re}{\left(1-\sqrt{\gamma}\,\Re\right)^2}\sin^2\left(\frac{2\pi L}{\lambda_0}\right)} \tag{5.19}$$

where L the cavity length, $\Re$ the mirror reflectance, λ_o the free space wavelength and the quantity $\gamma = e^{-2\alpha L}$ defined as the power attenuation factor after a full round-trip inside the cavity, where α is the attenuation coefficient per unit length. In our case, the attenuation mechanism is ascribed to light beam divergence and γ is also referred as the intra-cavity round trip coupling efficiency. Our first objective was to combine both the characteristics of the high reflectivity mirrors (up to 99.99%) and the long cavity lengths, while keeping low loss. We adopted the following equation (5.20) for the quality factor Q to quantify the selectivity of the cavity [22]:

$$Q = \frac{2\pi L}{\lambda_0}\left(\frac{\sqrt{\sqrt{\gamma}\,\Re}}{1-\sqrt{\gamma}\,\Re}\right). \tag{5.20}$$

We notice from equation (5.20) that as the cavity length L increases the Q-factor increases accordingly for the case of a lossless cavity. On the contrary, if the cavity is lossy and, as $\gamma = e^{-2\alpha L}$, then Q increases first and then it decreases since the losses become important at large lengths where the exponential factor embedded in γ dominates. Therefore, one can potentially attain unequalled performances in terms of Q-factor on larger cavities, provided that the attenuation factor γ can be maintained close to unity, for instance, by implementing a focusing technique using curved mirrors, as it is considered in this work. For each mode order *(m,n)*, $\gamma_{m,n}$ relates to the corresponding cavity losses and it is mainly due to the light beam divergence inside the cavity. This parameter is estimated using the related cavity modes $\Psi_{m,n}$ solely.

The intra-cavity round trip coupling efficiency $\gamma = \gamma_{m,0}$ of the *(m,0)* modes is estimated at different input positions (z_{in}) of the excitation fiber, as illustrated in Fig 5.7. $\gamma_{m,0}$ is obtained from the following overlap integral between the mode fields before and after full round trip along the cavity length, respectively:

$$\gamma_{m,0} = \frac{\left|\iint_{(D)} \Psi_{m,0}(x,y,0)\ .\ \Psi^{*}_{m,0}(x,y,2L)\,dx\,dy\right|^2}{\iint_{(D)}\left|\Psi_{m,0}(x,y,0)\right|^2 dx\,dy\ .\ \iint_{(D)}\left|\Psi_{m,0}(x,y,2L)\right|^2 dx\,dy} \tag{5.21}$$

where (D) is the mirror domain. The obtained values of $\gamma_{0,0}$ and the corresponding Q-factors derived from equation (5.20) are presented in table 5.4, where we considered a mirror reflectance $\Re$ = 72% corresponding to an ideal single layer Bragg reflectors. It was found that the intra-cavity round trip

coupling efficiency increases as z_{in} increases due to the fact that the beam divergence becomes significant for values of z larger than the fiber working distance of 300 μm. We notice a discrepancy between the analytical and the experimental Q-factors. This issue is due to many reasons: (i) the mirror roughness which degrades the reflection coefficients to less than the expected value of 72%, (ii) the silicon intrinsic losses over the single layer thickness of 3.67 μm, (iii) the non-ideality of the optical alignment caused by the lensed fiber pointing error, (iv) for the case of z_{in} = 460 μm, a portion of the light beam is passing over the filter. Calculation results show that $\gamma_{m,0}$ has negligible wavelength dependence (when considering different longitudinal mode orders q). Also, the values of $\gamma_{m,0}$ were found to be mainly related to the mode order $n = 0$ and keep unaffected by the values of mode order m. This can be understood as all $\Psi_{m,0}$ transverse modes expand similarly in the y direction, which is the major direction of energy loss. However, the most significant conclusion is that Q-factor is affected by $\gamma_{m,0}$, which, in turn, is a function of the fiber coupling distance z_{in}. This is consistent with the wavefunction dependence on the spot size and the beam radii of curvature, as stated in equation (5.16)

Table 5.4 Intra-cavity round-trip coupling efficiency $\gamma_{0,0}$ and Q-factor for a cavity with single silicon layer, with expected mirror reflectance $\Re$ = 72%, calculated at λ = 1535 nm for mode (0,0) at three different coupling distances z_{in}

Position of input fiber	**Calculated intra-cavity round trip coupling efficiency $\gamma_{0,0}$**	**Theoretical Q-factor**	**Experimental Q-factor**
z_{in} = 150 μm	0.6196	1036.6	665.32
z_{in} = 300 μm	0.5795	952.77	792.77
z_{in} = 460 μm	0.4788	770.22	769.7

5.5 Effect of the number of Bragg layers

In this experiment, Single Mode Fibers (SMF-28 from Corning) cleaved at 90° were used for recording the spectral response of different devices, which mainly differ in the number of Bragg layers per mirror, and this in turn, translates into different reflectance values. Fig. 5.9 shows the spectral responses obtained for three different cavities, corresponding to single, double and triple silicon layer per mirror respectively. Inspecting the results, the single layer cavity has a Full Width at Half Maximum (FWHM) = 3.11 nm, the double layer cavity has FWHM = 1.73 nm, and the 3 layers cavity has FWHM = 1.42 nm. As expected, we conclude that as the number of silicon layer/mirror increases, the filter roll-off improves. It is noteworthy that the spectral responses of the three cavities are slightly shifted with respect to each other because their respective cavity effective lengths are slightly different due to the different thicknesses of the Bragg mirrors. Analyzing the spectral responses, we deduced the values of the effective reflectance $\Re_{eff}$, which represents the product of the mirror reflectance $\Re$ and the half-

round-trip attenuation γ with typically $\gamma = e^{-2\alpha L}$ to account for the distance-dependent loss. By calculating the finesse F from the previous data, and using equation (5.22):

$$F = \frac{FSR}{FWHM} = \frac{\pi\sqrt{\Re_{eff}}}{1-\Re_{eff}} \tag{5.22}$$

where FSR is the Free Spectral Range of the cavity. Note that the use of the previous equation is a valid approximation as long as we are working in the limits of the paraxial approximation. Indeed, it helps getting a rough estimation of $\Re_{eff}$. Moreover, from the knowledge of $\Re_{eff}$ and based on the theoretical values for $\Re$, one can evaluate the half-round-trip attenuation γ_{Exp} of the measured structures. The corresponding results are given in table 5.5.

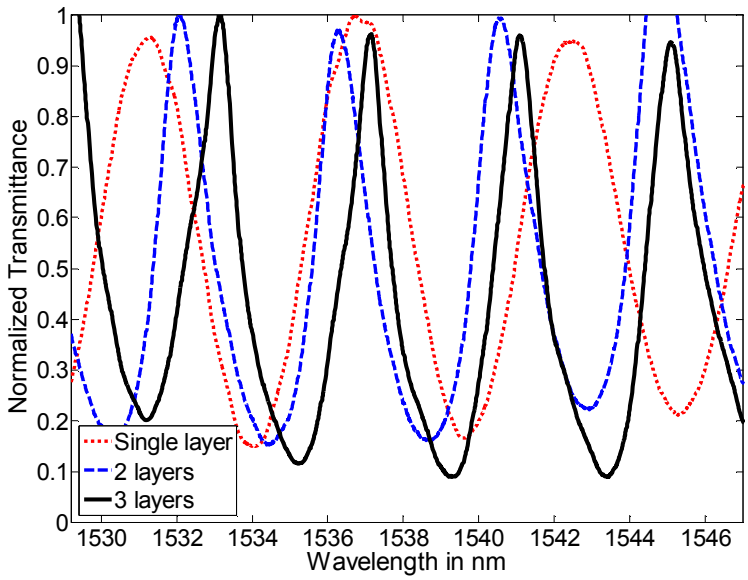

Fig. 5.9 Spectral response of FP cavities having one, two and three silicon Bragg layers per mirror, respectively, revealing decreasing linewidths. The response of the single layer cavity is shifted with respect to the other responses due to the difference in the cavity effective length.

Table 5.5 Characteristics of single, double and three layers cavities as deduced from experimental results

	FSR (nm)	***FWHM (nm)***	***F***	$\Re_{eff}$	γ_{Exp}	$\Re_{theory}$
Single layer	*5.79*	*3.11*	*1.862*	*21.59%*	*0.299*	*72%*
Double layer	*4.31*	*1.7273*	*2.495*	*30.48%*	*0.3133*	*97.3%*
Three layers	*3.935*	*1.4238*	*2.764*	*33.86%*	*0.3394*	*99.77%*

5.6 Potential applications

Looking again over the experimental results in Fig. 5.10, we come out with various useful applications for this device.

(i) The first observation suggests that the device behaves as a *Mode Selective Filter*, In this case, the device can be used for the purpose of selecting only longitudinal modes (TEM_{00}) and reject the transverse modes (TEM_{20} and higher order modes). In the context of such application, the user

will keep the distance *D* constant at 300 µm, leading to the transmission of (TEM_{00}) modes only, whatever was their wavelength.

(ii) On the contrary, in another application, the concern can be about the distribution of light intensity inside the cavity; then switching from mode (TEM_{00}) to mode (TEM_{20}) can be exploited. In the context of such practical application, the user will keep the distance *D* constant at 150 µm, then, switch the excitation λ from 1535 nm (TEM_{00}) to 1532 nm (TEM_{20}).

(iii) The third application is about *Wavelength selective switching*. In this application, we keep the excitation λ at 1532 nm corresponding to the (TEM_{20}) transverse mode, and we vary *D* between 150 µm and 300 µm. Controlling the distance *D* (the fiber-to-cavity distance), we can switch the mode TEM_{20} (at 1532 nm) from ON to OFF states and vice versa, while the mode TEM_{00} (at 1535 nm) is unaffected and stays always in the ON state. These positions for the distance *D* correspond to the maximum and the minimum power level for mode TEM_{20}, respectively. The extinction ratio, defined as the ratio between the highest and the lowest power level is 7:1. Besides the previously reported MEMS-based wavelength-selective switching solution [65], our device is an alternative MEMS-compatible switching technique, in which the control of the distance D can be implemented for instance by adding a movable mirror, whose motion acts on the optical path from the fixed fiber to the fixed cavity.

(iv) The latter behavior also suggests another application, which consists of an *Add-Drop multiplexer*. In such application, we inject the wavelengths of 1532 nm and 1535 nm, corresponding to different communication channels ; then by switching *D* from 150 µm to 300 µm, we notice that λ = 1532 nm is either added or dropped to the readily existing 1535 nm. This function suggests a potential deployment for such device in WDM systems. By proper design for the cavity length and the mirrors reflectance, one can target meeting the International Telecommunication Union (ITU) grid standards for WDM systems.

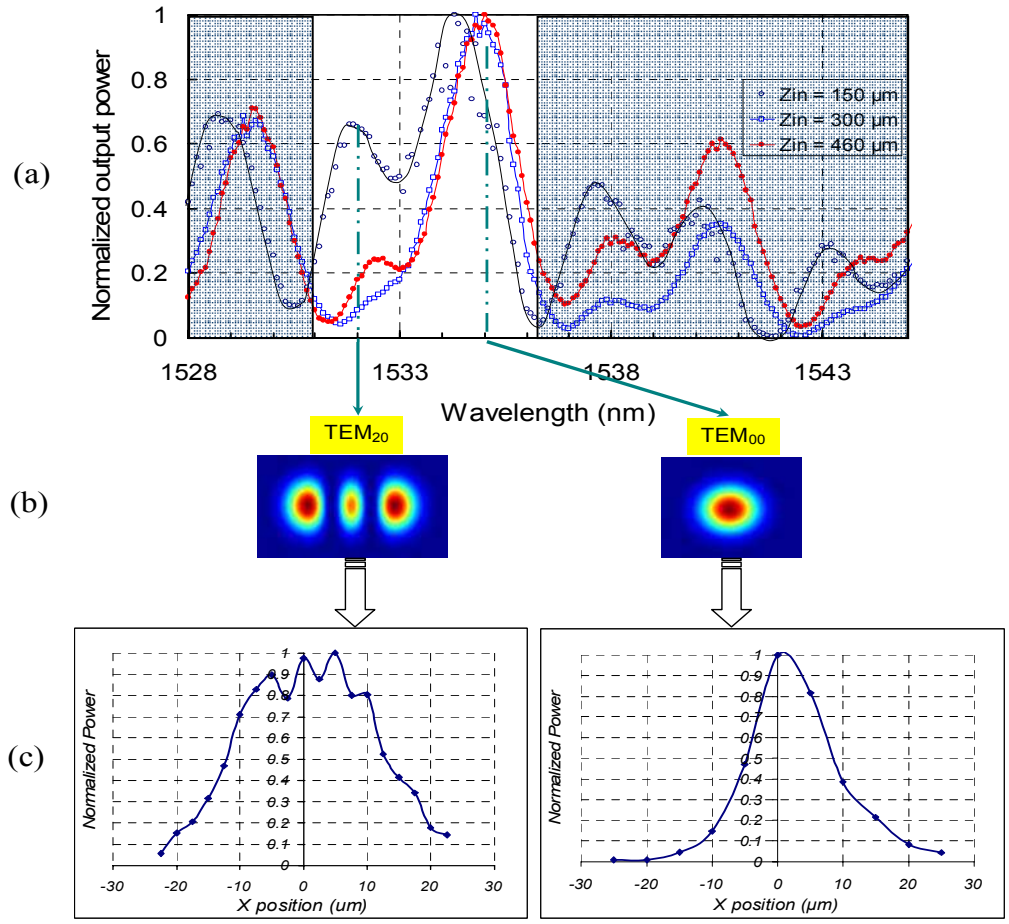

Fig. 5.10 Demonstration of Wavelength Selective Switching (and Mode Selective Filtering) of the FP cavity with cylindrical mirrors (a) Recorded spectral responses of the cavity, measured with lensed fiber while varying the fiber-to-cavity distance *D*. The curves reveal selective excitation of the resonant transverse modes TEM_{20} around 1532 nm in addition to the fundamental Gaussian mode TEM_{00}. Varying *D* leads to different levels for mode TEM_{20} with an extinction ratio of 7:1. (b) Theoretical intensity distribution of TEM_{00} and TEM_{20} modes. (c) Measured intensity profiles (of modes TEM_{00} and TEM_{20}) obtained by lateral in-plane scanning of the detection fiber in the groove.

5.7 Characterization of simple curved cavities by optical low coherence interferometry

5.7.1 Objective

It was discussed previously, that due to the distributed nature of the Bragg reflectors that have a non-negligible thickness, it is not straightforward to determine the positions of the mirrors. In the case of a Fabry Perot cavity made from such Bragg mirrors, it is even not straightforward to determine the cavity length. We have seen before that the effective cavity length is different from the physical length taken from the borders of the two Bragg reflectors.

In order to deepen our study on such Fabry-Perot cavities based on silicon-air Bragg mirrors, we made new experiments using the so-called OLCI technique, with a setup constructed by Mrs. Anne-Françoise OBATON at LNE-Trappes.

As compared to the previously presented experimental results, we found that characterization by OLCI provided complementary information, namely about the mirrors locations and thickness of the Bragg layers. Before presenting these results, we briefly describe the OLCI technique in the next paragraph.

5.7.2 Theory of OLCI

In simple words, Phase sensitive-Optical Low Coherence Reflectometry PS-OLCR gives information in the spatial domain, on the local reflectivity or transmissivity of the device under test as a function of the displacement of a movable mirror. On another hand, as the acquisition is regularly sampled, thanks to a second coherent reflectometer, Fourier transform can be applied. Therefore, such technique also gives information in the spectral domain, on the spectral reflectivity or transmissivity i.e. the amplitude and above all *the phase* of the device under investigation as a function of the wavelength, hence the name of *Phase Sensitive*-OLCR or OLCI (PS-OLCR or PS-OLCI) in opposition to commercial OLCR, which only gives information in the spatial domain. A schematic diagram illustrating the principle is shown in Fig. 5.11. A schematic of the deployed setup is shown in Fig. 5.12.

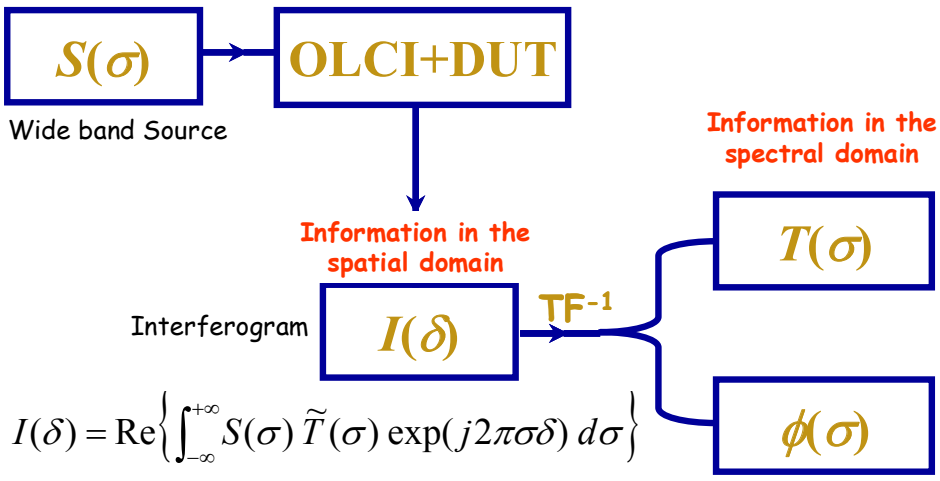

Fig. 5.11 Schematic diagram illustrating the principle of PS-OLCI technique

The idea is based on interfering two signals reflected (*transmitted*) from the reference arm and the test arm of a fiber based Michelson interferometer. The reflected (*transmitted*) signals interfere at the coupler (*detector*). If the system stops at this point, then, we acquire only the envelope of a white light interferometer. But the system designed by LNE-Trappes [87, 88] offers an incremental advantage over conventional OLCR (OLCI) which is the sampling. Hence, we have access to fringes contained within the interferogram. This, in turn, allows the calculation of the amplitude and the phase of the device under test in the spectral domain.

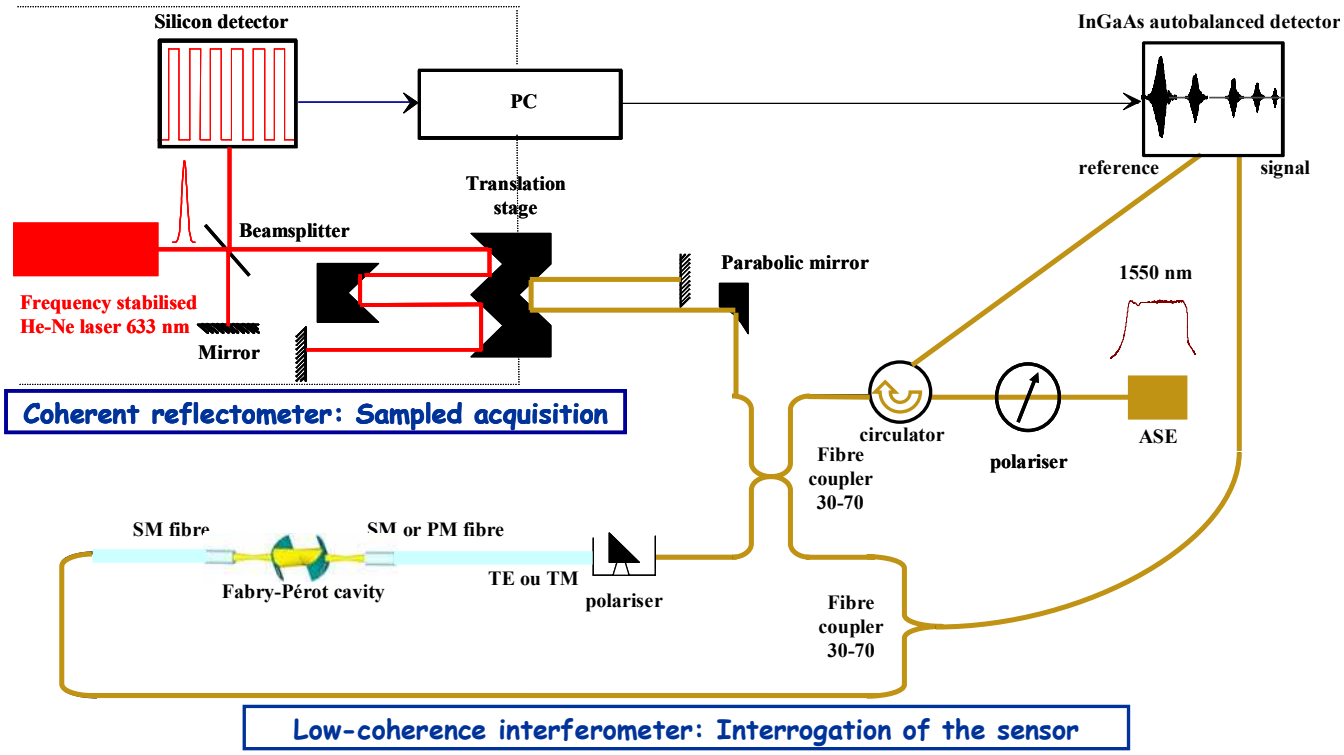

Fig. 5.12 Optical setup used to characterize the curved FP cavity. The connected configuration pertains to the measurements of the transmission interferogram where the light transmitted through the cavity is coupled together with the reflected reference signal in a 2x1 30:70 coupler to the InGaAs detector.

5.7.3 Experimental results

Various curved FP cavities have been measured using the PS-OLCI system. Fig. 5.13a shows the interferogram recorded for a design of a simple curved cavity based on three silicon layers per mirror, having a cavity gap length of 210 µm. Fig. 5.13b pertains to the envelope of the recorded interferogram and Fig. 5.13c is the spectral response of the cavity obtained after numerical treatment for the measured data. Lensed fibers of 25 µm working distance were used for light injection and detection.

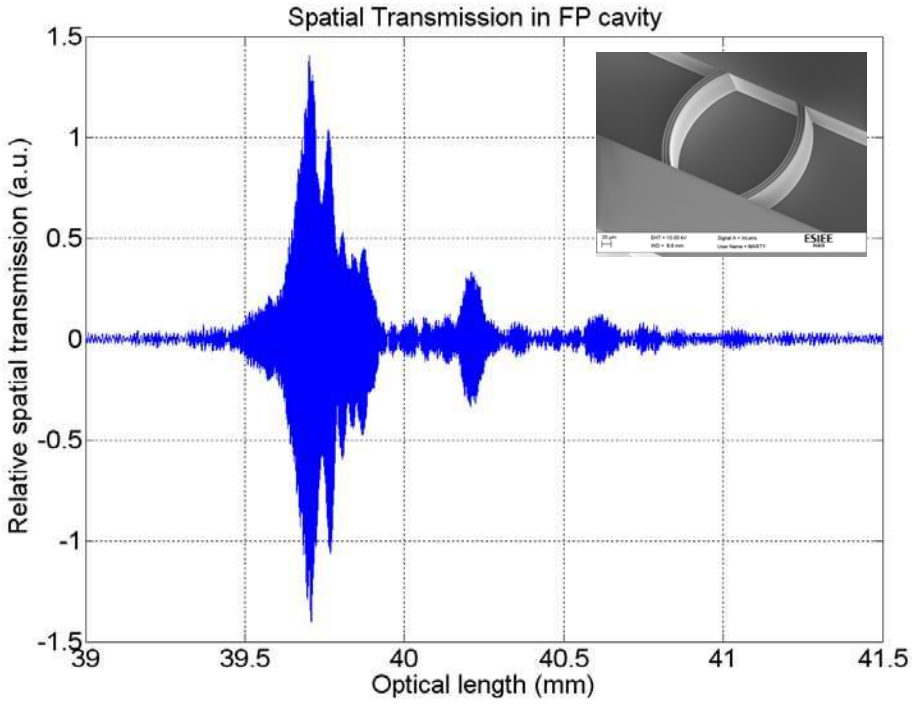

(a)

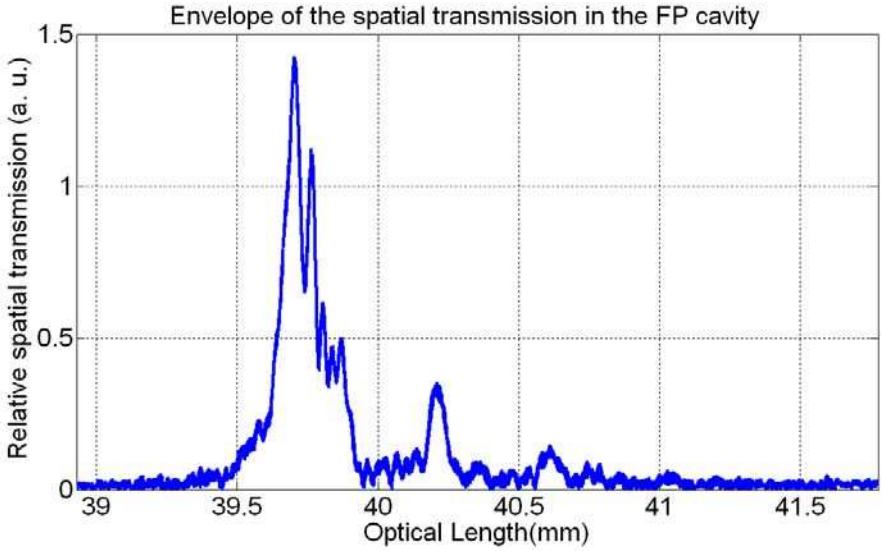

(b)

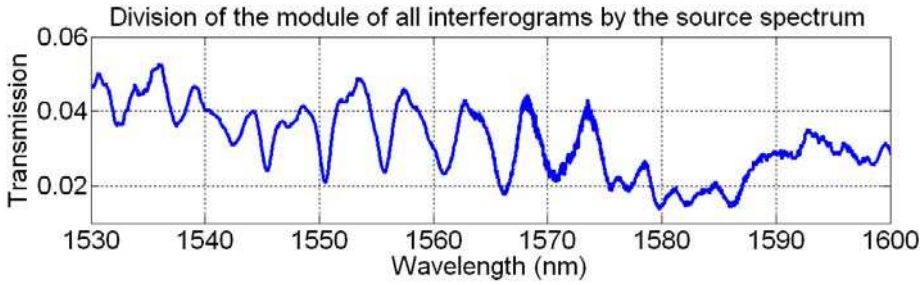

(c)

Fig. 5.13 (a) Interferogram recorded using the PS-OLCI technique for a simple curved cavity having 3 silicon layers per mirror (b) Envelope of the interferogram in (a). (c) Cavity spectral response calculated from the data in (a)

Similar results are obtained for simple cavity based on two silicon layers per mirror and having a cavity gap length of 210 µm. Corresponding results are shown in Fig. 5.14. Standard fibers SMF-28 cleaved at 90° were used for light injection and detection.

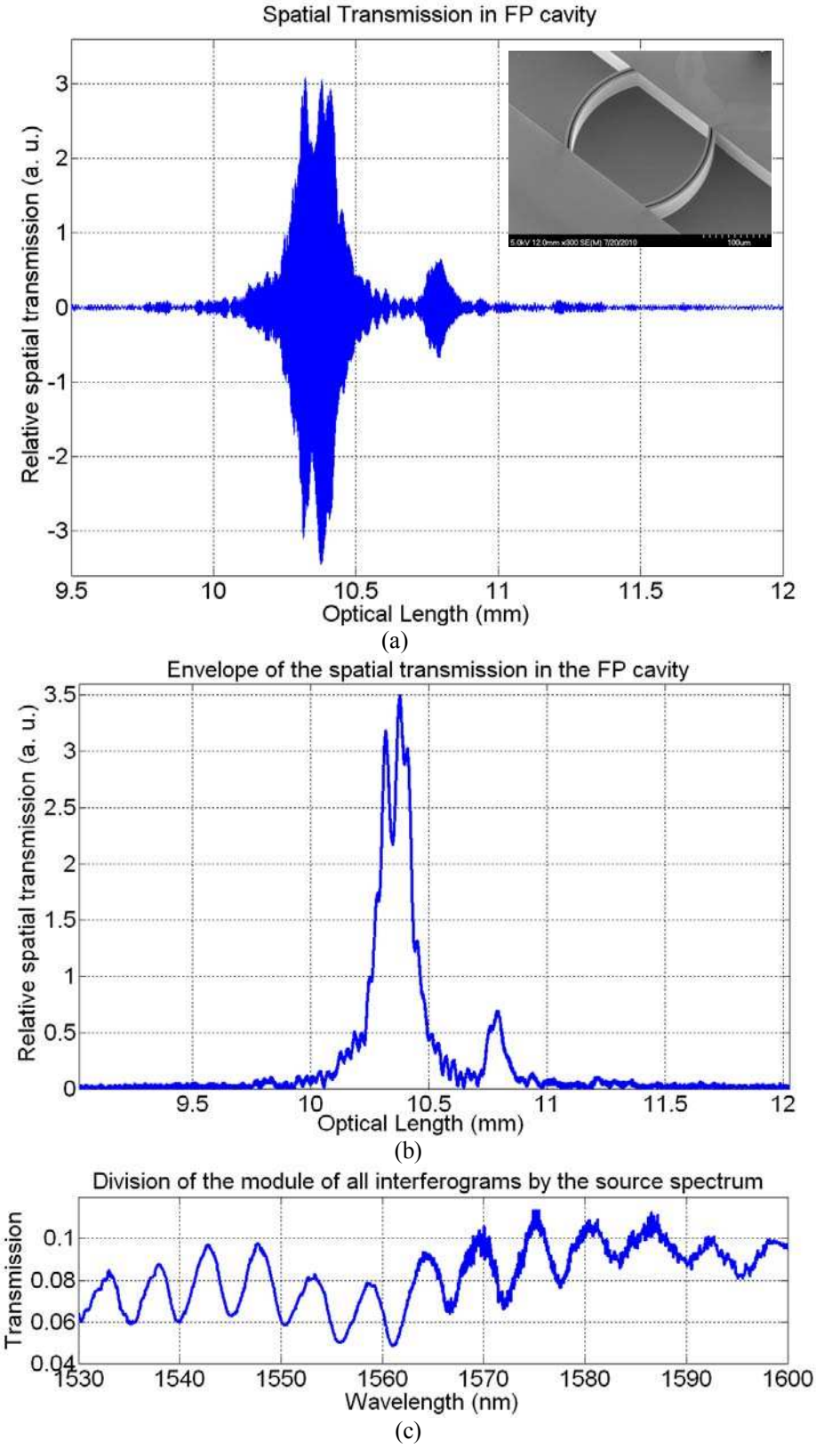

Fig. 5.14 (a) Interferogram recorded using the PS-OLCI technique for a simple curved cavity having 2 silicon layers per mirror (b) Envelope of the interferogram in (a). (c) Cavity spectral response calculated from the data in (a)

Inspection of the envelopes of the interferograms in Fig. 5.13b and Fig. 5.14b show that several peaks appear in the spatial transmission of the FP cavity. These peaks are located at positions different from double the path difference of the cavity *2L* (where *L* is the cavity gap length). Calculations reveal that these peaks are due to reflections at both the inner and the outer interfaces of each Bragg layer. An illustration of the reflection schemes that take place inside the curved FP cavity is shown in Fig. 5.15. This result is interesting as it enables the characterization of the thickness of the Bragg layer resulting about the fabrication process.

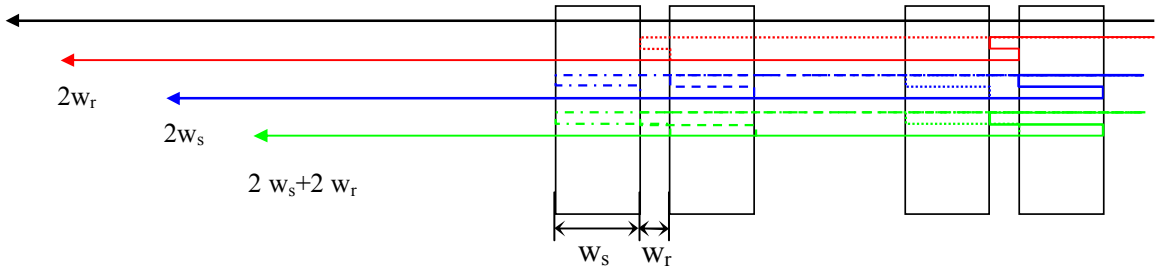

Fig. 5.15 Schematic illustration of the reflection schemes taking place inside the curved FP cavity of two silicon layers per mirror. The thick rectangles represent the silicon Bragg layers whose physical thickness w_s = 3.67 µm and refractive index n_{Si} = 3.478, they are separated by quarter wavelength air layer w_r of physical thickness = 3.49 µm.

The result presented earlier is a fair proof of concept for the potential of using our cavities with the PS-OLCI technique, for the purpose of detection of molecular species inserted inside the cavity. In fact, if the medium inside the cavity is filled with liquid or gaz, the refractice index varies and then the optical path increases. Measurement will reveal a path length greater than the physical length which allows the determination of the refractive index on one hand. On the other hand, if the PS-OLCI technique is associated with absorption from the characterized species, then by comparing the measured spectrum with the traces of standard absorption spectra for the different molecules, we can not only measure the refractive index of the unknown molecule but also, the kind of the absorbing molecules can be recognized. Based on these observations, we come out with the conclusion that the curved cavity lies at the core of lab-on chip analysis microsystems.

5.8 Conclusion

The first conclusion relates to the analysis and the characterization of simple curved cavities using the tunable laser source setup. Analytical model has been set for the cylindrical cavity for calculate coupling between the injected field and the cavity modes. The intra-cavity loss has been calculated as well. Both analytical and experimental results fit quite well and they reveal selective excitation of higher order mode TEM_{20} under certain conditions, governed by the fiber-to-cavity distance We notice a reduction in the FWHM as the number of Bragg layers per mirror increases.

The second conclusion relates to the experimental work of the PS-OLCI, In fact that we were able to determine the values for the physical length of the cavity as well as the thickness of the silicon and air Bragg layers. These values are in good agreement with design values and values extracted from SEM photos. Further work is required to determine the precision and accuracy on these values.

Chapter 6

Stable Optical Resonator with Cylindrical Bragg Mirrors and Fiber Rod Lens

6.1 Introduction

In this chapter, we describe in details the second resonator whose architecture was outlined in chapter 4. As mentioned earlier, the objective is to provide further improvement to the Q-factor using 2D confinement of light. The introduced structure emulates the spherical resonators in the sense that the effect of mirror sphericity is still maintained using a combination of two cylindrical components: Cylindrical Bragg mirrors and Fiber Rod Lens as shown in Fig. 6.1.

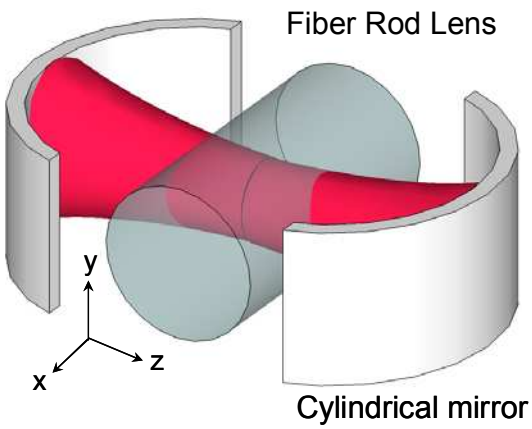

Fig. 6.1 Additional resonator with Fiber-Rod-Lens (FRL) ensures out-of-plane confinement, leading to a complete solution for 2D confinement and reduced optical loss.

6.2 Analytical modeling

Since the architecture introduced in this chapter is novel, there is no analytical model for it in the literature. So, in order to design a stable resonator involving a fiber Rod Lens (FRL), we have to derive analytical relations to know the criteria of its stability. Our analysis is based on the ray matrix approach explained in chapter 2 of the thesis [78]. Remember that in this approach, each ray is defined by a position "y" and angle "Θ" with respect to the optical axis. Our intention is to get a closed form relation between the different geometrical parameters of the cavity: the radius of curvature R, the free space propagation distance d_{air} and the fiber diameter d_f.

In the following treatment, we assume that the cavity is symmetric and that the distributed Bragg mirror is a shell of high reflectance.

The treatment of this design will be somewhat different than the simple cavity presented in the previous chapter since its aim to focus the light in 2D. In this case, the ray matrix can still be applied if

we take cross sections in XZ and YZ planes. The problem turns to be a couple of 1D problems which is a valid manipulation since the focusing behaviors in the two directions are decoupled. This fact is illustrated in Fig.6.2 which show the cross sectional views of the system that will be analyzed later.

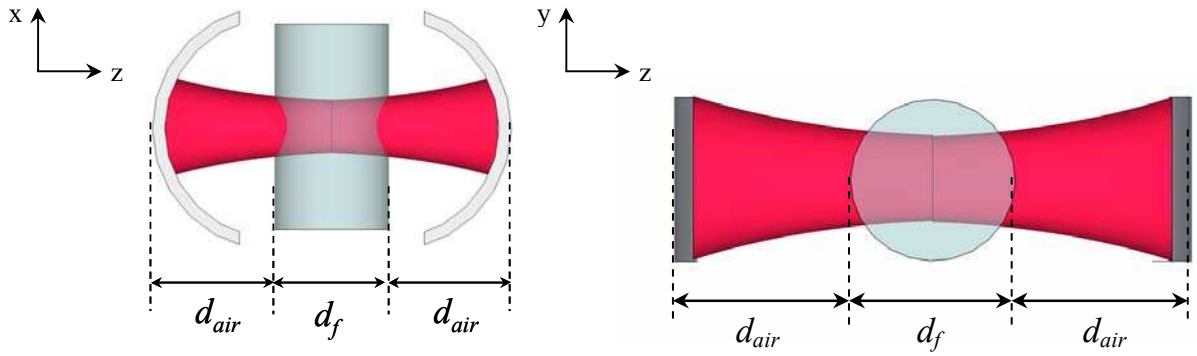

Fig. 6.2 Top view and front view of the Fiber-Rod-Lens resonator architecture seen in the XZ and the YZ transverse planes respectively, illustrating the distances of propagation inside the fiber d_f and in air: twice d_{air}.

Observing the XZ cross section, we notice that the focusing is governed by the curved Bragg mirror. The fiber acts a refracting slab having a width d_f and a refractive index n_f. For the YZ cross section, the curved mirror becomes a straight mirror and the fiber acts as a converging thick lens. As previously mentioned, the curvature of the conventional spherical mirror has been distributed in two planes and on two different components.

Herein, we present the calculation of the condition of stability in the XZ plane. The propagating beam faces the following components:

1. Reflection from a concave mirror given by:

$$K_1 = \begin{pmatrix} 1 & 0 \\ -2/R & 1 \end{pmatrix} \tag{6.1}$$

2. Free space propagation region given by:

$$K_2 = \begin{pmatrix} 1 & d_{air} \\ 0 & 1 \end{pmatrix} \tag{6.2}$$

3. Refraction from air to fiber:

$$K_{3I} = \begin{pmatrix} 1 & 0 \\ 0 & 1/n_f \end{pmatrix} \tag{6.3}$$

4. Propagation inside the fiber:

$$K_{3II} = \begin{pmatrix} 1 & d_f \\ 0 & 1 \end{pmatrix} \tag{6.4}$$

5. Refraction from fiber to air:

$$K_{3III} = \begin{pmatrix} 1 & 0 \\ 0 & n_f \end{pmatrix} \tag{6.5}$$

We assume that the multilayer Bragg mirror is simply a single interface having a high reflectance $\Re$. Also, we consider that the refractive index distribution of the fiber is uniform and so we do not discriminate between the refractive indices of both the core and the cladding.

For the case of study, the round trip equivalent matrix becomes:

$$K_{eq} = K_1 K_2 K_{3I} K_{3II} K_{3III} K_2 K_1 K_2 K_{3I} K_{3II} K_{3III} K_2 \tag{6.6}$$

After lengthy mathematical manipulations based on matrix multiplication, we obtain a complex and very long 2x2 matrix for K_{eq}.

Finally, applying the condition of stability (refer to ch.2), we get:

$$0 \le \frac{d_{RT}}{|R|} \le 2 \tag{6.7}$$

where d_{RT} is given by:

$$d_{RT} = 2d_{air} + \frac{d_f}{n_f} \tag{6.8}$$

Now, if we analyze the YZ cross section to its basic elements, we shall get:

1. Reflection from a straight mirror given by:

$$K_1 = \begin{pmatrix} 1 & 0 \\ 0 & 1 \end{pmatrix} \tag{6.9}$$

2. Free space propagation region given by:

$$K_2 = \begin{pmatrix} 1 & d_{air} \\ 0 & 1 \end{pmatrix} \tag{6.10}$$

3. Propagation inside the fiber as given by (6.4)

$$K_{3II} = \begin{pmatrix} 1 & d_f \\ 0 & 1 \end{pmatrix} \tag{6.11}$$

4. Refraction from air to curved fiber interface given by:

$$K_{3I} = \begin{pmatrix} 1 & 0 \\ 2(1-n_f)/n_f d_f & 1/n_f \end{pmatrix} \quad (6.12)$$

5. Refraction from curved fiber interface to air given by:

$$K_{3III} = \begin{pmatrix} 1 & 0 \\ 2(1-n_f)/d_f & n_f \end{pmatrix} \quad (6.13)$$

In this case, the round trip equivalent matrix becomes:

$$K_{eq} = K_1 K_2 K_{3III} K_{3II} K_{3I} K_2 K_1 K_2 K_{3III} K_{3II} K_{3I} K_2 \quad (6.14)$$

After lengthy mathematical manipulations, we obtain another 2x2 matrix for K_{eq}.
Finally, applying the condition of stability (refer to ch.2), we get:

$$0 \le (1-2/n_f) + (4d_{air}/d_f)(1-1/n_f) \le 1 \quad (6.15)$$

By solving (6.7) and (6.15) for d_{air}, we will obtain two different stability ranges in the XZ and YZ planes. This means that the cavity might be stable in one dimension and unstable in the other dimension. So, whenever we design FRL cavities, we shall look for values of d_{air} that satisfies both inequalities.

In order to appreciate the impact of these equations on our resonator, we will take a numerical example. Let's consider the cavity A with a radius of curvature R = 140 µm, the fiber diameter d_f= 125 µm, the refractive index n_f= 1.47 and the free space propagation length d = 78 µm. This cavity is stable since its "d_{air}" falls in the common stability regions of XZ and YZ. Table 6.1 lists the stability and instability regions for this specific design. Another example is for the cavity B holding the same parameters for the fiber but its R = 200 µm and its d_{air} = 137.5 µm. This cavity is stable in XZ but unstable in YZ. Table 6.2 lists the stability and instability regions for this design also.

Table 6.1 Stability ranges for cavity A with R = 140 µm

"d_{air}" range	Stability in XZ	Stability in YZ
d_{air} = [0 , 27.5 [	No	No
d_{air} =] 27.5 , 35 [	Yes	No
d_{air} =] 35 , 97.5 [	***Yes***	***Yes***
d_{air} =] 97.5 , 133 [	No	Yes
d_{air} =] 133 , ∞ [	No	No

Table 6.2 Stability ranges for cavity B with R = 200 µm

"d_{air}" range	Stability in XZ	Stability in YZ
d_{air} = [0 , 35 [	No	No
d_{air} =] 35 , 57.5 [	No	Yes
d_{air} =] 57.5 , 133 [	***Yes***	***Yes***
d_{air} =] 133 , 157.5 [	Yes	No
d_{air} =] 157.5 , ∞ [	No	No

Design for stability

The two cavities A and B studied above exhibit different behaviors in terms of stability; the first is stable whether the second is unstable. This fact can be confirmed by the following analytical calculations, which also give the guidelines for further designs of optical resonators ensuring a stable behavior.

For this purpose, and starting from the analytical model presented above, we develop new relations that link the cavity radius of curvature to the free space propagation distance inside the FRL cavity as shown in Fig. 6.2, where the geometrical parameters used in our model are defined. Considering the XZ cross section (top view as shown in Fig. 6.2), and for the YZ cross section (front view), respectively, the stability conditions are given by (6.7) and (6.15):

$$0 \le \frac{\left(2d_{air} + d_f / n_f\right)}{2|R|} \le 1 \tag{6.16}$$

$$0 \le \left(1 - 2/n_f\right) + \left(4d_{air}/d_f\right)\left(1 - 1/n_f\right) \le 1 \tag{6.17}$$

So, we get at the upper limits:

$$\left(1 - \frac{2}{n_f}\right) + \left(\frac{4d_{air}}{d_f}\right)\left(1 - \frac{1}{n_f}\right) = 1 \tag{6.18}$$

$$d_{air} = R - \frac{d_f}{2n_f} \tag{6.19}$$

From equations (6.18) and (6.19), we obtain at the end:

$$d_{air-\max} = \frac{d_f}{2\left(n_f - 1\right)} \tag{6.20}$$

$$R_{\max} = \frac{d_f}{2}\left\{\frac{2n_f - 1}{n_f\left(n_f - 1\right)}\right\} \tag{6.21}$$

Similarly, one obtains for the lower limits:

$$d_{air-\min} = \frac{d_f}{4}\left\{\frac{2 - n_f}{n_f - 1}\right\} \tag{6.22}$$

$$R_{\min} = \frac{d_f}{4}\left\{\frac{2}{n_f} + \frac{2 - n_f}{n_f - 1}\right\} \tag{6.23}$$

For the FRL cavities considered in this example, knowing that d_f = 125 µm and n_f = 1.47, one obtains the range of dimensions leading to a stable behavior, as summarized in table 6.3. This table also includes the specific characteristics and stability behavior of cavities A and B that were studied experimentally.

Table 6.3 Design parameters for reaching the stability conditions for resonator architecture including the fiber rod lens. The studied Cavity A has a length L = 265.8 µm and radius of curvature R = 140 µm and is stable. The studied Cavity B has L = 385.6 µm and R = 200 µm and is unstable.

		Studied devices	
	Ranges for stability	**Cavity A**	**Cavity B**
d_f (µm)	125 (fixed)	125	125
R (µm)	Range [77.8, 175.5]	140	200
d_{air} (µm)	Range [35.2, 133.0]	70.2	130.3
Stability	Yes, as long as conditions on R, d_{air} and d_f are satisfied simultaneously	Yes	No

6.3 Design description

As mentioned above, the architecture schematically depicted in Fig. 6.1 provides a complete solution for 2D confinement of light, due to the additional cylindrical surface of the fiber rod lens (FRL) inserted inside the cylindrical silicon cavity. Such devices were designed, realized and measured. All fabricated devices share common parameters. Every silicon layer has a width of 3.67 µm, while the air layer has a width of 3.49 µm. A long recess opening (~1 cm) of 128 µm width is shared between all the devices to facilitate the insertion of the FRL, whose width is 125 µm. On the contrary, the fabricated FP cavities differ from each other, either in their physical length of the cavity or in the number of Bragg layers per mirror. Based on these settings, many combinations were generated, measured and then analyzed. Photographs of a fabricated device are shown in Fig. 6.3

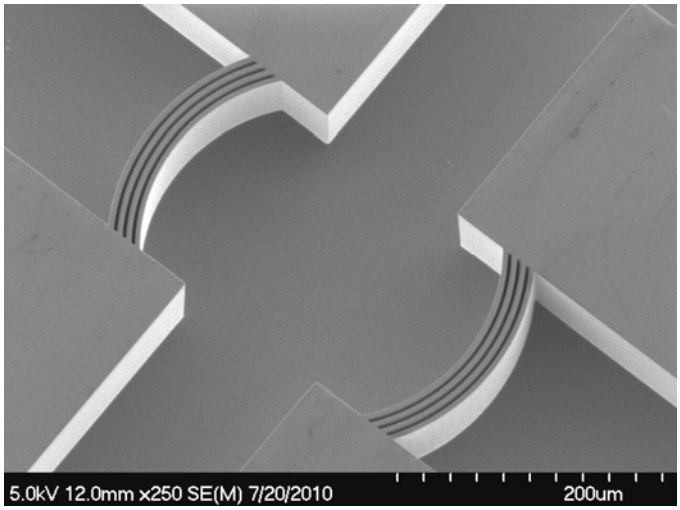

(a)

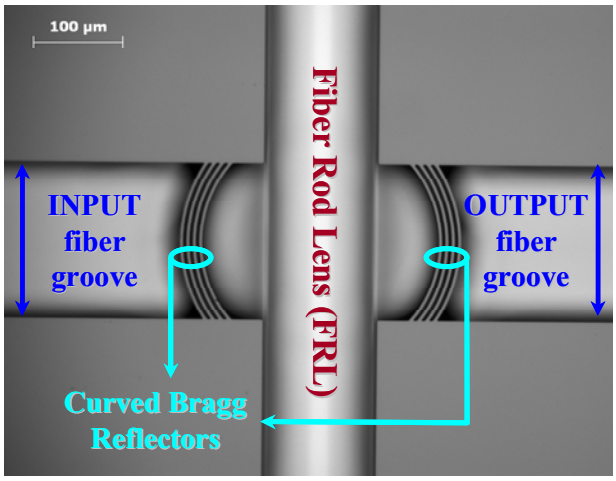

(b)

Fig. 6.3 Fabricated resonator for 2D confinement of light (a) SEM photos of FP cavity with Bragg mirrors of cylindrical shape (Here 4 silicon-air layers with the wide DRIE trench for the FRL (b) Microscopic photo of the silicon structure including the FRL placed inside the DRIE recess for the purpose of 'vertical' out-of-plane collimation.

6.4 Experiments and analysis

The fabricated devices were measured using in-plane injection and detection by cleaved fibers. A tunable laser source is used in conjunction with a power-meter for achieving the wavelength sweep and recording the spectral response. 5 axes positioners were used for aligning both the injection and the detection fibers. Photo of the measurement setup is shown in Fig. 6.4. The minimum recorded full width at half maximum (FWHM) is 0.1765 nm leading to a Q-factor of 8818. These values are obtained for the cavity A having four silicon-air layers per mirror and a physical length L = 265.8 µm and R = 140 µm. Fig. 6.5 shows the measured spectral response of this device. It is noteworthy, in our case, that the physical length is different from the optical length due to the presence of the FRL whose refractive index n = 1.47. Thus, the optical length is equal to 324.6 µm.

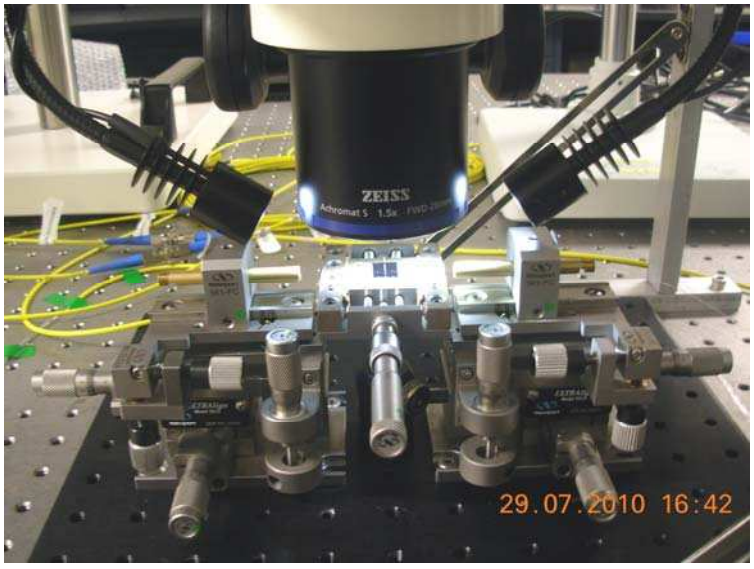

Fig. 6.4 Photo of the measurement setup showing the device under test (DUT), the micropositioners and the optical microscope

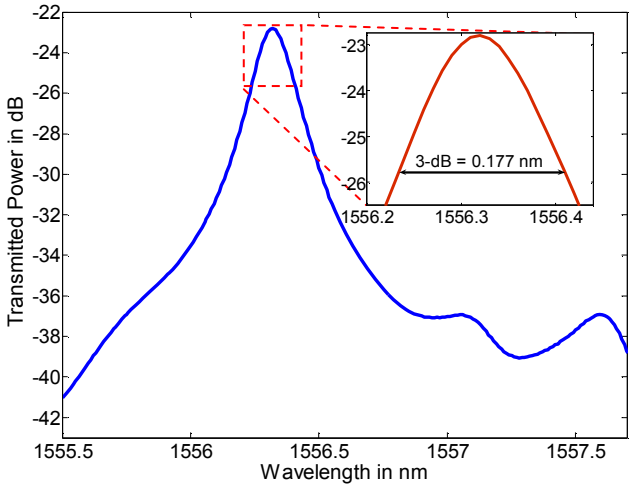

Fig. 6.5 Measured spectral response on a cavity of length L = 265.8 µm. designed with cylindrical mirrors of radius of curvature R = 140 µm with 4 silicon-air Bragg layers. The linewidth is 0.177 nm also corresponding to a Q-factor of 8818.

Other devices with different number of Bragg layers were tested to study the impact of the mirror reflectance on the Q-factor. The corresponding results are shown in Fig. 6.6. We find that as the number of layers N increases, the Q-factor increases accordingly up to N = 4 where Q = 8818. The results obtained confirm the trend of the Q-factor observed in an ideal FP cavity with planar mirrors and given by:

$$Q = \frac{2\pi nL}{\lambda_0}\left(\frac{\sqrt{\Re_{eff}}}{1-\Re_{eff}}\right) \qquad (6.24)$$

with $\Re_{eff} = \gamma.\Re$, where γ denotes the intra-cavity coupling efficiency identified as the major source of losses in these cavities as will be explained later in this chapter.

The relation between Q and N breaks as N increases furthermore, since the Q-factor diminishes to 6068. This might be attributed to the loss of the critical dimension which becomes more pronounced as N increases. The loss of the critical dimension reduces $\Re$ below the theoretically estimated values, which degrades Q. A similar trend was observed for cavity B with R = 200 µm. Fig. 6.6b shows a magnified view of Fig. 6.6a for the cavity B having R = 200 µm illustrating a similar degradation in the Q-factor as observed for the first cavity with R =140 µm. It is worth to mention that the latter cavity was found to perform better since the cavities with larger R tend to the behavior of the cavities based on planar reflectors.

Using equation (6.24), for estimating $\Re_{eff}$ from the experimental result shown in Figure 6.6, we found that for an FSR = 3.5 nm and FWHM = 0.1765 nm, $\Re_{eff}$ = 85.51% compared to $\Re_{theory}$ = 99.98%. The discrepancy between both values is due to many reasons. Among these, we can cite: (1) The loss of the critical dimension which introduce overetching in the Bragg layers and reduces the reflectance below the expected value. (2) The mirrors surfaces which are not perfectly smooth, they exhibit some

roughness which induce scattering losses. (3) The reflections at the interfaces of the FRL and (4) the intra-cavity coupling efficiency γ which is supposed to be higher than in the first architecture but is still well below 100%.

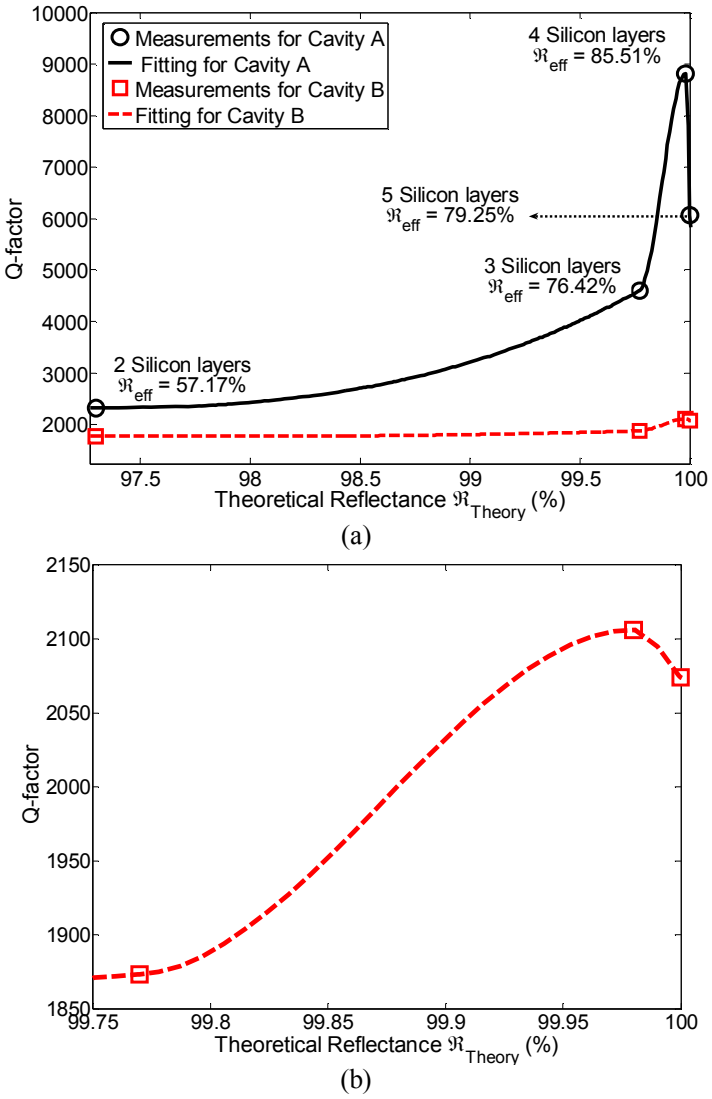

Fig. 6.6 (a) Experimental values of *Q*-factor vs. theoretical reflectance of the curved Bragg mirrors for the two cavities A and B: Cavity A has a length $L = 265.8$ µm and radius of curvature $R = 140$ µm. Cavity B has $L = 385.6$ µm and $R = 200$ µm. (b) The lower curve gives a magnified view for cavity B. illustrating a similar degradation in the *Q*-factor as observed for cavity A.

The loss of the critical dimension has been simulated by introducing a finite error (± 60 nm) in the silicon layer thickness. The simulations are based on the developed model for multilayered stack theory [79] used for planar mirrors. We assume that the use of this model is valid in our case as we are in the limits of the paraxial approximation. The simulation results are shown in Fig. 6.7.

The introduced error (± 60 nm) shifts the overall reflectance bandwidth about (± 20 nm). So, if the fabrication technological introduces an error of -60 nm, and considering our operating point the wavelength λ= 1556 nm, then instead of getting $\Re$ =99.98% in the ideal design, we get $\Re$ =96%.

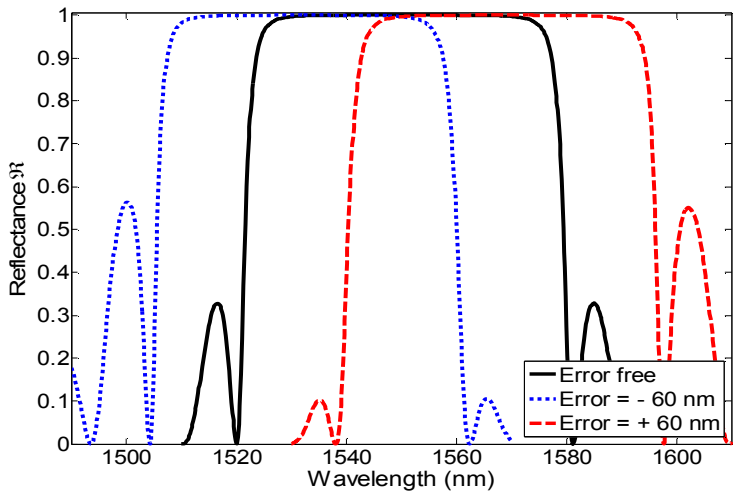

Fig. 6.7 Simulated reflectances of the multilayered Bragg mirrors with an introduced error ± 60 nm to study the impact of the technological error on the device performance. The error free response is also shown in the graph, as a reference.

In order to mimic the tunability behavior of our resonators, spectral measurements have been carried out for cavities having similar design but differing only in their physical lengths. Two different cavity physical lengths (L = 265.8 and 280 µm) have been measured, both are based on 4 silicon layers per mirror with a radius of curvature R = 140 µm. The spectral responses are superimposed in Fig. 6.8.

Furthermore, a simple test has been done to highlight the importance of the FRL on the cavity performance. In this test, a design based on two silicon-air layers per mirror has been measured with and then, without the insertion of the FRL. Though the reflectance of the two silicon-air layers is not very high, this device has been chosen for this specific illustration because it obeys the stability conditions (as discussed in the next section) in both cases: with and without the FRL. The corresponding measurements results, shown in Fig. 6.9, reveal that the Q-factor improves by a factor of 3.68x for resonance wavelength around 1615 nm, also revealing transverse modes. A similar improvement (4x) of the Q-factor has also been recorded for a cavity based on mirrors with 3 silicon layers.

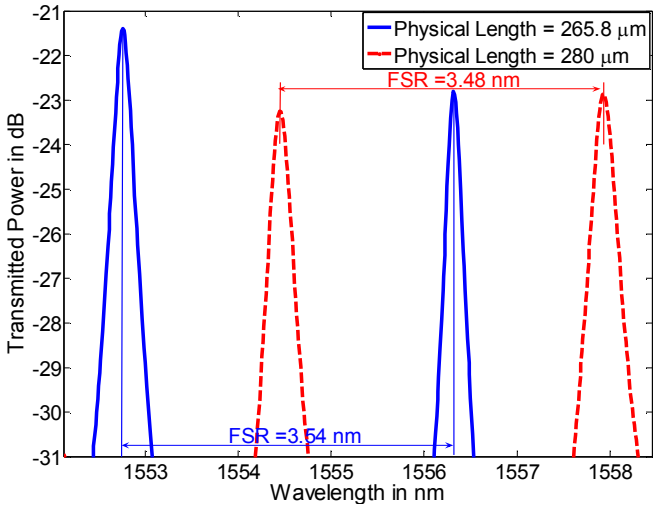

Fig. 6.8 Measured spectral response of FRL cavities with two different cavity lengths L = 265.8 and 280 µm. (The cylindrical mirrors have 4 silicon-air layers).

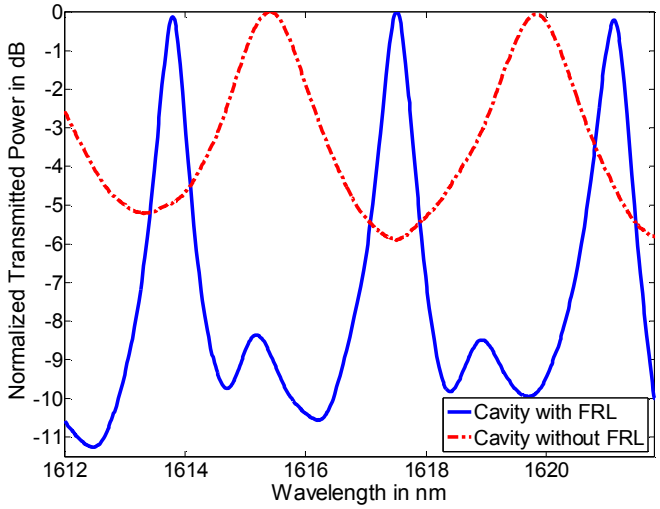

Fig. 6.9 Comparison of measured responses with and without the FRL, illustrating the (3.68x) improvement in the *Q*-factor. (Here the mirrors consist of 2 silicon-air layers).

6.5 Numerical simulations

Since the architecture is novel and is quite different from the conventional spherical resonators, the modes propagating inside these structures are not determined using closed form relations. Obviously, numerical simulations can be done using commercial FEM simulators like HFSS, COMSOL multiphysics...etc, but the dimensions of the structures (>250 µm) are enormous with respect to λ/10 ~ 0.15 µm (typical required meshing pitch) for being executed by running a single for the whole structure.

6.6 Discussion on Optical loss in Fabry-Perot cavities

If we consider the case of ideal cavities, referring to equation (6.25), the Q-factor would increase linearly with the cavity length *"L"* without any bounds. Practically, the cavity exhibits non-negligible losses because the light beam expands and finishes by escaping from the boundaries of the cavity. This issue is modeled by equation (6.25) in the term γ. In the ideal case, the intra-cavity coupling efficiency, γ, defined as the overlap between the mode $\Psi_{m,0}$ and itself after one full round trip equals 1 (6.26). In the case of lossy cavity, γ is different from 1 and the *Q*-factor behaves differently as explained hereafter. This second case will be considered over all the rest of this discussion for both the planar and the cylindrical cavities.

$$Q = \frac{2\pi nL}{\lambda_0}\left(\frac{\sqrt{\gamma\Re}}{1-\gamma\Re}\right) \tag{6.25}$$

where n is the cavity refractive index, λ_0 is the wavelength in free space and $\Re$ is the mirror reflectance.

$$\gamma_{m,0} = \frac{\left|\iint_{(D)} \psi_{m,0}(x,y,0)\cdot\psi^{*}_{m,0}(x,y,2L)dxdy\right|^2}{\iint_{(D)}\left|\psi_{m,0}(x,y,0)\right|^2 dxdy \cdot \iint_{(D)}\left|\psi_{m,0}(x,y,2L)\right|^2 dxdy} \tag{6.26}$$

Looking over the behavior of Q for both the curved cavities based on cylindrical mirrors and the planar cavities, we notice that the Q-factor exhibits a linear increase at small L. Further increase in L leads to degradation of the Q-factor. This might be explained by the fact that the Gaussian beam expansion is not very significant at small L's, and we can say that the Q-factor keeps increasing almost linearly with L. On the other hand, when L increases, the loss mechanism becomes dominant since Γ becomes lower than 1. The performance in terms of the Q-factor becomes rather poor which renders the combination of both long L and large Q almost unfeasible for cavities with planar mirrors. This issue is depicted from equation (6.25).

Fig. 6.10 illustrates a plot of γ versus L for the cylindrical cavities and the planar cavities for two different spot sizes for the Gaussian beam. In both cases, the coupling efficiency is higher for the case of the cylindrical cavities and this translates into an improved Q-factor as shown in Fig. 6.11. In Fig.6.11, the tendency of the Q-factor for the planar and the cylindrical cavities is illustrated together with the ideal case. The simulation parameters were as follows: λ_0 = 1550 nm, $\Re$ = 99.98%, the waist of the Gaussian beam = 19 μm, and the mirror radius of curvature R = 140 μm for the curved cavity. Obviously, the performance of the cylindrical cavities surpasses that of the planar cavities due to its better focusing capability along one transverse direction.

For the same design presented here, an increase of the spot size to 50 μm shifts the peak of the Q-factor to the right. This can be explained by looking to the beam characteristics: the larger the spot size, the longer will be the working distance. Thus, the coupling efficiency Γ maintains a high value which increases the Q-factor.

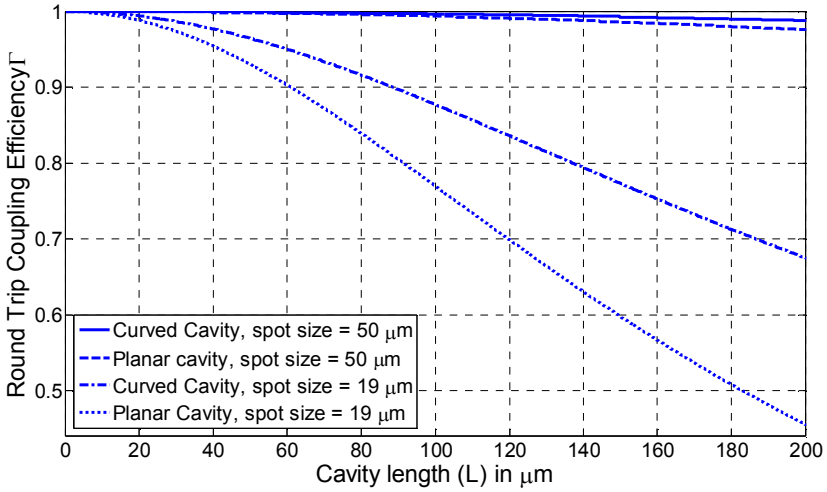

Fig. 6.10 Round Trip Coupling Efficiency γ versus the cavity length L for planar and curved cavities having R = 140 μm. Two different spot sizes were considered 19 μm and 50 μm. The performance of the curved cavities overcomes that of the planar cavities for the two spot sizes.

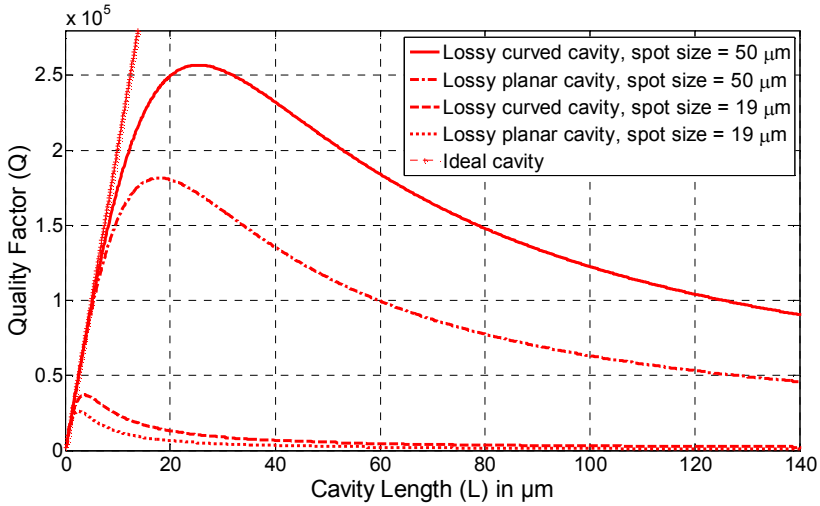

Fig. 6.11 Quality factor versus the cavity length L for planar and curved cavities having R = 140 µm. Ideal and lossy cavities are compared for 2 different spot sizes were considered 19 µm and 50 µm. In the ideal case, the Q-factor increases linearly with L. For the other cases, the performance of the curved cavities overcomes that of the planar cavities for the two considered spot sizes. The peak of the Q-factor shifts to longer L for the 50 µm spot size for its long working distance.

For applications involving Cavity Enhanced Absorption Spectroscopy CEAS [89, 90], the designers focus on the figure of merit FxL where F is the cavity finesse. From this point of view, this quantity, referred to as the enhanced optical path L_{enh}, has an importance as it represents the gain in the optical path needed to provide strong interaction between the detected species and the resonating optical power. This, in turn, leads to cavity enhancement. The deployment of F is more attractive than Q because if the cavity dimensions change, F does not change as it is related to the cavity reflectance only. However, there is direct relation between F and Q that is given by equation (6.27):

$$F = \frac{FSR \times Q}{\lambda_0} \tag{6.27}$$

Which leads to: $L_{enh} = F \times L = \frac{\lambda_0 \times Q}{2n}$ (6.28)

Obviously, L_{enh} has the same tendency as the Q-factor plotted previously as shown in Fig. 6.12.

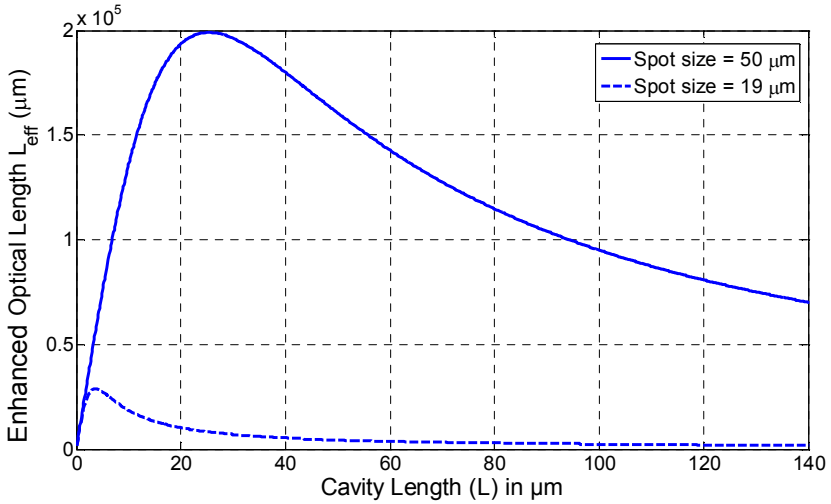

Fig. 6.12 Enhanced Optical Length L_{eff} versus the cavity length L for curved cavities having R = 140 µm. Two different spot sizes were considered 19 µm and 50 µm.

In this context, we propose another figure of merit for FP cavities: *QxL*. The interest in this parameter comes from the difficulty of combining both High *Q* and large *L*. To highlight the importance of this quantity, we plot *QxL* versus *L* for both planar and cylindrical cavities based on fully integrated silicon-air cavities. The simulation of curved cavities is based on *R* = 140 µm and a spot size of 19 µm. The operating points for the previously developed works [12, 55, 56, 58] are illustrated in Fig. 6.13 together with the operating points coming out from this work as detailed earlier.

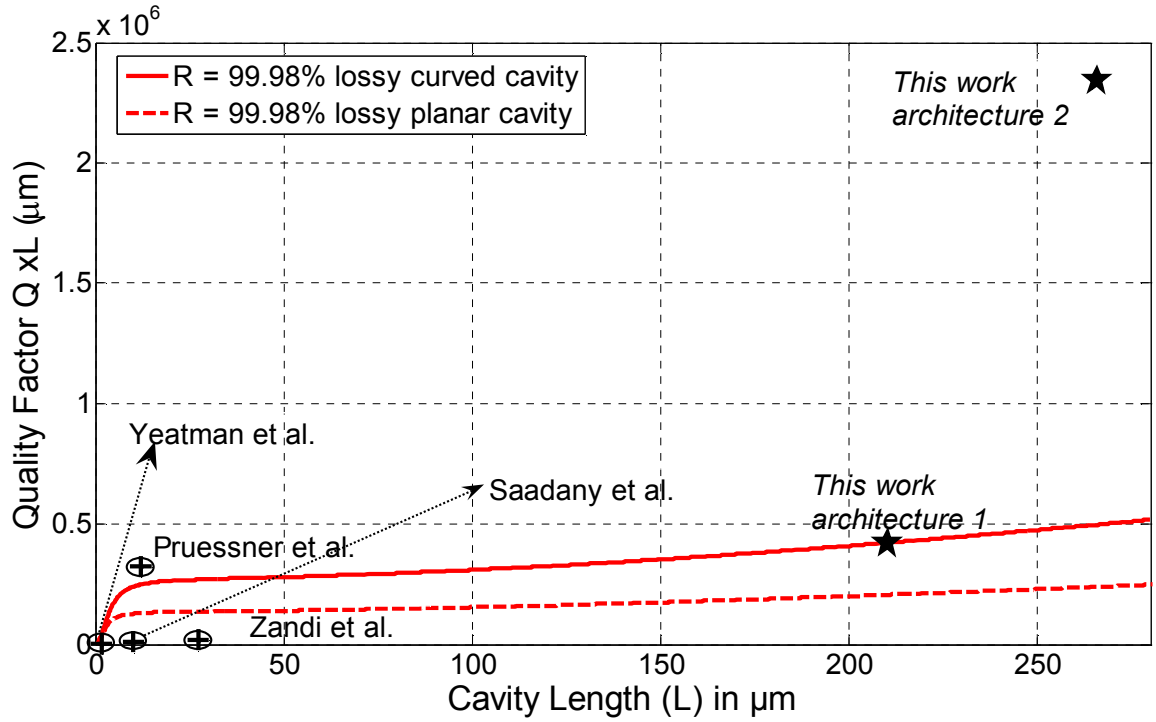

Fig. 6.13 QxL versus L for the Silicon-Air Fabry-Pérot cavities. The different operating points of the previous works are illustrated with the simulation curves for the planar and the curved cavities having R = 140 µm and spot size = 19 µm. The operating points of the proposed architecture are also presented.

As shown in fig. 6.13, three designs lie below the *QxL* curve for planar cavities. The design presented in [82] lies above both curve because his cavity is based integrated rib waveguide, unlike the three other designs. This improves the *Q*-factor above the curved cavities but his design has a drawback since the cavity length is quite low = 12 µm and also the cavity is made of silicon which limits the application domains away from microfluidics.

Even though the work presented by [91] has an excellent performance ($QxL = 7.83 \times 10^8$ µm), it is not shown in this graph because the device dimensions are above the micrometric range and not fully integrated and so, it is not adequate for applications involving chemical analysis.

For the work that has been detailed earlier, $QxL = 4.2 \times 10^5$ is obtained µm for a cavity with cylindrical mirror with *L* = 210 µm for the structure with one dimensional confinement of light. On another hand, $QxL = 2.34 \times 10^6$ µm is obtained for a cavity with *L* = 265.8 µm for the structure with two dimensional confinement of light.

6.7 Conclusion

In conclusion, a new design of Fabry-Pérot (FP) cavity based on curved surfaces and Fiber Rod Lens has been presented. Our first motivation was to improve the performance as compared with the FP cavities based on planar mirrors. The design combining both the cylindrical Bragg mirrors and a Fiber Rod Lens (FRL) shows a higher performance in terms of Q-factor. The maximum recorded value was Q = 8818 for a cavity built with Bragg reflectors having 4 silicon layers. The corresponding finesse is 20 and remains much below the values that can be found in previous reports. In our case, both this device and the one presented in chapter 5 share the advantage of high Q-factor and long cavity length L > 200 µm, which can also be expressed in terms of a figure of merit $Q.L$, up to $Q.L = 2.10^6$ µm for the second design.

Relations have been derived between the maximum (minimum) values of mirror radius of curvature R and the free space propagation distance d_{air} in air that maintain a stable behavior for the optical resonator of the 2D design. The measured data have been analyzed to deduce the effective reflectance of the curved mirrors. The impact of the technological error has been evaluated through simulations.

PART III

Sensing Applications of Optical Interferometers: Optical Profilometry

Chapter 7

All-silicon Optical Interferometric Probe for Profile Measurement in Tiny Holes

7.1 Objective and Motivation

This chapter is devoted to study, design, fabrication and preliminary characterization of an optical microsystem based on Michelson interferometer for the purpose of dimensional measurement, including the distance to an obstacle which is demonstrated in this work. Our ultimate goal is to evolve to applications such as surface profile measurement and metrological-grade characterization of the dimensions and shape of tiny holes. The optical microsystem width falls in the sub-millimeter range and its length is about 1 cm. The configuration proposed here represents the core of the optical profiler. The proposed microsystem is an optical probe designed to achieve non-contact measurements of diameters and of defects of circularity, in confined spaces such as in injector nozzles. Therefore, we implemented an optical method, proposed as an alternative to other previously reported techniques based mainly on mechanical contact of a stylus [92-95].

High performance metrology requires highly stable references. When considering measurement of dimensions, the optical wavelength is among the most stable dimension references to date. Therefore, we can take advantage of this wavelength stability for achieving metrological-grade dimensional measurements through implementing an interferometric method which is our ultimate goal in this research. Interferometric methods are being already widely used in macroscopic instruments for the purpose of measuring film thickness, distance to obstacles as well as surface profiles.

Beside the use of stable monochromatic light, other interferometric methods rely either on white light or on wavelength sweep. The latter method is firstly used in this preliminary work, to provide a quick evaluation of our fabricated device.

7.2 Architecture of the optical probe

In this section, the design is presented, it is designed to operate in the infrared range around 1550 nm. A Schematic view of the envisaged optical probe and a zoom on the interferometer architecture are shown in Fig. 7.1a and 7.1b.

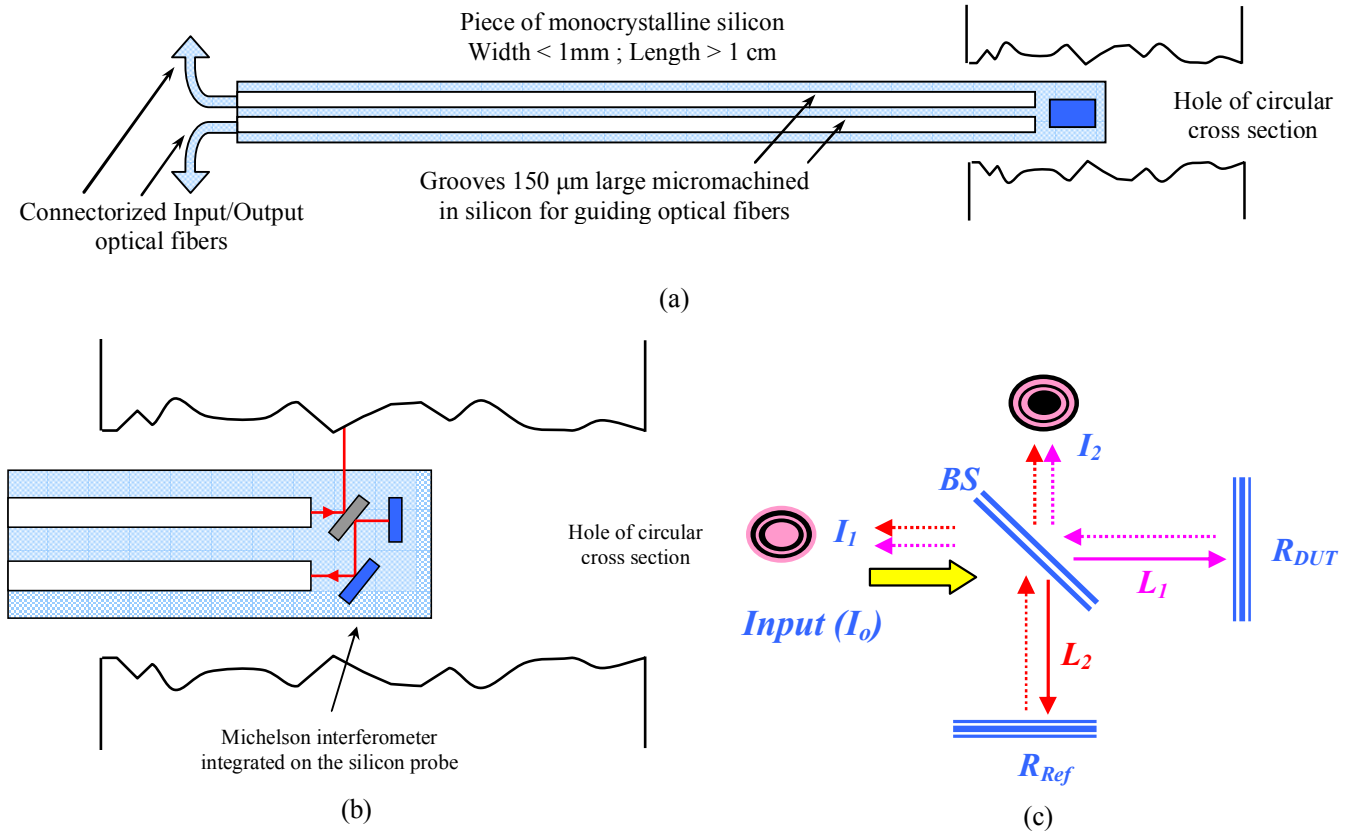

Fig. 7.1 (a) Schematic view of the entire optical probe formed from a block of single crystal silicon and incorporating a Michelson interferometer (the head of the probe) and grooves forming guides for input/output optical fiber. The input is designed to inject the light (monochromatic) and the output is designed to gather the interferogram when the piece is rotated around the axis and translated along the axis. (b) Architecture envisaged for the Michelson interferometer (c) Reminder for the Michelson interferometer

The Michelson interferometer has been explained in details in chapter 2. The few lines here serve only as a reminder before going into deep details about the new design. In its simplest form, the Michelson interferometer consists of a Beam Splitter BS (45° tilted mirror of 50% reflectance and 50% transmittance) and two mirrors named *reference mirror* and *test mirror*. Light incident on the beam splitter is partially transmitted and partially reflected to the reference and the test mirrors which, in turn, reflect the light back to the beam splitter. In general, light beams reflected by the mirrors are not identical since they may run different path lengths. Thus, they combine at the beam splitter and they produce an interference signal called the interferogram. Again, the beam splitter partially reflects and partially transmits the interferogram. A schematic representation of the Michelson interferometer is shown in Fig. 7.1c.

7.3 Optical interferometeric probe operating in the near infrared range

7.3.1 Design description

The conventional architecture of Michelson interferometer shown in Fig. 7.1c cannot be used directly to accomplish the assigned function of detecting surface profiles in cylindrical holes. Some

modifications have to be introduced to the classical architecture in order to get a probe similar to the one shown in Fig. 7.1. Also, issues related to design and measurements have to be considered. In what follows, the different points are listed:

- One of the two mirrors (called test mirror) is replaced by the surface of the Device Under Test DUT.
- As we are also interested in measuring the interferogram of transmission, a novel architecture is realized to obtain parallel input and output optical fibers, aligned on the same side of the device. Thus, we insert a third mirror tilted at 45°, parallel to the BS. It reflects the transmission interferogram into the output fiber as shown in Fig. 7.2.
- Both input and output fibers are glued after alignment. We therefore tackle a new point which is the packaging of optical components.
- Unlike FTIR microspectrometers based on Michelson interferometers [96-98], the micro-profilometer has the optical path difference as unknown. To determine the length of the optical path, which in turn gives the distance, many methods are possible. To fasten the characterization of the fabricated devices, we dediced to proceed by recording the optical power while scanning over the wavelength, and then we apply FFT on the resulting interferogram to find the optical path difference. After numerical treatment, the distance to the surface – and ultimately the surface profile h(x, y) - is fully determined. The numerical treatment is outside the scope of the thesis and the related work will not be addressed here.
- The optical path (x2) might be greater than the working distance of standard fibers as illustrated in Fig. 7.3. So, lensed fibers with large working distance (1 – 2 mm) shall be used.
- Since the surface of DUT might be rough and of low reflectance with respect to the reference mirror, then the reflectance of the BS has been adapted accordingly to improve the contrast of the measured interferogram. Different designs have been produced to accommodate for the different qualities of the measured surfaces.

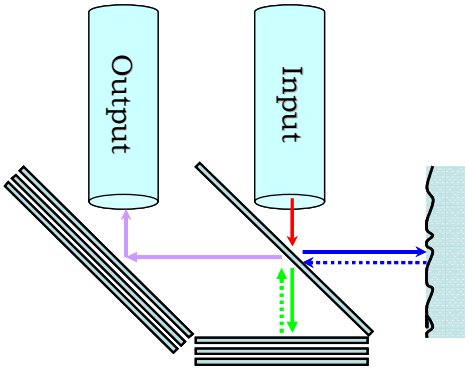

Fig. 7.2 Proposed architecture for the Michelson interferometer.

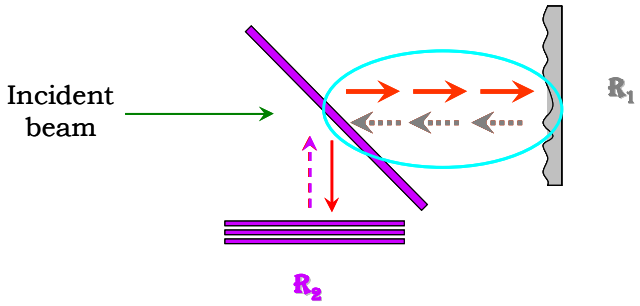

Fig. 7.3 Large optical path might be run in the path to the DUT.

7.3.2 Layout of the optical probe

A typical layout of the unit cell is shown in Fig. 7.4 along with the fiber grooves and the reservoirs used to collect the excess of glue used for packaging. Also, a zoomed view of the Michelson interferometer is shown as well. In the figure, we can see the BS, one Bragg mirror acting as reference mirror (placed horizontally) and another Bragg mirror (parallel to the BS) used to reflect the transmission interferogram to the output fiber. The test mirror of the Michelson interferometer has been removed and it is replaced by the external surface of the tested elements as illustrated earlier in Fig. 7.1. The basic unit cell is attached to the surrounding rigid silicon frame using two small silicon links. These links are broken by torsion to separate the unit cell from the wafer after the fabrication is completely finished. The probe width is 550 µm and the probe length is 4 mm. The width of the fiber grooves is 150 µm.

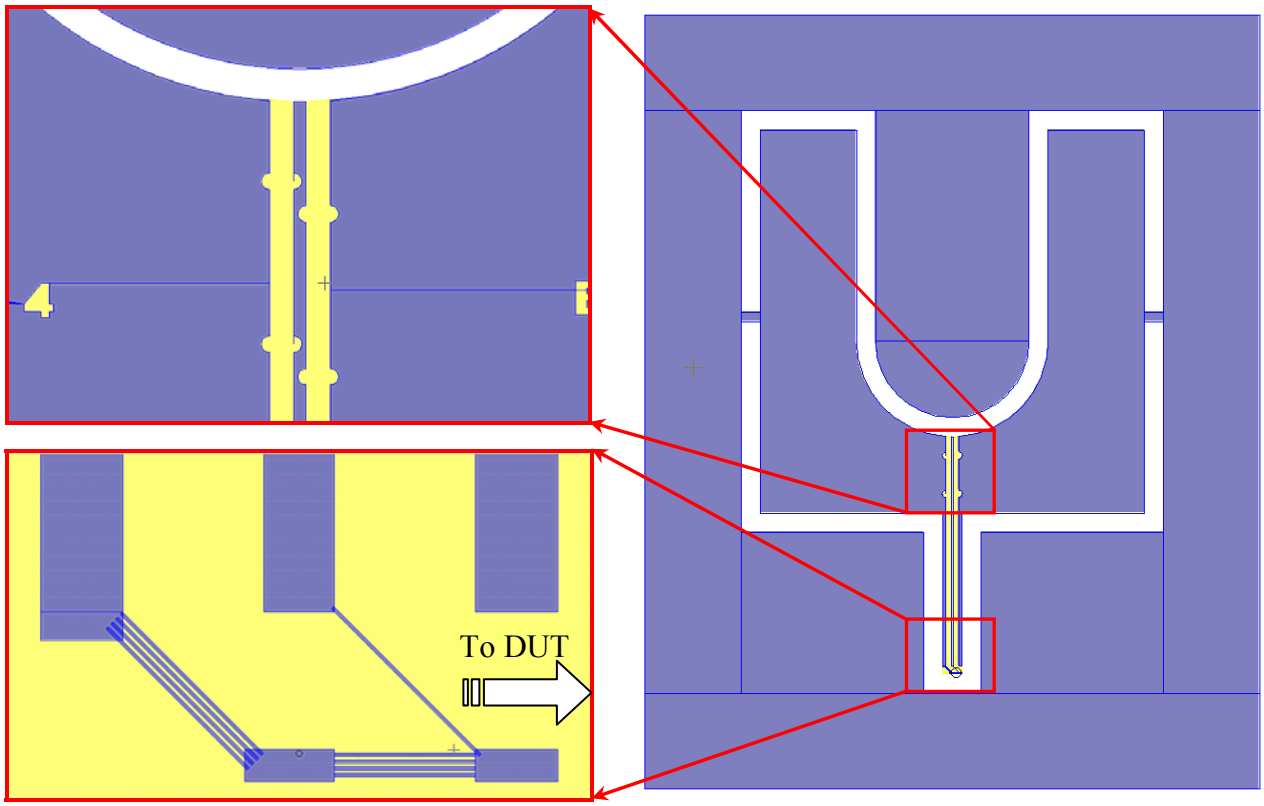

Fig. 7.4 Layout of the device with zoom on the fiber grooves + reservoirs and the interferometer.

7.3.3 Layout of the optical probe with ball lens

Though compact, the device presented above might not perform perfectly regarding the lateral resolution. In the best cases, the spot size of the injected light will be 50 µm. The resolution cannot be attain values lower than 50 µm unless we reduce the spot size or we implement "sub-pixel"resolution algorithms. To overcome this problem and to improve the resolution limit, we thought about packaging of a ball lens together with the interferometer.

For this purpose, we devised the layout shown in Fig. 7.5. It resembles the previous design except that a third wide groove has been introduced to facilitate the insertion of the ball lens whose path ends in front of the BS. A circular opening has been drawn in the backside mask to provide a stable support for the ball lens and avoid that it runs in the die. The role of the ball lens is to focus light reflected by the BS to the DUT and back from the DUT to the BS. This way, we can reduce the spot size incident of the measured surface and the resolution can be improved. Only ball lenses having diameter of 125 µm will be suitable because they maintain the optical axis of the propagating light unchanged. The probe width is 750 µm and the probe length is 4 mm. The width of the fiber grooves is 150 µm.

Snapshot of the full mask is shown in Fig. 7.6. Different variations of the design shown above have been integrated on the mask. They differ mainly in the BS splitting ratio and the number of Bragg layers for the reference mirror which translates into different reflectances.

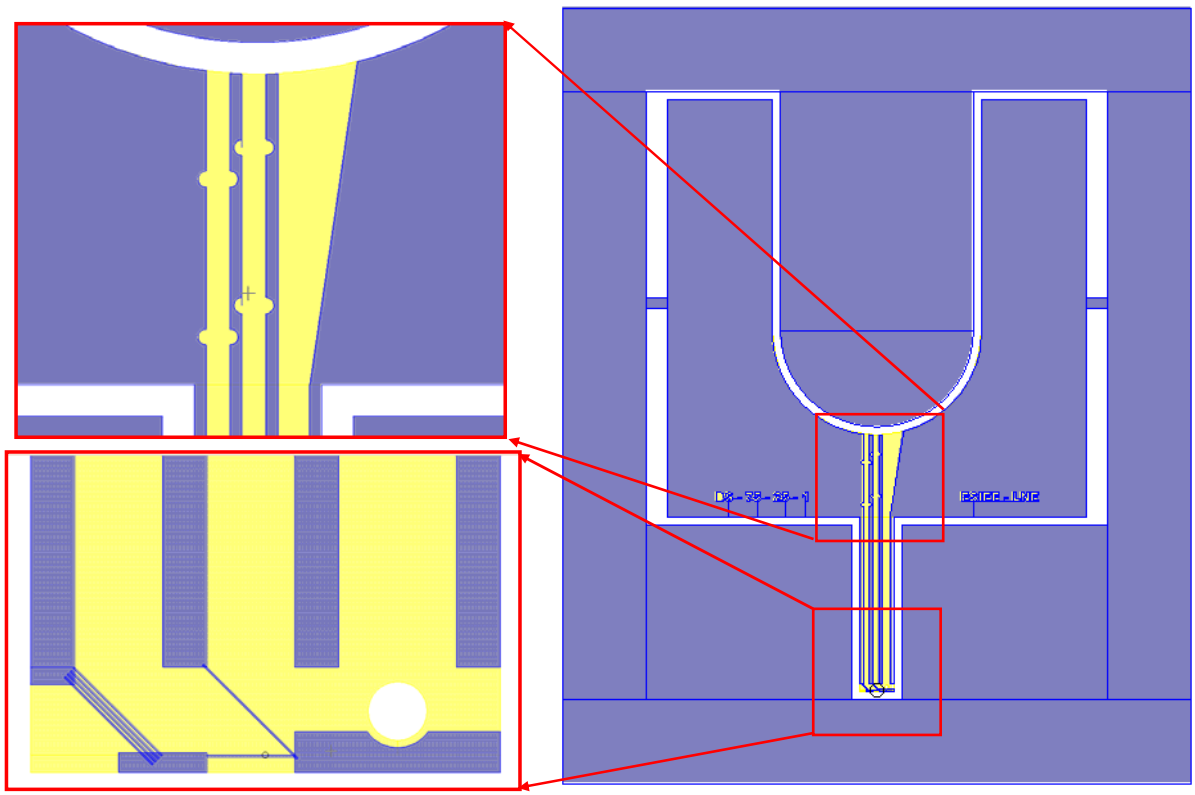

Fig. 7.5 Layout of the device with ball lens together with zoom on the fiber grooves + reservoirs and the interferometer.

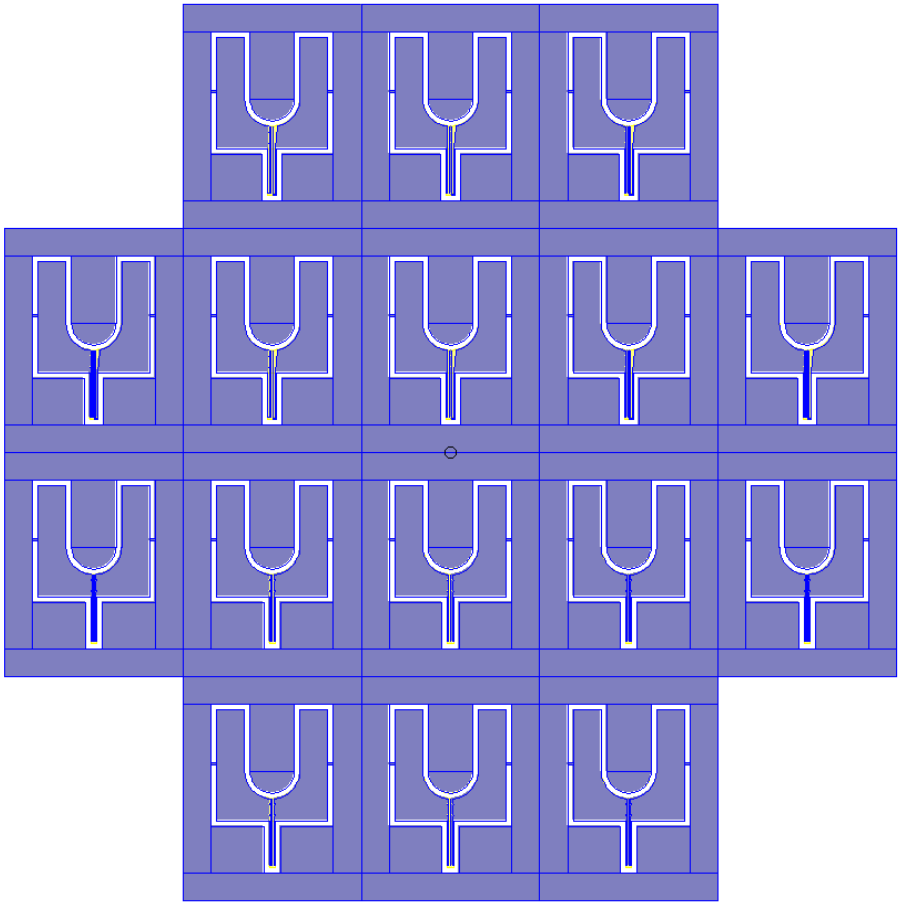

Fig. 7.6 Full mask used to fabricate the optical probe based on Michelson interferometer.

7.3.4 Fabrication

The devices have been fabricated following the process explained in chapter 3 and using the layout presented in the previous section. The structures are vertically etched on silicon using DRIE over 103 μm. Backside etching was necessary in order to liberate areas surrounding the probe which also facilitate the separation of the dies later. SEM photos of the fabricated devices are shown in Fig.7.7. Photos of the wafer and the entire device are shown in Fig. 7.8.

Although the yield of the fabrication process was satisfying and most of the mirrors and the thin BS slabs were produced without being damaged, the opening of the ball lens was never produced after the backside etching step due to the non-verticality of this etching process. This defect will be addressed in later fabrication processes to allow the investigation of the interferometer with ball lens.

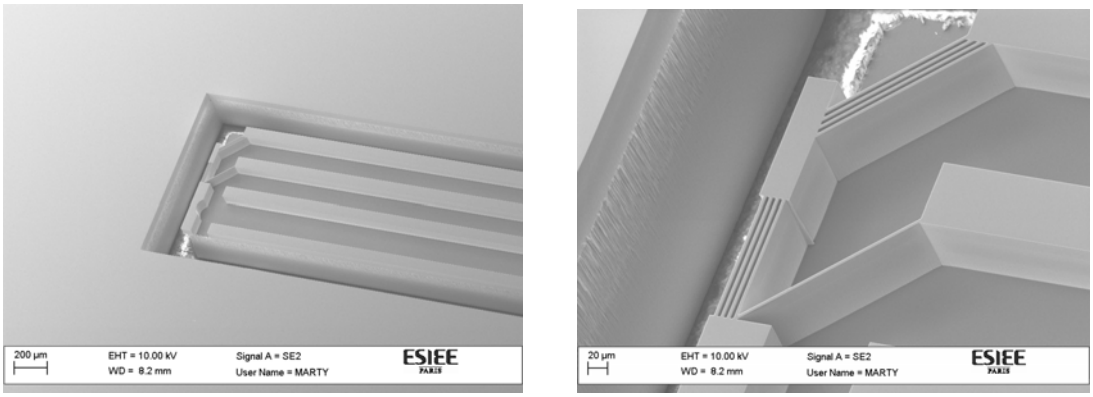

(a) (b)

Fig. 7.7 (a) SEM photo of the fabricated device showing the area released around.
(b) Zoom on the interferometer showing its architecture with the BS and Bragg mirrors.

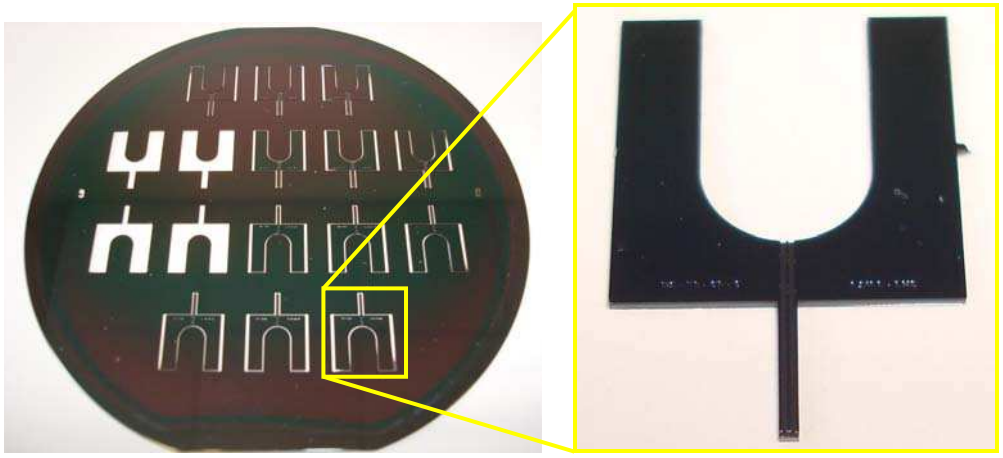

(a) (b)

Fig. 7.8 (a) Photo of the realized wafer (b) Photo of the entire device

7.3.5 Modeling and simulation

In this section, we highlight the analytical model used to design the interferometer. With the aim of simulating in a realistic manner the interferogram resulting from the whole optical probe (with special interest to contrast and related design optimization), we developed theoretical modeling taking into account several effects:

a. The different reflections, transmissions encountered by the light beams propagating in the Michelson interferometer (light absorption in silicon is neglected in the near infrared range. Light absorption in air is neglected as well).
b. The Gaussian nature of the light beam which expands while propagating is taken into account, leading to a reduction of light intensity coupled back to the fiber.
c. The effect of light scattering over the surface to be charcterized (due to sub-micron roughness) is embedded in the effective reflectivity of the tested surface.

The BS is a thin silicon slab of controlled thickness. Based on the multilayered stack theory outlined in section 3.2; we can deduce the transmittance T and the reflectance R of a thin film. Starting from equation (3.38) and (3.25), we have:

$$T = \frac{4\eta_0 \,\mathrm{Re}(\eta_m)}{(\eta_0 B + C)(\eta_0 B + C)^*} = \frac{4{\eta_0}^2}{4{\eta_0}^2 \cos^2(\delta) + \left(\frac{{\eta_0}^2}{\eta_1}\sin(\delta) + \eta_1 \sin(\delta)\right)^2} \quad (7.1)$$

$$R = \left(\frac{\eta_0 B - C}{\eta_0 B + C}\right)\left(\frac{\eta_0 B - C}{\eta_0 B + C}\right)^* = \frac{\left(\frac{{\eta_0}^2}{\eta_1}\sin(\delta) - \eta_1 \sin(\delta)\right)^2}{4{\eta_0}^2 \cos^2(\delta) + \left(\frac{{\eta_0}^2}{\eta_1}\sin(\delta) + \eta_1 \sin(\delta)\right)^2} \quad (7.2)$$

Where the definitions are kept unchanged as in chapter 3. *B* and *C* are got from the characteristic matrix of the thin film (BS in our case) and the emergent medium is the air with impedance η_0.

Based on these relations, we proceed to the design of the BS by controlling its thickness. Thickness control is important as it impacts the BS splitting ratio. MATLAB simulation for BS gives the result shown in Fig. 7.9:

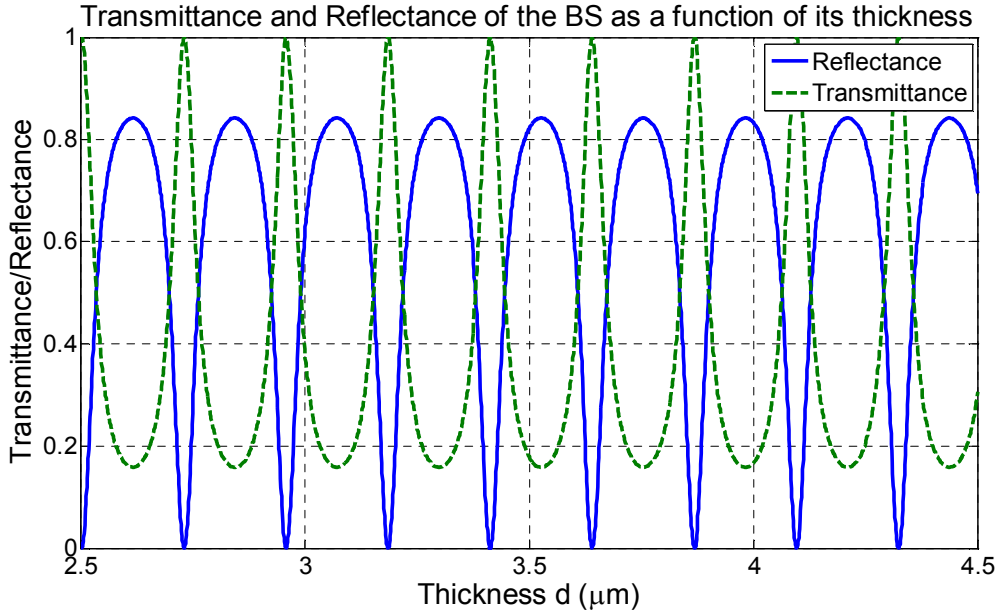

Fig. 7.9 MATLAB simulation for the BS transmittance T_{BS} /reflectance R_{BS} versus its thickness.

For absorbing free material, the BS exhibits a periodic response. In order to satisfy a certain splitting ratio, we select thicknesses lying over 3 μm because it can be produced technologically with good quality. Accordingly, we have the following dimensions h_{BS} for selected combinations of the BS reflectance –transmittance (R_{BS} – T_{BS}):

- (R_{BS} – T_{BS}) = 25% - 75% → h_{BS} = 3.623 μm

- $(R_{BS} - T_{BS}) = 50\% - 50\% \rightarrow h_{BS} = 3.609\ \mu m$
- $(R_{BS} - T_{BS}) = 75\% - 25\% \rightarrow h_{BS} = 3.58\ \mu m$

Now, we inspect the interferometer performance, from the contrast point of view, taking the expansion of the Gaussian beam into account. Denoting L_{DBR} and L_{DUT} as the distances from the BS to the reference mirror and from the BS to the Device Under Test respectively. Also, we denote R_{DBR} and R_{DUT} as the reflectances of the reference mirror and the Device Under Test respectively. The different parameters are shown in Fig. 7.10 below along with I_{1t}, I_{2t}, I_{1r}, I_{2r}

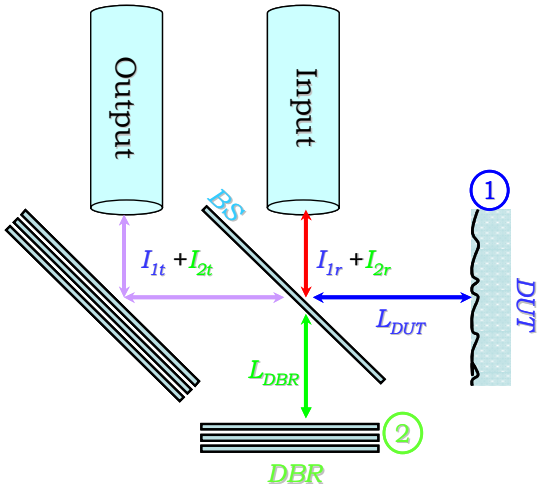

Fig. 7.10 Michelson interferometer with the different parameters used in the analytical model

On one hand, we have for the normalized intensities of the two light components interfering at the output fiber reflected (components of the transmission interferogram). One of them is reflected back from the DUT and one is reflected back from the reference mirror:

$$I_{1t} = R_{BS}T_{BS}R_{DUT}\frac{1}{1+\left(\frac{2L_{DUT}}{Z_0}\right)^2},\ I_{2t} = R_{BS}T_{BS}R_{DBR}\frac{1}{1+\left(\frac{2L_{DBR}}{Z_0}\right)^2} \tag{7.3}$$

On the other hand, we have for the normalized intensities of the two light components interfering at the input fiber (components of the reflection interferogram). One of them is reflected back from the DUT and one is reflected back from the reference mirror:

$$I_{1r} = R_{BS}R_{BS}R_{DUT}\frac{1}{1+\left(\frac{2L_{DUT}}{Z_0}\right)^2},\ I_{2r} = T_{BS}T_{BS}R_{DBR}\frac{1}{1+\left(\frac{2L_{DBR}}{Z_0}\right)^2} \tag{7.4}$$

Where Z_0 is the depth of focus of the Gaussian beam (refer to chapter 2). It is given by:

$$Z_0 = \frac{\pi W_0^2}{\lambda} \tag{7.5}$$

The transmission (t) and the reflection (r) interferograms are then given by:

$$I_{tot\_trans} = I_{1t} + I_{2t} + 2\sqrt{I_{1t}I_{2t}}\cos\left(\frac{2\pi}{\lambda}\left(L_{DUT} - L_{DBR}\right)\right) \tag{7.6}$$

$$I_{tot\_ref} = I_{1r} + I_{2r} + 2\sqrt{I_{1r}I_{2r}}\sin\left(\frac{2\pi}{\lambda}\left(L_{DUT} - L_{DBR}\right)\right) \tag{7.7}$$

So, the contrast of transmission (t) or reflection (r) interferograms can be calculated from the formula:

$$C = \frac{2\sqrt{I_{1(t,r)}I_{2(t,r)}}}{I_{1(t,r)} + I_{2(t,r)}} \tag{7.8}$$

According to the previous formulae, we can predict the performance of the interferometer. Considering a lensed fiber with spot size = 59 μm and working distance = 2 mm, $R_{DUT} = R_{DBR} = 90\%$, $L_{DBR} = 100$ μm and operation at $\lambda = 1550$ nm, we get the following results shown in Fig. 7.11 and 7.12:

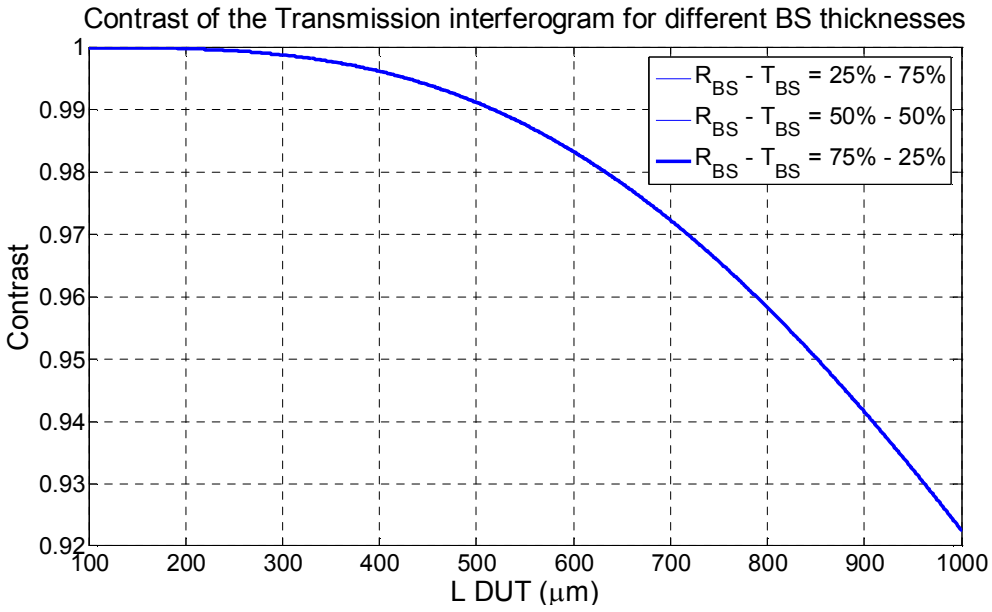

Fig. 7.11 Contrast of the transmission interferogram for different h_{BS} thicknesses.

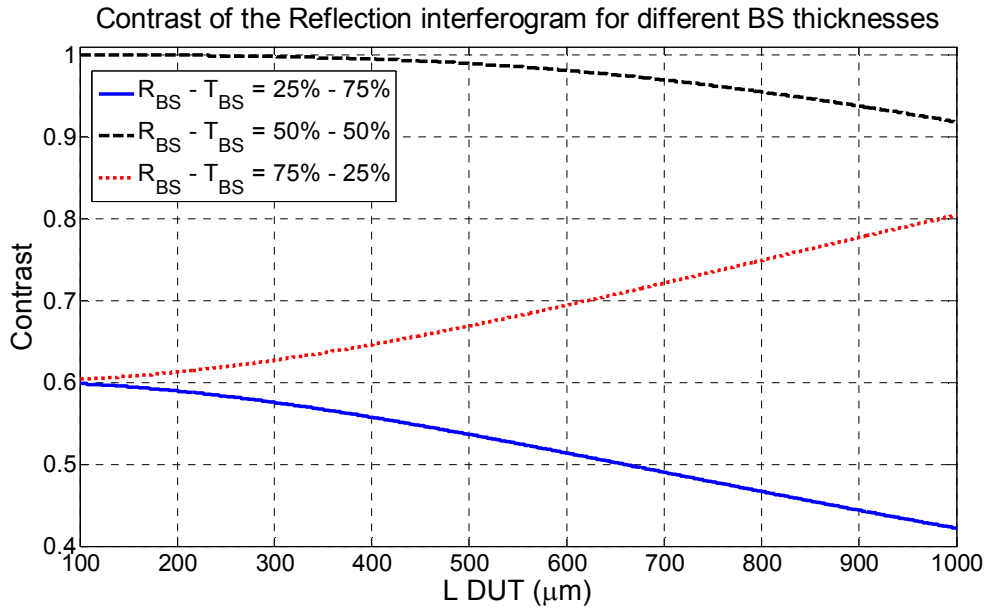

Fig. 7.12 Contrast of the reflection interferogram for different h_{BS} thicknesses.

Inspection of both interferograms for BS of 50%-50% splitting ratio at h_{BS} = 3.609 μm, we can calculate the interferogram by varying the distance L_{DUT}. We obtain the curves shown in Fig. 7.13 and Fig. 7.14 which reveal a large transmitted power.

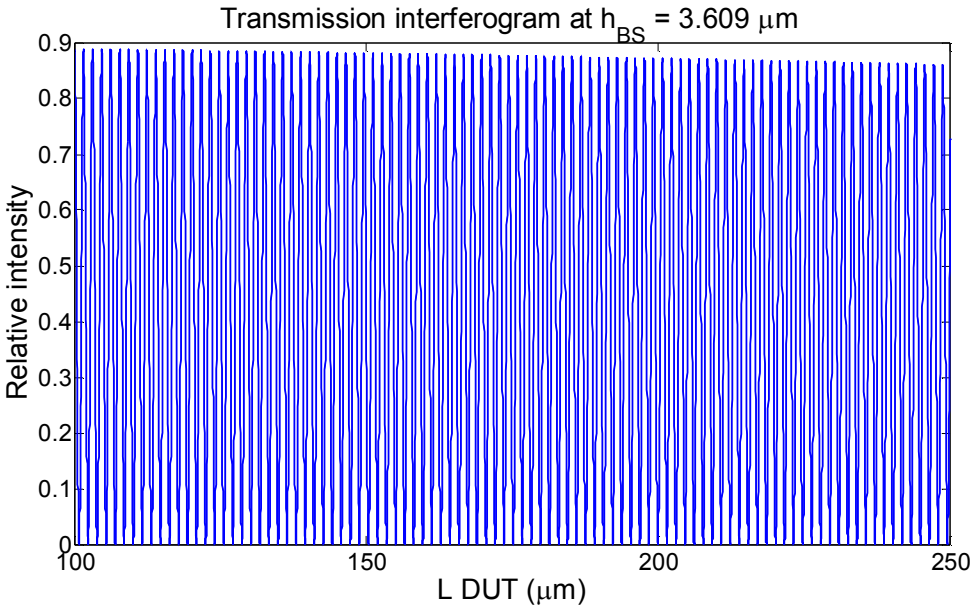

Fig. 7.13 Transmission interferogram at h_{BS} = 3.609 μm (50-50 splitting ratio).

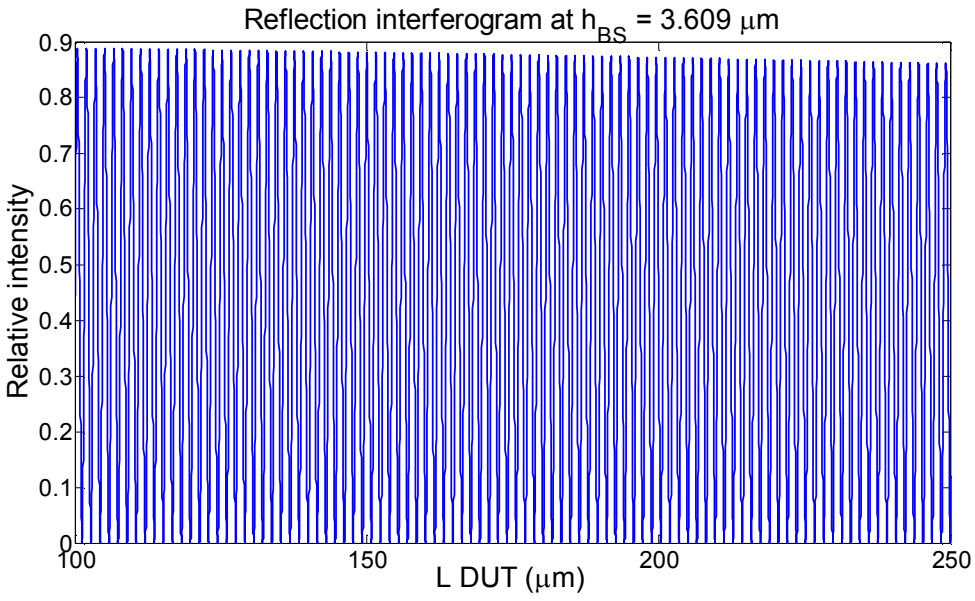

Fig. 7.14 Reflection interferogram at h_{BS} = 3.609 μm (50-50 splitting ratio).

We finalize this part by comparing the contrast for three different spot sizes as graphed in Fig. 7.15. We assume that the injection and the collection fibers are located very close to the BS and the output mirror respectively and hence the Gaussian beam diffraction in air has negligible effect on the beam characteristics. Obviously, the contrast degrades, as the spot size decreases especially at larger L_{DUT}*'s* since the Gaussian beam expands largely over small distance for smaller spot sizes.

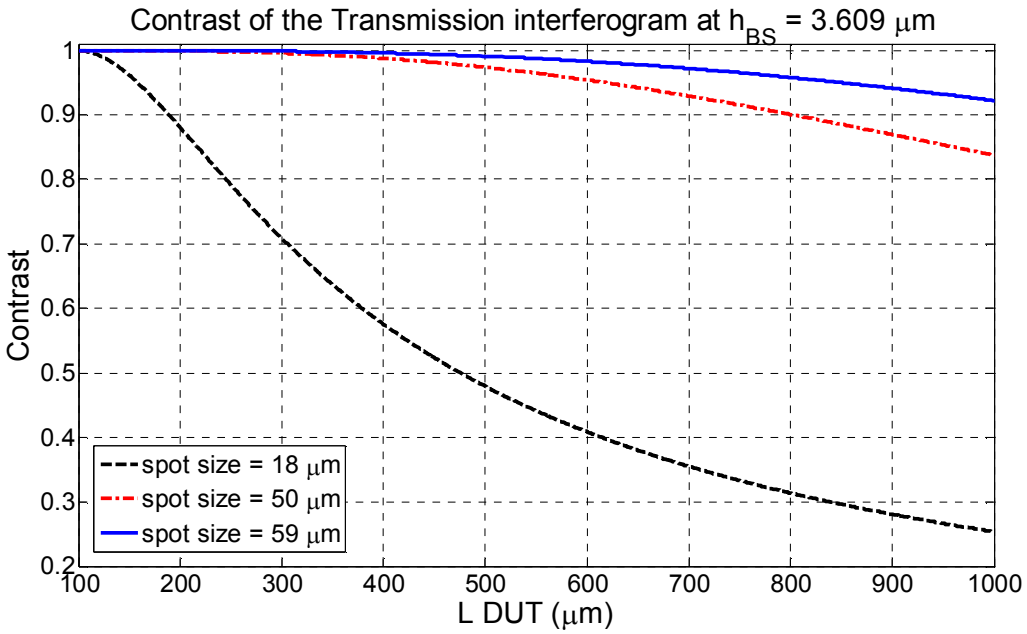

Fig. 7.15 Contrast of transmission at h_{BS} = 3.609 µm for different spot sizes.

Obviously, these results will vary if the reflectances of both the DUT and the reference mirror are different from the used values. In such case, the contrast may exhibit better performances for BS with splitting ratios different from 50-50. That is why we designed BS with ratios = 25%-75% and 75%-25%. Unequal $R_{BS} - T_{BS}$ compensates the difference between R_{DBR} and R_{DUT} which maintains the contrast unchanged.

7.3.6 Experimental results

The devices described earlier in this chapter have been fabricated and some of them have been tested. The experimental setup is schematized in Fig. 7.16. It consists of a laser source tunable in the C and L bands. Laser beam is injected to the tested device through an AR-coated lensed optical fiber of 1 mm working distance. The fiber is coupled to the laser source through a circulator to allow the measurement of the spectral interferogram of reflection. The light coupled back is measured using an optical powermeter. Both the source and the detector are connected to computer using GPIB interface for data acquisition and analysis. Both the AR-coated fiber and the test mirror are mounted each on a five axis micropositioners for precise and accurate alignement with 1 µm resolution. The device is mounted on a 2D micropositioner instead. The measurement procedure starts by the alignement of the lensed fiber in its U-groove. The test mirror is then aligned. After that, wavelength sweep is carried over the spectral range of interest; the acquired data are processed by FFT to determine the optical path difference between the tested surface and the reference mirror.

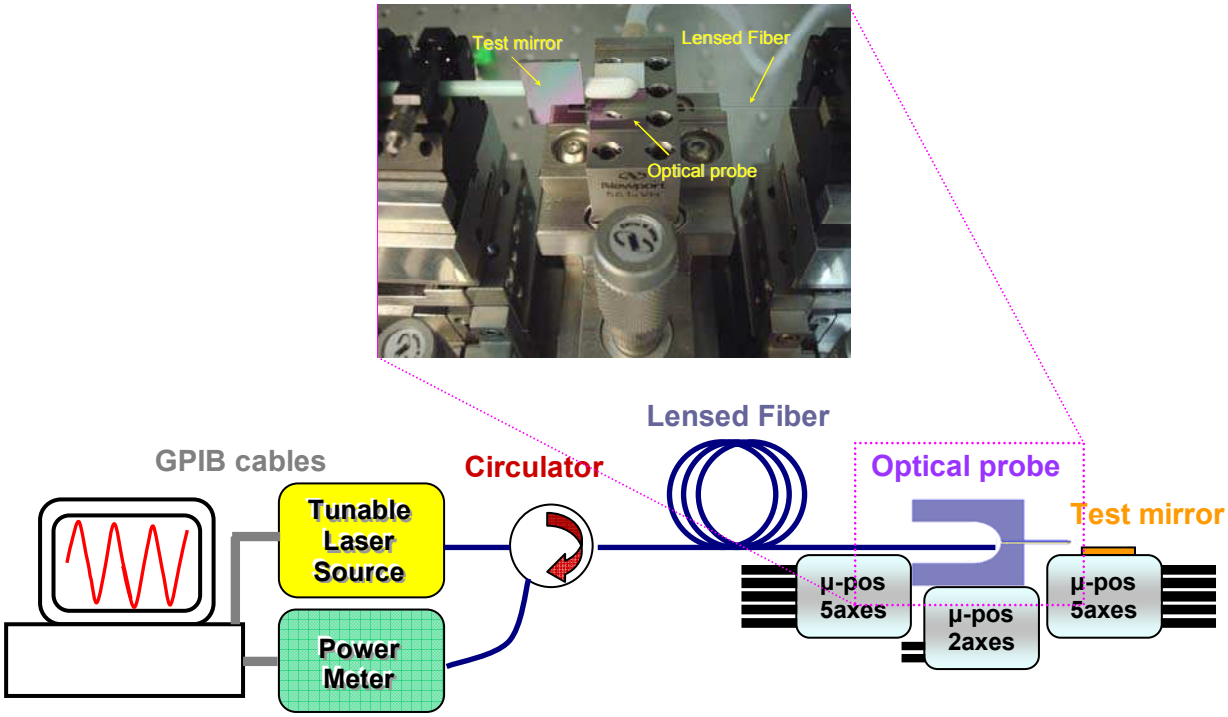

Fig. 7.16 Experimental setup used for testing the optical probes. The inset shows a zoom of the optical probe and surrounding elements in the experimental setup

We achieved measurement using two probes A and B having different BS splitting ratios (Reflectance - Transmittance=75%-25% and 25%-75%, respectively). These probes were optimized for use with low and high reflectance samples, respectively. Reflection interferograms for probe A used on a silicon wafer are shown in Fig. 7.17a for various distances *D*. Though the mismatch between the reflectances of the reference Bragg mirror (99.98%) and the test silicon wafer (R_{Si}~30%), the device exhibits a good contrast (~50%). Fig. 7.17b exhibits additional peaks related to silicon wafer thickness. The FFTs superimposed in Fig. 7.18a relate to probe B used with aluminum mirror, revealing side peaks whose location give the optical path difference and hence the distance *D*. The observed decrease in the amplitude of the side peaks is due to contrast degradation at the longest distances. This trend, graphed in Fig. 7.19, also shows that Probe A used with silicon exhibits a better performance over probe B used with aluminum. This confirms the effectiveness of optimizing the beam splitting ratios of our designs.

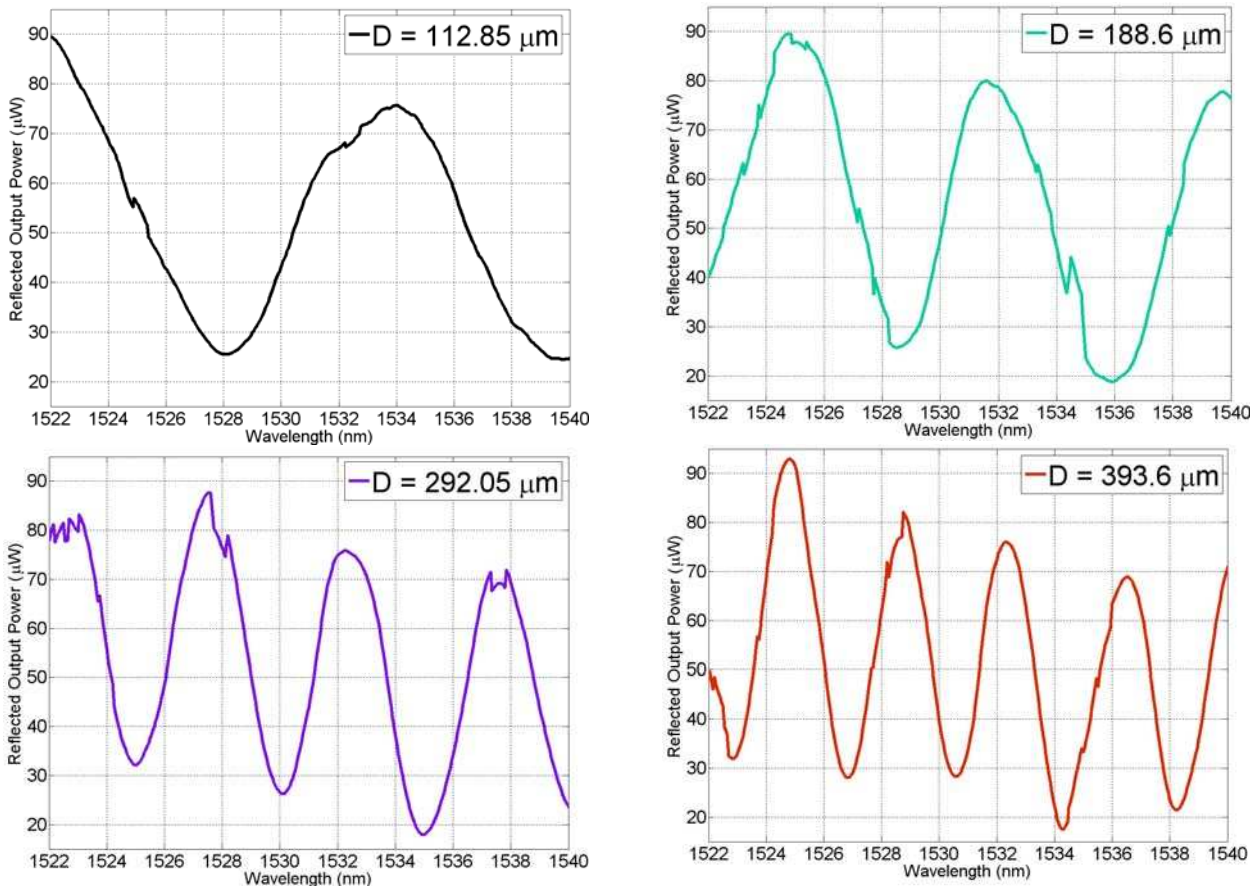

(a)

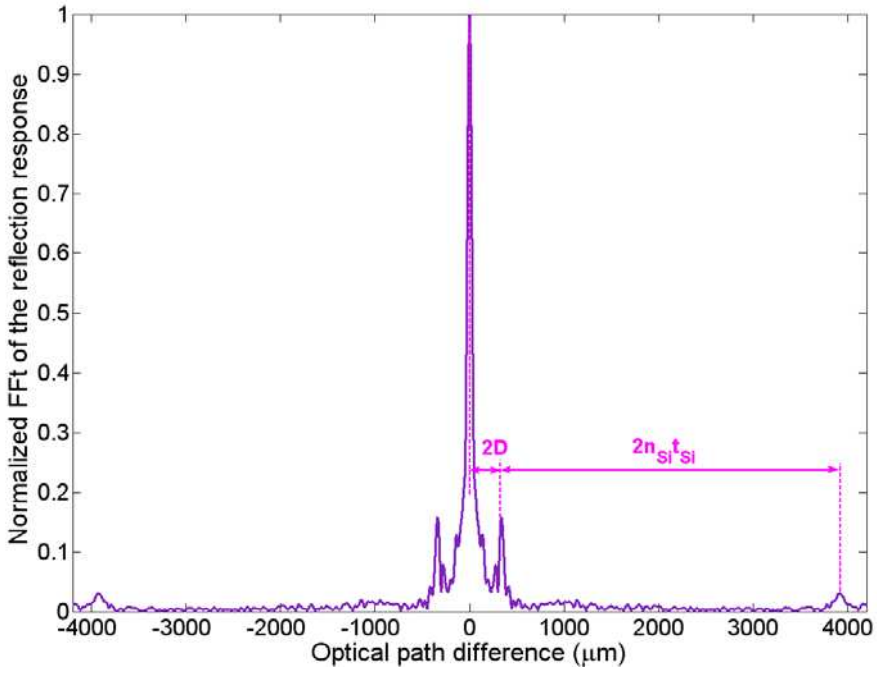

(b)

Fig. 7.17 (a) Reflection response of the optical probe A at various distances D from a silicon wafer used as reflective surface. BS splitting ratio = 75%-25%. (b) Silicon wafer used as a test mirror together with probe A. Both sample-to-surface distance (1st peak) and wafer thickness (2nd peak) are obtained from this last experiment.

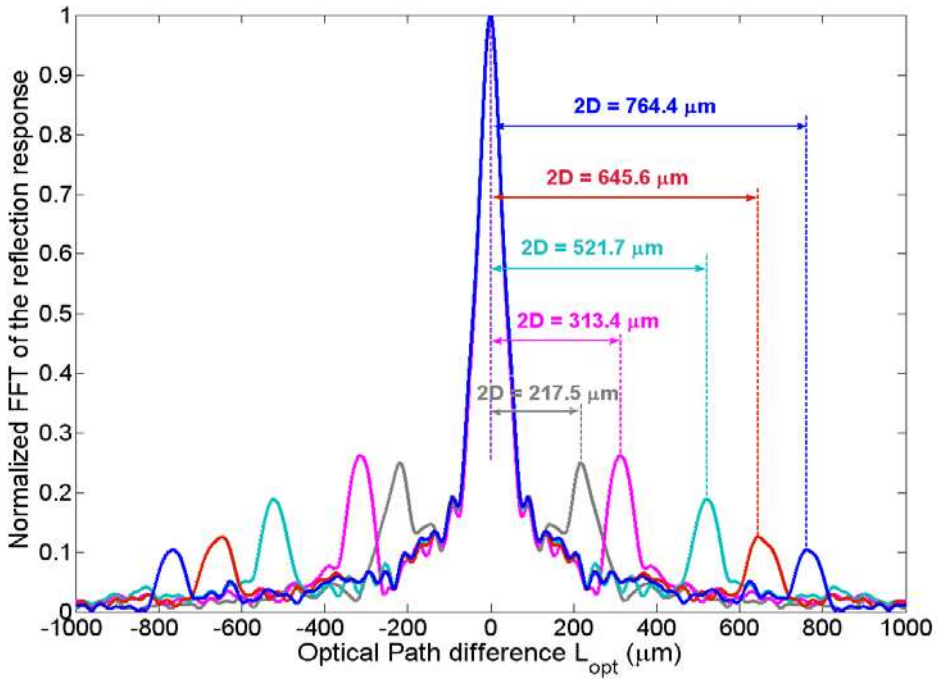

Fig. 7.18 FFT of reflection responses recorded at several path differences. Aluminum slab is used as a test mirror together with probe B.

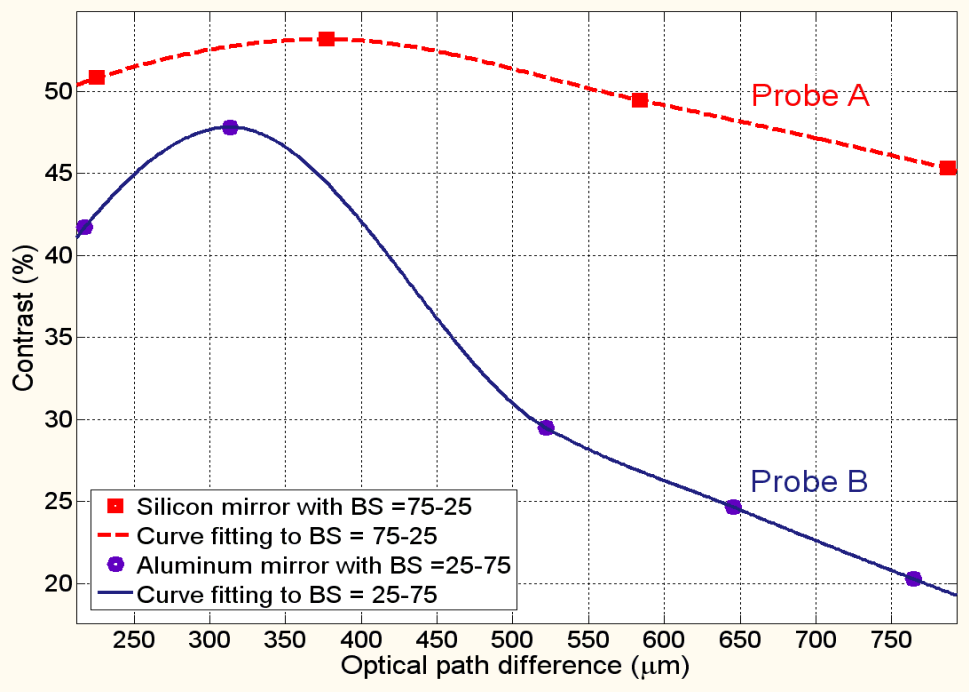

Fig. 7.19 Contrast versus optical path difference (2D) for the 2 probes deployed in our experiments. Probe A with 75%-25% splitting ratio shows a higher performance in accordance with the readily developed analytical model.

7.3.7 Experimental setup for further measurements of hole diameters

For further experimentation on the optical probe, optical fibers need to be packaged to the device so that the system becomes solidary. At this time, the system is interfaced with any other measurement setup using fiber connectors. The 4 mm length probe can be inserted in the measured

tubular hole and the form of the surface can be depicted by scanning the system over θ and Z axes. Schematic of the considered optical setup is shown in Fig. 7.20.

It is worthmentioning that such experiments will not use a tunable source and subsequent FFT. Instead, a stable monochromatic light will be used and another interferometric method will be implemented.

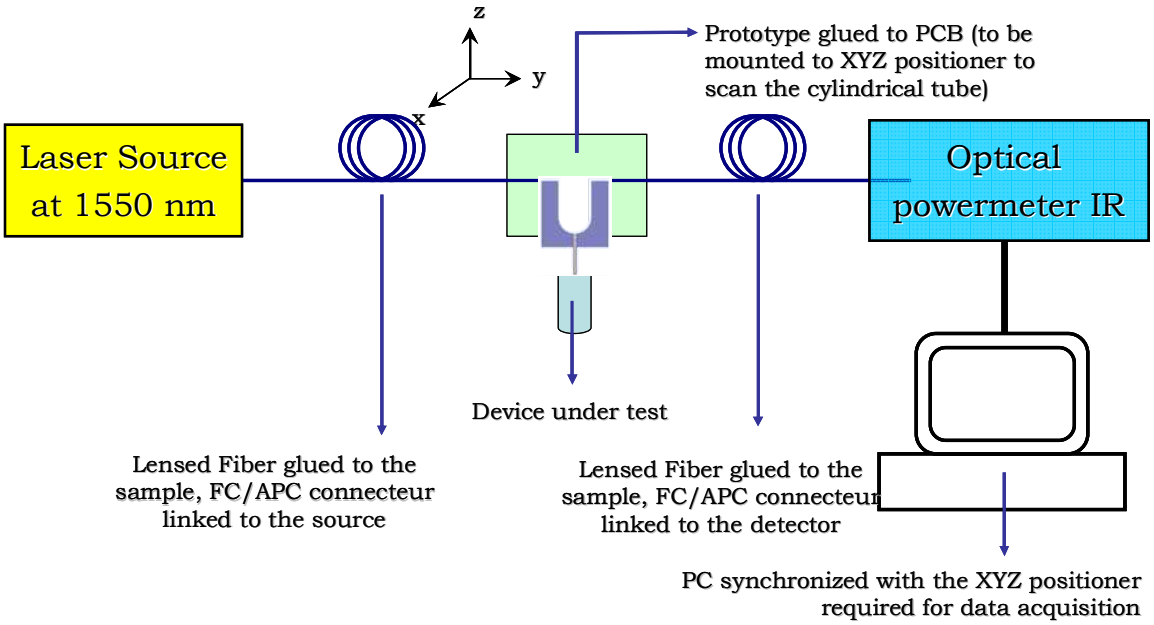

Fig. 7.20 Schematic illustration of the optical setup for measurements of the form in cylindrical tubes.

7.4 Conclusion and discussion

Though promising, results presented in this chapter are still preliminary as they are based on theoretical prediction. This research work is not yet complet and it is still going to confirm many points. Among them, we can cite: The measurements that need to be carried at LNE to determine the performance of our device for its application to diameter measurement, especially in terms of metrological performance. Another point concerns the confirmation of the measurements to be carried for the transmission response, since only operation in the reflection mode has been achieved to date. A last point of interest concerns the device with integrated ball lens for which either layout may need to be adapted or the process need to be modified.

PART IV

Concluding Remarks

Chapter 8

Conclusion and Perspectives

8.1 Conclusion

In this thesis, we presented design, modeling and measurements for different architectures of optical micro-cavities and optical interferometers.

First, we focused on the study of a new generation of FP cavities mainly based on curved Bragg mirrors. The first design based on cylindrical Bragg mirrors that help focusing light beam in one transverse plane. They exhibit a higher Q than similar cavities based on planar Bragg mirrors, the maximum recorded Q = 1999 corresponding to the minimum recorded FWHM = 0.775 nm for a device based on 4 silicon layers per mirror. In that case, the cavity length was 210 μm which is much larger than the previously reported micromachined cavities based planar Bragg mirrors. In fact, cavities with planar Bragg mirrors exhibit similar or even smaller *Q*-factors when their gap cavity length is limited to few microns. It is to be noted that the increased length is attractive for applications related to optical cavity enhancement. Beside the incremental performance improvement offered by the first architecture, it also opens the way for further exploration of physical phenomena particularly, the selective excitation of transverse modes TEM_{20}. This issue was verified both analytically and experimentally as detailed in chapter 5. In addition, selective excitation of the transverse modes was verified experimentally and this suggests potential applications for the device as a wavelength selective switch, mode selective filter or even as an Add-Drop multiplexer. The chapter is concluded with the measurement results obtained with the PS-OLCI characterization technique. The advantages and the potential directions offered by this technique are pointed out as well.

The second design also based on cylindrical Bragg mirrors; includes in addition a Fiber Rod Lens (FRL) which helps in focusing the light in both transverse planes. Since the architecture is novel, a simple model was derived to deduce the stability limits and corresponding radii of curvature. Various designs were packaged and tested experimentally to study the tendency of the Q factor versus mirror reflectance. The maximum recorded *Q* is 8818 corresponding to the minimum recorded *FWHM* = 0.177 nm for a device based on 4 silicon layers per mirror for a cavity physical length of 265.8 μm. Calculations have been done to extract the mirror effective reflectance out of the experimental results. We can conclude that this class of cavities offers the combined advantages of the high Q and the large length which is an asset for a lot of applications, notably, those based on cavity enhanced absorption spectroscopy (CEAS).

In the third part of this thesis, we focused on the application of optical interferometers. One of these applications puts the Michelson interferometer into the frame of practical application by using it as a probe for optical profiling in infra-red range. In that spectral range, the device was extensively modeled and simulated to predict its performance (visibility and percentage of power obtained in transmission and reflection interferograms) under the effect of Gaussian beam expansion and for various spot sizes. Preliminary results seem to be promising for both applications and research is still going in both of them to draw more results and conclusion.

8.2 Perspectives for the curved Fabry-Perot cavity

Following the performance recorded for the FRL cavity, the research is now open for investigation in various directions. The objective is to improve the Q-factor of the cavity and to start deploying the FP cavity into new areas where it was excluded previously because of its limited performance and its small gap length. The improvement and applicability directions can be classified into technology aspect, design aspect and application aspect. The technology aspect concerns the treatment of the FRL and the fabrication of the Bragg mirrors. The design aspect concerns the variation of the geometrical parameters. The application aspect concerns the use of the FRL cavity for environmental analysis.

Evidently, incorporating a FRL inside the curved cavity, introduces parasitic reflections at the fiber-air interfaces. This is of the residual factors that still contribute to the devices losses. One step toward performance improvement might consist of making antireflection (AR) coating for the FRL. The coating may be done using dip coating or (Atomic Layer Deposition) ALD for the FRL. Hence, parasitic reflections at the FRL interfaces will reduce.

A point to mention about the fabrication is that the DRIE step was not followed as usual by post treatment. Therefore, the mirrors sidewalls have not been smoothed. A technological improvement implies using either DRIE process using oxidation as a post treatment step for smoothing the sidewalls. Another direction consists of employing cryogenic etching to obtain a better quality for the mirrors sidewalls but this will be on the account of longer fabrication time.

Another technological direction may be followed to improve the quality of the curved mirrors. Focused Ion Beam (FIB) might be used to etch the Bragg mirrors. This results in Bragg layers with dimensions in the sub-micron range. According to our simulations, Bragg mirrors based on thin layers exhibit a large bandwidth ($\geq$ 200 nm). So, Fabry-Perot cavities, fabricated with this technique, have a strong potential in applications involving spectrometry.

Another issue is to deploy the FRL cavity into the frame of a practical application. The idea consists of creating a lab-on-chip by replacing the FRL with a microfluidic tube. The tube will achieve the same function as the FRL by focusing the light beam in the out-of-plane direction. Chemical or

biological species inserted into the tube may be analyzed through spectral analysis. The objective is to gain benefit from the large cavity length and the high Q-factor. This suggestion is supported by some simulations carried on the simple curved cavity to predict the optical loss in the cavity for under different conditions of gap length and excitation as detailed in chapter 6.

8.3 Perspectives for the optical profiler

In the project of the optical profiler, many challenges were raised up. Among them we can cite, the reduction of the probe width and the improvement of the lateral resolution. Aside from the suggested solution in the frame of the thesis, other solutions are proposed for further improvements of the device characteristics.

The reduction of the device width may be achieved by targeting operation in the reflection mode only. Thus, the width of the probe could reach 300 µm. In such case, the prototype will be designed to integrate a single optical fiber for both light injection and detection. The optical setup will be modified to contain a circulator in order to operate in the infra-red range.

The fabrication process needs to be refined to produce the deep hole of the ball lens. This in turn will permit the integration of the ball lens. On one hand, the ball lens will help in reducing the projected spot size in one direction and hence the resolution could be improved. On the other hand, the ball lens will collect the light scattered from the sample and hence the collection efficiency and the contrast could be improved.

8.4 Perspectives for the FP MEMS structures

FP cavities can be used for vibration detection. In this section, we illustrate some of the proposed designs that might be deployed to accomplish opto-mechanical transducers for vibration detection.

8.4.1 FP cavity with two MEMS mirrors

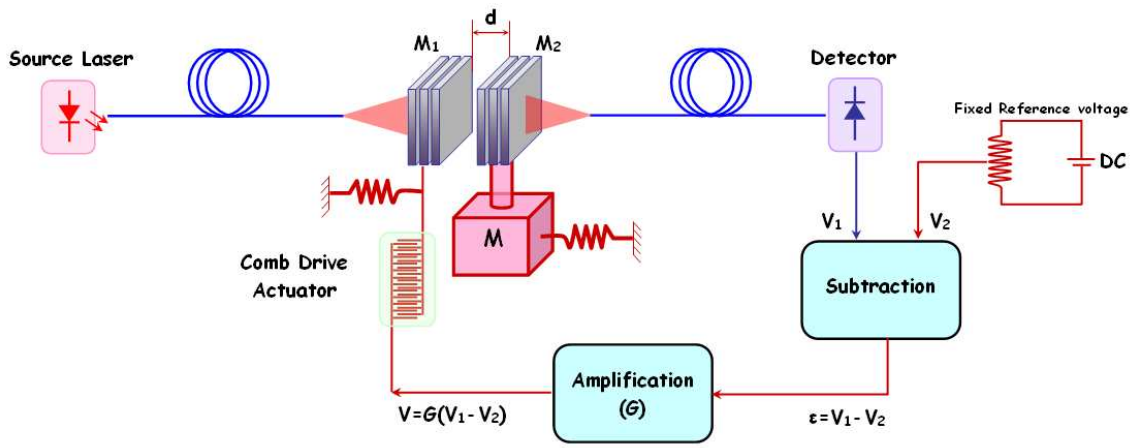

Fig. 8.1 Schematic representation of the optical vibration sensor.

Fig. 8.1 illustrates the block diagram of the proposed vibration sensor which is suitable for measurement of large amplitudes. A fiber coupled laser source injects optical power through a FP interferometer of cavity length '*d*'. An output power P_1 is obtained corresponding to this length and to the actual operating point. Under the effect of the proof mass sinusoidal motion, mirror M_2 moves and the cavity length varies and so is the interferometer output power P_1. This optical output is converted using a photodiode into an electrical signal. This signal is compared to the fixed DC reference voltage of the potentiometer. And using a subtractor, the difference signal is obtained and then amplified and fed to a group of 2 comb drive actuators. Being, attached to the interferometer mirror M_1, the actuators provide the displacement necessary to compensate the one provoked by the proof mass motion.

The amplified difference signal is an indicator for the amplitude of vibration of the proof mass. Through processing and analysis, the unknown vibration amplitude of the proof mass could be determined. Figure 8.2a shows a close up view of the optical cavity and figure 8.2b shows a global view of the cavity with the actuators.

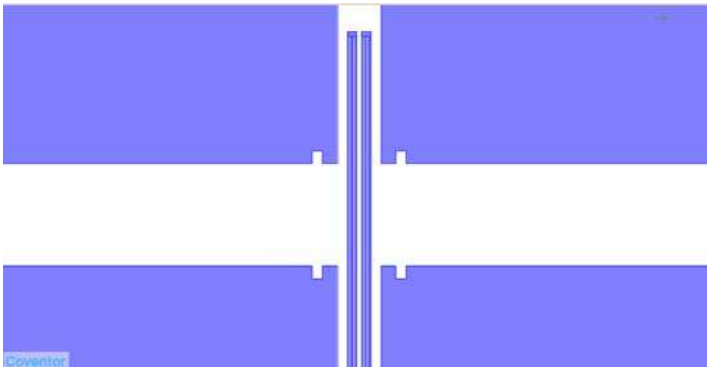

(a)

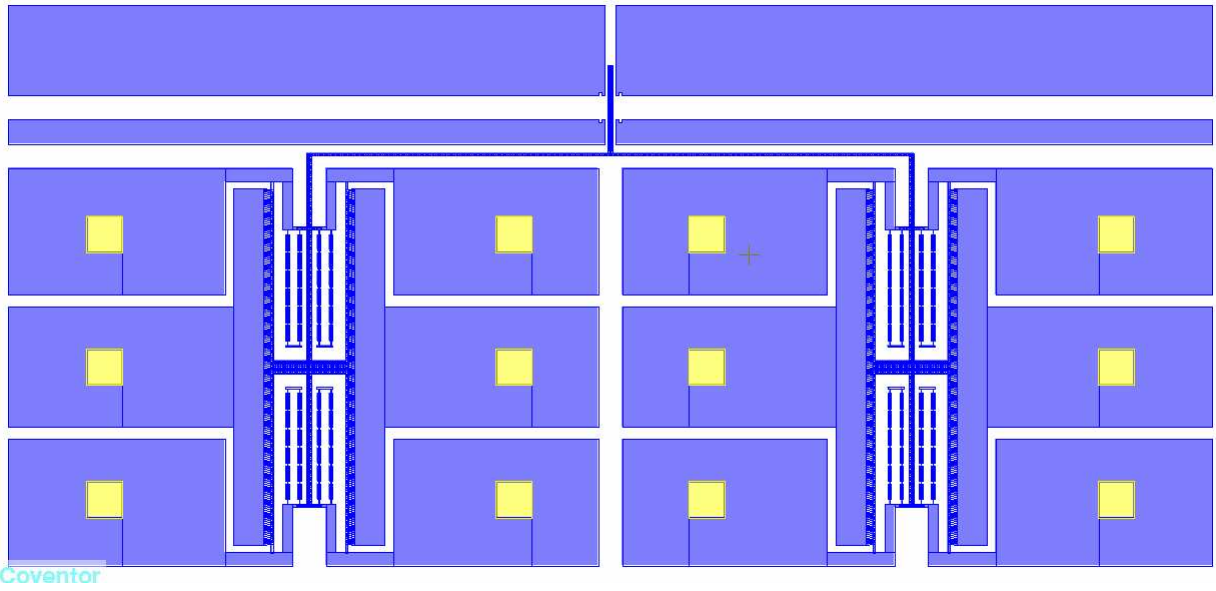

(b)

Fig. 8.2 Layout of FP cavity with two moving mirrors (a) FP cavity (b) Global view of the cavity with the actuators.

This feedback system has been implemented on MATLAB simulink as shown in figure 8.3 to design the different elements of the system: actuator, detector, subtraction and amplification circuits.

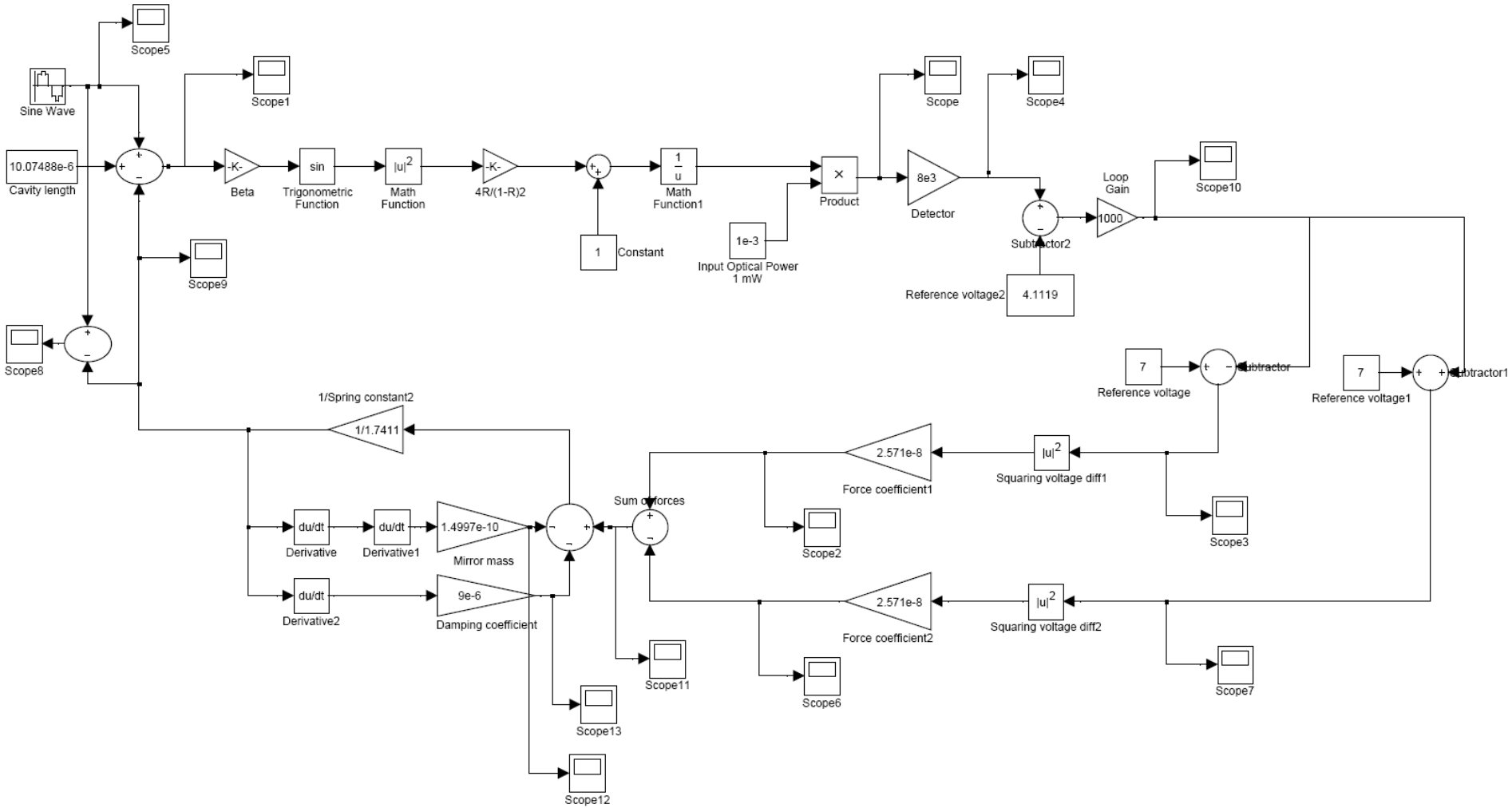

Fig. 8.3 Simulink model used to design the vibration sensor with optical feedback

8.4.2 FP with coupling mirror and coupled FP cavities

The design is based on coupled FP cavities and it acts as a sensor for the optical detection of small vibration amplitudes. The design is based on coupled FP cavities wherein the differential gap measurement might lead either to a sharp resonance peak or to mode degeneragy. Hence, the vibration amplitude can be determined. The design consists of a moving silicon slab inserted in the middle of FP cavity based on Bragg mirrors. The slab is patterned either as a Bragg mirror or as two coupled Bragg mirrors. The slab movement is controlled by a comb drive actuator. Applying AC signal voltage to the moving slab, leads to sinusoidal fluctuation of the optical power around the operating wavelength which lies at the point of highest slope on the resonator response. By treatment, we can convert the fluctuation of the optical power to corresponding vibration amplitude.

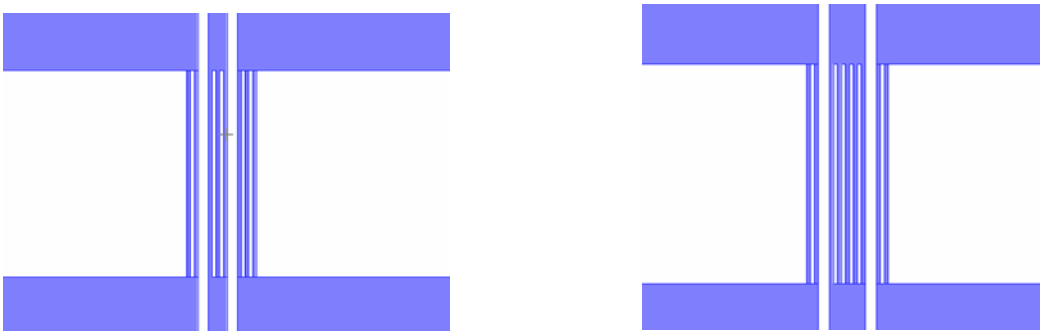

(a) (b)

Fig. 8.4 Layout of the FP cavity with (a) coupling mirror and (b) coupling cavity

8.4.3 FP with Joule heating

The design aims to compensate the technological errors translated into reduced thickness for the silicon layers. The issue has been highlighted in chapter 6 for the cylindrical Bragg mirrors where simulations show a reduction in the mirror reflectance. To calibrate this error, the device described herein has been conceived. The idea relies on the compensation of the reduced thickness by varying the refractive index through electrical current. The application of current is associated with the phenomenon of Joule heating wherein the temperature of the silicon layer increases and the refractive index increases in turn. Heating is achieved by applying an electrical current to the Bragg mirrors via pads as shown in figure 8.5b. Doing inverse calculations, we can quantify the technological error in the layers. Besides, we can tune the cavity electrically to achieve the best performance.

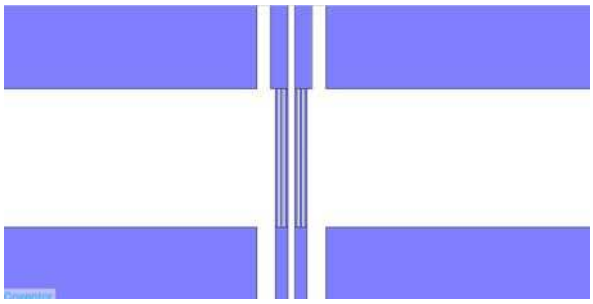

(a)

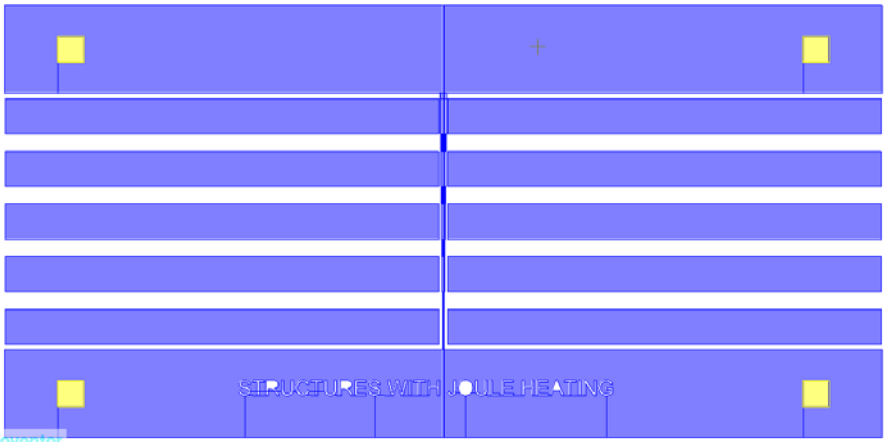

(b)

Fig. 8.5 Layout of FP cavity based on Bragg mirrors (a) FP cavity (b) Global view of the cavity with the electrical pads.

8.4.4 FP with tilted slab

The design aims to introduce a novel architecture for thermally tuned FP cavity. The design consists of a FP cavity enclosing a tilted silicon slab. The slab is tilted to avoid the creation of two parasitic FP cavities with both the left and right hand side mirrors. The tilted slab is heated by electrical current. As the current is applied, the peak of the resonance wavelength shifts due to variation of the refractive index. This way, we can achieve a thermally tuned FP cavity. The design may be adapted to function as a vibration sensor by making one of the mirrors movable. Thus, if the operating point varies under the effect of applied current, the mirror will be moved to restore the original operating point. Then, the vibration amplitude can be determined.

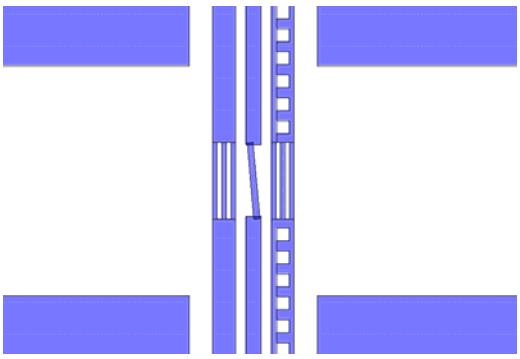

Fig. 8.6 Layout of the FP cavity with tilted slab

References

[1] M. C. Wu, O. Solgaard, and J. E. Ford, "Optical MEMS for Lightwave Communication", Journal of Lightwave Technology, Vol. 24, No. 12, pp. 4433-4454, December 2006

[2] W. Noell, P. A. Clerc, L. Dellmann, B. Guldimann, H. P. Herzig, O. Manzardo, C. R. Marxer, K. J. Weible, R. Dandliker, N. de Rooij, "Applications of SOI based optical MEMS", IEEE Journal of Selected Topics in Quantum Electronics, Vol. 8, issue 1, pp. 148-154, 2002

[3] C. Marxer, C. Thio, M.-A. Gretillat, N. F. de Rooij, R. Battig, O. Anthamatten, B. Valk, and P. Vogel, "Vertical Mirrors Fabricated by Deep Reactive Ion Etching for Fiber-Optic Switching Applications", Journal of Microelectromechanical Systems, Vol. 6, No. 3, pp. 277- 285, 1997

[4] D. Sadot and E. Boimovich, "Tunable optical filters for dense WDM networks", IEEE Communication Magasine, Vol. 36, No. 12, pp. 50–55, Dec. 1998.

[5] D. Hohlfeld, M. Epmeier and H. Zappe, "A thermally tunable, silicon-based optical filter" Sensors Actuators. A, Physical, Vol. 103, no. 1-2, pp. 93-99, 2003

[6] B. Saadany, M. Malak, M. Kubota, F. Marty, Y. Mita, D. Khalil, and T. Bourouina, "Free-space Tunable and Drop Optical Filters Using Vertical Bragg Mirrors on Silicon", IEEE Journal of Selected Topics in Quantum Electronics, Vol 12, No. 6, pp.1480-1488, 2006.

[7] M. W. Pruessner, T. H. Stievater, M. S. Ferraro, and W. S. Rabinovich, "Thermo-optic tuning and switching in SOI waveguide Fabry-Perot microcavities", Optics Express, Vol. 15, Issue 12, pp. 7557-7563 (2007)

[8] T. H. Stievater, D. Park, M. W. Pruessner, W. S. Rabinovich, S. Kanakaraju, and C. J. K. Richardson, "A microelectromechanically tunable asymmetric Fabry-Perot quantum well modulator at 1.55 μm" Optics Express, Vol. 16, Issue 21, pp. 16766-16773 (2008)

[9] J. Masson, R. St-Gelais, A. Poulin, and Y.-A. Peter, "Tunable Fiber Laser Using a MEMS-Based In Plane Fabry-Perot Filter", Journal of Quantum Electronics, vol 46, no. 9, pp.1313-1319, 2010.

[10] A. Q. Liu, "Photonic MEMS devices", CRC press, Taylor and Francis Group, 2009

[11] X. M. Zhang, A. Q. Liu, D. Y. Tang, and C. Lu, "Discrete wavelength tunable laser using microelectromechanical systems technology," Applied Physics Letters vol. 84, pp.329–331, 2004.

[12] A. Q. Liu , X. M. Zhang, D. Y. Tang and C. Lu, "Tunable laser using micromachined grating with continuous wavelength tuning," Applied Physics Letters vol. 85, pp.3684–3686, 2004.

[13] X. M. Zhang, A. Q. Liu, C. Lu, and D. Y. Tang, "Continuous wavelength tuning in micromachined Littrow external-cavity lasers," IEEE Journal of Quantum Electronics vol. 41, pp.187–197, 2005.

[14] X. M. Zhang, H. Cai, C. Lu, C. K. Chen and A. Q. Liu, "Design and experiment of 3-dimensional micro-optical system for MEMS tunable lasers," Proceedings of MEMS'2006, Turkey, 22–26, Jan.2006, pp. 830–833.

[15] L. K. Chin, A. Q. Liu, , C. S. Lim, C. L. Lin, T. C. Ayi, and P. H. Yap, "An optofluidic volume refractometer using Fabry–Pérot resonator with tunable liquid microlenses", Biomicrofluidics, Vol 4, pp. 024107-1/7, 2010

[16] R. St-Gelais, J. Masson, and Y.-A. Peter, "All-silicon integrated Fabry–Pérot cavity for volume refractive index measurement in microfluidic systems", Applied Physics Letters, Vol. 94, pp. 243905-1/3, 2009

[17] W. Z. Song, X. M. Zhang, A. Q. Liu, and C. S. Lim, "Refractive index measurement of single living cells using on-chip Fabry-Pérot cavity", Applied Physics Letters, Vol. 89, pp. 203901-1/3, 2006

[18] M.A. Perez, and A. M. Shkel, "Design and Demonstration of a Bulk Micromachined Fabry–Pérot μg-Resolution Accelerometer", IEEE Sensors Journal, Vol. 7, No. 12, pp. 1653 – 1662, December 2007

[19] K. Reddy, Y. Guo, J. Liu, W. Lee, M. Kyaw, K. Oo, X. Fan, "On-chip Fabry–Pérot interferometric sensors for micro-gas chromatography detection", Sensors and Actuators B 159, pp.60-65, (2011)

[20] H. Alause, F. Grasdepot, J. P. Malzac, W. Knap, and J. Hermann, "Micromachined optical tunable filter for domestic gas sensors," Sensors and Actuators B, Chemical, vol. B43, pp. 18–23, 1997.

[21] G. Lammel, S. Schweizer, P. Renaud, "MEMS infrared gas spectrometer based on a porous silicon tunable filter", The 14th IEEE international conference on Micro Electro Mechanical Systems MEMS 2001.

[22] J. T. Verdeyen, " Laser Electronics," Prentice Hall, New Jersey, 3rd edition, 1995

[23] W. Liu and J. J. Talghader, "Thermally invariant dielectric coatings for micromirrors," Applied Optics, Vol. 41, pp. 3285–3293, June 2002.

[24] C. Zener, Physical Review 53, 90 (1938).

[25] D.F. McGuigan, C.C. Lam, R.Q. Gram, A.W. Hoffman, D.H. Douglas, and H.W. Gutche, "Measurements of the mechanical Q of single-crystal silicon at low temperatures", Journal of Low Temperature Physics, Vol. 30, pp. 621-629, 1978.

[26] F. Brückner, D. Friedrich, T.Clausnitzer, M. Britzger, O. Burmeister, K. Danzmann, E.-B. Kley, A. Tünnermann, and R. Schnabel, "Realization of a Monolithic High-Reflectivity Cavity Mirror from a Single Silicon Crystal", Physical Review Letters 104, pp. 163903/1-4 2010.

[27] G.M. Harry, A.M. Gretarsson, P.R. Saulson, S.E. Kittelberger, S.D. Penn, W.J. Startin, S. Rowan, M.M. Fejer, D.R.M. Crooks, G. Cagnoli, J. Hough and N. Nakagawa, "Thermal noise in

interferometric gravitational wave detectors due to dielectric optical coatings", Classical and Quantum Gravity, Vol. 19, pp. 897-917, 2002.

[28] D. Kleckner and D. Bouwmeester, "Sub Kelvin optical cooling of a micro-mechanical resonator", Nature 444, pp. 75-78, 2006.

[29] O. Arcizet, et al., "Radiation-pressure cooling and optomechanical instability of a micromirror", Nature 444, pp.71-74, 2006.

[30] H. Mabuchi and A.C. Doherty, "Cavity quantum electrodynamics: coherence in context", Science 298, pp. 1372-1377, 2002.

[31] K.J. Vahala, "Optical Microcavities", Nature 424, pp. 839-846, 2003.

[32] D. K. Armani, T. J. Kippenberg, S. M. Spillane and K. J. Vahala, "Ultra-high-*Q* toroid microcavity on a chip", Nature 421, pp. 925-928, 2003.

[33] D. W. Vernooy, V. S. Ilchenko, H. Mabuchi, E. W. Streed, and H. J. Kimble, "High-*Q* measurements of fused-silica microspheres in the near infrared", Optics Letters, Vol. 23, Issue 4, pp. 247-249 (1998)

[34] D.R. Burnham and D. McGloin, "Holographic Optical Trapping of Aerosol Droplets", Optics Express, Vol. 14, pp. 4176-4182, 2006.

[35] D. Collin, F. Ritort, C. Jarzynski, S.B. Smith, I. Tinoco, Jr and C. Bustamante, "Verification of the Crooks fluctuation theorem and recovery of RNA folding free energies", Nature 437, pp. 231-234, 2005.

[36] S. Kassi, M. Chenevier, L. Gianfrani, A. Salhi, Y. Rouillard, A. Ouvrard, and D. Romanini, "Looking into the volcano with a Mid-IR DFB diode laser and Cavity Enhanced Absorption Spectroscopy", Optics Express, Vol. 14, Issue 23, pp. 11442-11452, 2006.

[37] J. M. Langridge, T. Laurila, R. S. Watt, R. L. Jones, C. F. Kaminski, and J. Hult, "Cavity enhanced absorption spectroscopy of multiple trace gas species using a supercontinuum radiation source", Optics Express, Vol. 16, Issue 14, pp. 10178-10188 (2008)

[38] M.W. Pruessner, T. H. Stievater, and W.S. Rabinovich, "In-plane microelectromechanical resonator with integrated Fabry-Perot cavity," Applied Physics Letters 92, 081101, 2008.

[39] M. W. Pruessner, T. H. Stievater, and W. S. Rabinovich, "Integrated waveguide Fabry-Perot microcavities with silicon/air Bragg mirrors", Optics Letters 32, 533-535, 2007.

[40] A. Lipson and E. M. Yeatman, "A 1-D Photonic Band Gap Tunable Optical Filter in (110) Silicon" Journal of Microelectromechanical Systems, vol. 16, no.3, pp. 521-527, 2007.

[41] http://www.rp-photonics.com/optical_resonators.html

[42] D. G. Rabus, "Integrated Ring Resonator. The Compedium", Springer, 2007.

[43] http://web.mit.edu/hujuejun/www/Teaching/3.46%20Photonic%20Materials%20and%20Devices/Optical%20Resonators.ppt

[44] C. Fabry and A. Perot, “A Multipass Interferometer,” Annales de Chimie et de Physique, vol. 16, pp. 115, 1899.

[45] Dominik G. Rabus, “Realization of Optical Filters using Ring Resonators with integrated semiconductor optical Amplifier in GaInAsP/InP”, PhD thesis, Technical University of Berlin, 2002

[46] Herbert Venghaus, “Wavelength Filters in Fibre Optics”, springer, 2006

[47] John Heebner, Rohit Grover, Tarek A. Ibrahim, “Optical Microresonators: theory, fabrication and applications”, springer , 1st edition, 2008

[48] Coastas M. Soukoulis, “Photonic crystals and light localization in the 21st century”, Kluwer Academic publisher, The Netherlands, 2001

[49] V.S. Ilchenko, A.B. Matsko, “Optical resonators with whispering-gallery modes-part II: applications”, Journal of Selected Topics in Quantum Electronics, Vol. 12 Issue 1, pp. 15 - 32 , 2006

[50] Yu A Anan'ev, “Unstable resonators and their applications (review)”, Soviet Journal of Quantum Electronics, Vol. 1 pp. 565, 1972

[51] A. Lipson, and E. M. Yeatman, "Low-loss one-dimensional photonic bandgap filter in (110) silicon," Optics Letters 31, 395-397 (2006).

[52] John D. Joannopoulos, “Photonic crystals: Molding the flow of light”, Princeton University Press, New Jersey, 2md edition, 2008

[53] http://web.mit.edu/hujuejun/www/Teaching/3.46%20Photonic%20Materials%20and%20Devices/Fiber%20Optics%20&%20Photonic%20Crystals.ppt

[54] http://www.faculty.iu-bremen.de/dknipp/c320352/Projects/Presentations%202005/DP%20Fiber%20Bragg%20Grating.pdf

[55] http://www.broptics.com/data/FBG_and_Applications.ppt

[56] E. A. J. Marcatili, “Bends in Optical Dielectric Guides,” The Bell System Technical Journal, vol. 48, pp. 2103-2132, 1969

[57] Kerry Vahala, “Optical Microcavities: Advanced series in applied physics, volume 5”, World Scientific Publishing, California, 2004

[58] http://metrology.hut.fi/courses/s108-j/Nano2.pdf

[59] Michael Bass, “Handbook of Optics : Devices, Measurements and Properties” Volume II, McGraw-Hill, 2nd edition, 1995 (Michelson and others)

[60] Michael Bass, “Handbook of Optics : Devices, Measurements and Properties” Volume I, McGraw-Hill, 2nd edition, 1995 (FP)

[61] Wolfgang Osten, “Optical inspection of Microsystems”, CRC Taylor and Francis, 1st edition, 2007

[62] P. Hariharan, “Optical Interferometry”, Academic Press, ELsevier, 2nd edition, 2003

[63] Eugene Hecht, “Optics”, Pearson Education, San Francisco, 4th edition, 2002

[64] Y. Ohtuka, H. Nishikawa, T. Koumura, T. Hattori, “2-Dimensional Optical Scanner Applying a Torsional Resonator with 2 Degrees of Freedom”, In Proceedings of IEEE: Micro-electro-Mechanical Systems, MEMS'95, pp. 306-309, 1995

[65] W. Piyawattanametha, P. Patterson, G.D. Su, H. Toshiyoshi, M.C. Wu, “Surface- and Bulk-Micromachined Two-Dimensional Scanner Driven by Angular Vertical Comb Actuators”, Journal of Microelectromechanical Systems 14 (6), pp. 1329-1338, 2005

[66] T. Bourouina, H. Fujita, G. Reyne, M. E. Motamedi, Chapter 7 « Optical Scanning » in MOEMS – Micro-Opto-Electro-Mechanical Systems, M.E. Motamedi Editor, SPIE Press, 2005

[67] Y. Ohira, A. Checkovskiy, T. Yamanoi, T. Endo, H. Fujita, H. Toshoyoshi, “A High-Power Handling MEMS Optical Scanner for Display Applications”, In Proceedings of IEEE: IEEE/LEOS Internationall Conference on Optical MEMS and Nanophotonics, pp. 70-71, 2008

[68] H. Choo, D. Garmire, J. Demmel, R.S. Muller, “Simple Fabrication process for Self-Aligned High-Performance Microscanners -Demonstrated Use to Generate 2-D Ablation Pattern”, Journal of Microelectromechanical Systems 16 (2), pp. 260-268, 2007

[69] D.L. Dickensheets, G.S. Kino, “Silicon-micromachined scanning confocal optical microscope", Journal of Micromechanical Systems, Vol. 7, No. 1, pp. 38-47, 1998

[70] H. Miyajima, K. Murakami, M. Katashiro, “MEMS Optical Scanner for Microscopes”, IEEE Journal of Selected Topics in Quantum Electronics, Vol. 10, No. 3, pp. 514-527, 2004

[71] W. Piyawattanametha, P. Patterson, G.D. Su, H. Toshiyoshi, M.C. Wu, “A MEMS Non-Interferometric Differential Confocal Scanning Optical Microscope”, In Proceedings of: The 8th International conference on Solid-State Sensors, Actuators, and Microsystems (Transducers 2001 & Eurosensors XV), pp. 590-593, 2001

[72] M. Zara, S. Yazdanfar, K.D. Rao, J.A. Izatt, S.W. Smith, "Electrostatic micromachine scanning mirror for optical coherence tomography," Optics Letters 28, pp. 628-630, 2003

[73] W. Jung, J. Zhang, L. Wang, P. Wilder-Smith, Z. Chen, D.T. McCormick, N.C. Tien, “Three-Dimensional Optical Coherence Tomography Employing a 2-Axis Microelectromechanical Scanning Mirror”, IEEE Journal of Selected Topics in Quantum Electronics, Vol 11, No. 4, pp. 806-810, 2005

[74] K. Kumar, J.C. Condit, A. McElroy, N.J. Kemp, K. Hoshino, T.E. Milner, X. Zhang, "Forward-Imaging swept Source Optical Coherence Tomography using Silicon MEMS Scanner for High-Speed 3-D Volumetric Imaging", In Proceedings of IEEE, IEEE/LEOS International Conference on Optical MEMS and Nanophotonics pp. 10-11, 2007

[75] http://inst.eecs.berkeley.edu/~ee233/sp06/lectures/233-Optical_MEMS.pdf

[76] Digital Light Processing (DLP) technology, Texas Instruments DMD chip, online: http://dlp.com/dlp_technology/default.asp

[77] A. Yariv, Quantum Electronics, John Wiley & Sons, 3rd edition, 1989.

[78] Bahaa E. A. Saleh and Malvin Carl Teich, "Fundamentals of Photonics", 1991 John Wiley & Sons, USA, 1991

[79] H. A. Macleod, "Thin Film Optical Filters", Institute of Physics Publishing, 3rd edition, 2001

[80] K. Zandi, B. Wong, J. Zou, R. V. Kruzelecky, W. Jamroz and Y.-A. Peter, "In-Plane Silicon-On-Insulator Optical MEMS Accelerometer Using Waveguide Fabry-Perot Microcavity With Silicon/Air Bragg Mirrors", in Proceedings of 23rd IEEE International Conference Micro Electro Mechanical Systems, MEMS'2010, pp. 839-842, 2010.

[81] S. Yun and J. Lee, "A Micromachined In-Plane Tunable Optical Filter Using the Thermo-optic Effect of Crystalline Silicon" Journal of Micromechanics and Microengineering, vol. 13, pp.721-725, 2003.

[82] M.W. Pruessner, T.H. Stievater, and W.S. Rabinovich, "Reconfigurable Filters Using MEMS Resonators and Integrated Optical Microcavities", in Proceedings of 21st IEEE International Conference Micro Electro Mechanical Systems, MEMS'2008, pp.766-769, 2008.

[83] M. Malak, N. Pavy, F. Marty, Y.-A. Peter A.Q. Liu and T. Bourouina "Micromachined Fabry–Perot resonator combining submillimeter cavity length and high quality factor", Applied Physics Letters , vol. 98, No.22, pp. 211113-1/3, 2011

[84] T. Bourouina, T. Masuzawa, H. Fujita"The MEMSNAS Process: Microloading Effect for Micromachining 3D structures of Nearly All Shapes", Journal of Microelectromechanical Systems, Vol. 13 N° 2, pp. 190-199, 2004.

[85] A. Yariv, "Quantum Electronics", John Wiley & Sons (1989)

[86] F.Marty, L.Rousseau, B.Saadany, B.Mercier, O.Français, Y.Mita, T.Bourouina, "Advanced Etching of Silicon Based On Deep Reactive Ion Etching For Silicon High Aspect Ratio Microstructures and Three-Dimensional Micro and NanoStructures", Microelectronics Journal, Vol. 36, No.7, pp. 673-677, 2005.

[87] Anne-Françoise Obaton, Yacouba Sanogo, Jimmy Dubard, "Développement d'un moyen d'interrogation de bio-capteurs photoniques sur la base d'un interferomètre en lumière incohérente", Revue Française De Métrologie, n° 26, Volume 2011-2, pp. 11-20

[88] Anne-Françoise Obaton, "Développement au LNE d'un interferometer en lumière incohérente sensible à la phase", Revue Française De Métrologie, n° 16, Volume 2008-4, pp. 21-35

[89] Timothy McGarvey, André Conjusteau, and Hideo Mabuchi, "Finesse and sensitivity gain in cavity-enhanced absorption spectroscopy of biomolecules in solution", Optics Express, Vol. 14, Issue 22, pp. 10441-10451, 2006

[90] Joshua B. Paul, Larry Lapson, and James G. Anderson, "Ultrasensitive Absorption Spectroscopy with a High-Finesse Optical Cavity and Off-Axis Alignment", Applied Optics, Vol. 40, Issue 27, pp. 4904-4910, 2001

[91] W. Liu and J.J. Talghader, "Spatial-Mode Analysis of Micromachined Optical Cavities Using Electrothermal Mirror Actuation", Journal of Microelectromechanical Systems, vol. 15, no.4, pp. 777-785, 2006.

[92] B.J. Kim, T. Masuzawa, T. Bourouina, "The vibroscanning method for the measurement of micro-hole profiles", Measurement Science and Technology, Vol.10, pp. 697-705, 1999

[93] P. Ruther, S. Spinner, M. Cornils, O. Paul, "Cantilever-Based Tactile Sensor with Improved Sensitivity for Dimensional Metrology of Deep Narrow Drillings", Proceedings of Transducers, pp. 1469-1472, 2007

[94] Y. Hamaguchi, M. Kubota, J.-B. Pourciel, Y. Mita, "High-aspect-ratio vertical surface profiler using sensitive displacement detection by optomecanical probe", in Proceedings of 21st IEEE International Conference Micro Electro Mechanical Systems, MEMS'2008, pp. 884-887, 2008

[95] E. Peiner, L. Doering, "Characterization of diesel injectors using piezoresistive sensors", Proceedings of IEEE Sensors, Vol. 23, pp. 2083-2087, 2010

[96] O. Manzardo, H. P. Herzig, C. Marxer and N. F. de Rooij, "Miniaturized time scanning Fourier transform spectrometer based on silicon technology", Optics Letters, Vol. 24, No. 23, pp.1705-1707, 19999

[97] B. Saadany, T. Bourouina, M. Malak, M. Kubota, Y. Mita, and D. Khalil, "A Miniature Michelson Interferometer using Vertical Bragg Mirrors on SOI" , IEEE/LEOS International Conference on Optical MEMS and Their Applications, 2006, pp. 50-51

[98] B. Saadany, H. Omran, M. Medhat, F. Marty, D. Khalil, T. Bourouina, "MEMS tunable Michelson interferometer with robust beam splitting architecture", IEEE/LEOS International Conference on Optical MEMS and Nanophotonics, 2009, pp.49-50

Author's publication

Journal papers

1. **"Study of Black Silicon Obtained by Cryogenic Plasma Etching - Approach to Achieve the Hot Spot of a Thermoelectric Energy Harvester"**
   Kim Ngoc Nguyen, David Abi-Saab, Philippe Basset,Elodie Richalot, Maurine Malak, Nicolas Pavy, Frédéric Flourens, Frédéric Marty, Dan Angelescu, Yamin Leprince-Wang,Tarik Bourouina
   Submitted for publication in the Journal of Microsystem Technologies.

2. **"Cylindrical Surfaces Enable Wavelength-Selective Extinction and Sub-0.2 nm Linewidth in 250 µm - Gap Silicon Fabry-Pérot Cavities"**
   Maurine Malak, Frédéric Marty, Nicolas Pavy, Yves-Alain Peter, Ai-Qun Liu, Tarik Bourouina
   Accepted for publication in the Journal of Microelectromechanical Systems - JMEMS.

3. **"Micromachined Fabry–Perot resonator combining submillimeter cavity length and high quality factor"**
   M. Malak, N. Pavy, F. Marty, Y.-A. Peter A.Q. Liu and T. Bourouina
   Published in « Applied Physics Letters », volume 98, No.22, (2011) pp. 211113-1/3.

4. **"Design, modeling and characterization of stable, high Q-factor curved FabryPérot cavities"**
   Maurine Malak, Nicolas Pavy, Frédéric Marty, Elodie Richalot, Ai-Qun Liu and Tarik Bourouina
   Published in the Journal of Microsystem Technologies, Volume 17, No. 4 (2011), pp. 543-552.

5. **"Design of CWDM Multiplexers Based on Series Coupled Ring Resonators: Analysis, Potential and Prospects on MEMS Fabrication Technologies"**
   Maurine Malak, Ahmed H Morshed, Khaled Hassan, Tarik Bourouina, Hanan Anis, Diaa Khalil
   Published in the Journal of Microsystem Technologies, Volume 16, No. 7 (2010), pp. 1139-1156

6. **"Analysis of Novel Building Blocks for Photonic MEMS Using Deep 1D Photonic Crystals"**
   Maurine Malak, François Duport, Hong Cai, Bassam Saadany, Pierre Nicole, Jean-Luc Polleux, Frédéric Marty, Stéphane Formont, Ai Qun Liu, Tarik Bourouina
   Published in Advanced Material Research, Volume 74 (2009), p 55-58
   Also: International Conference on Materials for Advanced Technologies, ICMAT 2009, Singapour, 28 June – 3 July 2009

7. **"Design of an arrayed waveguide grating optical demultiplexer for CWDM applications"**
   Khaled Hassan, Diaa Khalil, Maurine Malak, Hanan Anis
   Published in the Journal of Optics: A Pure and Applied Optics, Volume 10, Issue 7, 2008, pp. 075307.

8. **"Free-Space Tunable And Drop Optical Filters Using Vertical Bragg Mirrors On Silicon"**
   B. Saadany, M. Malak, M. Kubota, F. Marty,Y. Mita, D. Khalil, and T. Bourouina
   IEEE Journal of Selected Topics in Quantum Electronics, Volume 12, Issue 6, Part 2, Nov.-dec. 2006 Page(s):1480 – 1488

Conference papers

9. **"All-Silicon Interferometric Optical Probe For Non-Contact Dimensional Measurments In Confined Environments"**
   Maurine Malak, Frederic Marty, Hichem Nouira, José Salgado, and Tarik Bourouina

Accepted for publication in the 25th IEEE international conference on Micro Electro Mechanical Systems (MEMS 2012)

10. **"Mode Selective Optical Filtering and Wavelength Switching Through Fabry-Pérot Cavity With Cylindrical Reflectors"**
M. Malak, N. Pavy, F. Marty, T. Bourouina
Published in the 16th International conference on Solid-State Sensors, Actuators and Microsystems (Transducers 2011), Beijing, China, 5-9 June 2011, pp. 534-537

11. **"Study of Black Silicon Obtained by Deep Reactive Ion Etching – Approach to Achieving the Hot Spot of a Thermoelectric Energy Harvester"**
K.N. Nguyen, D.Abi-Saab, M. Malak, P. Basset, E. Richalot, N. Pavy, F. Flourens, F. Marty, D. Angelescu, Y. Leprince-Wang and T.Bourouina
Symposium on Design, Testing, Integration and Packaging conference, DTIP 2011, Aix-en-Provence, France, 11-13 May 2011

12. **"Stable, High-Q Fabry-Pérot Resonators With Long Cavity Based On Curved, All-Silicon, High Reflectance Mirrors"**
M. Malak, N. Pavy, F. Marty, Y.-A. Peter A.Q. Liu and T. Bourouina
Published in the 24th IEEE international conference on Micro Electro Mechanical Systems (MEMS 2011), Cancun, Mexico, 23-27 January 2011, pp. 720-723

13. **"Design and Modeling of Stable, High Q-factor Curved Fabry-Pérot cavities"**
Maurine Malak, Tarik Bourouina, Nicolas Pavy, Elodie Richalot, Frédéric Marty and Ai-Qun Liu
Symposium Design, Testing, Integration and Packaging Conference, DTIP 2010, Seville, Spain, 5-7 May 2010, pp. 165-170

14. **"Design of CWDM Multiplexers Based on Series Coupled Ring Resonators: Analysis and Potential of MEMS Technologies"**
Maurine Malak, Ahmed Hisham Morshed, Khaled Hassan, Tarik Bourouina, Hanan Anis and Diaa Khalil
Symposium on Design, Testing, Integration and Packaging Conference, DTIP 2009, Rome, Italy, 1-3 Avril 2009, pp.209-213

15. **"A miniature Michelson Interferometer using vertical Bragg Mirrors on SOI"**
B. Saadany, T. Bourouina, M. Malak, M. Kubota, Y. Mita, D. Khalil
IEEE Optical MEMS 2006, 21 - 24 Août 2006 Big Sky, Montana, USA.

16. **"An all Silicon Micro-machined Add-Drop Optical Filter"**
B. Saadany, D. Khalil, M. Malak, M. Kubota, F. Marty, Y. Mita, T. Bourouina
IEEE Optical MEMS 2006, 21 - 24 Août 2006 Big Sky, Montana, USA.

17. **"Electrostatically-tuned Optical Filter Based on Silicon Bragg Reflectors"**
B. Saadany, M. Malak, F. Marty, Y. Mita, D. Khalil, T. Bourouina
IEEE Optical MEMS 2006, 21 - 24 Août 2006 Big Sky, Montana, USA.

Book chapter

18. **"MEMS Deep 1D Photonic Crystals"**
Maurine Malak and Tarik Bourouina, accepted for publication in Photonic Crystals/Book 1 published by Intech, 2011

Résumé

Ce travail de recherche a été mené afin d'introduire une nouvelle classe de résonateurs Fabry-Pérot (FP): Les cavités FP incurvées basées sur des miroirs de Bragg sans revêtement, de forme cylindrique et obtenues par micro-usinage du silicium. Une autre spécificité est la longueur de la cavité assez grande (L> 200 μm) combinée à un haut facteur de qualité Q (jusqu'à 10^4), pour répondre aux applications de type spectroscopique d'absorption améliorée par résonance optique, dans laquelle le produit est Q.L une figure de mérite. Dans ce contexte, l'architecture de base a été modélisée analytiquement pour déterminer les modes transverses d'ordre élevé soutenus par de telles cavités. Par conséquent, les conditions expérimentales qui conduisent à une excitation préférentielle (ou rejet) de ces modes ont été testées expérimentalement menant à la validation de notre modèle théorique et à une meilleure compréhension du comportement de la cavité. Une seconde architecture, basée sur la cavité FP incurvée avec une lentille cylindrique a été développée dans le but de fournir une architecture plus stable. Cette dernière a été également modélisée, fabriquée et caractérisée menant à l'amélioration attendue en termes de performances.

Enfin, comme complément à notre étude sur les résonateurs, nous avons commencé à explorer les applications des interféromètres optiques à base de miroirs de Bragg en silicium. À cette fin, un microsystème de mesure optique a été conçu, fabriqué et caractérisé, il consiste en une sonde optique pour la profilométrie de surface dans des milieux confinés, basé sur un interféromètre de Michelson monolithique en silicium.

Abstract

This research work has been conducted to introduce a novel class of Fabry-Perot (FP) resonators: Curved FP cavity based on coating-free Bragg mirrors of cylindrical shape, obtained by silicon micromachining. Another specificity is the rather large cavity lengths (L>200 μm) combined with high quality factor Q (up to 10^4), for the purpose of applications requiring cavity enhanced absorption spectroscopy, in which the product Q.L is a figure of merit. In this contest, the basic architecture has been modeled analytically to know the high order transverse modes supported by such cavities. Hence, the experimental conditions which lead to preferential excitation (or rejection) of these modes have been tested experimentally leading to the validation of our theoretical model and to a better understanding of the cavity behaviour. A second architecture, based on the curved FP together with a fiber rod lens has been developed for the purpose of providing stable designs. It was also modeled, fabricated and characterized leading to the expected performance improvements.

Finally, as a complement to our study on resonators, we started exploring applications of optical interferometers based on similar micromachined silicon Bragg mirrors. For this purpose, an optical measurement microsystem was designed, fabricated and characterized; it consists of an optical probe for surface profilometry in confined environments, based on an all-silicon Michelson interferometer.